Finite Reynolds number effects in fluid mixtures: an investigation using numerical simulation methods.

Vivien Mary Kendon

Thesis submitted for the degree of Doctor of Philosophy

Department of Physics and Astronomy
University of Edinburgh
1999

Abstract

The scaling theory of the spinodal decomposition of a symmetric binary fluid mixture in the inertial region has been reviewed, and extended by considering energy balance, as well as the momentum balance described by the Navier-Stokes equation (NSE). The prediction for the asymptotic growth rate of the size of the separating fluid domains is $\sim t^{2/3}$, as in simple scaling theory, but the ratio of the nonlinear to viscous terms in the NSE (the Reynolds number) is predicted to remain finite. This is due to the viscous term remaining important to the system dynamics, in contrast to simple scaling theory where the viscous term is assumed to be negligible.

Spinodal decomposition in binary fluid mixtures has been successfully simulated using a lattice-Boltzmann method. The simulation results were combined using a characteristic length and time obtained from the physical parameters (density, viscosity, interfacial tension) to scale the domain size, the resulting single scaling plot covers five decades of length and eight of time from the viscous hydrodynamic region (linear scaling) through a broad crossover region to the inertial region. This is a larger range than all previous results combined, and the first unambiguous simulation results for the inertial region.

Both the order parameter and the fluid velocity in the spinodal system have been analysed in detail. The order parameter shows good scaling behaviour (collapse of the structure factor) while various velocity-related quantities, such as the dissipation rate, were found not to scale. A comparison of the relative magnitude of the terms in the NSE confirmed that the results include simulation of the inertial region where the inertial terms dominate the dynamics. Careful analysis of the growth rate due to diffusion also allowed this to be discounted from making a significant contribution to the hydrodynamic coarsening under observation in this study.

The persistence behaviour of the spinodal system has been studied, although the order parameter data are not sufficient for a precise determination to be made of the value of the persistence exponent. It was possible to show that the persistence behaviour follows a power law decay (as opposed to exponential) and to show that there is some dependence on the domain growth exponent (linear/$t^{2/3}$).

Acknowledgements

One can safely say that this PhD did not go as expected. Nontheless, the end result is a satisfying piece of work, and along the way some fine fun times were had in the City of Edinburgh and the wilds of Scotland, shared with a great set of friends and colleagues.

First thanks must go to Mike Cates for being an excellent supervisor. I hope the work I've produced has been worth the extra load from acquiring an unanticipated student. Special thanks also go to Peter Bladon, without whom I'd have had to do far more programming than would have been possible in the time alloted to a PhD, and understand more of the theory of numerical simulation to boot. J-C Desplat and the team at EPCC assisted in producing a fine simulation code, and took over in receiving the onslaught of my requests once Peter left. Much useful help was also provided by many others in the condensed matter group, special mention goes to Martin Evans, Alastair Bruce, Nigel Wilding, Peter Pusey, Ignacio Pagonabarraga, not forgetting those in the rest of the department, Will Hossack, Eleanor McKirdy, Jim King, Bill Ross, Liz McIvor, Leslie Shaw, Victoria Burnett, and for encouragement when I needed it, Stuart Pawley, Anna Kenway, Richard Kenway, David Thomas.

In the turbulence group, I thank Prof David McComb for introducing me to turbulence theory and supervising the work in Chapter 4; and Craig, Adrian, Anthony, Gary and Alistair for making sure I still knew a smidgen about turbulence two years later when I finally needed to use it.

I'm sure Simon Jury does not want to be thanked for the months I spent helping to debug his code, but for the eventual use of that debugged code, for answers to many questions about how things worked, and for drunken evenings in the pub and escapades on the end of a rope, thanks are certainly due and given. Which brings me to the many other friends in the department and University who also spared me from too much work and too little play; Dave, Jon, Will, Mark, Fiona, Mark, Laura, Suzanne, Liz, Owen, Jo, Pete, Becky, Belinda, Kate, Jane, Pete, Kat, Charlotte, Kerstin, Andy, Richard, Stew, and the EU Mountaineering Club, for fun times on and off the hills. Special thanks to Joanna and Helen for being flatmates as well as friends, and all the mutual entertainment that relationship provides for.

Among my friends beyond Edinburgh, I thank Will and Reb for believing I could do this and encouraging me to go for it; Russell and Eiluned for proving that this is a good time of life for doing a PhD and I'm not alone in being forty and still a student; Diane, my constant email correspondent and holiday companion since we met in Berkeley

nearly twenty years ago, now in that "writing-up" phase of her own PhD; and Max, Lee, Karen, Jay, Edie and everyone else from the "first time round". Special thanks to Charling for being the first woman PhD student I knew, and still a physicist today.

For where I came from, thanks to Cilla, Jills, Karen, Sarah, Philip, Ash, Graham, Richard, Edie, Sally, Geoff, Steve, Scott, and all at GreenNet for letting me go when it was time to leave.

For where I'm going next, thanks are due to Kathy Whaler, Stephen Barnett, and Tony Chefles, for opening the next door far enough for me to step in through it.

Many thanks, too, to my sister, Gill, for being at Edinburgh first so I thought of coming here, and for coming back to visit several times despite the blizzards that greeted each arrival (the sun *does* shine in Edinburgh some of the time, honest), and, of course, but especially, thanks to my parents for much practical and emotional support, without which, as they say, none of this would have been possible.

It would be nice to round off with appropriate quotes from literary sources but that would involve having read things other than scientific papers over the last couple of years. Yes, it has been a bit of an epic, but I'll say without reservation that it has been worth it.

Viv Kendon, June 21, 1999

Contents

List of Figures

List of Tables

Notation

The main variables used throughout this work are listed in alphabetical order in the following tables.
Bold quantities, e.g. $\mathbf{v}(\mathbf{k})$, the fluid velocity field in Fourier space, are usually vectors, while tensors are generally given a double underline, e.g. $\underline{\underline{\Sigma}}$, the stress tensor, with individual components denoted $\Sigma_{\alpha\beta}$.
Some variables listed here without subscripts appear in the text with subscripts from time to time, the meaning of which should be made clear in the adjacent text. Greek letters α, β, γ, μ, ν, are occasionally reused as subscripts for Cartesian components; this should be clear from the context.

Greek letters

α	growth exponent for binary fluid system, $L = v_0(T-T_{\text{int}})^{\alpha}$
α'	growth exponent for binary fluid system, $L_{\nabla} \sim T^{\alpha'}$
α''	growth exponent for binary fluid system, $L_{\nabla^2} \sim T^{\alpha''}$
β	growth exponent for fluid velocity; – parameter in fitted form of pdfs; – arbitrary exponent in persistence equations
Δ	bin width for pdf moments calculations; – otherwise usually refers to difference, e.g. $\Delta\phi$
$\delta_{\alpha\beta}$	Kroneker delta function, $= 1$ for $\alpha = \beta$; $= 0$ for $\alpha \neq \beta$
ϵ	parameter controlling accuracy of moments calculations
ε	dissipation rate per unit volume
$\varepsilon_T = 2\nu \sum_k k^2 E(k)$	total dissipation rate
ε_{in}	energy transfer rate from interface to fluid velocity
η	shear viscosity
θ	persistence critical exponent
κ	coefficient in model free energy, Equation (3.28)
Λ	size of lattice in LB simulation
Λ_b	system size of turbulence simulation
λ_1, λ_2, λ_3	lengths from the eigenvalues of the curvature matrix
$\lambda = \sqrt{10 E_T \nu/\varepsilon_T}$	Taylor microscale (linked to L_{∇})
$\lambda_d = 2\pi\left(\nu^3/\varepsilon_T\right)^{1/4}$	Kolmogorov microscale (linked to L_{∇^2})
$\mu = \partial F/\partial\phi$	chemical potential
ν	kinematic viscosity, $\nu = \eta/\rho$ (turbulence theory); – subscript in LB method equations
ν_1, ν_2	viscosities in LGA version of NSE

Greek letters cont.

ξ	interface width/microscopic length scale
π	3.14159...
ρ	total fluid density, $\rho = \rho_A + \rho_B$
ρ_A	density of fluid A
ρ_B	density of fluid B
$\underline{\underline{\Sigma}}$	stress tensor, components $\Sigma_{\alpha\beta}$
σ	surface tension
τ	relaxation time
ϕ, $\phi(\mathbf{x})$	order parameter: $\phi = \rho_A - \rho_B$ for binary fluid system
ϕ^*	equilibrium value of ϕ
$\phi(\mathbf{k})$, $\phi(\mathbf{k}, T)$	Fourier transform of the order parameter
ϕ_{rms}	rms-average value of ϕ over whole system
χ, χ^2	standard probability distributions
ψ	parameter in fitted form of pdfs
$\boldsymbol{\omega} = \nabla \wedge \mathbf{v}$	vorticity
ω_i	coefficient in LB method, i specifies lattice direction
ω_ν; ω_0, ω_1, ω_3	coefficient in LB method, ν specifies value of $c_{i\alpha}$

Roman letters

A	coefficient in model free energy, Equation (3.28)
A_ν; A_0, A_1, A_3	coefficient in LB method, , ν specifies value of $c_{i\alpha}$
B	coefficient in model free energy, Equation (3.28)
$b(\alpha)$	prefactor in scaling relation $l = b(\alpha)t^\alpha$
b_1	value of $b(\alpha)$ in the linear region, $l = b_1 t$
b_2	value of $b(\alpha)$ in the inertial region, $l = b_2 t^{2/3}$
$\mathcal{C}$	collision operator
$\mathcal{C}_{int}$	interaction part of collision operator
$C(r)$	radial distribution function
C_V	specific heat
$c = c_L c_v$	prefactor in formula for the flip rate, $P_F = c/T$
c_1, c_2, c_3, c_4	parameters specifying the initial configuration for the decaying turbulence simulation
$c_{i\alpha}$	speed of propagation of n_i or f_i in LGA or LB method
c_L	prefactor in persistence theory, $c = c_L c_v$
c_v	prefactor in persistence theory, $c = c_L c_v$
$D_{\alpha\beta}$	curvature tensor
d	number of space dimensions
E	energy
$E(k) = \langle \rho \mathbf{v}(\mathbf{k}).\mathbf{v}(-\mathbf{k})/2 \rangle$	energy spectrum
$E_T = \sum_k E(k)$	total energy
F	free energy
$f_i(\mathbf{x}, T)$	particle distribution function in LB method
$f_i^{(eq)}$	local equilibrium value of f_i in LB method

$G_{\alpha\beta}$	coefficient in LB method equilibrium distribution
g	coordinate normal to the interface
$g(\rho)$	density-dependent factor in LGA version of NSE
$g_i(\mathbf{x}, T)$	order parameter distribution function in LB
$g_i^{(eq)}$	local equilibrium value of g_i in LB method
h	coefficient in LGA equilibrium distribution
i	$\sqrt{-1}$; when used as an index, denotes a lattice direction in LB and LGA methods
$\mathcal{K}$	curvature of the interface
Ko	Kolmogorov constant (turbulence)
$\mathbf{k}$	wave vector in Fourier space
$k = \lvert\mathbf{k}\rvert$	wavenumber in Fourier space
k_B	Boltzmann's constant
k_d	Kolmogorov wavenumber (turbulence)
$L(T)$	length scale from $S(k)$
L_∇	length scale associated with $\nabla\mathbf{v}$
L_{∇^2}	length scale associated with $\nabla^2\mathbf{v}$
L_ϕ	length scale from ϕ_{rms}
$L_{\lvert\phi\rvert}$	length scale from $\langle\lvert\phi\rvert\rangle$
$L_{\nabla\phi}$	length scale from interface curvature
$L_0 = \eta^2/\rho\sigma$	viscous-inertial crossover length scale
$L_C(T)$	length from first minimum of $C(r)$
$L_{\mathbf{gap}}$	length scale from mean distance between interfaces
L_i	length scale in inertial range (turbulence)
$L_{int} = 3\pi/4E_T \sum_{grid} \frac{\rho}{2} \frac{\mathbf{v(k)}.\mathbf{v(-k)}}{\lvert\mathbf{k}\rvert}$	integral scale (turbulence)
$L_{\mathbf{max}}$	upper cut-off for $L(T)$ usable data region
$L_{\mathbf{min}}$	lower cut-off for $L(T)$ usable data region
$L_v(T)$	length scale from $S_v(k)$
$l = L/L_0$	scaled length (non-dimensional)
M	mobility parameter that controls the diffusion
m	number of lattice velocity directions, i
N	number of lattice sites in one lattice direction
N_F	"no-flip fraction" in persistence analysis
N_i	equilibrium distribution of n_i in LGA
n	number of independent random variables
$n_i(\mathbf{x}, T)$	particle number at lattice site in LGA
n_k	number of points in Fourier shell k
O_F	"one-flip fraction" in persistence analysis
P_F	flip rate in persistence analysis
$P(T, T_{\mathbf{start}})$	flip probability in persistence analysis
$\underline{\underline{\mathcal{P}}}$	pressure tensor, components $\mathcal{P}_{\alpha\beta}$

Roman letters cont.

$\mathbf{q}$	coefficient in LGA equilibrium distribution
$q(k) = 1/n_k \sum_{\lvert\mathbf{k}\rvert=k} \mathbf{v}(\mathbf{k}).\mathbf{v}(-\mathbf{k})$	spectral density (turbulence, $\equiv S_v(\mathbf{k})$)
$R_1 = \lvert\rho\partial\mathbf{v}/\partial t\rvert_{rms}$ / $\lvert\eta\nabla^2\mathbf{v}\rvert_{rms}$	ratio of terms in the NSE, accelertaion to viscous
$R_2 = \lvert\rho(\mathbf{v}.\nabla)\mathbf{v}\rvert_{rms}$ / $\lvert\eta\nabla^2\mathbf{v}\rvert_{rms}$	ratio of terms in the NSE, nonlinear to viscous
$\mathrm{Re} = \frac{\text{(length)} \times \text{(velocity)}}{\text{(kinematic viscosity)}}$	Reynolds number, plus subscript for length
$\mathcal{S}$	entropy
$S(k) = 1/n_k \sum_{\lvert\mathbf{k}\rvert=k} \phi(\mathbf{k})\phi(-\mathbf{k})$	structure factor (also appears as $S(k,T)$)
$S_n(L_i)$	structure function (turbulence)
$S_v(k) = 1/n_k \sum_{\lvert\mathbf{k}\rvert=k} \mathbf{v}(\mathbf{k}).\mathbf{v}(-\mathbf{k})$	velocity structure factor
$\mathcal{T}$	temperatue
$\mathcal{T}_c$	critical temperature
T	time in simulation or unscaled units
$T_0 = \eta^3/\rho\sigma^2$	viscous-inertial crossover time scale
$T_E = L_{int}/v_{rms}$	eddy turnover time (turbulence)
T_{int}	offset to T to discard any initial diffusive growth
$T_{\mathbf{start}}$	initial reference time for persistence analysis
$t = (T - T_{\mathrm{int}})/T_0$	scaled time (non-dimensional)
$\mathcal{V}(\phi)$	potential in model spinodal system
V	volume
V_A	volume of interface in spinodal system
$\mathbf{v}(\mathbf{x})$	velocity in real space
$\mathbf{v}(\mathbf{k})$	Fourier transform of $\mathbf{v}(\mathbf{x})$
v_0	fit parameter in $L = v_0(T - T_{\mathrm{int}})^\alpha$
$v_{rms} = \sqrt{2E_T}$	root mean square velocity
$\mathbf{x}$	vector position in real space
z	critical exponent; replace by $1/\alpha$ in most of thesis

Abbreviations

Where possible, abbreviations have been avoided; the few that crept in are listed below.

AVS	visualisation software package used for imaging the interface and velocity fields
DPD	dissipative particle dynamics, simulation method
DNS	direct numerical simulation, turbulence simulation method
EPCC	Edinburgh Parallel Computing Centre
FFT	fast Fourier transform routines
FFTW	particular fast Fourier transform routines used in analysis code
LB	lattice-Boltzmann simulation method
MD	molecular dynamics simulation method
NSE	Navier-Stokes equation
`xmgr`	graph plotting software package used to prepare graphs and perform fits to the experimental data

Chapter 1

Introduction

This thesis is an investigation into the dynamics of the phase separation of a binary mixture of simple fluids that undergo spinodal decomposition. Such a basic system contains many subtleties arising from the interplay between the hydrodynamics, governed by the Navier-Stokes equation, and the driving force provided by the interface between the two fluids. The system chosen for detailed study here is kept as simple possible, in order to focus on the universal aspects of the behaviour. The two fluids have identical properties except that below a critical temperature, $\mathcal{T}_c$, they separate. The fluids are completely specified by their viscosity, η, their density, ρ (assumed constant), and by the interfacial tension, σ, at the boundary between the bulk phases when they demix. No microscopic details are required, except that for practical purposes in the numerical simulations, it is necessary to specify a finite interfacial width. The fundamental question that forms the main work of this study is: how quickly does the separation of such a fluid system proceed on the way from a completely mixed state to a completely demixed state?

This work concentrates exclusively on three dimensional systems; two dimensional systems have already been well-studied, see Wagner and Yeomans (1998), who showed that in 2-D, hydrodynamic spinodal decomposition does not show good scaling behaviour. In 3-D there have also been suggestions of scaling violations, Jury et al. (1999), providing strong motivation for a more thorough and comprehensive study. Recent suggestions

by Grant and Elder (1999) that there could be a further scaling regime in the inertial region also remain unresolved.

The theoretical description of this system is fleshed out in Chapter 2, where a brief overview of the kinetics of phase separation leads into a more detailed treatment of the system using model free energies and simple scaling arguments. The dynamics of the system are described by the Navier-Stokes equation coupled to a convection-diffusion equation for the difference in the concentrations of the two fluids. The concentration difference, ϕ, is the order parameter for this system, and along with the fluid velocity, this is sufficient information to describe the state of the system at each point in space and time during the demixing process. An average description of the system is provided by the average size of the domains of each fluid as they grow over time. There are a variety of ways to measure this length; the most widely used is the inverse of the first moment of the spherically averaged structure factor, $L(T)$, because it can be measured experimentally using light scattering techniques. In a numerical simulation, though, other methods are just as practical, and even a simple measure, such as the mean distance between interfaces along a straight line through the system, is equally good. Studies of two-dimensional systems (Wagner and Yeomans, 1998) found that different length measures could sensitively reveal the non-scaling behaviour of the system, so a number of different length measures will be compared here to see what information they can provide in the case of 3-D.

The existing predictions for how the domain size, $L(T)$, grows with time are explained in Chapter 2. After an initial period during which diffusion dominates while sharp interfaces form between small domains of fully separated fluid, hydrodynamics takes over. A period of linear growth ensues, $L(T) \sim T$, corresponding to hydrodynamics dominated by the viscous term in the Naver-Stokes equation, with the inertial terms negligible. Once the inertial terms become significant, the growth slows to $L(T) \sim T^{2/3}$. This simple theory is extended (in Section 2.4) in the inertial region where the fluid behaviour is expected to show turbulence, and a number of more detailed predictions are made for the time dependence of the various terms in the Navier-Stokes equation and the Reynolds numbers associated with the system. Two new length scales associated with the velocity field in the inertial region are introduced, predicted to scale more

slowly than the domain size, $L(T)$. These new lengths are identified with well-known lengths in turbulence theory, the Taylor and Kolmogorov microscales, providing a solid underpinning for the extensions to the scaling theory. A brief overview of turbulence theory, to set these lengths in context, concludes the theoretical discussion.

Given the intractability of more precise analytical treatment of this system, beyond the scaling theory already presented, numerical simulation is the next step to obtain more detailed information. The numerical methods used to simulate and analyse this system are reviewed in Chapter 3. The chosen simulation method, lattice Boltzmann, is outlined, although the code used, **Ludwig**, was not part of the original work of this thesis. The analysis code, while original work, is straightforward in its calculations and implementation, so is also only briefly described. As with all numerical methods, the limitations imposed by finite computational resources and accuracy must be taken seriously, and Chapter 3 concludes with several tests of the effects of the finite simulation grid on the results obtained from the simulations.

This study is particularly interested in investigating the behaviour of the binary fluid system in the region where the inertial terms are significant to the dynamics of the fluid. By way of a "warm-up" to this, Chapter 4 describes how a single fluid system was simulated under conditions where it displays fully developed turbulence. A completely different simulation method was used for this purpose, pseudo-spectral direct numerical simulation (DNS), already known to provide reliable results. This allowed the analysis code for the velocity field to be tested on a known system, and provided data for later comparison with the two fluid system.

The results from the simulations of the binary fluid system are presented in the next three chapters. These form the main body of original work in addition to the theory in Section 2.4. In Chapter 5, the domain growth is studied in detail by analysing the order parameter at regular intervals as the separation proceeds. The structure factor provides a basic test of whether the system is scaling in a self-similar way as the domains grow. If the shape of the fluid domains remains the same regardless of their size, then the structure factor will be the same shape, and appropriately scaled, will collapse onto a single curve. The data from these simulations passes this test well. Interestingly, though, the structure factors from simulations in the viscous region

are slightly different from those in the inertial region, implying that the interface is a subtly different shape. This is not readily apparent to the eye, in Appendix A some visualisations of the interface and velocity field can be found that illustrate this point.

Having determined that the simulation results are scaling nicely, the domain size is thoroughly analysed to obtain the growth rates with time over a wide range of parameters covering the viscous and inertial regions and the intervening crossover region. After comparison with other published work, and careful checks to ensure that diffusive growth has been eliminated, it is concluded that this is the first unambiguous simulation of inertial region growth where $L(T) \sim T^{2/3}$ (published in Kendon et al., 1999). This conclusion would not have been possible without a systematic and rigorous way to compare results between different simulations. The method used to do this, due to Jury et al. (1999), is to convert the domain size and time scale from simulation units to dimensionless length and time measures using characteristic length and time scales formed from the physical parameters of the system, viscosity, density and interfacial tension. The result for these simulations is an impressive composite curve covering many decades of scaled length and time, spanning the full range of simulation parameters from the viscous region through the crossover to the inertial region.

Following the solid results obtained in Chapter 5, the relatively uncharted waters of the velocity field are explored in Chapter 6. Here, the simple picture of straightforward scaling behaviour falters almost immediately; the average velocity is predicted (by both simple and extended scaling theories) to follow the domain size and scale as $\mathrm{d}L/\mathrm{d}T$. Although this hold reasonably well in the crossover region, in both the most viscous and the most inertial simulation runs, it deviates significantly from this. Nevertheless, many of the predictions for the velocity field are borne out in general, confirming that the inertial region really has been simulated as claimed in Chapter 5. Comparisons with the single fluid turbulence simulation results from Chapter 4 show that, as anticipated, the most inertial binary fluid systems are becoming turbulent in the bulk fluid away from the interfaces. However, a closer look at the scaling behaviour of the quantities derived from the velocity field, such as the dissipation rate, and the Taylor and Kolmogorov microscales, reveals that that most do not show good scaling behaviour when a single run is compared with the overall trends between different runs. Possible causes for this

non-scaling are discussed, but it was not possible within the resources of this study to completely answer all the questions raised. This chapter contains the first detailed study of the velocity field in a hydrodynamic spinodal system. While the limitations of the simulation method and computational resources prevented all the interesting questions from being answered conclusively, it has certainly provided a wealth of information not previously available to further the understanding of such systems.

A different aspect of the spinodal fluid system is investigated in Chapter 7, the persistence behaviour. Persistence is best explained in terms of the simulation system on a discrete lattice; the proportion of lattice sites that have never seen a change of fluid from one type to the other since the start of the system is called the "no flip fraction", N_F. In general $N_F \sim T^{-\theta}$, where θ is thought to be a new independent critical exponent (Derrida et al., 1996, Majumdar et al., 1996), hence the interest in this otherwise rather obscure quantity. Hitherto, persistence behaviour has only been studied in diffusive systems, so the effect of hydrodynamics is an open question. In Chapter 7, a simple theory of persistence quantities in this hydrodynamic spinodal system is developed. Predictions are made for the form of N_F and related quantities, but not for the value of the exponent, θ, itself. Calculations using the data from the simulations described in Chapter 5 are then carried out to obtain approximate values for θ. At these system sizes, it is difficult to obtain accurate results for 3-D systems, and significantly larger systems will require considerable increases in computing power. Nonetheless, some basic questions about the persistence exponent in 3-D hydrodynamics systems can be answered, viz., that the behaviour of N_F does follow a power law decay (in contrast to systems with non-conserved order parameter at finite temperature, where N_F decays exponentially), and there appear to be different values of θ for systems with viscous or inertial parameters. A brief look at 2-D spinodal systems is also included in this chapter.

This work has attempted to provide as much relevant detail as possible pertaining to the dynamics of the spinodal decomposition of a symmetric binary fluid mixture in three dimensions, without losing the overall picture of simple, universal behaviour. Even for a system as simple as this binary fluid mixture, the intricacies of nonlinear equations, such as the Navier-Stokes equation, and abstract numerical simulation methods such

as lattice Boltzmann, demand many careful checks and tests to ensure that the results arise only from the physical processes under investigation. At times, the details threatened to overwhelm the message. However, perseverence has been rewarded with some substantial advances in the understanding of this system, as should be made clear by the end of the following chapters.

Chapter 2

Theory of spinodal decomposition

2.1 Introduction

This chapter provides a brief introduction to the theory of the kinetics of phase separation, specialising quickly to the particular system that this work is concerned with, a symmetric, binary fluid mixture undergoing spinodal decomposition. Some background material on phase transitions is provided first to set the context in which the specific phase separation kinetics of this work have been studied; the aim is to draw general conclusions about the scaling behaviour of such systems where possible, while investigating the specific system in sufficient detail to be confident of the overall results.

Once the existing theory of the dynamics of the coarsening process has been covered, original work that extends the scaling predictions to give a more detailed description of the inertial regime is presented in Section 2.4.

All the work presented here is concerned with three-dimensional systems. The two-dimensional case is well-studied, but behaves rather differently. Wagner and Yeomans (1998) and Tanaka (1994) give a description of the non-scaling behaviour found in two-dimensional binary spinodal systems, while Osborn et al. (1995), Lookman et al. (1996) and Emerton et al. (1997) report basic two-dimensional simulation results. A brief consideration of the behaviour of a two-dimensional spinodal system will be made in Chapter 7, but the theory will not be considered at all in this chapter. The theory

pertaining to persistence behaviour will be presented in the chapter where that work is covered, Chapter 7.

2.2 Phase separation

The work in this thesis is concerned with a system which consists of two fluids with identical properties (viscosity, density, etc.), the difference between them being that below a certain critical temperature, $\mathcal{T}_c$, they won't mix, while above $\mathcal{T}_c$, they mix completely and have properties indistinguishable from a single fluid. The equilibrium behaviour is thus very simple. Below $\mathcal{T}_c$, the fluids form two separate regions, one of each type of fluid, while above $\mathcal{T}_c$, they mix completely. The aspect of this system that is of interest is the dynamics of the separation process that occurs when a system that is initially completely mixed at a temperature above $\mathcal{T}_c$ is quenched to a temperature far below $\mathcal{T}_c$. From the completely mixed initial state, the two fluids now find a way to demix themselves into separate domains consisting of only a single fluid. Such a macroscopic rearrangement of the system driven only by the mutual repulsion between the fluids must take a significant length of time to accomplish, and this study is, in essence, concerned with what the separation time depends on.

As with much of the study of phase transitions, the objective is to encapsulate the basic behaviour of the system in the simplest possible description, dependent only on a few physical parameters. To that end, the theoretical and computational models used are also simplifications of the complexities of real fluid systems, designed to capture the universal behaviour while ignoring irrelevant details.

In the following sections, a brief overview of the theory of phase separation will be presented, specialising quickly to the binary fluid mixture that is the main subject of this investigation. All of the relevant details of the model system under study will then be elaborated, in preparation for Chapter 3, which covers a description of the numerical methods used for the simulation and analysis.

2.2.1 Background

Phase separation is an example of the phenomena of phase transitions. In essence, phase transitions are exhibited by any physical system that can exist in two or more different macroscopic states, depending on the value of a state variable such as temperature. Generally the phase transition occurs for a change in temperature across a sharply defined critical temperature, $\mathcal{T}_c$. Examples are many and varied; liquid-vapour, solid-liquid, magnetized-demagnetized, dissolved-precipitated, mixed-separated, transitions between crystal structures. In all cases, the constituent atoms or molecules are the same throughout, there are no chemical reactions involved, and the system size, i.e. the total number of particles, remains fixed. Typically, some states are distinguished by being more "ordered" in some way i.e. entropy is crucial in driving the phase transition as well as energy. The appropriate thermodynamic quantity to characterise the system is thus the free energy, F,

$$F = E - \mathcal{T}\mathcal{S}, \tag{2.1}$$

where E is the energy, $\mathcal{T}$ the temperature and $\mathcal{S}$ the entropy of the system.

The energy, E, comes from the interactions between the particles in the system, so the equilibrium state will have the energy minimised subject to the opposing tendency to find the state of largest entropy, where the particles have the most configurational freedom of choice subject to the limits on energy fluctuations implied by the temperature ($k_B\mathcal{T}$). The equilibrium states are thus given by the minima of the free energy, F. In general, phase separation occurs when the shape of F changes (with temperature or equivalent variable) from having a single minimum to having two or more minima so that the system can reduce its overall free energy by separating into a mixture of different components.

Although on the microscopic level the system is composed of particles of some sort (atoms, molecules, spins on a lattice, etc.), the details of individual particles are not of interest here, what is desired is a macroscopic average description of the system that nevertheless captures all the essential physics. This is easy to accomplish by coarse-graining so that the smallest length scale under consideration is much larger than the average distance between particles. The individual states of particles are then subsumed into a local average on the scale of the coarse-graining, resulting in a smooth, continuum

description of the system. In equilibrium, this coarse-graining is a trivial operation, however, for the dynamical description desired here, certain conditions must be met. On scales smaller than the coarse-graining length, the system must be essentially in local equilibrium, while the variations of interest, i.e. at scales larger than the coarse-graining length, must be slow on the scale of the time it takes for local equilibrium to be reached.

This does not mean that the microscopic scales can be forgotten from here on. Although most of the time the macroscopic description is sufficient to fully understand the system, ultimately it is still the microscopic interactions that are driving the system and determining the dynamics. It is always a possibility that the microscopic behaviour can intrude at the macroscopic level and change the results predicted by the simple macroscopic model. In particular, since this study is concerned with numerical models, care must be taken that the microscopic behaviour in these models is correct. It will be seen later that it is by no means a trivial task to accomplish this, see, for example, Sections 5.4.1 and 6.4.3.

2.2.2 Universality classes

The theory of phase transitions hinges on the idea that the details of the particular system don't matter to the basic description, and the simple models can capture the essential behaviour of whole sets of different examples. The key step is to identify the relevant variables in the system that are essential to the description and ignore or simplify the rest. The most fundamental variable is the one that will play the role of the *order parameter*. This parameter (in general a function of position within the system) must distinguish between the different phases of the system. For example, in a spin system, the (coarse-grained) order parameter is the net magnetisation, i.e. the excess of up-spins over down-spins, or vice versa. Above the critical temperature, when the system is disordered (mixed) the net magnetisation is zero. Below the critical temperature, the net magnetisation is either all spins up or all spins down, with a sharp transition between the two at any domain boundaries. For a liquid-vapour system, the density is the order parameter, since the essential difference between the liquid and vapour phases is that liquid is high density while vapour is low density.

For the two-fluid system that is the subject of this study, the order parameter is the difference in densities (concentrations) of the two fluids. If the total fluid density is ρ, and the density of one fluid is ρ_A, the other, ρ_B, then $\rho = \rho_A + \rho_B$, and the order parameter, $\phi = \rho_A - \rho_B$. For a 50:50 mixture in the mixed state, $\rho_A = \rho_B$, and $\phi = 0$, while for a separated system (deep quench), in the region of one fluid, $\rho_A = \rho$ and $\rho_B = 0$ so $\phi = +\rho$, and in the region of the other fluid, $\rho_A = 0$ and $\rho_B = \rho$ so $\phi = -\rho$. In the simulations studied here, the total fluid density has usually been set equal to unity, and, since the fluid is basically incompressible, ρ remains constant over the whole system throughout the simulation. In principle, however, ρ is a parameter that can be varied, so will be retained as such throughout the theoretical discussion.

Despite being apparently very different systems, all three of the examples just described, the spin system (Ising model), the liquid-vapour system and the two-fluid system, are equivalent in terms of their equilibrium behaviour. All of them are described by a single scalar order parameter and all have a phase transition from a single phase to just two separate phases. A rod-like liquid crystal, for example, is fundamentally different, because the molecules can align at any angle with neighbouring molecules, and the ordering depends on how closely the molecules line up with each other.

However, there is a crucial difference between the two-fluid system and the Ising system when it comes to the dynamics of the phase separation. The Ising spin system rearranges itself through individual spins flipping from up to down or vice versa, thus the total number of up spins can and does change. In the two-fluid system, the fluids have to separate by individual fluid molecules moving from one position to another, they can't change into the other type of fluid. So the proportions of fluid A and fluid B are fixed from the start.

This difference in dynamics is enough to put the two-fluid system into a different *universality class* from the Ising spin system. The order parameter is *conserved* in the binary fluid system, whereas the Ising model has a *non-conserved* order parameter. Binary alloys, that is, mixtures of two different metals, are similar to the two-fluid system in that the proportions of the two metals are fixed, but being solid, there is no fluid flow to contribute to the dynamics of the separation process. They therefore consitute yet another universality class. More complicated systems, such as spin systems in which

the spin is allowed to take any angle (Heisenberg model), or liquid crystals where the molecules can take up many orientations, have order parameters that are vectors rather than simple scalars and constitute further universality classes.

Clearly, the more complicated systems present considerable challenges for analysis, however, by concentrating on the essential features of the system, progress can be made in finding simple descriptions of the basic behaviour, see Bray (1994). One key concept that has furthered the theoretical description of such systems is that of topological defects. In simple systems with a conserved scalar order parameter, the topological defect is the boundary between the different domains. How it moves depends on the system dynamics, but there is in principle nothing to stop the boundary shrinking and breaking or rejoining as it wishes. A system with a vector order parameter, however, can have various singularities where the order parameter rotates from one value to another, that cannot be removed from the system without meeting a similar defect with a rotation in the opposite direction. Topological defects thus move through the system and influence the dynamics of the separation process.

The simpler systems are themselves by no means completely understood, as this work will show in the case of a binary fluid mixture. Even for the Ising model, exact analytical solution has only been possible in equilibrium, in one and two dimensions, Onsager (1940). A variety of approximate techniques, mean field theory, Landau-Ginsburg theory, renormalisation group, and a range of more subtle methods, see Bray (1994), have been developed, but the field remains full of unresolved questions and one in which numerical simulations, such as is the central technique of this study, play a key role.

2.2.3 Critical exponents and simple models

Critical exponents are crucial to quantifying the behaviour of a system that undergoes a phase transition. Typically, the phase diagram of such a system will contain a critical point where the behaviour changes from one form to the other (mixed to separated). In Figure 2.1, the critical point is at $\mathcal{T} = \mathcal{T}_c$, at the centre top of the binodal line. Thermodynamic quantities such as the specific heat, C_V, diverge as the critical point

is approached,

$$C_V \sim \left|\frac{\mathcal{T} - \mathcal{T}_c}{\mathcal{T}_c}\right|^{-\alpha} \tag{2.2}$$

The form of the divergence, a power law in the temperature, defines the critical exponent, α. There is a whole set of critical exponents for a given system, one for each key quantity, like the pair correlation function, correlation length and order parameter. Relationships between the different critical exponents reduce this set to just two independent (static) exponents, more details on this can be found in Bray (1994) or Yeomans (1992). Critical exponents make precise the idea of universality classes, systems with the same critical exponent values are in the same universality class.

A further set of critical exponents is found when the dynamics of the phase transition are considered. The quantity of most interest in this work is the size, L, of the macroscopic domains of the two phases as the system separates and it scales with time, T, as $L \sim T^{1/z}$. From here on, the notation used is $\alpha \equiv 1/z$ (α is reserved for one of the static exponents in the standard literature, but static exponents are not discussed further here). There is also a dynamic exponent describing how the order parameter pair correlation function diverges at the critical point. This exponent is not discussed in this study, which is concerned only with deep quenches and does not consider the behaviour of the system near the critical point. Finally a further independent dynamic exponent, the persistence exponent, θ, has been proposed by Derrida et al. (1994). The persistence exponent describes the decay of the fraction of sites that have not changed colour/spin since the start of the separation process, and will be considered in more detail in Chapter 7.

The simple case of a system described by a single scalar order parameter that separates into just two distinct phases will now be considered in more detail. Figure 2.1 shows a schematic phase diagram for such a system. The binodal line divides the region of phase space in which the system is mixed from the region in which it separates into domains dominated by one fluid or the other. The final composition of the domains is given by the value of the order parameter, ϕ, on the binodal line for the final temperature of the quench. The spinodal line, shown dashed, separates the region close to the binodal line where the system is metastable and separation only proceeds after nucleation, i.e. sufficiently large fluctuations in the composition of the fluid mixture, from the spinodal region where separation proceeds immediately after the quench. The spinodal line is

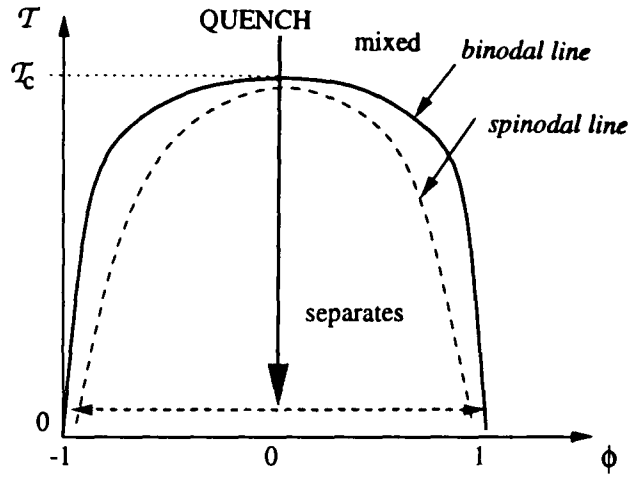

Figure 2.1: *Phase diagram for spinodal decomposition. The order parameter,* $\phi = \rho_A - \rho_B$*, is the difference in density between the two fluids, with* $\rho = \rho_A + \rho_B = 1$*. The temperature axis shows the critical temperature,* T_c*, below which the system starts to separate, and above which it remains completely mixed.*

defined within mean field theory by $\partial^2 F/\partial\phi^2 = 0$, it corresponds to the point where the size of fluctuations necessary for nucleation goes to zero, and there is thus a smooth transition through to the spinodal region. Beyond mean field theory the spinodal line is not well-defined, but in any case, the linear theory used to predict the position of the spinodal line breaks down at very early times. However, the basic distinction between spinodal and nucleation behaviour is valid, and for a deep quench of a symmetric (50:50) fluid mixture such as is being studied here, the system begins the coarsening process firmly inside the spinodal region and starts to separate immediately.

The free energy for the system in the phase-separated region can be modeled by the Landau free energy functional,

$$F[\phi] = \int \mathrm{d}\mathbf{x} \left\{ \mathcal{V}(\phi) + \frac{\kappa}{2}(\nabla\phi)^2 \right\}, \tag{2.3}$$

where $\mathcal{V}(\phi)$ is a function of the form shown in Figure 2.2, and $\kappa(\nabla\phi)^2/2$ is the energy stored in the interface. Strictly speaking, free energies are equilibrium quantities, and the system is not in equilibrium immediately after the quench, but it can be viewed as sitting at the point in the potential $\mathcal{V} = 0$, $\phi = 0$ in Figure 2.2 (for a 50:50 mixture) and then proceeding to separate into single-phase domains with $\phi = \pm\phi^*$. The equation of motion for this conserved order parameter, ϕ, is,

$$\begin{aligned} \frac{\partial\phi}{\partial T} &= M\nabla^2 \frac{\delta F}{\delta\phi} \\ &= -M\nabla^2 \left\{ \kappa\nabla^2\phi - \frac{\partial\mathcal{V}(\phi)}{\partial\phi} \right\}, \end{aligned} \tag{2.4}$$

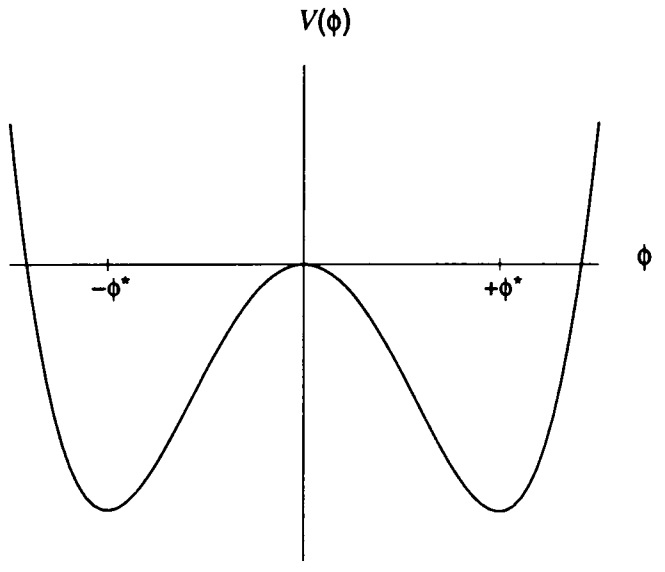

Figure 2.2: *Model potential for phase separation, typical "mexican hat" double well. The equilibrium values of the order parameter are* $\pm\phi^*$.

a diffusive transport equation, where M is a mobility parameter (assumed independent of ϕ) that controls the strength of the diffusion. This equation is known as the Cahn-Hilliard equation. In this model, the only way the system can coarsen is by diffusion; the model with hydrodynamics added will be considered in the next section. The corresponding equation of motion for the case of a non-conserved order parameter is a reaction-diffusion equation, $\partial\phi/\partial t = -\Gamma\delta F/\delta\phi$, known as the time dependent Ginsburg-Landau equation. This case will not be studied at all in this work.

To follow the separation process quantitatively, the average size of the domains, $L(T)$, of each phase must be measured. By convention, this is done using the inverse of first moment of the spherically averaged structure factor, $S(k,T)$,

$$L(T) = \frac{\int S(k,T)\mathrm{d}k}{\int kS(k,T)\mathrm{d}k}, \tag{2.5}$$

where k is the modulus of the wave vector in Fourier space, and,

$$S(k,T) \equiv \int_{|\mathbf{k}|=k} \phi(\mathbf{k},T)\phi(-\mathbf{k},T)\,\mathrm{d}^3\mathbf{k}, \tag{2.6}$$

where $\phi(\mathbf{k},T)$ is the Fourier transform of the order parameter. Many other equivalent length measures are possible, some are described in Section 3.5 and the values observed in the simulation compared in Section 5.5.2.

The *dynamical scaling hypothesis* is that, at late times (i.e. once the domains are large enough to be well-defined single-phase regions), there exists a characteristic length scale, $L(T)$, such that the domain structure is statistically independent of time when lengths

are scaled by $L(T)$. One way to quantify this is in terms of the structure factor, which is a measure of the shape of the domains as well as the size, so the scaling $S(k)/L^d(T)$ (d = spatial dimension) plotted against $kL(T)$ for different times T should produce a collapse onto a single curve. The results of this procedure for the simulations done in this work are shown in Section 5.3.1.

Next, consider the properties of the interface between the domains. Since the bulk of the domains is at the equilibrium values of ϕ, all the excess energy in the system must be localised in the interface. By introducing a coordinate normal to the interface, g, the equilibrium properties of the interface can be investigated. From Equation (2.4) with $\partial\phi/\partial T = 0$,

$$\kappa\nabla^2\phi = \kappa\frac{\partial^2\phi}{\partial g^2} = \frac{\partial\mathcal{V}(\phi)}{\partial\phi}. \tag{2.7}$$

Integrating this once across the interface and setting $g = 0$, $\phi = 0$ at the centre of the interface, gives,

$$\frac{\kappa}{2}\left(\frac{\partial\phi}{\partial g}\right)^2 = \mathcal{V}(\phi) - \mathcal{V}(\phi^*). \tag{2.8}$$

The interfacial tension, σ, i.e., the energy per unit area of interface, is given by,

$$\sigma = \int \partial g \left[\frac{\kappa}{2}\left(\frac{\partial\phi}{\partial g}\right)^2 + \mathcal{V}(\phi) - \mathcal{V}(\phi^*)\right]. \tag{2.9}$$

By integrating through an interface and assuming that $\nabla\phi \to 0$ in the bulk fluid away from the interface,

$$\sigma = \int_{-\phi^*}^{+\phi^*} \mathrm{d}\phi\ (2\kappa)^{1/2}\left[\mathcal{V}(\phi) - \mathcal{V}(\phi^*)\right]^{1/2}, \tag{2.10}$$

using Equation (2.8). Given a form for the potential, $\mathcal{V}(\phi)$, a theoretical value for the interfacial tension can be calculated. This will be done later for the model used in the simulation, see Section 3.3.

In order to work out the growth rate of the domain size, $L(T)$, consider the chemical potential, $\mu = \delta F/\delta\phi = \partial\mathcal{V}/\partial\phi - \kappa\nabla^2\phi$, from Equation (2.3). Again rewriting ∇^2 using a coordinate normal to the interface, g, the expression for μ near an interface can be written,

$$\mu = \frac{\partial\mathcal{V}(\phi)}{\partial\phi} - \kappa\left(\mathcal{K}\frac{\partial\phi}{\partial g} + \frac{\partial^2\phi}{\partial g^2}\right), \tag{2.11}$$

where $\mathcal{K} = \nabla.\hat{\mathbf{g}}$ is the curvature of the interface ($\hat{\mathbf{g}}$ is a unit vector in the direction normal to the interface). Equation (2.11) can be integrated by multiplying through by $\partial\phi/\partial g$, which is sharply peaked at the interface since ϕ is constant at its equilibrium

values in the bulk fluid. The result is the Gibbs-Thomson boundary condition for the value of μ at the interface, μ_I,

$$\mu_I \Delta\phi = -\sigma\mathcal{K}, \tag{2.12}$$

where Equation 2.10 for σ has been used. Rewriting Equation (2.4) as,

$$\frac{\partial\phi}{\partial T} = M\nabla^2\mu, \tag{2.13}$$

simple scaling arguments, Bray (1994), can be used as follows to determine the growth rate of the domain size. The chemical potential will vary over scales of the order of the domain size, so write $\nabla^2 \rightarrow 1/L^2$. The curvature of the interface, $\mathcal{K}$ is approximately $2/L(T)$, since $L(T)$ is approximately the diameter of the domains[1], and curvature (as defined here) is the reciprocal of the radius. Take the value of μ as μ_I, equation (2.12), and write $\partial\phi/\partial T \rightarrow \Delta\phi/T$, to get,

$$\frac{\Delta\phi}{T} \simeq \frac{2M\sigma}{\Delta\phi L^3}. \tag{2.14}$$

Since $\Delta\phi \sim 2\phi^*$, this gives,

$$L^3 \simeq \frac{M\sigma T}{\phi^{*2}}, \tag{2.15}$$

i.e.,

$$L \sim (M\sigma T)^{1/3}, \tag{2.16}$$

as the growth rate for a system with a conserved order parameter and diffusive transport of the order parameter as the only coarsening mechanism.

For mixtures in which one phase has a much larger concentration than the other, so droplets form rather than a continous interface, there are a number of important phenomena in the late stage coarsening dynamics such as Ostwald ripening, which was first described by Lifshitz and Slyozov (1961) and Wagner (1961). Since droplets are only considered in this study as static configurations for testing the simulation and analysis methods, further theory relevant to droplet mixtures will not be covered here.

There are two important results derived in this section that will be refered to later on; the growth rate for a system dominated by diffusion as the transport mechanism, $L \sim T^{1/3}$, Equation (2.16), and the expression for the interfacial tension, σ, Equation 2.10.

[1] This will be shown later when other length measures are discussed and compared, including one directly derived from the curvature of the interface, see Sections 3.5 and 5.5.2.

2.3 Spinodal decomposition of a binary fluid system

The addition of hydrodynamics to the basic binary system described in the previous section will be considered next, in order to derive the theoretical results for the particular model used for this study, a binary fluid mixture. The system to be studied consists of a mixture of two fluids with the same physical properties and a mutual repulsion causing them to demix below a critical temperature, $\mathcal{T}_c$. The system is prepared in a completely mixed state and quenched to far below $\mathcal{T}_c$. As already noted, equilibrium results for the basic binary system can be carried over for use with this model, since only the dynamical behaviour is fundamentally different.

The first stage of separation is diffusive, as described in Section 2.2.3, until for mixtures above the percolation limit (approximately 15% of the minority phase in 3-D), a bicontinuous structure of interlocking domains forms, separated by sharp, well-defined interfaces. The system then enters the hydrodynamic phase and the domains grow as the interface rearranges itself under the action of surface tension coupled to the fluid flow. For a mixture below the percolation limit, droplets form instead. The time evolution of a droplet mixture (once the droplets have become spherical and thus minimised their surface area as far as possible by interface movement alone), is governed by diffusion, both of individual fluid particles through the other phase, and of the droplets themselves until they bump into each other. This all proceeds at the same overall $T^{1/3}$ growth rate for domain (droplet) size, and is not the subject of this study, for further details see Bray (1994). The early, diffusive stage is also not the main subject of this study, which is concerned with the hydrodynamic behaviour of the system.

The addition of hydrodynamics to the system modifies the Cahn-Hilliard equation for the time evolution of the order parameter, ϕ, to give,

$$\frac{\partial \phi}{\partial T} + \mathbf{v}.\nabla\phi = M\nabla^2\mu, \tag{2.17}$$

where $\mathbf{v}(\mathbf{r})$ is the fluid velocity, M is a transport coefficient characterising the diffusion, and $\mu = \delta F/\delta\phi$ is the chemical potential. This equation says simply that in addition to diffusion ($M\nabla^2\mu$ term), the order parameter also changes with time because it is advected by the fluid flow ($\mathbf{v}.\nabla\phi$ term).

The fluid velocity obeys the Navier-Stokes equation (NSE),

$$\rho\left[\frac{\partial \mathbf{v}}{\partial T} + (\mathbf{v}.\nabla)\mathbf{v}\right] = \eta\nabla^2\mathbf{v} - \nabla.\underline{\underline{\mathcal{P}}}, \tag{2.18}$$

with a term, $-\phi\nabla\mu$, from the repulsion between the different fluids, included in $\nabla.\underline{\underline{\mathcal{P}}}$, with the pressure tensor, that couples the fluid flow to the order parameter.

2.3.1 Late stage hydrodynamic growth

After being quenched from a completely mixed state to a temperature well below the critical temperature, the system starts off by diffusing until interfaces form between separated domains of each fluid. The initial size of the domains depends on the interface thickness; clearly they have to be at least twice the width of the interface. Diffusion is relatively slow, the domain size grows as $T^{1/3}$, as shown in Section 2.2.3. Once interfaces have formed, they take over from diffusion in driving the separation. Since all the excess energy in the system is now contained in the interfaces, this being the only region where the fluid is not fully separated, the system evolves in such a way as to minimise the interfacial area. To do this, the interfaces flatten and shrink, moving the bulk fluid around. The fluid motion is resisted by viscous drag and by inertial forces due to the finite fluid mass density. Since the initial interface configuration has a high topological connectivity (many "handles") the coarsening process cannot proceed without also reducing the connectivity by breaking "handles" in addition to the shrinking and flattening. This occurs when a "handle" shrinks to a narrow fluid "neck" connecting larger domains. For pictures of this process from the simulation data, see Appendix A. An analysis that investigates the dynamics by considering the decrease in the density of "handles" as the system coarsens has been done by Jury (1999). This analysis has not been repeated in this study.

In order to quantify the time evolution of the separation process, the size of the domains has to be measured, and the time dependence of the domain size determined. As with the diffusive system, the domain size can be measured by the inverse of the first moment of the spherically averaged structure factor, $L(T)$, Equation (2.5). The pair of coupled nonlinear differential equations that describe the dynamics of this system, Equations (2.17) and (2.18), are intractable to exact analytical solution, however, as

in the previous section, simple dimensional analysis may be used to find out how fast the domains grow once the diffusive period is over. See Bray (1994) for a thorough description of many different applications of dimensional analysis to this and other related systems; the following will cover only the points needed for this specific system.

The aim is to find the form of the time dependence of $L(T)$ by making simplifying assumptions in the Navier-Stokes equation, Equation (2.18). The technique is to balance the force from the interface contained in the pressure tensor, $\underline{\underline{\mathcal{P}}}$, against the viscous and inertial terms which tend to oppose the motion of the interface. First, a simple expression for the interfacial force, $-\phi\nabla\mu$, is needed. The results from the previous section for the Gibbs-Thomson boundary condition can be used for this system too. Thus μ can be approximated by its value at the interface, μ_I, given by, $\mu_I\Delta\phi = -\sigma\mathcal{K}$, Equation (2.12), and the interfacial force, $-\phi\nabla\mu$, can be approximated as follows. The curvature, $\mathcal{K}$, is of the order of $2/L(T)$, where $L(T)$ is the domain size, since $L(T)$ is roughly the "diameter" of the domains and curvature is the reciprocal of the radius. The gradient operator, ∇, can be approximated by $1/L(T)$, since the chemical potential varies over distances of the order of the domain size. Finally, $\Delta\phi \simeq 2\phi$ since it corresponds to the difference between the two equilibrium values of ϕ. Putting all this together gives,

$$-\phi\nabla\mu \simeq \frac{\sigma}{L^2}. \tag{2.19}$$

Similarly, the fluid velocity, $\mathbf{v}$, can be approximated by the velocity of the interface, $\dot{L}(T) = \mathrm{d}L/\mathrm{d}T$. Substituting into the Navier-Stokes equation, Equation (2.18), gives for the viscous term,

$$\eta\nabla^2\mathbf{v} \simeq \eta\frac{\dot{L}}{L^2}, \tag{2.20}$$

and for the inertial terms,

$$\rho\left[\frac{\partial\mathbf{v}}{\partial T} + (\mathbf{v}.\nabla)\mathbf{v}\right] \simeq \rho\ddot{L} + \rho\frac{\dot{L}^2}{L}. \tag{2.21}$$

Under conditions in which the inertial terms are neglible, the force from the interface will be entirely balanced by the viscous dissipation, giving,

$$\frac{\dot{L}}{L^2} \simeq \frac{\sigma}{\eta}\frac{1}{L^2}, \tag{2.22}$$

integrating this gives,

$$L \sim \frac{\sigma}{\eta} T, \tag{2.23}$$

i.e. the domain size is predicted to grow linearly with time in the region where the fluid flow is dominated by viscous hydrodynamics. This result was first obtained by Siggia (1979). Linear growth has been reported in experiments by, for example, Kubota et al. (1992), Chen et al. (1993c), Hashimoto et al. (1994), and in simulations incorporating hydrodynamics by Koga and Kawasaki (1991), Puri and Dünweg (1992), Alexander et al. (1993), Laradji et al. (1996), Bastea and Lebowitz (1997) and Jury et al. (1999). Some of these simulation results will be discussed in more detail in Section 5.6, where they are compared to the simulation results in this study.

To find the growth rate in the inertial region, the argument can be reversed to consider the case where the viscosity is low enough for the viscous term to be small compared to the inertial terms. The force from the interface is then equated with the inertial terms,

$$\ddot{L} + \frac{\dot{L}}{L} \simeq \frac{\sigma}{\rho} \frac{1}{L^2}. \tag{2.24}$$

Integrating this twice gives,

$$L^3 \simeq \frac{\sigma}{\rho} T^2, \tag{2.25}$$

i.e. in the region where the fluid is dominated by the inertial terms, the domain size grows as $T^{2/3}$. This result was first predicted by Furukawa (1985); there are a few claims to see this in simulation, Ma et al. (1992), Appert et al. (1995), Lookman et al. (1996), but none reliably establish dominance of inertial over viscous forces, see Section 5.6. The work of this study, recently published as Kendon et al. (1999), does claim to provide an unambiguous simulation of the inertial regime behaviour.

This derivation of $T^{2/3}$ scaling is the standard argument found in the literature, see for example, Bray (1994). In Section 2.4, a more thorough analysis will be presented which takes account of the energy balance in the system, and makes a number of more detailed predictions for the relative size of the inertial and viscous terms.

Equating these two results for the growth rate of $L(T)$, Equations (2.23) and (2.25), produces a prediction for the order of magnitude of the domain size, L_0, and time, T_0 at which the viscous and inertial terms are of equal importance to the dynamics,

$$L_0 = \frac{\eta^2}{\rho\sigma}, \tag{2.26}$$

$$T_0 = \frac{\eta^3}{\rho\sigma^2}. \tag{2.27}$$

For $L(T) \ll L_0$, viscous hydrodynamics dominates, while for $L(T) \gg L_0$, the inertial terms dominate.

A prediction of a further scaling regime beyond $L(T) \sim T^{2/3}$ by Grant and Elder (1999) is discussed below, starting in Section 2.3.3, once some further definitions and notation have been introduced.

2.3.2 Comparisons: length and time scales

In order to make meaningful comparisons between different simulation and experimental results, dimensionless measures of length and time need to be given in some universally equivalent way. This can be done by using length and time scales based on the physical parameters of the system. For given values of η, ρ and σ, it is possible to form a single pair of characteristic length and time, L_0 and T_0, introduced above as the length and time characterising the crossover between the viscous and inertial regimes, Equations (2.26) and (2.27). The length, $L(T)$, corresponding to the domain size, can be scaled using L_0, to give the reduced length, $l = L(T)/L_0$ and similarly, the time can be scaled to give the reduced time, $t = T/T_0$, thus providing a dimensionless description of the system dynamics. (Note that these scaling parameters, L_0 and T_0, are only appropriate for examining the behaviour of this type of hydrodynamic spinodal system in the viscous to inertial region, where is is assumed that no other physical parameters are relevant. For other systems or transitions, from diffusive to viscous for example, different scaling parameters would be needed.)

Rewriting the growth equations in this way gives,

$$\begin{aligned} l &= b_1 t \quad \text{viscous region} \\ l &= b_2 t^{2/3} \quad \text{inertial region,} \end{aligned} \tag{2.28}$$

where the relationships are now equalities, and the prefactors, b_1 and b_2, that have been introduced are universal constants[2]. This is the dynamical scaling hypothesis, that all

[2] If, on the other hand, there is another relevant length scale affecting the hydrodynamic growth, such as a microscopic length, then b_1 and b_2 will not be universal constants (Jury et al., 1999). If

hydrodynamic spinodal symmetric binary systems[3] can be scaled onto the same l, t, curve, with the same values of b_1 and b_2. Testing this dynamical scaling hypothesis is one of the main aims of this work, the results are presented in Chapter 5.

There is no scaling prediction for the behaviour in the crossover region between linear and inertial scaling, but the transition is expected to be smooth, so it can conveniently be approximated by an intermediate exponent, α, and written,

$$l \simeq b(\alpha)t^{\alpha}, \tag{2.29}$$

where $b_1 = b(1) \leq b(\alpha) \leq b(2/3) = b_2$, and $1 \leq \alpha \leq 2/3$.

2.3.3 Comparisons: Reynolds numbers

Clearly it is useful for the study of this system in the viscous and inertial regions to compare the relative magnitude of the terms in the Navier-Stokes equation. Two ratios have therefore been defined, the ratio between the acceleration term and the viscous term,

$$R_1 = \frac{|\rho \partial \mathbf{v}/\partial t|}{|\eta \nabla^2 \mathbf{v}|}, \tag{2.30}$$

and the ratio between the nonlinear term and the viscous term,

$$R_2 = \frac{|\rho(\mathbf{v}.\nabla)\mathbf{v}|}{|\eta \nabla^2 \mathbf{v}|}. \tag{2.31}$$

These ratios, R_1 and R_2, are $\gg 1$ where the inertial terms dominate and $\ll 1$ where the viscous term dominates.

The Reynolds number,

$$\mathrm{Re} = \frac{\text{typical velocity} \times \text{typical length}}{\text{kinematic viscosity}}, \tag{2.32}$$

is a simpler non-dimensional quantity that provides an estimate of R_2. When R_2, Equation (2.31), is simplified using the kind of simple scaling employed in Section 2.3.1

---

the fluid density, ρ, varies significantly then this could also influence the value of b_1 and b_2; here the fluids are assumed to be incompressible, the compressibility of the fluid in the numerical simulations is checked in Section 3.6.5.

[3] Asymmetric binary systems would also be expected to follow this scaling (with $b_{1,2}$ depending on composition) provided they remain percolated throughout the separation process. However, such systems have not been considered here. For all systems, symmetric and asymmetric, the quench needs to be deep enough to be far from the critical point.

(to obtain the time dependence of the domain size), in which $\nabla \rightarrow 1/L$, the result is the following Reynolds number,

$$\frac{\rho \mathbf{v}.\nabla \mathbf{v}}{\eta \nabla^2 \mathbf{v}} \simeq \frac{\rho v^2/L}{\eta v/L^2} \simeq \frac{vL}{\eta/\rho}. \tag{2.33}$$

Usually, a sensible choice of typical length and velocity in Equation (2.32) will provide a reasonable prediction of the system dynamics based on the Reynolds number estimating the likely magnitude of R_2. However, the actual values obtained for the Reynolds number can be quite geometry dependent, (pipe flow vs. flow around an obstacle, for example) and it is sensible to be cautious and match up the same choices of length and velocity, where possible, for comparisons between different systems.

Often, too, there is more than one useful choice of typical length and velocity for any particular system. Specifically, for the binary hydrodynamic spinodal system studied here, one possible choice for length and velocity, the domain size, $L(T)$, and the interface velocity, $\dot{L}(T)$, give the Reynolds number Re_ϕ, where the subscript ϕ indicates that this Reynolds number is entirely calculated from the order parameter,

$$\mathrm{Re}_\phi = \frac{\rho}{\eta} L(T) \frac{\mathrm{d}L}{\mathrm{d}T} = l\dot{l} = \alpha b^2(\alpha) t^{2\alpha - 1}. \tag{2.34}$$

Here, Re_ϕ is only the same as R_2, if the simple scaling for velocity gradients of $\nabla \rightarrow 1/L$ holds. In the viscous region where $\alpha = 1$, $\mathrm{Re}_\phi = l\dot{l} = b_1^2 t$, while in the inertial region where $\alpha = 2/3$, $\mathrm{Re}_\phi = l\dot{l} = (2/3) b_2^2 t^{1/3}$. Thus as the domain size, l, becomes indefinitely large, so does Re_ϕ.

Grant and Elder (1999) considered this prediction of Re_ϕ growing indefinitely with domain size and argued that this was unphysical, and that instead, the increasingly turbulent dynamics would lead to the interface being disrupted by turbulent mixing, thus slowing the domain growth to the point where the Reynolds number stayed finite. By considering the α dependence of Equation (2.34), they deduced that to keep Re_ϕ finite, it is necessary to have the growth exponent, $\alpha \leq \frac{1}{2}$. In order to comment properly on this claim, some more detailed scaling analysis must be done.

2.4 New scaling predictions using energy balance

This section presents original work in the form of a more detailed analysis of the scaling predictions for the hydrodynamic binary fluid mixture undergoing spinodal decomposition as described in the previous sections. In Section 2.3.1, predictions for the time dependence of the domain size were obtained by applying a simple scaling analysis to the Navier-Stokes equation, which is the momentum conservation equation for the fluid in this system. In addition to this, energy balance should also be considered (the full set of Navier-Stokes equations includes mass conservation, which reduces to $\nabla.\mathbf{v} = 0$ for an incompressible system, and the energy balance equation, see Appendix B). Once the initial diffusive period is over, the excess energy is localised in the interface, and transfered into fluid motion as the interface moves and shrinks. At the same time, energy is lost from the fluid motion through viscous dissipation. Globally, therefore, the energy input from the interface must be equal to the rate of change of kinetic energy, minus the energy lost through dissipation,

$$\frac{\mathrm{d}}{\mathrm{d}T}\left(\rho\langle v^2/2\rangle\right) = \langle\varepsilon_{\mathrm{in}}\rangle - \eta\langle(\nabla\mathbf{v})^2\rangle, \tag{2.35}$$

where $\varepsilon_{\mathrm{in}}$ is the energy transfered from the interface to the fluid motion, and the angle brackets denote system averages. Of course it is possible in principle that energy is also transfered from the fluid motion back into the interface, but this will stretch the interface again and thus won't be counted in the overall reduction of interfacial area as the system evolves. These and other local variations are included in the full local energy balance equation, see Appendix B, but are not needed here.

The average energy loss from the interface, $\langle\varepsilon_{\mathrm{in}}\rangle$, can be estimated by considering how the interfacial area A_ξ, changes with time. By dimensional arguments, A_ξ must scale as $1/L(T)$; the system volume, V, remains constant and $V \simeq A_\xi L(T)$, so per unit volume, $A_\xi \simeq 1/L(T)$. The energy stored in the interface is then $\sigma A_\xi \simeq \sigma/L(T)$, thus the rate of energy loss is,

$$\langle\varepsilon_{\mathrm{in}}\rangle \simeq -\frac{\mathrm{d}}{\mathrm{d}T}\left(\frac{\sigma}{L}\right) = \sigma\frac{\dot{L}}{L^2}. \tag{2.36}$$

The simple scaling assumptions made to obtain the time dependence of $L(T)$ in the viscous and inertial regions from the NSE in Section 2.3.1 were,

$$\mathbf{v} \sim \dot{L}(T),$$

$$\begin{aligned} \nabla &\sim 1/L(T) \\ L(T) &\sim T^{\alpha}. \end{aligned} \tag{2.37}$$

Applying these scaling assumptions to the energy balance equation should be consistent with the results obtained for the same procedure applied to the NSE; both energy and momentum must balance in the system. Substituting the scaling expressions from Equations (2.36) and (2.37) into the energy balance equation, Equation (2.35), gives,

$$\rho(\alpha-1)\ddot{L}\dot{L} \simeq \sigma\alpha\frac{\dot{L}}{L^2} - \eta\left(\frac{\dot{L}}{L}\right)^2. \tag{2.38}$$

Further expressing all the factors of L as powers of T, gives,

$$\rho(\alpha-1)T^{2\alpha-3} \sim \sigma\alpha T^{-\alpha-1} - \eta T^{-2}. \tag{2.39}$$

where the prefactors have been left in to facilitate identification of the terms.

Consider the case of the viscous regime first, where the inertial terms in the NSE are negligible. From analysis of the NSE, see Section 2.3.1, the domain size, $L(T)$, is found to scale as $L(T) \sim T$. Looking at Equation (2.39) for the linear case, $\alpha = 1$, the l.h.s. is zero, and the viscous dissipation exactly balances the energy input to the fluid motion from the interface. Both the dissipation, $\eta(\nabla \mathbf{v})^2$, and the energy lost from the interface, ε_{in}, are predicted to scale as T^{-2}. For a fluid that starts out at rest in the fully mixed initial state, with $\partial(\rho v^2/2)/\partial T = 0$, the fluid velocity must stay approximately zero throughout the separation, any motion imparted to the fluid by the interface must be immediately damped by viscous dissipation. Hence the description "creeping flow" often used to describe the viscous regime[4].

However, in the inertial region with $\alpha = 2/3$, it is a different story entirely. As it stands, Equation (2.39) cannot be made to balance. The l.h.s is negative (prefactor $\alpha - 1 = -1/3$), but the energy input from the interface is larger ($T^{-5/3}$) than the dissipation rate (T^{-2}). So the scaling assumptions made so far and used in Section 2.3.1 to derive $L(T) \sim T^{2/3}$ in the inertial region, don't actually work once energy balance is also taken into account. This isn't so very surprising, since in the inertial region the fluid may be expected to become turbulent, and turbulence introduces length

[4]Obviously, to get anywhere at all in the separation process in a finite time, there must be fluctuations in which the fluid does move significantly, Sections 5.4.3 and 6.2.2 describe what was found in the simulation results.

scales of its own into the velocity field. The next step, therefore, is to try relaxing the assumptions $v \sim \dot{L}(T)$, and $\nabla \sim 1/L(T)$ for the velocity derivatives. Note that the assumption of $\nabla \sim 1/L(T)$ for the energy input from the interface can remain, since for scaling to work at all, the length scale relevant for gradients relating to the interface must be on a scale of the domain size. The velocity, however, may be varying over different length scales.

To relax these assumptions, two new exponents and a new length are defined,

$$\mathbf{v} \sim T^{\beta}, \tag{2.40}$$

$$L_{\nabla} \sim T^{\alpha'}, \tag{2.41}$$

with $\nabla \sim 1/L_{\nabla}$. The time dependence of the energy balance equation, Equation (2.38) then becomes,

$$\rho\beta T^{2\beta-1} \sim \sigma\alpha T^{-\alpha-1} - \eta T^{2\beta-2\alpha'}. \tag{2.42}$$

In the viscous region where $\alpha = 1$, this gives $\alpha' = 1$ and $\beta = 0$ as before [5]. In the inertial region where $\alpha = 2/3$, a three-way balance between the terms such that they all have the same time dependence produces the solution, $\alpha' = 1/2$, with $\beta = -1/3 = \alpha - 1$ as before. In other words, the velocity still scales like $\dot{L}(T)$, but the velocity gradients are varying on smaller length scales. Note that there is no solution to Equation (2.42) for intermediate values of α between $\alpha = 1$ and $\alpha = 2/3$ that is valid for all times T, but since the crossover region only occurs for a finite range of T, this is not a problem, and a smooth transition can be expected in which the system finds a transitional balance that works only for restricted values of T. So, it *seems* that it is possible to satisfy the energy balance equation while retaining the scaling of $L(T) \sim T^{2/3}$ in the inertial region with the addition of just one new scaling length for the gradients of the velocity, $L_{\nabla} \sim T^{1/2}$.

Next, it is necessary to check whether this new scaling also works in the Navier-Stokes equation, and if so, what effect it has. Turning all the NSE terms into powers of T based on $L(T) \sim T^{2/3}$, $v \sim T^{-1/3}$ and $\nabla \sim T^{-1/2}$, gives

$$\rho T^{-4/3} + \rho T^{-7/6} \sim \eta T^{-4/3} - \sigma T^{-4/3} \tag{2.43}$$

[5] For a full discussion of all the possible solutions for the exponents, see Appendix B.

instead of the simple scaling prediction ($L_\nabla \sim L(T)$) of,

$$\rho T^{-4/3} + \rho T^{-4/3} \sim \eta T^{-5/3} - \sigma T^{-4/3} \tag{2.44}$$

In other words, if the length scale associated with the velocity gradients is decoupled from $L(T)$ to make energy balance work, then it has the twin effects of making the dissipation stay relevant to the momentum balance even in the inertial region, and, increasing the size of the nonlinear term relative to the time derivative, i.e. growing turbulence. The ratio of the nonlinear to the viscous terms (Reynolds number) now grows as $T^{1/6}$, this is smaller than the naive prediction of $\mathrm{Re}_\phi \sim T^{1/3}$, but still increasing indefinitely.

Evidence for this picture at least being along the right lines will be shown in Chapter 6, where Figure 6.9 (right) does show the nonlinear term becoming larger than $\partial \mathbf{v}/\partial T$ in the simulation furthest into the inertial region.

However, while it is no longer a problem for Re_ϕ to grow without bound if it is decoupled from the length scales associated with the velocity gradients, it is still unphysical for a single term in the NSE to decay slower than all the rest as it would eventually come to dominate the equation with no other term large enough to balance it. So, it is necessary to try going one step further with the velocity gradients and decouple ∇^2 from ∇, introducing $L_{\nabla^2} \sim T^{\alpha''}$. This does not affect the energy balance scaling since there are no ∇^2 terms in that, but the NSE becomes,

$$\rho T^{-4/3} + \rho T^{-7/6} \sim \eta T^{-1/3-2\alpha''} - \sigma T^{-4/3}, \tag{2.45}$$

where the same scalings, $\alpha = 2/3$, $\beta = -1/3$ and $\alpha' = 1/2$ as before have been used. Now the driving term can balance against $\partial \mathbf{v}/\partial T$, while the nonlinear term is balanced by slightly higher dissipation, giving a prediction of $2\alpha'' = 5/6$, or $L_{\nabla^2} \sim T^{5/12}$. The ratio of the nonlinear to viscous terms is now constant, i.e. R_2 stays finite, while the scaling of $L(T)$ remains as $L(T) \sim T^{2/3}$. These new scaling predictions are summarised in Table 2.1.

It has thus been possible to find a way to answer the assertion from Grant and Elder (1999) that the Reynolds number, now meaning R_2, the actual ratio of the nonlinear to the viscous terms, should stay finite, while still maintaining the inertial scaling growth

quantity	*viscous region*	*inertial region*	
		simple scaling	*new scaling*
$L(T)$	1	2/3	2/3
L_∇	1	2/3	**1/2**
L_{∇^2}	1	2/3	**5/12**
$\mathbf{v}$	0	-1/3	-1/3
$\partial\mathbf{v}/\partial T$	$=0$	-4/3	-4/3
$\mathbf{v}.\nabla\mathbf{v}$	$=0$	-4/3	**-7/6**
$\eta\nabla^2\mathbf{v}$	-2	-5/3	**-7/6**
$\phi\nabla\mu$	-2	-4/3	-4/3
$\mathrm{Re}_\phi = l\dot{l}$	1	1/3	1/3
Re_λ	1	1/3	**1/6**
R_1	$=0$	1/3	**-1/6**
R_2	$=0$	1/3	**0**
$\varepsilon = \eta(\nabla\mathbf{v})^2$	-2	-2	**-5/3**
$\lambda = \sqrt{5\eta\langle v^2\rangle/\varepsilon}$	1	2/3	**1/2**
$\lambda_d = 2\pi(\eta^3/\rho^3\varepsilon)^{1/4}$	1/2	1/2	**5/12**

Table 2.1: *Summary of predicted scaling exponents for the viscous and inertial regions. The new theory has the same predictions for the viscous region as the simple theory. Entries are powers of* T*, an entry of* 0 *indicates the quantity is constant, while an entry of* $=0$ *indicates the quantity is assumed to be zero in the viscous approximation. Bold entries indicate new scaling predictions that differ from the simple theory. The lengths* λ*, the Taylor microscale, and* λ_d*, the Kolmogorov microscale or dissipation scale, are discussed in Section 2.5.*

of $L(T) \sim T^{2/3}$. The Reynolds number given by $\mathrm{Re}_\phi = l\dot{l}$ still grows without bound, but it no longer provides an accurate estimate of the actual ratio R_2. This result has been achieved at the expense of introducing subsidiary lengths associated with the velocity derivatives. In fact, there is no particular reason why there should not instead be a continuum of velocity length scales rather than just two[6], but in a system restricted to derivatives up to second order, (the NSE is, itself, an approximation based on separation of macroscopic and molecular length and time scales), one length scale per derivative would seem to be a reasonable maximum for the purpose of simple scaling arguments. For a full discussion of all the possible solutions for the new exponents introduced here that shows that the cases discussed above are the only physically sensible ones, see Appendix B.

Notice in Table 2.1, that in the new scaling theory for the inertial region, the lengths

[6] It is tempting to suggest a series of decreasing lengths for higher derivatives converging on $L_{\nabla^\infty} \sim T^{1/3}$, based on the sequence, 2/3, 1/2, 5/12 for $L(T)$, L_∇ and L_{∇^2}.

L_∇ and L_{∇^2} have the same scaling as the turbulent length scales λ and λ_d respectively. They must, therefore, apart from numerical prefactors, be the same length scales. These two length scales, the Taylor and Kolmogorov microscales, have long been known as key characteristic quantities in turbulence theory (see Section 2.5), to find them appearing in appropriate roles in this new scaling theory for the inertial region behaviour of spinodal decomposition is strong support for the new theory.

One can now describe a picture of what is happening to the energy in the system as it coarsens in the inertial region. Energy is first transfered from the interface $(-\phi\nabla\mu)$ to large scale fluid motion $(\rho \mathrm{d}\mathbf{v}/\mathrm{d}T)$. The nonlinear term $(\rho\mathbf{v}.\nabla\mathbf{v})$ then transfers the energy from the large scales down through to smaller scales where dissipative forces $(\eta\nabla^2\mathbf{v})$ finally remove it from the system. There can be a significant time delay between the energy input and the energy dissipation while it moves through the length scales from the domain size down to the smaller scales where dissipation is taking place; the turbulent dynamics decouples the energy input scales from the dissipation scales. It thus seems quite reasonable to have a range of associated length scales with this process, in contrast to the viscous region where everything happens on the single length scale set by the domain size. This picture of the fluid behaviour in the inertial region is known as the "energy cascade" to turbulence theorists, and is certainly more complicated than the simple picture presented here with just two extra length scales. It can be neatly visualised by considering the velocity structure factor, Equation (6.1), (energy spectrum, or actually spectral density to turbulence theorists), see Figure 3.4 for examples of spinodal and turbulent velocity structure factors from the simulations in this study. A brief description of the relevant aspects of turbulence theory is given in the next section, to place these new results in context.

To summarise this section, which describes original work, it has been found that by allowing the gradients of the velocity to scale differently from the domain size, the inertial region scaling of $L(T) \sim T^{2/3}$ is maintained, while the Reynolds number, measured as the actual ratio of the nonlinear to the viscous terms in the NSE, remains finite. The assumption made in the simple scaling theory (Furukawa (1985), Bray (1994)) that the viscous term is negligible is not a correct assumption for determining asymptotic scaling because the viscous term involves the highest order in derivatives and is thus a a singular perturbation in the NSE: however small η is, the asymptotic physics is rad-

ically altered from that with $\eta = 0$. When energy balance is also taken into account, a consistent set of exponents can be found, at the expense of introducing two extra length scales in the inertial region for the velocity gradients. Even if the idea of extra length scales for the velocity derivatives is unconventional, note that the key point for the scaling behaviour of $L(T)$ is that the driving force balances against the acceleration term alone, so is decoupled from what happens in the remainder of the fluid motion. The nonlinear and viscous terms are free to find their own balance independent of the driving force, provided that they transport energy from length scales of order $L(T)$, down to smaller scales. Finding a balance implies that, however they do it, their ratio, the true Reynolds number, R_2, will be finite, while the domain growth rate goes as $L(T) \sim T^{2/3}$.

2.5 Turbulence

Turbulence is another example of a universal scaling phenomenon. Away from boundaries or driving forces, the structure of a turbulent fluid is independent of the nature of the particular fluid. Turbulence occurs when the velocity gradients in the fluid flow become large, either through high flow rates, or through shearing or stirring forces being applied. This was quantified by Reynolds (1894), as the ratio of the nonlinear to viscous terms in the Navier Stokes equation, the Reynolds number, Equation (2.32). The simplest picture of turbulence comes from Richardson (1922) who suggested an "energy cascade" of eddies carrying the energy from large scale motion down through smaller and smaller scales until viscosity causes it to be finally dissipated as heat. This has led to many different "cascade" models of turbulence, which attempt to predict the statistics of a turbulent fluid by making assumptions about the form of the energy cascade. Richardson also pointed out that this picture of turbulence implies that the important physics is in the statistics of velocity derivatives and differences, $\delta\mathbf{v}(\mathbf{x_1}, \mathbf{x_2}) = \mathbf{v}(\mathbf{x_1}) - \mathbf{v}(\mathbf{x_2})$, rather than in the velocity itself, which still contains information about the large scale motion.

Kolmogorov (1941) took these ideas further and proposed the idea of the "inertial range"[7]. For very large Reynolds numbers, the separation between the large scale

[7]Not to be confused with the "inertial regime" or "inertial region" in spinodal decomposition.

energy input and the small scale dissipation leaves a wide range of length scales over which the energy is simply flowing through, and for a stationary state in which the energy input is equal to the dissipation rate, the energy transfer will also be at the same rate, ε. Thus for any particular length scale $L_i = |\mathbf{x}_1 - \mathbf{x}_2|$ (equivalent to a particular wavenumber in Fourier space) at which the statistical properties of the turbulence are investigated, the only relevant physical quantities are the length, L_i, the energy flow rate, ε, and the fluid density, ρ. These can be combined to form quantities of any dimensionality, leading to predictions for the form of the structure functions of the velocity differences, $S_n(L_i) \equiv \langle |\delta\mathbf{v}(\mathbf{x}_1, \mathbf{x}_2).(\mathbf{x}_1 - \mathbf{x}_2)/L_i|^n \rangle$, that form the basis for scaling theories of turbulence. This gives, for example, $S_2(L_i) \sim (\varepsilon L_i)^{2/3}$, the Kolmogorov "2/3" law.

Experiments and simulations show that Kolmogorov was nearly right in this theory, the relationships are in the form of power laws, but the exponents do not agree with his predictions. This is known as "anomalous scaling" and it means that another length scale must in fact be relevant to the problem. The two remaining length scales in the system are the energy input scales (call them L here since for the spinodal system they come from the interface), and the dissipation scales. Experiments (and, in recent years, simulations) to test the scaling predictions are not easy to perform to the required accuracy, and it took a long time to work out that it is the energy input scales, L, rather than the dissipation scales, that affect the scaling (for example, Stolovitzky et al. (1993)). Theoretically this is not at all obvious, but the accumulating evidence seems to be that the Navier-Stokes equations are continuous across all sorts of situations in which small scale singularities occur, such as dissipation, pinchoff when droplets form or necks break (see Eggers (1995)) whereas correlations from the large scale motions persist to influence the "inertial range" scaling behaviour in some presumably universal way[8].

Further details of current theories of turbulence scaling are not needed for this work, but a basic description of the phenomenology of isotropic, homogeneous turbulence follows as it will be useful for comparison with the results in Chapters 4 and 6. Isotropic, homogeneous turbulence may be studied experimentally in the form of turbulence cre-

[8] Note also that turbulence in 2-D is rather different, the descriptions in this section refer to 3-D turbulence.

ated by a mesh of wires placed in a fluid stream (grid turbulence), or as a small section of a much larger turbulent system (atmospheric, oceanic), and by numerical simulation, see Section 4.2.

Since the main theoretical focus for the understanding of turbulence is the behaviour across different length scales, it is natural to start from the Fourier space representation of the velocity field $\mathbf{v}(\mathbf{k})$. The velocity structure factor, $S_v(k) = \langle \mathbf{v}(\mathbf{k}).\mathbf{v}(-\mathbf{k}) \rangle_{|\mathbf{k}|=k}$, Equation (6.1), is known to turbulence theorists as the spectral density. Equally useful is the energy spectrum, $E(k)$, given by,

$$E(k) = \frac{\rho}{2} \int_{|\mathbf{k}|=k} \mathrm{d}^3\mathbf{k}\ \mathbf{v}(\mathbf{k}).\mathbf{v}(-\mathbf{k}) = 4\pi k^2 \frac{\rho}{2} S_v(k), \tag{2.46}$$

which gives the total energy associated with each wavenumber, k. A plot of $E(k)$ thus gives a picture of how the energy is distributed through the turbulence from large to small length scales. The typical shape of $E(k)$ is shown in Figure 2.3 (left). The inertial

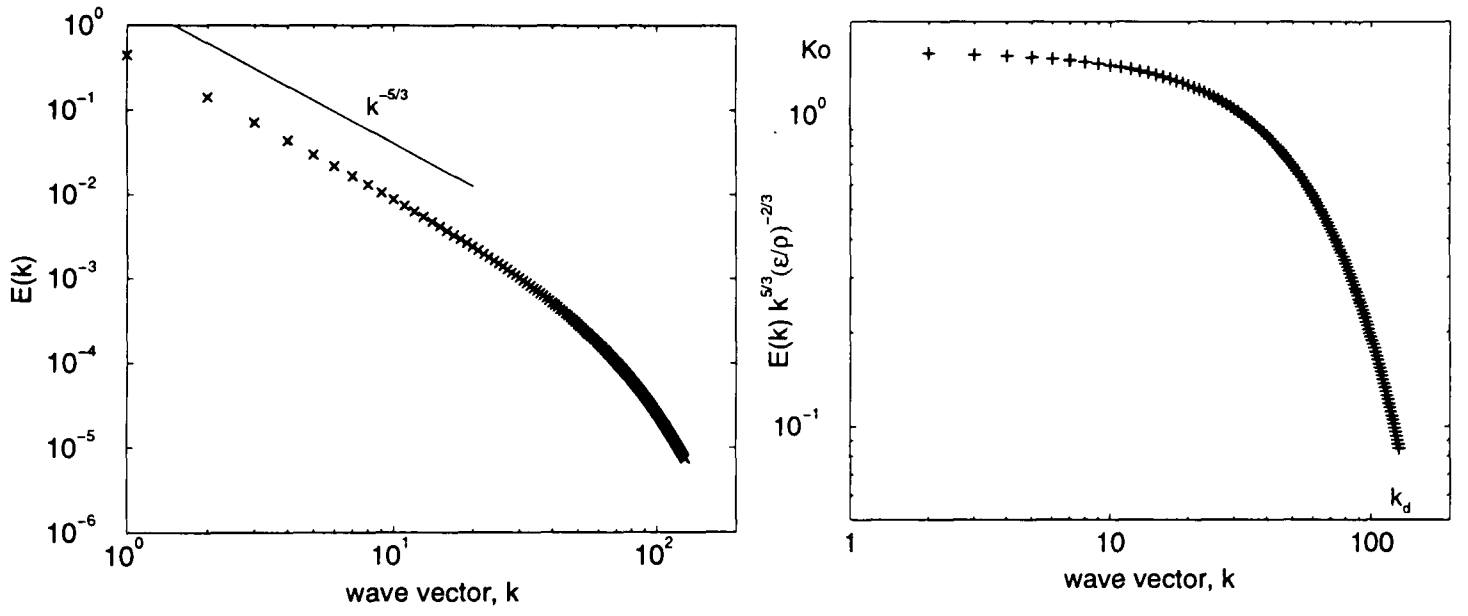

Figure 2.3: *Typical shape of the energy spectrum, $E(k)$, for fully developed homogeneous isotropic turbulence. Left: Energy spectrum. Right: Energy spectrum in Kolmogorov scaling.*

range was predicted by Kolmogorov to scale as,

$$E(k)/\rho = \mathrm{Ko}\, k^{-5/3} (\varepsilon/\rho)^{2/3}, \tag{2.47}$$

where Ko is the Kolmogorov constant (the value of which seems to be around $1.5-2$, and is still a subject of disagreement). For this reason, energy spectra are often plotted in *Kolmogorov scaling*, $k^{5/3}\rho E(k)/(\varepsilon/\rho)^{2/3}$, which turns the inertial range into a horizontal line at the value of Ko, see Figure 2.3 (right). The section of $E(k)$ beyond the inertial range is the dissipation range, and decays exponentially.

The key quantities by which a turbulent system can be characterised are, the dissipation rate, ε,

$$\varepsilon = \eta\langle(\nabla \mathbf{v})^2\rangle = 2\nu \int \mathrm{d}k\, k^2 E(k), \tag{2.48}$$

the rate of energy input (equal to the dissipation rate for steady state turbulence), and the energy input length scales, L. Various characteristic length scales can also be defined. The largest of these, the integral scale,

$$L_{int} = \frac{3\pi\rho}{4E} \int \mathrm{d}\mathbf{k}\, \frac{1}{2k} \mathbf{v}(\mathbf{k}).\mathbf{v}(-\mathbf{k}), \tag{2.49}$$

where $E = \int \mathrm{d}k\, E(k)$, is the total energy, represents the correlation length of the velocity in real space (Monin and Yaglom, 1975, page 35)[9]. The integral scale is similar to the definition used for $L(T)$, the length used to characterise the domain size, Equation (2.5). A length can similarly be defined for the velocity field, L_v,

$$L_v = \frac{\int \mathrm{d}k\, S_v(k)}{\int \mathrm{d}k\, k S_v(k)} = \frac{\int \mathrm{d}\mathbf{k}\, k^{-2}\, \mathbf{v}(\mathbf{k}).\mathbf{v}(-\mathbf{k})}{\int \mathrm{d}\mathbf{k}\, k^{-1} \mathbf{v}(\mathbf{k}).\mathbf{v}(-\mathbf{k})}, \tag{2.50}$$

by writing L_{int} as,

$$L_{int} = \frac{3\pi}{2} \frac{\int \mathrm{d}\mathbf{k}\, k^{-1}\, \mathbf{v}(\mathbf{k}).\mathbf{v}(-\mathbf{k})}{\int \mathrm{d}\mathbf{k}\, \mathbf{v}(\mathbf{k}).\mathbf{v}(-\mathbf{k})}, \tag{2.51}$$

it can be seen that L_{int} and L_v are just different ratios of the moments of $S_v(k)$. The Taylor microscale[10],

$$\lambda = \sqrt{\frac{10\nu E}{\varepsilon}}, \tag{2.52}$$

is usually smaller than the integral scale and is a measure of the length scales in which dissipation is important. By writing λ as,

$$\lambda = \left(\frac{5\langle \mathbf{v}.\mathbf{v} \rangle}{\langle \nabla \mathbf{v}.\nabla \mathbf{v} \rangle} \right)^{1/2}, \tag{2.53}$$

and applying simple dimensional analysis, it can be seen that (apart from numerical prefactors) the Taylor microscale is essentially the length associated with ∇, i.e. L_∇ from the previous section. The Kolmogorov microscale,

$$\lambda_d = 2\pi \left(\frac{\rho\nu^3}{\varepsilon} \right)^{1/4} = \frac{2\pi}{k_d}, \tag{2.54}$$

[9] Monin and Yaglom use $\pi/2$ in place of $3\pi/4$ for the numerical prefactor, there seems to be no agreement on the definition of the intergral scale between the authors surveyed.

[10] In place of the Taylor microscale, Monin and Yaglom describe a "differential length scale" of essentially the same definition apart from the numerical prefactor. In total, three variations on the numerical prefactor were noted in the literature for this quantity. The definitions used here are consistent with Young (1999), the author of the simulation code, and in any case, the precise numerical prefactors are of no significance in this study.

is an even smaller length scale than λ, most of the dissipation takes place at larger length scales than λ_d. Although it is not so easily seem by scaling arguments, in the previous section where the scaling behaviour with time of the binary fluid mixture was discussed, λ_d shares the same scaling as L_{∇^2}, see Table 2.1, so must be, in effect, the same length scale. The correspondence of L_∇ to λ and L_{∇^2} to λ_d, well-known length scales from turbulence theory with the appropriate properties, is strong support for the scaling theory developed in the previous section.

The total energy (per unit volume) gives the rms average velocity, $v_{rms} = \sqrt{2E}$, and from this a time scale, the eddy turnover time, is defined as $T_E = L_{int}/v_{rms}$, which gives an estimate of the time it takes for an eddy of size L_{int} to form. This gives a natural timescale over which (for gathering statistical data) the independence of successive measurements can be characterised.

The statistics of the velocity components in isotropic homogeneous turbulence are completely random (Gaussian) in both space and time (once small scale and time correlations are discounted). However, one striking signature of turbulence is to be found in the skewness (third moment) of the longitudinal velocity derivatives, which takes the value -0.5 in fully developed turbulence. Velocity derivatives come in two types, longitudinal, e.g., $\mathrm{d}v_x/\mathrm{d}x$, and transverse, e.g., $\mathrm{d}v_x/\mathrm{d}y$ or $\mathrm{d}v_x/\mathrm{d}z$. Transverse derivatives are obviously symmetric, so show no skewness, but due to the incompressibility condition, the variance of the transverse derivatives is expected to be twice that of the longitudinal derivatives, the von Kármán condition (1937), see, for example, Monin and Yaglom (1975).

As already mentioned, those studying turbulence invest a great deal of time calculating higher moments of the velocity derivatives and velocity increments to characterise the scaling behaviour in full detail. None of this will be necessary or possible given the limited statistics available for the simulations studied here. The accuracy with which higher moments can be calculated from simulation or experimental data is discussed in Section 4.4.2.

Two further concepts in the study of turbulence warrant mentioning. The first, intermittency effects, shows up in, for example, the variation of the dissipation rate spatially and with time. The departure of the local dissipation rate from the mean dissipation

rate does not follow a Gaussian distribution, rather there is a preponderance of large deviations. A precise statistical description and prediction of this patchiness – intermittency – is the basic problem still to be solved in turbulence.

Secondly, a further manifestation of this patchiness is to be found in the vorticity, $\boldsymbol{\omega} = \nabla \wedge \mathbf{v}$. The nonlinear term can also be written in terms of the vorticity as $\mathbf{v}.\nabla\mathbf{v} = -\mathbf{v} \wedge \boldsymbol{\omega}$. Thus the vorticity naturally appears in the analysis of the Navier-Stokes equation, and simplifies some of the calculations both for theory and simulation methods such as the pseudo-spectral direct numerical simulation used to generate the turbulence data analysed in Chapter 4. Regions of high vorticity develop into structures such as sheets or thin tubes that persist in the same region for considerable lengths of time. The appearance of complex structures on many length scales like this has led to ideas from fractal geometry being applied to turbulence, Mandelbrot (1974), and see for example, Frisch (1995).

This overview has barely touched on the rich phenomenology of turbulence, and has not attempted to present a summary of the latest results and theories, for a recent summary and pointers to further reading, see L'vov and Procaccia (1996). Hopefully, however, it has achieved the aims of providing background links to the new scaling theory presented in Section 2.4, and of describing a clear picture of the basic concepts that will be needed for the analysis of the velocity fields studied in Chapters 4 and 6.

2.6 Summary

In this chapter, a brief overview of the basics of phase separation has been presented, followed by more detailed consideration of the dynamics of the hydrodynamic model system studied here.

The simple scaling analysis usually applied to the model system was reviewed, followed by original work extending and revising the scaling in the inertial region, finding new predictions for the length scales and exponents involved once the inertial terms in the Navier-Stokes equation are large enough to play a full role in the dynamics. Two new scaling lengths are found to be necessary to satisfy scaling in both the Navier-Stokes

equation and energy balance equation. This does not alter the basic prediction of domain size growing at $T^{2/3}$, but does predict a finite Reynolds number in this region when the actual ratio of the nonlinear to viscous terms is considered, in contrast to the predictions of Grant and Elder (1999), but in the spirit of what they were suggesting. The predictions of the new scaling theory are summarised and compared to the simple scaling theory in Table 2.1 on page 29. The new length scales were identified with well-known length scales that appear in turbulent fluids, the Taylor microscale and the dissipation length or Kolmogorov microscale.

A brief overview of turbulence theory and phenomenology was then presented to set the new predictions in context and provide reference material for the analysis in later chapters.

Chapter 3

Computational methods

3.1 Introduction

Having, in the previous chapter, introduced and analysed the theoretical model to be studied, the numerical methods for simulating the model and analysing the results will now be described. No further motivation is needed for turning to numerical simulation methods, the intractability of the model equations to anything beyond the simple dimensional analysis presented in Sections 2.3.1 and 2.4 is sufficient incentive. Out of the wide variety of numerical methods available for modelling dynamical systems, care must be taken to choose one that will be able to simulate the system under study in sufficient breadth and detail. Review of the literature in this field shows that there are many possible choices that have been made by other researchers, so a brief overview of relevant simulation methods is first given to introduce and provide background for the method used here, lattice-Boltzmann. A short historical description of how the lattice-Boltzmann method grew out of lattice gas automata models allows the complexities of the method to be understood in a coherent framework. The wide range of situations to which lattice gas automata and lattice-Boltzmann methods may be applied is mentioned.

After this general description of the lattice-Boltzmann method and what it is capable of simulating, specific details are given of the code used for this study, called **Ludwig**, which was written by Bladon and Desplat (1999). This code is written in a modular

and flexible way, and can be used both in serial form on workstations, and on larger parallel-processing computers.

Attention is then turned to the analysis code written to interpret the output from the lattice-Boltzmann simulations. The simulation produces "snapshots" of the state of the system consisting of the order parameter and velocity at each lattice point. These must be processed to obtain average quantities that describe the system statistically, enabling comparisons to be made with theory and with the results of other work. This analysis code is part of the original work in this project. It is quite straightforward code, written in a fairly modular way, thus it is easy to understand what the code does and why, so it is not necessary to describe it in great detail. Some of the quantities calculated are described in further detail, such as the various length measures used to estimate the average domain size.

Finally, a section on testing and validating the code is included, where some of the limitations of the method are first explored and, where possible, quantified. Part of the original work of this project was to determine the optimal parameters for the lattice-Boltzmann code to produce the useful results presented in Chapters 5 to 7. It will become very clear as the chapters progress that this was by no means a trivial task when very little was known in advance about the characteristics of the limitations inherent in the lattice-Boltzmann method as implemented in the **Ludwig** code.

Those not wishing to consider the details of the simulation methods can turn straight to Section 3.4 where the description of the analysis code begins. There are few references in the rest of the chapters to details of the simulation code, **Ludwig**; those that do occur will be explained sufficiently as they are made.

3.2 Simulation methods

In choosing a simulation method to study the binary fluid system described in Section 2.3, the key requirements are:

- A wide range of parameters so that systems with both high and low viscosity can be studied, allowing the linear and inertial regimes to be reached.

- Large system size so that data can be collected over a sufficient range of domain sizes to allow the growth rate to be determined accurately.
- Efficiency, so that large simulations can be done with a reasonable amount of computational resources.
- Full hydrodynamics for the fluid flow. The model is already as simple as possible, any further approximations in the way the fluid is modeled, for example, to the "creeping flow" regime where the inertial terms are neglected, would obviously rule out finding the full spectrum of scaling behaviour this study is interested in.

A further useful criterion is simplicity. There is no need for any detail on the molecular level since the scaling behaviour being studied is expected to be independent of the details of any particular fluid.

With these points in mind, a brief overview of the available methods that could or have been used in other work is given next, followed by details of the lattice-Boltzmann simulation method chosen for this study.

3.2.1 Overview of numerical simulation methods

Relevant simulation methods for dynamical physical systems can be broadly grouped according the approach they take:

- molecular models: simulate a collection of many (the more the better) particles and their microscopic interactions, and get the macroscopic behaviour out by looking at the large-scales in the system. An example of a molecular dynamics (MD) simulation of the spinodal decomposition of a binary fluid can be found in Laradji et al. (1996). The MD method is computationally intensive, interactions are generally long range and costly to compute even with approximations, and the particle positions have to be individually tracked in a continuum of space variables. Importantly, however, no assumptions need be made about the macroscopic behaviour, it arises solely from the microscopic interactions.
- macroscopic models: at the other end of the length scales, the continuum equations, such as the Navier-Stokes equation, that are impossible to solve analytically

for the situations of interest, are evolved in time on a discrete grid. Examples include turbulence DNS (direct numerical simuation), the method used to study single fluid decaying turbulence in Chapter 4. The challenge here is to find an efficient and sufficiently accurate computational method for the equations to be simulated, and, of course, it presupposes that a good set of model equations exist for the situation of interest. Numerical solution of a set of macroscopic equations has often been the method of choice for others investigating hydrodynamic spinodal decomposition, see for example, Lookman et al. (1996).

- mesoscale models: to bridge the gap between molecular and macroscopic simulation methods, molecular models were abstracted in various ways, for example, into lattice gas automata, where particles live on regular lattices, move with the same speed and don't correspond to physical particles. This allowed faster algorithms and larger simulations, while still retaining the basic idea that the macroscopic behaviour arises solely from microscopic interactions. Appert et al. (1995) use lattice gas automata methods to simulate spinodal decomposition. A further abstraction to deal with particle distribution functions rather than particles on a lattice produced the lattice-Boltzmann method, which allowed even larger simulations, but at the cost of a less stable algorithm. Lattice-Boltzmann methods can be used to solve model equations, and thus meet up with macroscopic methods by providing a fast, efficient, general method for solving continuum model equations (this is the method chosen for this work, described in more detail in Section 3.2.3). Dissipative particle dynamics (DPD) is also considered a mesoscale model even though MD algorithms are used for the particle dynamics, because the particles have been abstracted into "fluid particles" rather than individual molecules, with the addition of pairwise noise and damping terms to the interparticle forces to model the interactions. An example of DPD used for studying spinodal decomposition can be found in Jury et al. (1999). A further example of a mesoscale method is the solution of Boltzmann-Vlasov equations using Monte Carlo and particle-in-cell methods by Bastea and Lebowitz (1997).

Most of the methods mentioned above have already been applied to hydrodynamic binary fluid spinodal decomposition; some of these results are considered in more detail in Section 5.6. The lattice-Boltzmann method was selected here because a good imple-

mentation was available, **Ludwig**, see Section 3.3, and because the method certainly has the potential to fulfill the criteria laid out at the beginning of this section for what is needed to model this system. In practice, of course, no model works perfectly, and the lattice-Boltzmann method turns out to have some significant limitations, which will be discussed in later chapters, particularly Chapters 5 and 6, where their impact on the results will be assessed.

3.2.2 Lattice gas automata method

By way of a historical introduction to lattice-Boltzmann methods, that will illustrate some of the key points about how the method works, a brief description of lattice gas automata models (LGA) will first be given. Lattice gas automata models have diverse roots in the 1960's from attempts to produce discrete models of fluids. The more general concept, cellular automata, was first introduced by von Neumann and Ulam in the 1940s, see von Neumann (1966). The best known example is from the 1980's, when the growth of computing power brought about a resurgence of interest; Conway's *"Life Game"* is a generalisation of spin-flipping dynamics where the states of neighbouring sites determine whether the site flips "on" or "off". Much research has been done on cellular automata motivated by ideas such as self-replicating models of living systems, equation solving, and so on.

Lattice gas automata models were first were described by Hardy et al. (1973), with further details in Hardy et al. (1976), but they were using a square lattice in two dimensions which conserves too many quantities to produce useful macroscopic equations. Thus they remained a curiosity until ten years later when Frisch et al. (1987) showed that a two-dimensional hexagonal lattice had the right symmetries to produce the Navier-Stokes equation. This paper, Frisch et al. (1987), covers all the basic theory showing how the general lattice gas automata model works.

Lattice gas automata models consist of a lattice with the right symmetries, see Appendix C, with a population of particles, $n_i(\mathbf{x}, T)$, at each lattice site $\mathbf{x}$, where i is one of a total of m lattice directions. For the 2-D hexagonal lattice, for example, $m = 6$, i.e., $i = \{1 \ldots 6\}$. The particle density, $n_i = \{0, 1\}$, where 0 means no particle and 1 means exactly one particle, in other words, the particles obey a simple exclusion rule

whereby at most one particle can occupy each state. This leads to the equilibrium distribution being a Fermi-Dirac distribution, $N_i(\mathbf{x}, T)$, the one particle distribution function, is given by,

$$N_i^{(eq)} = \frac{1}{1 + \exp(h + \mathbf{q}.\mathbf{c}_i)}, \tag{3.1}$$

where h and $\mathbf{q}$ are constants determined by the lattice and number of particles. For full details of the derivation of Equation (3.1), see Frisch et al. (1987).

The particle number density at site $\mathbf{x}$ at time T, $\rho(\mathbf{x}, T)$ is given by,

$$\rho(\mathbf{x}, T) = \sum_{i=1}^{m} n_i(\mathbf{x}, T), \tag{3.2}$$

and the momentum by,

$$\rho(\mathbf{x}, T)\mathbf{v}(\mathbf{x}, T) = \sum_{i=1}^{m} n_i(\mathbf{x}, T)\mathbf{c}_i. \tag{3.3}$$

The collision-propagation steps are represented by,

$$n_i(\mathbf{x} + \mathbf{c}_i\Delta T, T + \Delta T) = n_i(\mathbf{x}, T) + \mathcal{C}[\{n_j(\mathbf{x}, T)\}], \tag{3.4}$$

where the collision operator, $\mathcal{C}$ depends (in the simplest LGA models) only on the particles present at the local site $\mathbf{x}$. The collision operator can be written explicitly in terms of Boolean operators, since the particle numbers and directions form discrete, finite sets. Simple integer and Boolean operations mean fast computation.

In order to obtain macroscopic equations from the model, just as in real systems, a local coarse-graining is done so that space and time derivatives are well defined. Then Equation (3.4) can be Taylor-expanded, and moments taken to obtain conservation of particles,

$$\frac{\partial}{\partial T}\sum_i \langle n_i \rangle + \nabla.\sum_i \langle n_i \rangle \mathbf{c}_i = 0, \tag{3.5}$$

and conservation of momentum,

$$\frac{\partial}{\partial T}\sum_i \langle n_i \rangle \mathbf{c}_i + \nabla.\sum_i \langle n_i \rangle \mathbf{c}_i\mathbf{c}_i = 0, \tag{3.6}$$

which looks a little odd because the $\mathbf{c}_i$ are constants. Substituting $\rho(\mathbf{x}, T) = \sum_i \langle n_i \rangle$ and $\rho\mathbf{v} = \sum_i \langle n_i \rangle \mathbf{c}_i$ gives,

$$\frac{\partial \rho}{\partial T} + \nabla.(\rho\mathbf{v}) = 0, \tag{3.7}$$

and,

$$\frac{\partial(\rho \mathbf{v})}{\partial T} + \nabla . \underline{\underline{\Sigma}} = 0, \tag{3.8}$$

where,

$$\underline{\underline{\Sigma}} = \sum_i \langle n_i \mathbf{c_i} \mathbf{c_i} \rangle, \tag{3.9}$$

is the momentum flux tensor.

All derivations of hydrodynamical equations involve some kind of approximation about the form of $\underline{\underline{\Sigma}}$, depending on the particular physics of the situation under study. The rigorous method is a discrete version of the Chapman-Enskog approximation, see Frisch et al. (1987), out of which the LGA model produces something very close to the Navier-Stokes equation,

$$\begin{aligned} \frac{\partial}{\partial t}(\rho \mathbf{v}) + \nabla . [g(\rho) \rho \mathbf{v} \mathbf{v}] &= -\nabla P(\rho, v^2) \\ &+ \nabla . \{\nu_1 [\nabla(\rho \mathbf{v}) + (\nabla(\rho \mathbf{v}))^\dagger]\} \\ &+ \nabla [\nu_2 \nabla . (\rho \mathbf{v})], \end{aligned} \tag{3.10}$$

where ν_1 and ν_2 are viscosities, and $g(\rho)$ is a density dependent factor. The pressure, P is also dependent on the velocity, unlike the real NSE. However, it is generally possible to rescale time and space to remove these extra dependencies, and obtain the true NSE under a few reasonable conditions, for example, for an incompressible fluid.

Once lattice gas automata had been shown to do something useful, namely, model the Navier-Stokes equation, and alongside the expansion of available computing power, the method underwent rapid development. Rest particle states were added at each site to improve the rescaling (Frisch et al., 1987). Other lattices are possible by weighting the different directions such that the lattice algebra is isotropic, allowing cubic lattices with diagonals to be used, which are easier to visualise and work with. See Appendix C for details of the lattice symmetry requirements. Lattice gas automata turned out to have many desirable computational characteristics. The algorithm can be proved to be stable under reasonable conditions (Frisch et al., 1987), it is also fast, local and hence readily parallelised to take advantage of the fastest computers. Additionally, it scales well (i.e. computer time and memory doesn't grow as too fast a power of N for larger systems).

Lattice gas automata methods have been adapted to work for systems as diverse as buoyancy effects, seismic P-waves, magnetohydrodynamics, reaction-diffusion models, combustion, Burgers' equation, emulsions, sedimentation and high Reynolds number turbulence. The addition of boundaries at and between lattice sites allowed complex geometries to be modeled, and shear to be applied; multiple particle species with interactions were introduced to model fluid mixtures, and interactions between particles at neighbouring sites produced models with phase transitions. The first two-phase simulation was done by Rothman and Keller (1988) who give results for two dimensional simulations. An extensive overview of the theory and results for single and two phase system are reported in the review article by Rothman and Zaleski (1994). Three-dimensional two phase simulation results are reported in Appert et al. (1995) (their work is discussed in more detail in Section 5.6.3).

Despite the necessity of coarse-graining to get useful macroscopic quantities from the simulations, lattice gas automata remain an important simulation method because there is guaranteed stability in the algorithm.

3.2.3 Lattice-Boltzmann method

Not content with the successes of the lattice gas automata method, yet further extensions soon appeared. In order to obtain physical quantities from the lattice gas automata data, it is necessary to coarse-grain the lattice to smooth out small scale fluctuations. This reduces the effective system size that can be simulated.

Within two years of the key lattice gas automata paper by Frisch et al. (1987), Higuera et al. (1989) came up with the idea of working directly with the locally averaged values, f_i, where i is a lattice direction, instead of the particles n_i, thus removing the need for coarse-graining and freeing up the full size of the lattice for useful data.

Instead of particles, each lattice point, $(\mathbf{x})$, has associated with it m one-particle distribution functions, $f_i(\mathbf{x}, T)$, $(i = 1 \ldots m-1)$, where i is the lattice direction, such that the density is given by,

$$\rho(\mathbf{x}, T) = \sum_{i=1}^{m} f_i(\mathbf{x}, T). \tag{3.11}$$

Exactly as with the lattice gas automata, see Section 3.2.2, the f_i propagate with fixed velocities, $\mathbf{c}_i$ along each lattice direction, and the rest of the physical quantities are given by,

$$\rho(\mathbf{x},T)\mathbf{v}(\mathbf{x},T) = \sum_{i=1}^{m} f_i(\mathbf{x},T)\mathbf{c}_i, \tag{3.12}$$

for the momentum, and,

$$\underline{\underline{\Sigma}}(\mathbf{x},T) = \sum_{i=1}^{m} f_i(\mathbf{x},T)\mathbf{c}_i\mathbf{c}_i, \tag{3.13}$$

for $\underline{\underline{\Sigma}}(\mathbf{x},T)$, the momentum flux, tensor.

The next part of the algorithm to receive attention was the collision operator. A coarse-grained form of the microscopic collision rules used in the lattice gas automata method was used at first, but this is unnecessarily complicated. Qian et al. (1992) instead applied the BGK approximation, Bhatnagar, Gross, and Krook (1954), to obtain a new, simpler set of collision rules. A description of the BGK approximation along with a simple derivation can be found in Appendix D. Translated into the discrete directions of the lattice, the BGK approximation becomes,

$$f_i(\mathbf{x}+\mathbf{c}_i\Delta T, T+\Delta T) - f_i(\mathbf{x},T) = -\frac{1}{\tau}[f_i(\mathbf{x},T) - f_i^{(eq)}(\mathbf{x},T)], \tag{3.14}$$

where τ is a relaxation time. The equilibrium distribution $f_i^{(eq)}$ is now chosen to correspond to the model equations for the system under investigation, by assuming a form up to the second power in the velocity, $\mathbf{v}(\mathbf{x},T)$, and substituting it into Equations (3.11) to (3.13). To derive the NSE and find the transport coefficients in terms of the model parameters, a Taylor expansion of Equation (3.14) is performed and solved by successive approximation, see Higuera et al. (1989).

There are two different ways to use the lattice-Boltzmann (LB) method.

- To look at interacting systems by choosing the collision operator, for example,

$$\mathcal{C}[f_i] = -\frac{1}{\tau_r}(f_i - f_i^{(eq)} + \mathcal{C}_{int}[f_i,\mathbf{F}]), \tag{3.15}$$

  the normal BGK term plus an interaction term; $\mathbf{F}$ is a local potential, e.g. species gradient in two-fluid systems, see, for example, Gunstensen et al. (1991), Grunau et al. (1993).

- To simulate macroscopic model equations, for example,

$$\Sigma_{\alpha\beta} \equiv \mathcal{P}_{\alpha\beta} + \rho v_\alpha v_\beta, \tag{3.16}$$

  where the physics is specified by the choice of $\mathcal{P}_{\alpha\beta}$.

The method used here to simulate spinodal decomposition is the second of these, model equations have been chosen corresponding to the model described in Chapter 2, with the particular choice of $\mathcal{P}_{\alpha\beta}$ described in Section 3.3.

The main disadvantage of the lattice-Boltzmann method is that the algorithm not particularly stable. In fact, there is no guaranteed stability at all for the lattice-Boltzmann method, unlike for lattice gas automata method where an H-theorem can be used to show the algorithm will converge, Frisch et al. (1987). Choosing parameters that do remain stable within the time-scale of the simulation is very much a matter of trial and error.

On the plus side, the extra system size obtained by being able to use the whole lattice without coarse-graining means that lattice-Boltzmann methods can do basically everything lattice gas automata methods can do, but bigger, and with more generality. The LB method is a computationally efficient equation solver. As noted by Succi et al. (1991), the number of floating point operations required by the LB algorithm is of order N^d compared with $N^d \log_2 N$ for the pseudo spectral DNS method described in the next chapter for turbulence simulation. The ease with which arbitrary boundaries can be added to the simulation lattice allows more complicated systems to be simulated, for example, the flow of oil and water through porous media, Buckles et al. (1994). Colloids in solvent can be modeled by putting a boundary round spherical regions to form the colloid particles, see Ladd (1994a,b). Other systems can be modeled provided the model equations can be mapped onto the lattice-Boltzmann scheme, for example, diffusion-driven reactions are described in Qian and Orszag (1995). Further details and examples of the many uses to which the LB method has been put can be found in a recent review article by Chen and Doolen (1998).

Early results for spinodal decomposition in two and three dimensions using lattice-Boltzmann methods are reported in Alexander et al. (1993), Results for more than

two component fluids and off-critical quenches are given by Chen and Lookman (1995). However, a more thermodynamically correct version of two component fluids using the lattice-Boltzmann method, employing the free energy approach adopted for this work, was done by Swift et al. (1996). Two-dimensional spinodal decomposition of binary fluid mixtures was studied using this LB methods by Wagner and Yeomans (1998).

3.3 Ludwig - LB code used for this study

The particular lattice-Boltzmann simulation code used for the simulations in this study was written by Bladon and Desplat, and full details of the algorithm and code may be found in Bladon and Desplat (1999). A brief overview of the code, called **Ludwig**, is given here, sufficient to illuminate the rest of the work.

3.3.1 Algorithm

The **Ludwig** code has been written in a general, modular fashion so that different models can easily be substituted into the basic code. The model used in this study has already been outlined in Section 2.3, and the lattice-Boltzmann method described in Section 3.2.3. It remains to fill in the details specific to the implementation in the **Ludwig** code that are necessary for following the rest of the work.

The **Ludwig** code is written in ANSI-C, with both serial and parallel versions, the parallel code uses the MPI (message passing interface) libraries which are standard on many MPP (message passing parallel) platforms. Any nearest-neighbour cubic lattice can be used with the **Ludwig** code, but in practice, nearly all codes use the D3Q15 lattice, which is basically a body-centred cubic lattice, see Figure 3.1. On this lattice, there are three speeds for the distribution functions, f_i. There is one f_i of speed zero ("rest particle"), six of speed one (along the Cartesian directions) and eight with speed $\sqrt{3}$ (diagonals). See Appendix C for more details on lattice symmetry.

In order to model the binary fluid, a second set of distribution functions, g_i, are also

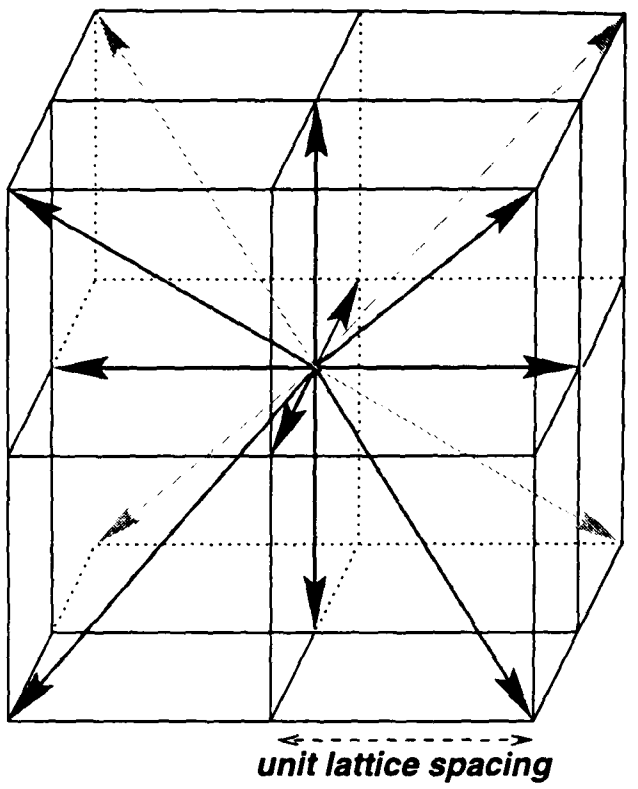

Figure 3.1: *Diagram showing the basic arrangement of nearest neighbours in the D3Q15 lattice used for the lattice-Boltzmann simulations.*

used. The f_i correspond to the total fluid,

$$\sum_i f_i = \rho = \rho_A + \rho_B, \tag{3.17}$$

where the sum is over all directions, i, at a single lattice point, while the g_i correspond to the order parameter,

$$\sum_i g_i = \phi = \rho_A - \rho_B. \tag{3.18}$$

The momentum, ρv_α, is given by,

$$\rho v_\alpha = \sum_i f_i c_{i\alpha}, \tag{3.19}$$

where the velocities are denoted $c_{i\alpha}$, with i an index for the lattice direction, $0 \leq i \leq 14$, while α is a cartesian vector component index. The stress tensor, $\Sigma_{\alpha\beta}$, is given by,

$$\Sigma_{\alpha\beta} = \sum_i f_i c_{i\alpha} c_{i\beta}. \tag{3.20}$$

The equilibrium distributions, $f_i^{(eq)}$ and $g_i^{(eq)}$, can be derived from a few simple conditions. These are, conservation of mass and momentum, Equations (3.17) – (3.19), that the order parameter is convected by the velocity,

$$\sum_i g_i^{(eq)} c_{i\alpha} = \phi v_\alpha, \tag{3.21}$$

and that the stress, Equation (3.20), and chemical potential difference, $\Delta\mu$, at equilibrium are given by,

$$\sum_i f_i^{(eq)} c_{i\alpha} c_{i\beta} = \mathcal{P}_{\alpha\beta} + \rho v_\alpha v_\beta \tag{3.22}$$

$$\sum_i g_i^{(eq)} c_{i\alpha} c_{i\beta} = M\Delta\mu\,\delta_{\alpha\beta} + \phi v_\alpha v_\beta, \tag{3.23}$$

where $\mathcal{P}_{\alpha\beta}$ is the pressure tensor and M is a mobility that controls the diffusion rate.

The equilibrium distributions can now be obtained by assuming a form for them including terms up to the square of the velocity, substituting into the above conditions and solving for the coefficients. The result is,

$$f_i^{(eq)} = \rho\omega_\nu \left\{ A_\nu + 3v_\alpha c_{i\alpha} + \frac{9}{2} v_\alpha v_\beta c_{i\alpha} c_{i\beta} - \frac{3}{2} v^2 + G_{\alpha\beta} c_{i\alpha} c_{i\beta} \right\}. \tag{3.24}$$

Here, ν is an index that denotes the speed, 0, 1, or 3, and ω_ν, A_ν and $G_{\alpha\beta}$ are constants given by,

$$\omega_0 = 2/9; \quad \omega_1 = 1/9; \quad \omega_3 = 1/72, \tag{3.25}$$

$$A_0 = \frac{9}{2} - \frac{7}{2} Tr\mathcal{P}_{\alpha\beta}; \quad A_1 = A_3 = \frac{1}{\rho} Tr\mathcal{P}_{\alpha\beta}, \tag{3.26}$$

$$G_{\alpha\beta} = \frac{9}{2\rho}\mathcal{P}_{\alpha\beta} - \left(\frac{3}{2\rho} Tr\mathcal{P}_{\alpha\beta}\right)\delta_{\alpha\beta}. \tag{3.27}$$

The equilibrium distribution for the order parameter distribution, $g_i^{(eq)}$, is the same as for $f_i^{(eq)}$, with $\mathcal{P}_{\alpha\beta}$ replaced by $M\Delta\mu\,\delta_{\alpha\beta}$. The above follows Swift et al. (1996), generalised to three dimensions.

So far, this is still quite general. The physical model is introduced by specifying the form of the pressure tensor and chemical potential difference via the choice of free energy. In this study, the model free energy is chosen to be a "ϕ^4" model and takes the form,

$$F = \int d\mathbf{x} \left\{ \frac{A}{2}\phi^2 + \frac{B}{4}\phi^4 + \frac{\kappa}{2}(\nabla\phi)^2 + \frac{1}{3}\rho \ln \rho \right\}, \tag{3.28}$$

where $\phi(\mathbf{x})$ is the density difference between the two fluids, and ρ is the total density of the fluid mixture (effectively constant for incompressible fluids as considered here). Other simple models for the free energy are possible, see Swift et al. (1996) for example.

In Equation (3.28), the constants A and B determine the shape of the free energy, if A is negative, it assumes the basic double well "mexican hat" potential necessary

for phase separation to occur, see Figure 2.2. The equilibrium values of the order parameter, ϕ^*, can be found by setting $\delta F/\delta\phi = 0$, giving $\phi^* = \pm\sqrt{-A/B}$. In all the simulation work presented in later chapters, the values of A and B have been chosen so that $\phi^* = \pm 1$. With the total fluid density, ρ set equal to unity, this corresponds to complete separation at equilibrium. The term $\kappa(\nabla\phi)^2/2$ models the energy of the interface between the fluids. The value of κ (relative to A and B) determines the interfacial tension, $\sigma = \sqrt{(-8\kappa A^3/9B^2)}$, see Equation (2.10), and the interfacial width, ξ, is determined by the microscopic length, $\sqrt{-\kappa/2A}$.

The chemical potential difference, $\Delta\mu$, is thus,

$$\Delta\mu = \frac{\delta F}{\delta\phi} = A\phi + B\phi^3 - \kappa\nabla^2\phi, \tag{3.29}$$

and the pressure tensor, $\mathcal{P}_{\alpha\beta}$, is,

$$\mathcal{P}_{\alpha\beta} = \left\{\rho + \frac{A}{2}\phi^2 + \frac{3B}{4}\phi^4 - \kappa\phi\nabla^2\phi - \frac{\kappa}{2}(\nabla\phi)^2\right\}\delta_{\alpha\beta} + \kappa\partial_\alpha\phi\partial_\beta\phi. \tag{3.30}$$

This particular model has a number of points in its favour for numerical simulation. The main terms in $\mathcal{P}_{\alpha\beta}$ and $\Delta\mu$ are simple powers of ϕ, so are easy and quick to evaluate. Models involving logarithms or trigonometric functions pay a heavy price in computational efficiency. Further, the shape of the "ϕ^4" potential is fairly smooth, avoiding very steep gradients that might lead to inaccuracy and instability when approximated numerically on a lattice.

It is necessary to evaluate gradients of ϕ for some of the terms in the pressure tensor, Equation (3.30), and $\Delta\mu$, Equation (3.29). This is done using all 26 nearest neighbours on the D3Q15 lattice (shown in Figure 3.1),

$$\nabla^2\phi(\mathbf{x}) \simeq \frac{1}{9}\left[\left(\sum_i \phi(\mathbf{x}+\mathbf{c}_i)\right) - 26\phi(\mathbf{x})\right], \tag{3.31}$$

and,

$$\partial_\alpha\phi(\mathbf{x}) \simeq \frac{\sum_i c_{i\alpha}\phi(\mathbf{x}+\mathbf{c}_i)}{\sum_i c_{i\alpha}c_{i\alpha}}. \tag{3.32}$$

Obviously finite difference methods for gradient calculations on a discrete lattice are only a good approximation where the quantity being differentiated is varying slowly with respect to the lattice spacing. Further discussion of the accuracy of the gradient calculations can be found in Sections 3.6.2 – 3.6.4.

3.3.2 Parameters

The model code in **Ludwig** has a large number of parameters that must be set by the user to produce the particular simulation required. These are:

- model free energy parameters, A, B, and κ. Between them, these determine the interfacial tension, σ, the quench depth, and the interfacial width.
- viscosity, η. More precisely, it controls the relaxation time, τ in Equation (3.14), for the fluid distribution functions, f_i. There is a second relaxation time for the order parameter distribution functions, g_i, that in this study was set to always relax the order parameter completely to equilibrium at each time step. This corresponds to the assumption in the physical model of local equilibrium over small scales.
- mobility, M. This controls the diffusion rate.
- density, ρ. This was set to unity for all simulations in this study.
- lattice size, Λ. This is chosen to be as large as possible within the available computational resources. In this study, the largest system size was 256^3, although due to limitations on the amount of disk storage available, the results from this system size could only be analysed by coarse-graining down to 128^3; runs at 128^3 and 96^3 were also done.
- number of time steps to run the simulation for. Each time step consists of a collision step for every site in the lattice, followed by a propagation step for all lattice sites. Around 10^4 time steps were typically needed to evolve the system as far as required for this study.
- boundaries. The spinodal decomposition simulation was run with periodic boundaries, but the **Ludwig** code can also simulate solid boundaries. These can be used for shear simulations, as well as more complicated structures.
- initial conditions. For studying spinodal decomposition, the initial configuration was always a completely mixed state. Some tests on spherical droplets were also done, these were initialised by specifying the value of the order parameter at each lattice site to form a sphere with a sharp interface; the interface was then allowed

to relax to its equilibrium profile by running the simulation for a few hundred time steps.

Few of the basic parameters can, in practice, be set independently. Typically, a random choice of parameters would produce a simulation that either did nothing over sensible timescales (evolved far too slowly), or became unstable very rapidly. Since the viscosity determines the time step for the fluid evolution, as the viscosity is reduced (larger time step), the interfacial tension (set by A, B and κ) also has to be reduced to keep the motion of the interface slow with respect to the time step. This is not a self-cancelling adjustment, and it was possible to simulate a wide range of values of the scaling length, $L_0 = \eta^2/\rho\sigma$. The value of the mobility, M, was also important to achieve a successful simulation, this is discussed in Section 5.4.1. Determining a collection of useful sets of simulation parameters was a significant part of the original work of this thesis.

3.4 Analysis methods

Having obtained a set of "images" of the system at regular time intervals, in the form of output files containing the value of the order parameter and fluid velocity at every lattice site, it is then necessary to process these files to obtain statistical information about the state of the system. The following quantities were calculated from the simulation data:

- 32^3 sections in a format suitable for input to the AVS package for visualisation. Examples of these pictures can be seen in Appendix A.

- Maximum values and system averages of the order parameter and the velocity components, to check that the simulation is behaving sensibly. The sudden appearance of large values of the velocity or unphysical values of the order parameter indicate numerical instability.

- The structure factor of the order parameter, $S(k)$, Equation (5.1).

- The average domain size, $L(T)$, calculated as the inverse of the first moment of the spherically averaged order parameter structure factor, Equation (2.28).

- Alternative estimates of the average domain size using different length measures based on the curvature of the interface and on the volume of the interface. These are described in more detail in Section 3.5.

- Velocity derivative quantities, the nonlinear term from the NSE, $\mathbf{v}.\nabla\mathbf{v}$, the viscous terms from the NSE, $\nabla^2\mathbf{v}$, the vorticity, $\boldsymbol{\omega}= \nabla \wedge \mathbf{v}$, longitudinal and transverse velocity derivatives (components of $\nabla\mathbf{v}$), and the dissipation rate, $\eta(\nabla\mathbf{v})^2$.

- The structure factors of the velocity and velocity derivative quantities.

- Length measures calculated from the structure factors of the velocity and velocity derivative quantities.

- The standard deviation, skewness, flatness and pdfs of the fluid velocity and velocity derivative quantities.

- Characteristics of turbulence such as the Taylor and Kolmogorov microscales (Equations (2.52) and (2.54)) and Reynolds numbers based on these lengths.

- A compressibility measure, see Section 3.6.5.

The analysis code is written in ANSI-C, in a fairly modular design, since many of the same statistics are required for more than one quantity. It runs in serial only, which, for 128^3 data, places considerable demands on the computer memory requirements. Since computers with sufficient memory were available, this meant there was no need to write the analysis code in parallel, a considerable saving of time and effort.

The data input routines can read both the binary and ASCII output formats produced by the **Ludwig** code, and also data from DPD and turbulence simulations, which were processed through the same analysis code and used for comparisons. There are output routines that reformat the data to be compatible with the AVS visualisation software. Fourier transforms have been implemented using the FFTW routines, see Frigo and Johnson (1999), to ensure that the code is portable between platforms (the analysis code has run on three different platforms during various stages of the work). Modules that produce statistics, one each for real and Fourier space fields, have been implemented with enough generality to be run over any vector or scalar field.

A typical analysis sequence goes as follows:

- read in the data, either the order parameter or fluid velocity,
- perform real space statistics and output results,
- Fourier transform the data,
- perform Fourier space statistics and output results,
- calculate derivatives by multiplying by factors of ik_α,
- reverse Fourier transform back to real space,
- perform real space statistics on the resulting derivative quantities and output results.

The above is for a single set of data. By repeating this over a whole series of data files, a time series of average quantities can be created. Calculation of quantities such as the nonlinear term, $\mathbf{v}.\nabla\mathbf{v}$, requires a more complicated sequence of Fourier transforms, both to create the term and to stay within computer memory limitations, but the basic operations are the same.

The analysis code was validated by running it on single fluid turbulence data, where many of the calculated quantities were also output by the simulation code when it originally ran, allowing direction comparison. Selected portions of the DPD data of Jury (1999) were also processed through the analysis code, and the results were found to be in agreement with Jury's own analysis.

3.5 Alternative length measures

The most important measure of the dynamics of spinodal decomposition is the size of the domains of separated fluid as they grow with time. The measure most commonly used by experimentalists and theorists, is the inverse of the first moment of the spherically averaged structure factor, $L(T)$, Equation (2.28). Two further length measures have been compared with $L(T)$ to see how well they characterise the domain size. There are several motivations for this. Firstly, it was found by Wagner and Yeomans (1998) in the analysis of two-dimensional hydrodynamic spinodal decomposition,

that the domain growth doesn't scale smoothly, and a key tool for uncovering this behaviour was the use of different length measures that picked out different features of the growth. Secondly, for a system under shear (not studied here), the isotropy necessary for spherically averaged quantities to be useful is no longer present in the system, so an alternative length measure capable of distinguishing the directions picked out by the shear is essential.

One or more lengths can be obtained directly from the curvature of the interface, see Wagner and Yeomans (1998). The curvature of the interface, $D_{\alpha\beta}$, is given by,

$$D_{\alpha\beta} = \frac{\sum\limits_{lattice} \partial_\alpha \phi \partial_\beta \phi}{\sum\limits_{lattice} \phi^2}, \tag{3.33}$$

By solving this curvature matrix for its eigenvalues, λ_1, λ_2 and λ_3, three lengths can be obtained, L_1, L_2 and L_3,

$$L_1 = \frac{1}{\lambda_1},\ L_2 = \frac{1}{\lambda_2},\ L_3 = \frac{1}{\lambda_3}. \tag{3.34}$$

For the isotropic (unsheared) case, these three lengths will be equal. In practice, the finite system size means the lengths are not exactly equal, and a single length can best be defined by averaging,

$$L_{\nabla\phi}(T) = \frac{3}{\lambda_1 + \lambda_2 + \lambda_3}. \tag{3.35}$$

For a sheared system, e.g. elliptical droplets, the three eigenvalues pick out the directions of longest and shortest length, plus the length in the direction orthogonal to these two. They thus provide a precise way to characterise the effect of the shear on the domains.

A third method of estimating the domain size is based on estimating the area of the interface, and noting that (by dimensional analysis) this must scale as the reciprocal of the domain size. A length can thus be defined by $L_{|\phi|} \equiv 1/A_\xi$. The area of the interface, A_ξ, is estimated by noting that, for the deep quench simulated in this work, the only place where the order parameter differs from complete separation is in the interface. Thus $\langle|\phi|\rangle$ can be related to the volume of the interface (per unit volume), V_A, by,

$$V_A = \xi_{|\phi|} A_\xi = 1 - \langle|\phi|\rangle/\phi^*, \tag{3.36}$$

where ϕ^* is the equilibrium value of ϕ and $\xi_{|\phi|}$ is a measure of the interfacial width. Substituting $A_\xi = 1/L_{|\phi|}$ gives,

$$L_{|\phi|} = \xi_{|\phi|}/(1 - \langle|\phi|\rangle/\phi^*). \tag{3.37}$$

To complete the calculation of $L_{|\phi|}$, a value for $\xi_{|\phi|}$ is required. The interfacial profile is tanh-shaped, as can be found by using the free energy equation for this model, Equation (3.28), to solve for the order parameter profile across an equilibrium interface. From this, a value for $\xi_{|\phi|}$ can be found in terms of the simulation parameters using Equation (3.36). Alternatively, Equation (3.36) can be used with simulations of interface profiles of known geometries such as spherical droplets and plane walls, from which $\xi_{|\phi|} = 1.33$ ± 0.1 was obtained for the simulation parameters used for all the main runs in this study.

In fact, because $\langle|\phi|\rangle$ was not one of the standard quantities calculated in the analysis, ϕ_{rms} was used instead. The resulting length was defined similarly,

$$L_\phi \equiv \xi_\phi/(1 - \phi_{rms}/\phi^*), \tag{3.38}$$

with $\xi_\phi = 3.25$. This choice of ξ_ϕ matches L_ϕ up with $L(T)$, for convenience when both are shown on the same graph.

By numerical comparison between $L_{|\phi|}$ with L_ϕ, it was found that for the interface topology in the symmetric spinodal decomposition system (but not for planes or droplets),

$$L_\phi \simeq 2.4 L_{|\phi|}, \tag{3.39}$$

for the standard interface width used in this study. In any case, the precise value of the prefactor is not important, what matters is whether these other length measures show the same growth rate as $L(T)$ obtained from the structure factor. This will be investigated in Section 5.5.2.

3.6 Testing the simulation and analysis code

General code testing and validation of the **Ludwig** code was done by Bladon and Desplat (1999). Tests described here relate specifically to the system in this study. Firstly,

a suitable range of stable input parameter sets was built up to cover the linear through to the inertial regimes of spinodal decomposition. Specific tests were done with different interfacial widths to determine how close the interface is to isotropic, modeled as it is over a highly directional lattice. The interfacial tension was measured and compared with the theoretical value calculated from the input parameters. To further probe the simulation accuracy, derivatives of the velocity field were calculated using both Fourier transforms and real space finite difference methods, and the compressibility of the fluid was investigated by considering the ratio of the radial to transverse velocity components in Fourier space. These tests are described in more detail in the following sections.

3.6.1 Simulation stability

This study is essentially using the lattice-Boltzmann method to solve the model equations given in Section 2.3, on a discrete lattice, by stepping forward in time with a finite time step. Clearly, in order to do this successfully, the lattice spacing and time step must be properly matched to the rate of change of spatial features and time evolution of the system. However, since the input parameters do not relate directly to the length and time scales, a more "trial and error" approach must be employed to work out the best parameter sets.

For an efficient simulation, it is also important to run the simulation with as large a time step as possible, otherwise an excessively long time (large amount of computational resources) would be required to run the simulation through to completion. Larger time steps, on the other hand, are less accurate, and accumulated inaccuracies can lead to the simulation becoming unstable. There is thus a delicate balance to be struck between accuracy and efficiency and stability.

Many dozens of tests were carried out using system sizes of 96^3 and smaller, to determine stable efficient sets of parameters. During this process, a reliable picture was acquired of the characteristic way in which the simulation becomes unstable. When the inaccuracies build up to the point of failure, the velocities become very large over a short number of time steps until numerical overflow causes the code to stop running. There seems to be no danger of taking data from a period when the system might be far from accurate but still apparently running successfully, since when it goes unstable it goes fast, in a

few tens of time steps. Presumably, all runs would eventually become unstable if run for long enough, as numerical inaccuracies will inevitably build up over time. There are several runs in the set used for final data analysis where the run ended prematurely due to instabilities, but the data prior to the instability has been considered sufficiently reliable to be used.

Some general trends in the parameters in moving from the linear to the inertial regions may be noted. Since the viscosity controls the size of the time step, as it is reduced (time step increased) it is necessary to also reduce the interfacial tension through reducing parameters A, B and κ to slow the interface motion down in line with the larger time step. At the same time, in order to maintain the interface in local equilibrium, the mobility must be increased, so diffusion will act fast enough to keep the interfacial profile correct. More details on how the diffusion was measured and controlled can be found in Section 5.4.1. The particular sets of parameters used for the runs in this study are given in Chapter 5 in Tables 5.1 and 5.2.

3.6.2 Isotropy

In order to test the isotropy of the interface at all angles to the Cartesian grid, a system consisting of a large spherical droplet of fluid B surrounded by fluid A was allowed to equilibriate. The interface profile was then measured by plotting the value of the order parameter against the distance from the centre of the droplet for each lattice point near the droplet interface. The result is presented in Figure 3.2 for two different interface widths, for spheres of radius 32 lattice spacings. The data have been collected into bins of width 0.1 lattice unit, and are shown with error bars of $\pm$ one standard deviation. Clearly the wider interface has a more isotropic profile. A closer look at the interface profile in each case reveals that what has actually happened to the sphere is that it has deformed slightly by squeezing along the Cartesian directions and expanding along the diagonals. This deformation is about 3.5% for the narrower profile and about 1.5% for the wider profile. A similar test was done with a sphere of radius 31.5 to check that this deformation was not due to the interface trying to align in the same position relative to the lattice points. This confirmed that the result is indeed due to anisotropy, in other words, the interfacial tension varies slightly depending on

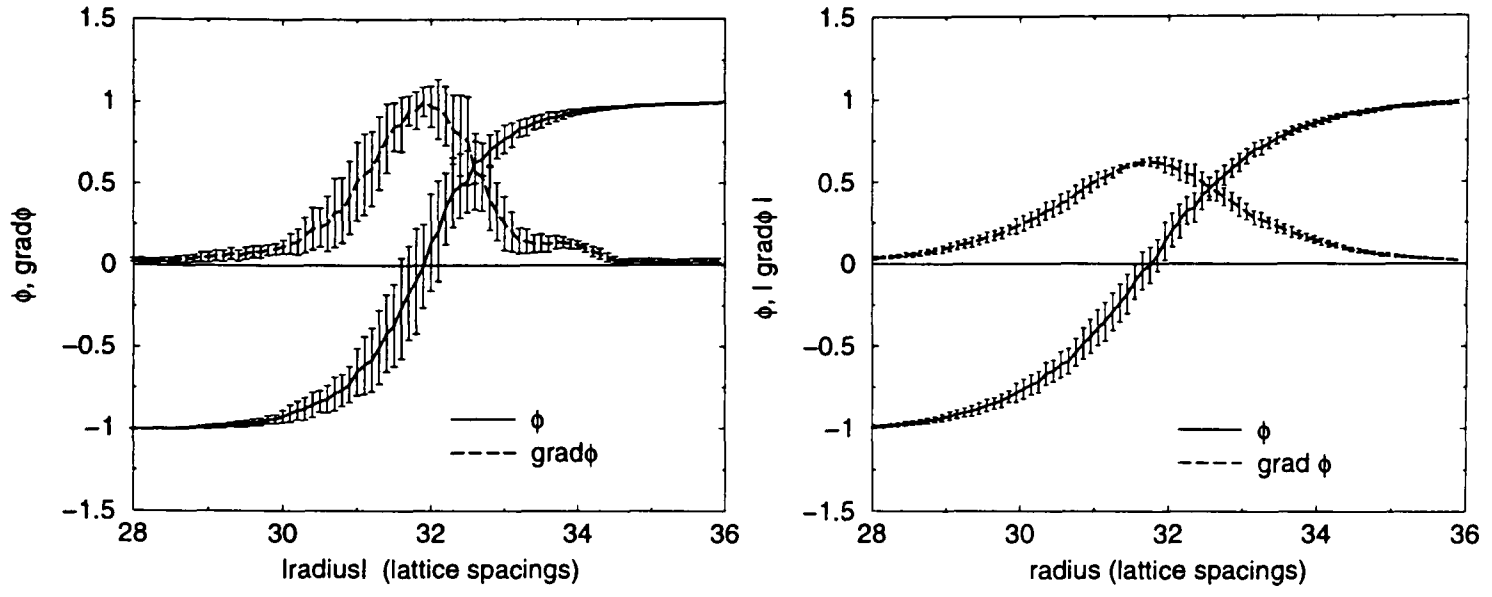

Figure 3.2: *Interface profiles (ϕ) and gradient profile ($|\nabla\phi|$), for spherical droplet equilibriated in opposite fluid. Data has been collected in bins of width 0.1 lattice spacings, and the error bars are one standard deviation. The sphere radius is* 32. *Left: interface width set by* $\sqrt{-\kappa/2A} = 0.57$. *The interface profile is given theoretically by,* $\tanh(g/\sqrt{-\kappa/2A})$, *for a flat interface, where g is a coordinate normal to the interface and* $\phi = \pm 1$ *in the bulk. This gives an interface width where the main variation in* ϕ *spans approximately* $5 \times \sqrt{-\kappa/2A}$, *here about 3 lattice units. Right: interface width set by* $\sqrt{-\kappa/2A} = 0.88$.

the orientation of the interface with respect to the lattice. The most likely cause of this is that the gradient calculations used in the **Ludwig** code are not perfectly isotropic. More isotropic schemes for gradient calculations are being considered for the **Ludwig** code, but were not available in time for this study.

If all else were equal, clearly the wider interface with the more isotropic profile would be the better choice. However, there is a huge penalty in computational efficiency to be paid for wider interfaces. In order to maintain a wider interface in local equilibrium, the diffusion rate must be high enough to diffuse across the whole width in a time of order of the time step size. Wider interfaces thus require faster diffusion, and this higher diffusion rate then contributes significantly to domain growth at larger domain sizes, see Section 5.4.1. It was thus found to be necessary to sacrifice some isotropy for computational efficiency, and the narrower profile with $\sqrt{-\kappa/2A} = 0.57$ was used for the main runs in this work.

It is difficult to estimate how the errors introduced by this anisotropy will propagate through to $L(T)$, particular because this is a systematic error, so may bias the evolution of the system. If the domain shape is not quite as isotropic as it should be due to the

anisotropic interfacial tension, then this will broaden the order parameter structure factor, but without a more isotropic system to compare with, it won't be detectable in the results. Analysis of the structure factor scaling is presented in Section 5.3.1. The uncertainty in the value of the interfacial tension is quite large in any case, see Sections 3.6.3 and 5.4, so it is likely that the anisotropy will not make a significant extra difference.

3.6.3 Interfacial tension

The interfacial tension was measured by allowing an interface to come to equilibrium and numerically performing the integration in Equation 2.10. Both terms were evaluated, and an average taken. This gives values for the interfacial tension, shown in

-A,B	κ	η	M	σ theory	σ measured
0.083	0.053	1.41	0.1	0.063	0.055
0.063	0.04	0.5	0.5	0.047	0.042
0.0063	0.004	0.025	4.0	0.0047	0.0042
0.0031	0.002	0.0014	8.0	0.0024	0.0021
0.0013	0.0008	0.0005	10.0	0.00094	0.00083

Table 3.1: *Interfacial tension, theoretical and measured values.*

Table 3.1, that are about 10–15% smaller than the theoretical value. The difference is due to the narrow interface leading to inaccuracies in the gradient calculations. As far as the simulation is concerned, this doesn't make any difference so long as the measured value of the interfacial tension is used in subsequent calculations, such as evaluation of L_0 and T_0, the scaling length and time, see Equations (2.26) and (2.27).

Further errors in the interfacial tension can arise if the interface is not completely in local equilibrium. This possibility is discussed further in Sections 5.4.1 and 5.5.2, where the role of diffusion is analysed in detail, and a measure that indicates whether the interface is properly in local equilibrium is identified.

3.6.4 Accuracy of derivative calculations

It was already mentioned in the previous section that the derivative calculations done as finite differences, see Section 3.3, are the source of inaccuracies in the interfaical tension. In the analysis code, derivatives are calculated using Fourier transforms, since structure factors require Fourier transforms to be performed anyway, and in the expectation that this is a more accurate method[1]. In order to take a closer look at the accuracy of the derivatives calculations, two derivative quantities calculated from the velocity field were compared. These were calculated both in real space using finite differences in the same scheme as the **Ludwig** code, and in Fourier space by multiplying through by the appropriate factors of ik_α. The comparison was then made by looking at the structure factors of each quantity. Since derivatives evaluated in real space are expected to be less accurate over smaller scales, this should show up in the high wavenumber region of the structure factor. Results of this comparison are shown in Figure 3.3 for Run027, which is in the linear region where the inertial terms in the Navier-Stokes region are expected to be negligible, and Run031, which is in the inertial region where the inertial terms are expected to be significant to the dynamics. Both runs were on 128^3 lattices, and are compared for time steps where the domain size is about 25 lattice units as measured by $L(T)$, defined in Equation (2.5).

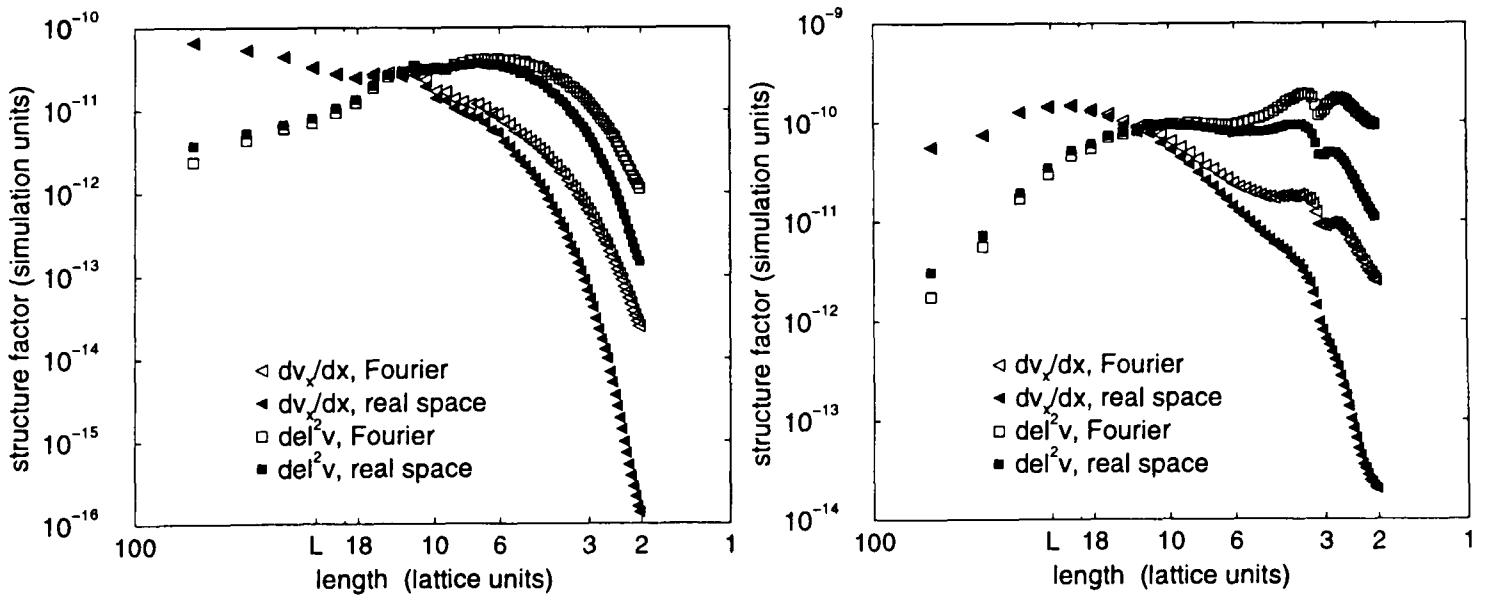

Figure 3.3: *Left: Comparison of the structure factors for Run027 for* $\mathrm{d}v_x/\mathrm{d}x$ *and* $\nabla^2\mathbf{v}$ *for timestep 9500 calculated by Fourier and real space methods. Right: Comparison of the structure factors for Run031 for* $\mathrm{d}v_x/\mathrm{d}x$ *and* $\nabla^2\mathbf{v}$ *for timestep 6000 calculated by Fourier and real space methods.*

[1]For an isotropic system; this is not true for a sheared system, for example, where the velocity gradient forms a sawtooth profile under periodic boundary conditions.

The first derivative matches well above about eight lattice spacings, below this the real space derivatives deviate to smaller values than the Fourier space ones. The second derivative deviates to larger values at large length scales as well as showing the same deviation to smaller values at small length scales. The overall rms average values of these quantities differ by a factor of two between the real and Fourier space calculations. The first derivatives are smaller when calculated in real space, while the second derivatives are larger.

The **Ludwig** code doesn't explicitly evaluate velocity derivatives, it works by finite differences to solve the NSE, which contains such terms. The pseudo-spectral turbulence DNS, on the other hand, does calculate velocity derivatives explicitly, but does so in Fourier space. Martínez et al. (1994) did a careful comparison of LB and pseudo-spectral DNS, and found results that were very similar between the two methods, thus validating the LB method as capable of producing an accurate simulation of the NSE. The particular implementations of the LB method in Martínez et al., and the **Ludwig** code are not the same, however, furthermore, the Martínez et al. study was only in two-dimensions, so it is still possible that the **Ludwig** code is less accurate. The **Ludwig** code does evaluate order parameter derivatives; for domain sizes of interest, this has been shown in the previous section to be inaccurate, and the inaccuracy subsumed into a measured value for the surface tension, σ. It is possible that problems will also arise if the simulation has steep velocity gradients in it, this will be considered in Section 6.5.4.

3.6.5 Compressibility and small scale structure

The **Ludwig** code will only work correctly at low Mach number[2] (the speed of sound is the speed, $c_{i\alpha}$, with which the distribution functions, f_i, propagate from site to site on the lattice). Under this condition, the binary fluid mixture under consideration here will be basically incompressible, except at small length scales. The condition for an incompressible fluid, $\nabla.\mathbf{v} = 0$, translates into the radial component of the Fourier space velocity being zero, $\mathbf{k}.\mathbf{v}(\mathbf{k}) = 0$. As a simple test of how much compression is occuring in the fluid during the simulation, the radial component of Fourier space

[2]The Mach number is the ratio of the speed of the interface to the speed of sound in the fluid. Low Mach number means interface speeds much less than the speed of sound.

velocity was compared with the transverse components. Figure 3.4 (left) shows the ratio of the radial to the transverse velocity components in Fourier space as a function of wavenumber for various runs. Since the relative magnitude at different wavenumbers also matters, Figure 3.4 (right) shows the spherically averaged velocity structure factor for the same runs. The velocity structure factor, $S_v(k)$, is the square-magnitude of the Fourier space velocity for a given wavevector. Also shown for comparison is single fluid turbulence[3], and a LB run with a single fluid (no interface) but otherwise the same parameters as Run031 (inertial region).

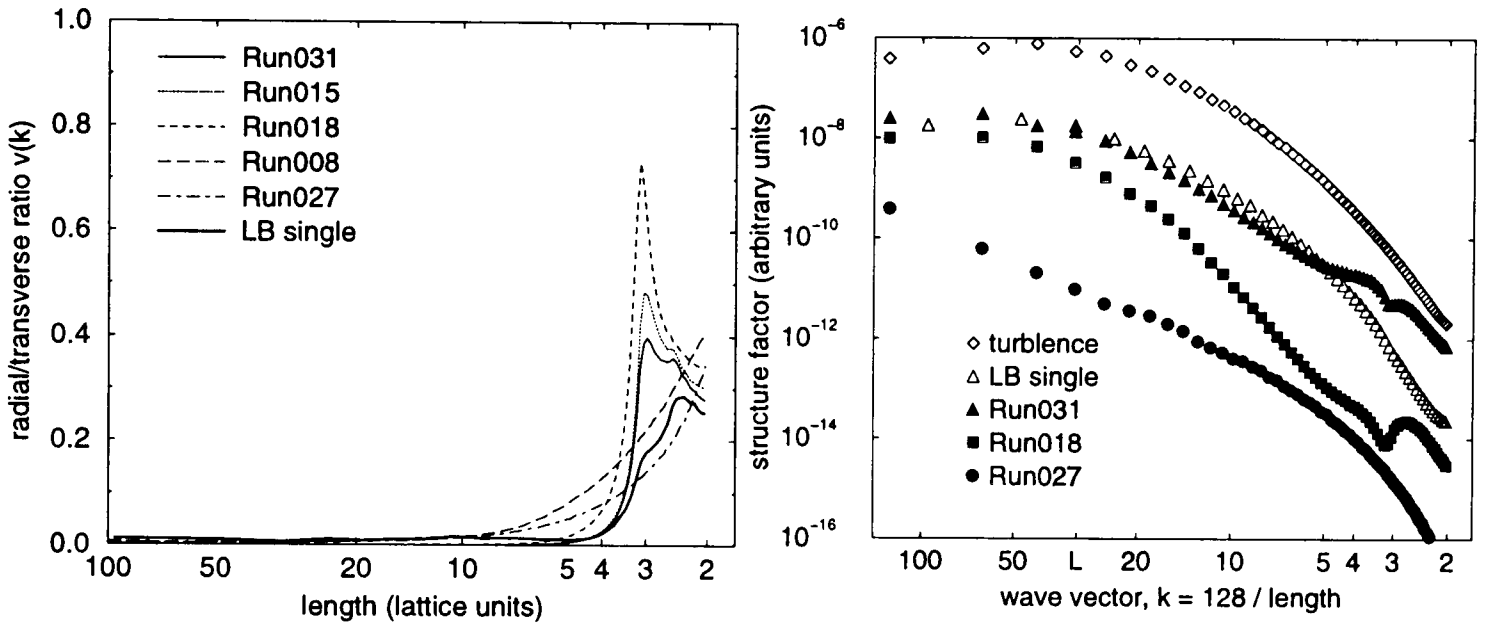

Figure 3.4: *Left: ratio of the radial to transverse velocity components in Fourier space for various runs. Right: velocity structure factor showing relative magnitude of the Fourier space velocity at different wave vectors. Wave vector axis has been labeled as length to aid comprehension; length = 128/wavenumber.*

At low wavenumbers the sytem is incompressible. At higher wavenumbers, i.e. shorter length scales, there is some compressibility, and the form of the compressible region changes over the different growth regimes. In the viscous region it simply rises, but comparing the actual magnitudes of the components forming the ratio (see Figure 3.4 (right)) it is clear that the rise is due to the transverse velocity components also being small, i.e. the contribution to the overall simulation dynamics from the shorter, more compressible length scales is small. This is still true in the crossover region, where the compressibility ratio is highest, a peak having formed at a wave vector corresponding to about 3 lattice spacings. Moving on to the inertial region, this peak shrinks, and splits into two peaks, at wave vectors corresponding to around 3.5 and 2.5 lattice spacings.

[3]The single fluid turbulence simulation method sets the radial component identically to zero thus guaranteeing perfect incompressibility.

The transverse component is now larger so more significant in the overall dynamics of the simulation, although still an order of magnitude smaller than the velocity at the peak of $S_v(k)$.

Comparison with the single fluid turbulence, both DNS and LB, shows that the peaks are largely due to the presence of the interface. The peaks are only present in the binary fluid mixture in the crossover and inertial runs, suggesting that perhaps capillary waves are forming on the interface and causing structure in the velocity field on scales of the order of the interface width. Capillary waves might be expected to appear at low viscosity when the fluid motion is less "damped". Further work was not done to investigate capillary waves due to the difficulty of observing them under controlled conditions. Attempts to set up systems with simpler geometries in which to measure capillary waves more directly were not successful as it was not clear how to provide a driving force to maintain the waves in motion. Others have apparently succeeded in doing this, see for example, Theissen et al. (1998), albeit with amphiphiles added to the fluid mixture.

Given that the peak of the small scale structure in $S_v(k)$ is an order of magnitude smaller than the peak of $S_v(k)$ even in the run, Run031, with the most inertial parameters, the slight compressibility and possible capillary waves are unlikely to be of significance to the overall dynamics of the fluid motion.

3.7 Summary

The chosen simulation method, lattice-Boltzmann, has been described and compared with other possible simulation methods. The power and efficiency of the LB method has to be balanced against the drawback of instability of the algorithm, but the large system size that LB can simulate make it the method of choice for this work.

The particular implementation of LB used, **Ludwig** has been briefly described. The analysis method for examining the output data from the simulations has been described, and the quantities to be calculated listed and explained.

Many preliminary tests have been performed using the **Ludwig** code to find viable

sets of parameters covering the range of physical parameters of interest to this study. The isotropy of the interfacial tension has been tested, and it was found necessary to sacrifice some isotropy for efficiency. The high diffusion rates that would be required by wider interfaces would increase the use of computational resources and lead to diffusive domain growth competing with hydrodynamic growth.

The interfacial tension was computed numerically and compared with theory. The measured values were found to be lower due to inaccuracies in the gradient calculations. This is not a problem provided the computed values of the interfacial tension are used in subsequent calculations. The accuracy of the derivative calculations was investigated further by comparing the Fourier space and real space gradient methods on the velocity field, and finding significant differences. For the isotropic fluid system the Fourier method is taken to be the most accurate.

Compressibility was tested by looking at the radial component of the Fourier space velocity. The compressibility was found to be negligible except at small length scales in systems in the inertial region. Here, peaks in the structure factor at small length scales were shown to be due to the interface; a possible explanation is capillary waves. This was not investigated further.

The system and methods have now been described in sufficient detail to proceed into the remaining chapters where the main results of this study are presented.

Chapter 4

Single fluid turbulent system

4.1 Introduction

For the purpose of understanding the limitations and accuracy of the analysis methods, and to provide a reference system for the behaviour of the binary fluid mixture studied as the main work of this thesis, the statistical properties of the velocity field of a single fluid, fully-developed, decaying, homogeneous, isotropic turbulence simulation have been investigated in both real and Fourier space. One important aim of the study of the binary fluid mixture is to simulate the region where the viscosity is low enough that the fluid flow may be expected to become turbulent during the spinodal decomposition process. A clear picture of the behaviour of the velocity field in a simple turbulent system is thus a valuable comparative tool.

The background theory and phenomenology of turbulence needed for this chapter were covered in Section 2.5. This chapter starts with a brief overview of the existing studies of turbulence DNS (direct numerical simulation) in Section 4.2, including a summary of the particular simulation used for this study and the characteristic turbulence results produced from it. In order to fully explain the comparisons made during the analysis of the velocity field of the binary fluid system in Chapter 6, the material contained in Section 4.2 covers sufficient background on single fluid turbulence.

A more extensive investigation into the statistics and error analysis has been done

in Sections 4.3 to 4.5 that is not required for the later chapters. A detailed look at shell-averaging and the statistics of the velocity field in Fourier space in Section 4.3 is followed by explicit consideration of error analysis in Section 4.4, and the results for the statistics of the velocity field in real space in Section 4.5. Various appendices provide supporting material, Appendix A contains visualisations of the velocity field, Appendix E gives the moments of χ and χ^2 distributions, and further statistical techniques are described in Appendix F.

4.2 Background to turbulence simulation

Turbulence, even in the simplest situations, is one of the more intractable problems of classical physics. To date, analytical approaches have only been partially successful in predicting the statistical form of the fluid velocity. The advent of powerful computers and numerical simulation methods has therefore provided an important tool for the study of turbulence to augment and complement the longstanding body of theoretical and experimental work.

Indeed, direct numerical simulation of turbulence (DNS) has been used since computers first became capable of such calculations over 30 years ago, producing deeper insights into the phenomenology than experimental measurements can provide. Numerical methods are particularly suited to analysis in Fourier space since the simulation algorithms generally employ Fourier transforms to speed up the computation. Furthermore, since key theoretical work, Kolmogorov (1941, 1962), Kraichnan (1959) and theories based on renormalisation, Forster et al. (1977), Yakhot and Orszag (1986), are concerned with the spectral analysis of turbulence, DNS is particularly helpful in providing more detailed comparisons with theory than are practicable from experiments.

Theorists and computationalists alike usually start with the simplest configuration, incompressible, homogeneous, isotropic turbulence filling an infinite space, or, since that is computationally impractical, the next best thing, a finite box with periodic boundary conditions. The main quantity of interest in the Fourier space analysis is the energy spectrum, Equation 2.46, or in discrete, lattice-based form, $E(k) = \rho/2 \sum_{|\mathbf{k}|=k\pm\frac{1}{2}} \mathbf{v}(\mathbf{k}).\mathbf{v}(-\mathbf{k})$. Predicting the form of the energy spectrum is the goal of

the theorists and the benchmark test for comparing simulations. In order to obtain a statistical quantity such as $E(k)$ from a simulation based on a discrete, finite computational grid, an averaging process must be done over a suitable set of data. Every step of the computational process introduces limits on the accuracy of the results.

4.2.1 Overview

The most basic measure of turbulence is the Reynolds number, see Section 2.3.3, defined as,

$$\mathrm{Re} = \frac{\mathrm{length} \times \mathrm{velocity}}{\mathrm{kinematic\ viscosity}}. \tag{4.1}$$

The velocity is usually chosen to be the root mean square velocity $v_{rms} = \sqrt{2E}$, and the length can be chosen from whatever characteristic lengths there are in the system under consideration, see Section 2.5.

Early simulations of isotropic homogeneous turbulence were limited by the lack of computing power to Reynolds numbers below a hundred. Even today the best DNS with Reynolds numbers in the hundreds is still quite limited compared to real life turbulence with Reynolds numbers in the tens or hundreds of thousands. Yet comparison with experiment shows that these simulations do provide accurate representations of turbulence. The first simulations used a 32^3 grid, e.g., Orszag and Patterson (1972), and soon progressed to 64^3, e.g., Siggia and Patterson (1978). Computational requirements scale as N^3 for memory and N^4 for computational time, where N^3 is the grid size (She et al. (1991)). Reynolds number is related to grid size by $\mathrm{Re} \sim N^{4/9}$ so even with the huge increases in computing power since 1978, only modest increases in the Reynolds number of DNS has been possible. Today's state-of-the-art DNS runs on grids of 512^3 or 1024^3, with Reynolds numbers around 240, see Yeung and Zhou (1997) for a recent review.

It should also be mentioned that simulation methods other than DNS, such as large eddy simulation (LES) can produce higher Reynolds numbers by modelling rather than simulating the high wavenumber dissipation range, e.g., Briscolini and Santangelo (1994), Métais and Lesieur (1992), Chasnov (1991). However, for the purpose of comparing with the binary fluid simulations of spinodal decomposition, a fully resolved dissipation

range is the most appropriate type of turbulence simulation.

In this study of turbulence DNS, the size of the computational grid has been set at 64^3 for the main work, with a single larger run at 128^3 to provide a test of the effects of grid resolution on the accuracy. Most theory and DNS is aimed at higher Reynolds numbers and/or greater resolution than a 64^3 grid can produce because the scaling regime, in which Reynolds number independent behaviour is expected, doesn't start until there is an appreciable "inertial range" separating the low wavenumbers (large scales) from the high wavenumbers (small scales, dissipation). Chen et al. (1993a), and Yeung and Zhou (1997) conclude that a proper "inertial range" cannot be achieved with DNS running on less than a 512^3 grid with Reynolds numbers above 100. Furthermore, Chen et al. explicitly examine the low Reynolds number regime and conclude that the direct coupling between the low and high wavenumbers produces a fundamentally different dynamics from the high Reynolds number regime with a substantial inertial range; see also Mansour and Wray (1994), whose investigations placed a lower limit on the Reynolds number of around 50 for Reynolds number independent behaviour to be observed.

However, the basic statistics of the velocity field and associated error analysis are likely to be informative for all Reynolds numbers. Furthermore, the binary fluid studies of spinodal decomposition with which this single fluid turbulence will be compared later, are also likely to be in the region of relatively low Reynolds numbers as far as any turbulent effects are concerned.

Although most DNS studies after the earliest have moved on from the range with which 64^3 can be compared, there are still ample studies in the existing literature to provide a solid comparison with the results from this turbulence DNS study. Especially useful basic results can be found in, Siggia and Patterson (1978), Schumann and Patterson (1978), Kerr (1985, 1990), Yamamoto and Hosokawa (1988) and Kida and Murakami (1989). Vincent and Meneguzzi (1991) have higher Reynolds numbers, but they give the probability distributions of velocity derivatives and velocity increments against which qualitative shape comparisons can be made. In addition, Mansour and Wray (1994) studied low Reynolds number scaling, and Chen et al. (1993a,b) and Martinez et al. (1997) are all specifically interested in the dissipation range at low Reynolds

numbers, although their larger grid and far larger dissipation range make comparisons less straightforward.

4.2.2 Data generation

The Fortran programs used to generate the velocity fields analysed in this chapter were written by Young (1999) following basic methods first given by Orszag (1969, 1971). The programs ran on the EPCC Cray T3D parallel computer, with appropriate parameters (listed in Table 4.2.2) to provide a fully resolved turbulence on a 64^3 grid.

parameter	64^3	128^3
viscosity, ν	0.01189	0.01189
c_1	0.028	0.028
c_2	4.0	4.0
c_3	0.14	0.14
c_4	2.0	2.0
box length	2π	4π
time step	0.004	0.002
density, ρ	1	1

Table 4.1: *Simulation parameters for the* 64^3 *and* 128^3 *decaying turbulence simulations. The length and time scales are arbitrary, but have been chosen consistently so that the* 128^3 *simulation is equivalent to the* 64^3 *system in terms of grid resolution and Reynolds number. The initial configuration is specified by the energy spectrum of the initial velocity field set to* $E(k) = c_1 k^{c_2} \exp[-c_3(k^{c_4})]$.

The 128^3 parameters have been set up to match the 64^3 system to investigate the effect of increasing the grid resolution so they don't give the best performance (in terms of Reynolds number) that can be obtained from a 128^3 grid.

An initial configuration is generated in Fourier space following Orszag (1971), using an energy spectrum

$$E(k) = c_1 k^{c_2} \exp[-c_3(k^{c_4})] \tag{4.2}$$

with four adjustable parameters, c_1–c_4, values used are given in Table 4.2.2. This is made up of random velocity components consistent with this spectrum and with the incompressibility condition, $\mathbf{k}.\mathbf{v}(\mathbf{k}) = 0$ (from $\nabla.\mathbf{v}(\mathbf{x}) = 0$). Most reported simulations seem to stick to the same tried and tested methods for setting up initial conditions,

especially since for a forced simulation the initial condition is irrelevant. For decaying turbulence, at very late times when only the largest length scales are left in motion, the final decay is determined by the initial energy spectrum, but at intermediate times and for the smaller length scales that are primarily of interest for turbulence analysis, the initial condition is also irrelevant. A few of the early papers do discuss interesting methods for initializing the simulation, including Siggia and Patterson (1978), Schumann and Patterson (1978); Siggia (1981) gives precise instructions on how to set up comparable runs at different grid sizes, which was useful here for matching up the 128^3 parameters to the 64^3 ones, see Table 4.2.2.

The evolution from the initial configuration through a fully developed turbulence until the total energy has been dissipated to around 1/10 of the initial value can be simulated on 32 processors in about half an hour (16 processor-hours of computation time). A similar run using a 128^3 grid uses about 250 processor-hours. The turbulence is recorded by saving the whole velocity field at regular intervals so that more detailed analysis can be carried out later, without using parallel processing time unnecessarily.

4.2.3 Basic characteristics of turbulent decay

The time evolution of decaying single fluid turbulence can be characterised by following the time evolution of a few quantities[1]:

- the total energy, $E = \sum_k E(k)$, where the energy spectrum, $E(k)$ is given by Equation (2.46), plotted in Figure 4.1 (left),
- the dissipation rate, $\varepsilon = 2\nu \sum_k k^2 E(k)$, plotted in Figure 4.1 (right),
- the characteristic length scales, the integral scale, Equation (2.49), or in discrete form,

$$L_{int} = \frac{3\pi\rho}{4E} \sum_{grid} \frac{1}{2} \frac{\mathbf{v(k).v(-k)}}{|\mathbf{k}|}, \tag{4.3}$$

  the Taylor microscale, Equation (2.52), $\lambda = \sqrt{10\nu E/\varepsilon}$, and the Kolmogorov microscale, Equation (2.54), $\lambda_d = 2\pi \left(\rho\nu^3/\varepsilon\right)^{1/4}$, all shown in Figure 4.2 (left).

[1] Note that turbulence theorists often work directly in Fourier space, and this DNS is no exception; the basic quantity from which all other quantities are calculated is $\mathbf{v(k)}$.

- the Reynolds numbers, Re_{int} and Re_λ, using the integral scale and the Taylor microscale respectively as the length in Equation (4.1), plotted in Figure 4.2 (right).

Most of the analysis on single runs was done for a time of around three eddy turnover times (defined as L_{int}/v_{rms} evaluated at T=0) when the turbulence can be considered "fully developed", i.e. settled into a self-similar state independent of the initial configuration. The behaviour of the skewness of the longitudinal velocity derivative, shown in Figure 4.3 (left), is a sensitive measure of this; it assumes a value around -0.5 for fully developed turbulence.

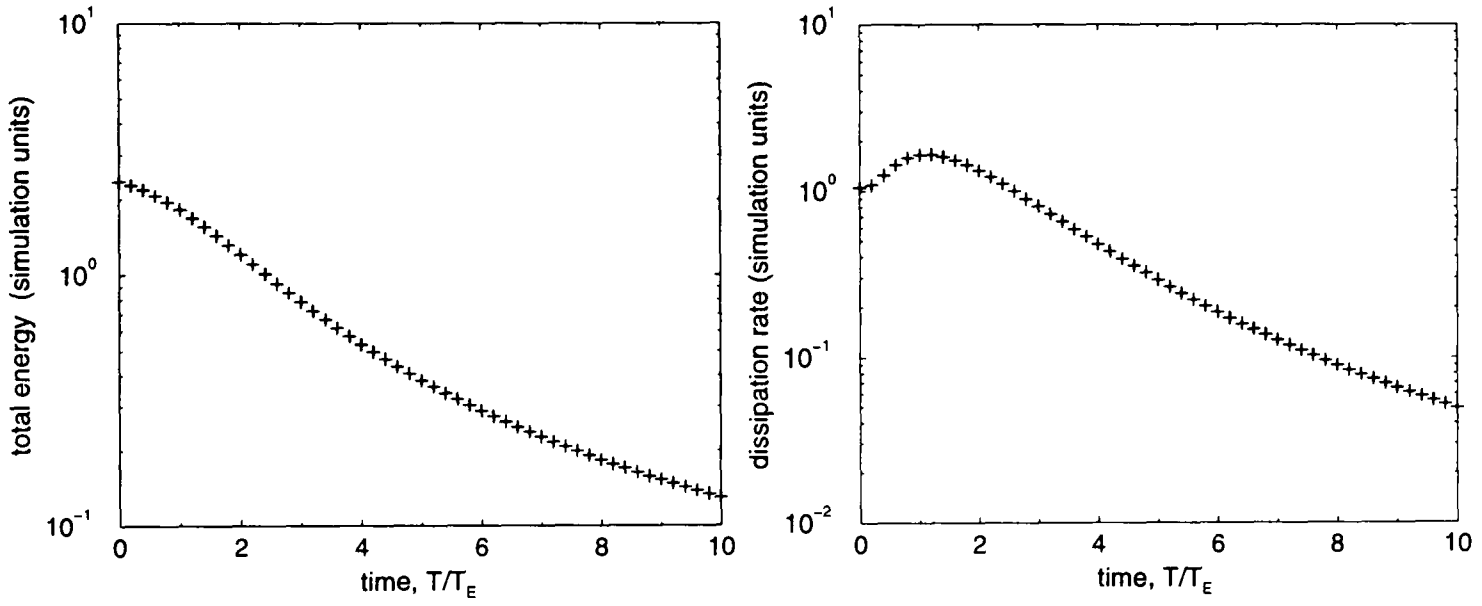

Figure 4.1: *Decaying turbulence run dec1000 on a* 64^3 *grid. Left: Total energy. Right: Dissipation rate. The time,* T*, is in units of the eddy turnover time,* T_E*, defined as* $T_E = L_{int}/v_{rms}$.

In Fourier space, the key characteristic is the energy spectrum, $E(k)$, shown in Figure 4.3 (right) using Kolmogorov scaling[2], where the dissipation takes place in the region of exponential decay at higher k, showing as a straight line on this linear-log plot. The slope and intercept of this line can be computed and compared with the literature. For $E(k)$ at around four eddy turnover times, the best fit to the exponential section has slope -4.77 ± 0.03 and intercept at $(k/k_d)^{5/3}E(k)/(\varepsilon\nu^5)^{1/4} = 2.18 \pm 0.04$. This compares with slope of -5.1 ± 0.1 and intercept 6.5 ± 0.1 from Kerr (1990), confirmed by Sanada (1991), both working on larger grids at higher Reynolds numbers. Agreement is reasonable given the Reynolds number dependence in this region; only simulations with closely similar parameters would be expected to give quantitatively similar results.

[2]Kolmogorov scaling is, $k^{5/3}\rho E(k)/(\epsilon/\rho)^{2/3}$, see Section 2.5.

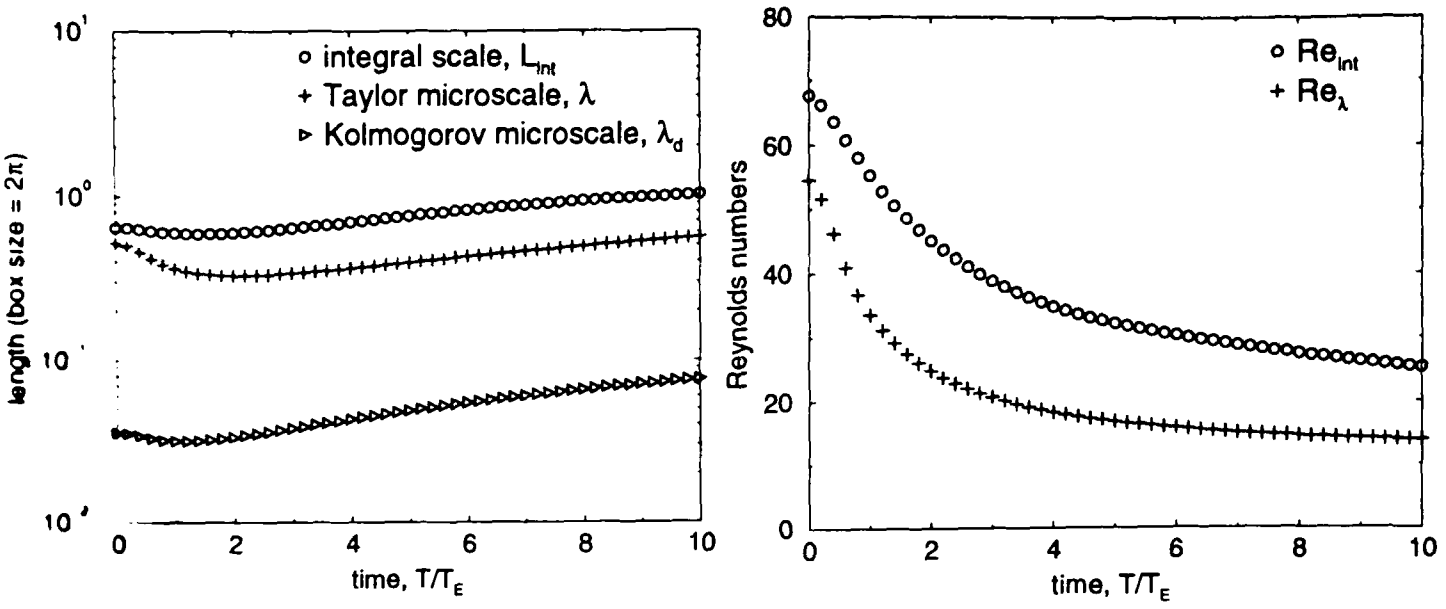

Figure 4.2: *Decaying turbulence run dec1000 on a* 64^3 *grid. Left: Length scales, integral scale (circles) and Taylor microscale (plus), and Kolmogorov microscale (triangles). Right: Reynolds numbers,* Re_{int} *based on the integral scale (circles) and* Re_λ *based on the Taylor microscale (plus). The time,* T*, is in units of the eddy turnover time,* T_E*, defined as* $T_E = L_{int}/v_{rms}$*.*

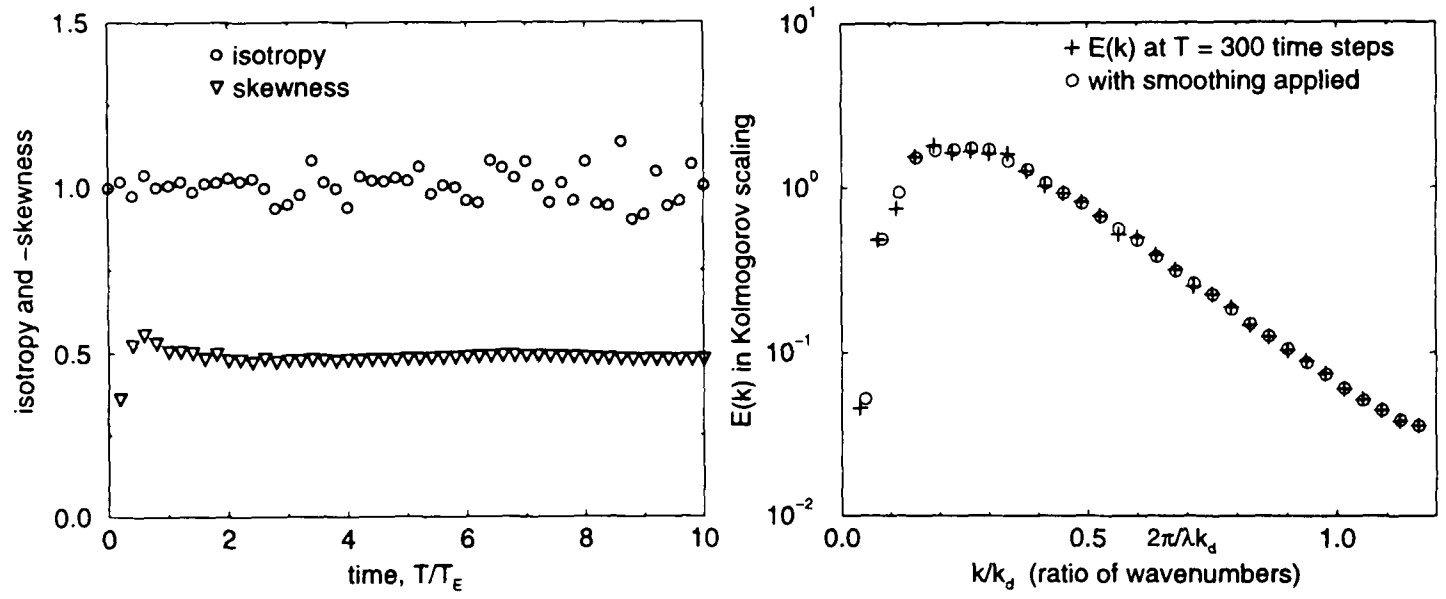

Figure 4.3: *Decaying turbulence run dec1000 on a* 64^3 *grid. Left: Skewness (plotted* $\times -1$*, triangles) and isotropy (circles). The time,* T*, is in units of the eddy turnover time,* T_E*, defined as* $T_E = L_{int}/v_{rms}$*. Right: Energy spectrum in Kolmogorov scaling. The smoothing is described in Section 4.3.2.*

4.2.4 List of quantities analysed

As well as the basic turbulent quantities just described, for the purpose of this analysis, the most useful comparative quantities with results reported in the literature are:

- moments and distributions of velocity components in real space;
- moments and distributions of velocity increments in real space;

- moments and distributions of velocity derivatives in real space;
- energy spectrum in Fourier space.

In addition, although not reported in any of the papers surveyed, in order to facilitate the more detailed error analysis presented in the rest of this chapter, the following quantities were calculated:

- moments and distributions of velocity components in Fourier space;
- moments and distribution of the energy density in real space;
- moments and distributions of $|\mathbf{v}(\mathbf{k})|$ and its real and imaginary parts;
- low order correlations between velocity components, increments and derivatives at the same grid point to test whether the components are independent;
- correlations, $\langle \mathbf{v}(\mathbf{k}).\mathbf{v}(-\mathbf{k}') \rangle$ for the case $|\mathbf{k}| = |\mathbf{k}'|$, and $\langle \mathbf{v}(\mathbf{x}).\mathbf{v}(\mathbf{x} - \boldsymbol{\Delta}\mathbf{x}) \rangle$.

For the purpose of comparing with the binary fluid system, the only results used from this list are that the pdf of the velocity components in real space is approximately Gaussian in single fluid isotropic homogeneous turbulence (see Section 4.5) and the qualitative shapes of the velocity derivative pdfs shown in Figure 4.5 (right). Reference is also made to corrections for low wavenumbers in shell-averaging described in Section 4.3.2.

The remainder of this chapter shows in detail that the statistical analysis methods as applied to single fluid turbulence are up to the job they are being asked to do, and quantifies the limits to the accuracy due to the finite discrete grid and finite numerical precision.

4.3 Fourier space analysis

This section covers the analysis in Fourier space of the energy spectrum and the velocity components, and the geometrical and statistical factors affecting the errors involved in shell-averaging. As well as the energy spectrum, the shell-averaging procedure is also used to obtain structure factors from numerical simulation data, so the error analysis developed for this method has wider applicability.

4.3.1 Energy spectrum

Theories predict the shape of the energy spectrum, $E(k)$, for incompressible turbulence of infinite extent at infinite Reynolds number. Thus the Fourier series become Fourier integrals and $E(k)$ is a smooth function of the continuous wavenumber k. In contrast, the DNS turbulence takes place in a rather small box of side $\Lambda_b = 2\pi$ (with periodic boundary conditions) so the Fourier space representation is a discrete Cartesian grid with grid-spacing $2\pi/\Lambda_b$. The largest wavenumber in Fourier space, $k = \pm N/2$, corresponds to two grid spacings in real space[3], there is enough information in Fourier space to reconstruct the single grid spacing real space data, but not to interpolate between grid points. The issue, then, is how well simulations on these finite, discrete grids can represent continuous, infinite turbulence.

The energy spectrum, $E(k)$, is a function of $k = |\mathbf{k}|$ alone only if the system is isotropic. The finite box, discrete Fourier space expression for $E(k)$ (compare Equation (2.46) is,

$$E(k) = \frac{4\pi k^2}{n_k} \sum_{|\mathbf{k}|=k} \frac{1}{2}\mathbf{v}(\mathbf{k}).\mathbf{v}(-\mathbf{k}), \tag{4.4}$$

where n_k is the number of points in the sum. Obviously for $|\mathbf{k}|$ exactly equal to k, there are only a few points in the Cartesian grid (integer solutions to the equation $k_x^2 + k_y^2 + k_z^2 = k^2$), not enough to provide a good average value for $E(k)$. Shell-averaging is the method used to overcome this problem by taking the set of points in a shell of width δk such that the sum is done over $|\mathbf{k}| = k \pm \delta k/2$. If $E(k)$ is a smooth and slowly varying function of k then δk can be chosen large enough to include sufficient points to provide a good approximation to $E(k)$, provided the statistical distribution of $\mathbf{v}(\mathbf{k})$ itself is well-behaved. The properties of $\mathbf{v}(\mathbf{k})$ are thus crucial to the question of the accuracy of $E(k)$, but before considering them in detail, some basic points to do with the geometry of shells will be elucidated.

[3]The box size, Λ_b, corresponds to the smallest Fourier mode, $k = 1$, and the N^3 grid points in real space map onto $N \times N \times N/2$ points in Fourier space each with a complex Fourier transform associated with it so the real plus complex parts provide the extra factor of 2 bringing the corresponding amount of data in Fourier space up N^3 to match real space.

4.3.2 Shell geometry in Fourier space

The common choice of $\delta k = 1$ corresponds to $n_k \simeq 4\pi k^2$, and these two factors are often cancelled from the sum in Equation 4.4, introducing additional inaccuracy into the calculation. Variations in the value of $|\mathbf{k}|$ and the total number of points in the shell relative to $4\pi k^2$ can be examined to quantify these errors. Since $\mathbf{v}(\mathbf{x})$ is real, $\mathbf{v}(\mathbf{k}) = \mathbf{v}^*(-\mathbf{k})$ so there is only half a shell of independent points for each value of k. The number of grid points in each half-shell of unit thickness (measured in grid spacings) is compared with the value of $\frac{1}{2}4\pi|\mathbf{k}|^2$ in Table 4.2.

k	n_k	$\frac{1}{2}4\pi k^2$	error %	$\langle\|\mathbf{k}\|\rangle$	error %
1	8	6.3	27	1.31	24
2	30	25.1	19	2.24	11
3	48	56.6	-15	3.14	4.4
4	104	100.5	3.5	4.06	1.5
5	174	157.1	11	5.10	2
6	224	226.2	-1.0	6.12	2
7	300	307.9	-2.6	7.07	1
8	380	402.1	-5.5	8.03	0.3
9	570	508.9	12	9.06	0.6
10	624	628.3	-0.7	10.09	0.9
15	1310	1413.7	-7	15.02	0.1
20	2516	2513.3	0.11	20.02	0.09
25	4016	3927.0	2.3	25.01	0.06
30	5612	5654.9	-0.8	30.02	0.08
60	22850	22619.5	1.02	60.01	0.02
120	90900	90477.8	0.47	120.00	0.00
240	361124	361911.2	-0.22	240.00	0.00

Table 4.2: *Number of data points in half-k-shells.*

The actual errors this produces will depend on how fast the quantity being calculated varies as a function of k. Corrections can easily be applied for the number of points in the shell and for the slightly different average value of k for each shell, beyond that some assumption has to be made about how the function varies with k. Kerr (1990) applies these types of corrections to his energy spectrum, including an assumption about the functional form of $E(k)$. Applying just the corrections for the number of points in each

shell and the average value of $|\mathbf{k}|$ to the energy spectrum in Figure 4.3 (right), smooths the spectrum significantly (circles) and changes the fit to the exponential region to a slope of -4.47 ± 0.03 and intercept of 1.91 ± 0.04, a difference well beyond the original fitting errors.

For 64^3 grids, Table 4.2 shows that errors due to finite shell widths on a Cartesian grid are appreciable over the whole range of k, up to 31 full shells before the corners of the box start to cut into the shells. Both Schumann and Patterson (1978) and Kerr (1985) choose to use $\delta k = 2$ to improve the statistics. For larger wavenumbers on larger grids, however, the errors are much smaller and Chen et al. (1993b) claim that for 512^3 grids and above the errors are negligible compared to the finite computational accuracy of the simulation.

4.3.3 Statistics of velocity components in Fourier space

The analysis of the velocity statistics is complicated by the incompressibility condition, $\nabla.\mathbf{v}(\mathbf{x}) = 0$, which transforms to $\mathbf{k}.\mathbf{v}(\mathbf{k}) = 0$, and which means that not all the velocity components are independent. The most natural way to accommodate this is to work in spherical polar coordinates, whence only the components of $\mathbf{v}(\mathbf{k})$ tangential to the surface of the shell are non-zero. Since $\mathbf{v}(\mathbf{k})$ is complex, there are thus four (real, scalar) components of the velocity in Fourier space, being the real and imaginary parts of the longitudinal and lateral spherical polar components.

The moments up to the fourth and the probability distributions of both these four spherical polar velocity components, and the six Cartesian velocity components, have been computed in each shell of width $\delta k =$ one grid spacing. The four spherical polar components follow a Gaussian distribution, Figure 4.4 (right), while the Cartesian components have distributions that are taller and thinner with slightly wider tails (small positive flatness) reflecting the effect of the incompressibility condition, Figure 4.4 (left). The cross correlations, $\langle v_\alpha v_\beta \rangle$ and $\langle v_\alpha^2 v_\beta^2 \rangle$, have also been computed, showing that, to this order, the spherical polar components are independent of each other.

As well as the velocity components at the same point being independent of each other, within each shell there are no direct correlations between the velocity components at

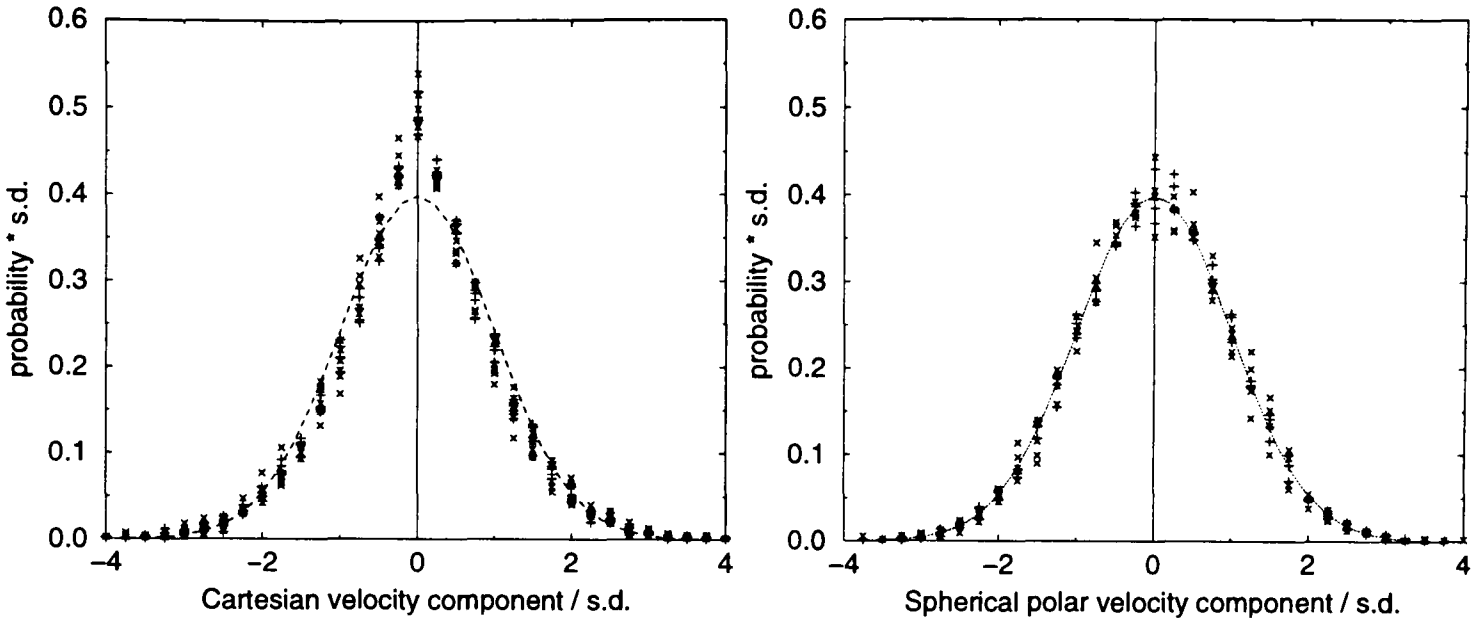

Figure 4.4: *Probability distributions of velocity components in Fourier space for decaying turbulence run dec1000 at time step 300, normalised by the standard deviation (s.d.). Left: Cartesian components. Right: Spherical polar components. Data shown is for shells at 19 (+) and 27 (×) lattice units. All six/four velocity components are shown on the same graph, with a Gaussian shown dotted for comparison.*

different points. Theory states that,

$$\langle \mathbf{v}(\mathbf{k}).\mathbf{v}(-\mathbf{k}')\rangle = 0, \tag{4.5}$$

unless $\mathbf{k} = \mathbf{k}'$, while for $\mathbf{k} = \mathbf{k}'$, $\langle \mathbf{v}(\mathbf{k}).\mathbf{v}(-\mathbf{k})\rangle$ is clearly just the average of the square modulus of the velocity at that point which is equal to twice the energy density (for unit mass density). Actually calculating $\langle \mathbf{v}(\mathbf{k}).\mathbf{v}(-\mathbf{k}')\rangle$ for selected k-shells in the velocity field of fully developed turbulence shows that it does take the form of a δ-function as far as a discrete, finite grid can approximate to it.

In fact, calculating the correlation is not a sufficient test of whether two random variables are independent, see Cramér (1946, Sec. 21.7 - 21.9). This point is covered in more detail in Appendix F.

Further support for the independent, Gaussian distribution of the velocity components in a k-shell comes from consideration of the moments and probability distributions of the spectral energy density, $\langle \mathbf{v}(\mathbf{k}).\mathbf{v}(-\mathbf{k})\rangle$, the modulus of the velocity, $\langle (\mathbf{v}(\mathbf{k}).\mathbf{v}(-\mathbf{k}))^{1/2}\rangle$, and the moduli of the real and imaginary parts of the velocity. Each of these quantities consists of the sum of squares of the velocity components and are thus expected to follow χ or χ^2 distributions of order n where n is the number of such independent random Gaussian variables involved in the sum. The order n can easily be determined from the moments, see Table E.1 in Appendix E, and the results

match the expected values well. Specifically, $\langle \mathbf{v}(\mathbf{k}).\mathbf{v}(-\mathbf{k}) \rangle$, and $\langle (\mathbf{v}(\mathbf{k}).\mathbf{v}(-\mathbf{k}))^{1/2} \rangle$ both have order $n = 4$, showing they are the sum of four independent Gaussian components, and, $\langle |Re(\mathbf{v}(\mathbf{k}))| \rangle$ and $\langle |Im(\mathbf{v}(\mathbf{k}))| \rangle$ both have order $n = 2$, for the two real and two imaginary components.

4.3.4 Conclusions from Fourier space analysis

The main result of this section of the analysis is that for isotropic homogeneous turbulence, the velocity components in Fourier space – meaning the real and imaginary parts of each of the two transverse spherical polar components – follow independent Gaussian distributions to a good approximation (up to the fourth moment) with no direct correlations between different points in the same k-shell. The literature appears to contain no analysis of the moments or probability distributions of the Fourier space velocity components – perhaps the fact they are independent and follow Gaussian distributions is just so "well known" it never gets mentioned or checked.

This result provides a solid underpinning for the shell-averaging procedure used in turbulence analysis. The statistical properties of quantities calculated from independent Gaussian variables are well-understood and easy to handle for error estimation, allowing straightforward calculation and presentation of errors for Fourier space turbulence calculations.

The results for the shell geometry, Table 4.2 allow accuracy to be assessed and corrections to be applied to shell-averaged quantities even without knowing the underlying distribution is Gaussian. Such corrections can thus be applied to the analysis of the binary fluid system wherever the structure factor is calculated.

4.4 Error estimation methods

This section covers error analysis in more detail. The limitations imposed by the number of independent data points in a simulation compared to the actual grid size are considered, along with a method of estimating errors in the moments of distributions.

Lastly, the bootstrap error estimation method is described, a very general numerical error estimation method that can be applied anywhere, provided enough data has been collected to provide good statistics.

4.4.1 Number of independent data points

The lack of any correlations between basic quantities within k-shells in Fourier space implies we can treat all points within one shell as independent for the purposes of error estimation, provided δk is reasonably small compared to $|\mathbf{k}|$. In real space the situation is quite different, at short range the velocity at two different points is correlated, as can be seen from the results of calculating $\langle \mathbf{v}(\mathbf{x}).\mathbf{v}(\mathbf{x}-\mathbf{\Delta x})\rangle$ for varying values of $\mathbf{\Delta x}$, see Figure 4.5.

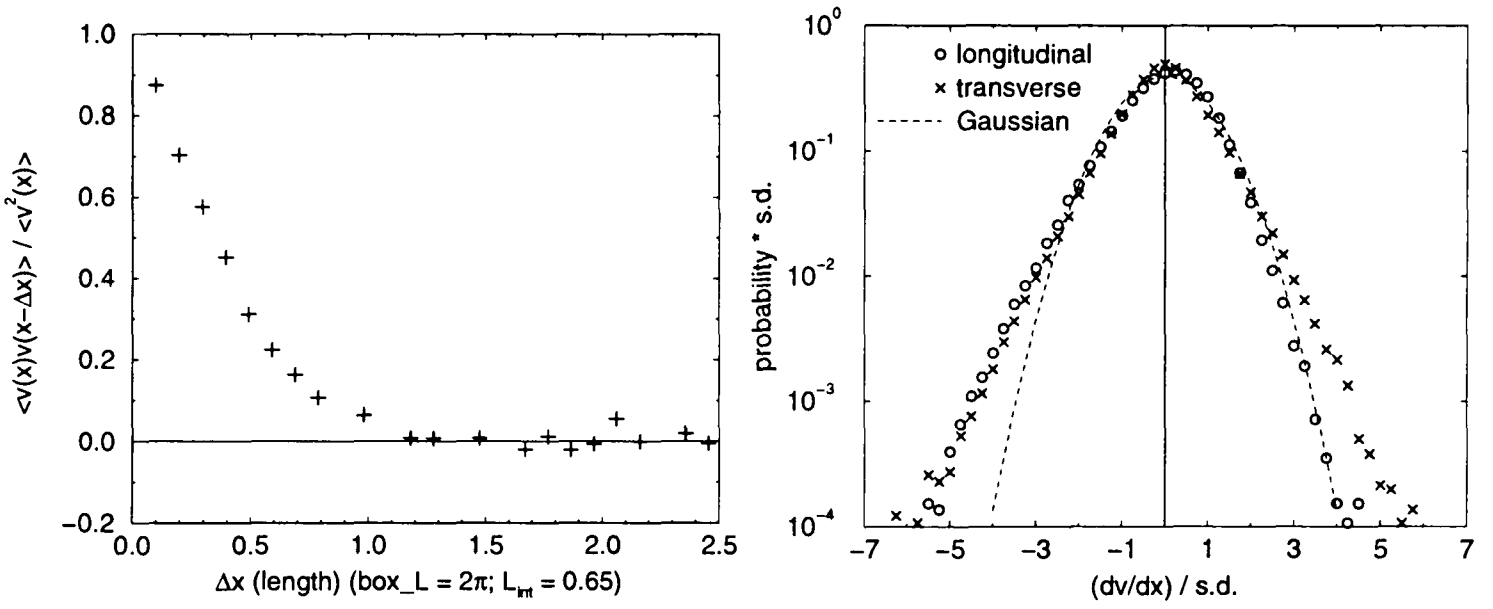

Figure 4.5: *Decaying turbulence run dec1000 at time t = 300 time steps. Left: Velocity correlations in real space. Right: Velocity derivative pdfs, longitudinal (circles) and transverse (cross), with Gaussian (dotted) for comparison.*

The correlation length is conveniently given by the integral scale, Equation (2.49), a quantity calculated in Fourier space from a simple sum over all grid points so the more time-consuming double sum in real space to get the correlation does not in general have to be carried out. For a typical 64^3 turbulence simulation at around three eddy turnover times (fully developed turbulence), the integral scale is around 0.64, one tenth of the box size. There are thus only around $(2\pi/0.64)^3 \approx 10^3$ independent data points in these runs, a rather small number from the point of view of statistical accuracy. Low energies and Reynolds numbers (necessary to ensure full resolution on the small 64^3 grid) mean relatively large integral scales, simulations on larger grids suffer much

less reduction in the number of data points through this adjustment, (Briscolini and Santangelo (1994)).

This way of thinking about a turbulence simulation, as a set of independent estimates of the quantities of interest, is rather different from the approach used to analyse the binary fluid spinodal system, where the data points are taken to represent a whole connected system and adjustments for the number of independent data points are not appropriate.

4.4.2 Accuracy of moments

Turbulence theorists are particularly interested in higher moments of the distributions of the various turbulence characteristic quantities, since these specify the departure from a Gaussian distribution; a pdf is completely specified if all of its moments are specified, Cramér (1946). The accuracy of higher moments is affected most acutely by low numbers of independent data points because the largest contribution comes from the tails of the distributions. Both Vincent and Meneguzzi (1991) and Briscolini and Santangelo (1994) give details on how they assessed the highest moment they could calculate. Vincent and Meneguzzi are only concerned with the moments of velocity increments in real space, which have stretched exponential tails. They extrapolate the tails of their distributions to infinity and calculate the correction this produces in the moments. When the corrections become too large, the moments are considered to be too inaccurate. Briscolini and Santangelo look directly at the distribution of the individual values in the sum used to compute the moments to see where it peaks and where the shape of the distribution becomes too messy. They also derive theoretically a formula for estimating the largest moment, p, that can be calculated to within a given accuracy,

$$p = \psi \ln(\epsilon^2 N_{tot} \Delta), \tag{4.6}$$

where ψ is given in terms of the probability distribution, $\exp(-\beta|v_a|^\psi)$, ϵ is the desired accuracy (e.g. 0.1 for 10%), N_{tot} is the number of independent data points, v_a is the velocity component or derivative under consideration, and Δ is the width of the bins used to form the distribution of the moments in units of the standard deviation of $|v_a|$. They find their method agrees with the method of Vincent and Meneguzzi.

A rough and ready way to see what their formula implies, is to find the position of the peak of the moment distribution, $v_a(p) = (p/(\beta\psi))^{1/\psi}$, calculate the value of the pdf for that value of v_a, and multiply by N_{tot} to get an idea of the number of data points falling in a bin of unit width around the peak of the moment. These points provide the largest contribution to the value of the moment, if there are too few of them the moment cannot be determined from the data. For a Gaussian distribution of unit variance ($\psi = 2$, $\beta = 1/2$) and $N_{tot} = 10^3$, this gives about 250 data points around the first moment, 150 around the second, 90 around the third and 50 around the fourth. This suggests that for 10^3 points, errors are likely to be substantial even for moments as low as the third and fourth. Briscolini and Santangelo amassed enough data to calculate moments up to the 16th, and Vincent and Meneguzzi calculate moments up to the 26th with accuracy of 10% or better.

In the analysis of the binary fluid spinodal system, only rough values of third and fourth moments will be considered, so the accuracy of higher moments will not be an issue.

4.4.3 Bootstrap methods

The importance of maximising the total number of independent data points has led to the development of various methods of partitioning the data, see, for example, Machiels (1997), Chen et al. (1993a), Hosokawa and Yamamoto (1990). Similar methods are also useful for determining the errors associated with the moments and probability distributions.

By dividing the 64^3 real space data points randomly into approximately 250 subsets of 10^3 points each and comparing results for each subset, estimates are obtained for the errors of around 3.2% for the mean, 4.5% for the variance, 7.5% for the skewness and 15% for the flatness. These are averages over several simulation runs, values for one particular run are shown in Table 4.3, and for 128^3 grid in Table 4.4.

A full bootstrap method, Efron (1982), using 100 selections of all 64^3 points with replacement, confirms the estimates from the 10^3 subsets method. On the other hand, for a quantity like the total energy for which all points are taken as significant, the full bootstrap method estimates the error at about 0.15%. The same selection techniques

have also been used in Fourier space to obtain errors estimates for k-shells, and for whole-grid quantities such as the dissipation rate. The error estimated for the total energy calculated in Fourier space is about 3%, much larger than the error estimated for the same quantity calculated in real space. The dissipation rate error is estimated at about 1% and the integral scale error at about 3.5%. The differences can be explained by the dependence on the wavevector, $\mathbf{k}$, in each sum.

Bootstrap methods are a powerful way to obtain reliable error estimates in situations where there is plenty of available computing power, and at least reasonably large amounts of data to provide good statistics from dividing it into subsets. No prior knowledge is required of the underlying probability distributions to apply a bootstrap analysis.

4.4.4 Errors in pdfs

Calculation of pdfs involves similar trade-offs to the shell-averaging procedures discussed in detail in Section 4.3.2. The bins used to evaluate the pdf need to be wide enough to provide good statistics, yet the finite width introduces errors dependent on the shape of the distribution. This is discussed in more detail in Appendix F. Since pdfs are only used for qualitative comparisons in this study, no quantitative evaulations of errors in the pdfs have been done. Instead, the moments have been used to characterise them quantitatively, thus avoiding any binning errors.

4.5 Real space analysis

To complete the investigation of the turbulence simulation, the real space representation of the velocity field has been analysed. The velocity components are expected to follow Gaussian distributions (apart from short range correlations discussed in Section 4.4.1), and to be independent of each other.

The velocity derivatives were also investigated, since they are expected to have more informative non-Gaussian pdfs. In particular, as already noted in Section 4.2.3, the

skewness of the longitudinal velocity derivatives is expected to take the value -0.5 in fully developed turbulence. Due to the incompressibility condition, the variance of the transverse derivatives is expected to be twice that of the longitudinal derivatives, see Setion 2.5.

4.5.1 Velocity components

The velocity components are found to follow a Gaussian distribution, and the x, y, and z components at a single point are independent of each other, in agreement with the literature for both experiment and simulation, see Monin and Yaglom (1975). Results for the moments and cross correlations for a typical velocity component in real space are shown in Table 4.3.

v_x	bootstrap error[a]	theory	normal error
mean	0.0E-13[b] ±0.02	0.0	0.004 ±0.032
variance	1.0995 ±0.05	1.0	0.999 ±0.045
skewness	0.113 ±0.082	0.0	-0.013 ±0.073
flatness	-0.072 ±0.14	0.0	0.004 ±0.15
$\langle v_x v_y \rangle$	-0.03 ±0.02	0.0	
$\langle v_x^2 v_y^2 \rangle$	-0.03 ±0.03	0.0	

Table 4.3: *Moments of velocity component v_x, typical results for 64^3 grid simulation at around three eddy turnover times from the start when fully developed turbulence has been established. The column "bootstrap" contains data analysed using the bootstrap method described in Section 4.4.3, the column "theory" is exact Gaussian values, and the column "normal" is from a Gaussian random number generator.*

[a] Based on dividing data randomly into 250 sets of around 8000 points each.

[b] Simulation dynamics ensure no net translation of the system thus keeping $\langle \mathbf{v} \rangle$ zero within double precision accuracy.

As can be observed in Table 4.3, apart from the mean there is a general tendency for the moments to differ from theoretical values by slightly more than their errors. However, the deviations are random when compared over several different runs. This could be due to the presence of anisotropy, Schumann and Patterson (1978) report seeing anisotropy[4] which could account for this, and Yeung and Zhou (1997) also discusses the effects of

[4] meaning significant statistical differences between the x, y and z grid directions.

anisotropy. To test whether this is an effect of the small grid size (64^3) or an intrinsic feature of the dynamics, results for 128^3 were compared and typical results are shown in Table 4.4.

v_x	bootstrap error[a]	theory	normal error
mean	0.0E-15[b] ±0.008	0.0	-0.0004 ±0.012
variance	1.012 ±0.015	1.0	1.0001 ±0.014
skewness	0.012 ±0.025	0.0	0.003 ±0.028
flatness	-0.157 ±0.051	0.0	-0.005 ±0.057
$\langle v_x v_y \rangle$	0.01 ±0.01	0.0	
$\langle v_x^2 v_y^2 \rangle$	-0.04 ±0.02	0.0	

Table 4.4: *Moments of velocity component v_x, typical results for 128^3 grid simulation at around 3 eddy turnover times from the start when fully developed turbulence has been established. The column "bootstrap" contains data analysed using the bootstrap method described in Section 4.4.3, the column "theory" is exact Gaussian values, and the column "normal" is from a Gaussian random number generator.*

[a]Based on dividing data randomly into 250 sets of around 8000 points each.

[b]Simulation dynamics ensure no net translation of the system thus keeping $\langle \mathbf{v} \rangle$ zero within double precision accuracy.

As can be seen from Table 4.4, the effects are still present but only in the flatness, supporting the idea that the small grid size is the cause. Further tests at 256^3 would be able to resolve this point, but have not been carried out for this study.

Essentially, the isotropy and homogeneity of the simulation is being invoked to allow data from the whole grid to be used to provide an ensemble from which the properties of the velocity field at a single "typical" point can be inferred. If the simulation is not completely isotropic and homogeneous then the results will be affected by this, in ways that will be difficult to predict. Tests which involve selecting only part of the data and comparing the results, see Section 4.4.3, can detect and quantify any effects due to inhomogeneity and anisotropy. However, a 64^3 grid is rather small to apply them to. The 128^3 grid can be divided into 8×64^3 cubes and the variations between them compared. Results from this test show that differences between the octants are about half the size of the errors for moments measured within each octant, so the system shows good homogeneity at this scale. Dividing the data into much smaller cubes of around the size of the correlation length produces much greater variation between

cubes, as would be expected.

4.5.2 Velocity derivatives and increments

The velocity derivative field is calculated in Fourier space by multiplying through by ik_α then transforming to real space, a method that is clearly (from the results) more accurate than considering finite differences in real space, but which introduces errors that are difficult to quantify through the numerical Fourier Transform routines (FFTs). The FFTs perform well when the high wavenumber terms are small, but not so well when these terms are large, and the process of calculating the derivative has just multiplied all the terms by a factor of k, i.e. increased the high-k terms relative to the low-k terms. Both Siggia (1981) and She and Orszag (1991) describe methods of estimating the effects of different regions of Fourier space both in and outside the range of the simulation by deleting or filtering different bands and seeing how the results are affected. These tests were not investigated further in this study.

Results for both the velocity derivatives and increments (calculated as differences in real space) match those in the literature at least qualitatively, compare Figure 4.5 (right) with Vincent and Meneguzzi (1991), but note they quote S_4 = flatness + 3, and get somewhat larger values. Numerical results for the moments and cross correlations of the velocity derivatives are given in Table 4.5.

	$\mathrm{d}u_y/\mathrm{d}y$ error	$\mathrm{d}u_x/\mathrm{d}y$ error	theory long	theory lat
mean	0.00 ±0.08	0.00 ±0.09	0.0	0.0
variance	1.00 ±0.05	2.01 ±0.13	1.0	2.0
skewness	-0.50 ±0.13	-0.03 ±0.2	-0.5	0.0
flatness	1.1 ±0.5	2.04 ±0.8	positive	positive
$\langle \mathrm{d}v_y/\mathrm{d}y.\mathrm{d}v_x/\mathrm{d}y \rangle$	-0.03 ±0.04			
$\langle (\mathrm{d}v_y/\mathrm{d}y.\mathrm{d}v_x/\mathrm{d}y)^2 \rangle$	0.48 ±0.22	expect correlations		

Table 4.5: *Moments of velocity derivatives* $\mathrm{d}v_y/\mathrm{d}y$ *and* $\mathrm{d}v_x/\mathrm{d}y$, *typical results for* 128^3 *grid simulation at around 3 eddy turnover times from the start when fully developed turbulence has been established.*

These results in particular will be used for comparison later when the velocity field of the binary fluid spinodal system is analysed for signs of developing turbulence.

4.6 Conclusions

The statistics of a single fluid isotropic, homogeneous, decaying turbulence simulation have been investigated in both real and Fourier space. The basic turbulence measures, energy, dissipation, skewness of the longitudinal velocity derivative, length measures and Reynolds numbers are found to agree qualitatively, and where direct comparison is possible, quantitatively with the existing results in the literature. These basic results provide a reference for comparisons with the binary fluid velocity field in Chapter 6 where signs of turbulence are looked for in the most inertial LB spinodal simulations.

More detailed analysis and error estimation showed that the turbulent velocity field components have distributions that can be considered Gaussian in both real and Fourier space to a good approximation (up to the fourth moment based on this analysis) when estimating errors in quantities calculated from them. The energy density is found to follow a χ^2 distribution, as expected for quantities composed of sums of squares of independent, normally distributed quantities.

The shell-averaging procedure used to obtain various quantities such as the energy spectrum and the spherically averaged structure factor has been investigated for accuracy. Care must be taken to estimate the errors properly, and a table of errors for low-numbered k-shells has been calculated, Table 4.2.

Further error estimation techniques such as a simulation using random Gaussian components can be helpful to determine finite bin and grid size effects for more complicated quantities, and a bootstrap error analysis can be used to estimate errors when it is impractical to use analytical error formulas.

A particular problem for generating a useful ensemble from decaying turbulence is matching the energy across different runs. Unless this can be done accurately enough, the dominant errors will be due to the energy differences and will mask other variations one might be hoping to detect. Approximately ten runs were done in total to check that the results obtained from the current study of single runs were representative. Further studies using a larger grid size, would also provide a useful check on the results.

A number of further tests and studies could be done on the turbulence system to refine

the error analysis and confirm some of the deductions:

- the same tests on larger grids, 256^3 say, to see if the trends in the size of the errors and fluctuations seen between 64^3 and 128^3 continue to improve the simulation accuracy.

- sectioning and selected deletion of parts of Fourier space to further quantify the errors in Fourier space quantities.

- tests at higher Reynolds number (on larger grids) to investigate how dependent the errors are on the extent to which the simulation is pushed to its limits (highest possible Re for k_d still resolved).

- tests where the Reynolds number is pushed too high for the grid resolution to determine how badly this affects the results.

- the same analysis applied to a forced turbulence simulation rather than decaying to check that both provide a good approximation to real turbulence.

None of these tests were considered necessary for this study where the primary interest is in comparisons with the binary fluid mixture.

The analysis methods have thus been tested and found to provide effective characterisation of the turbulence velocity field where the expected results are well known in advance. The same methods can now be applied with confidence to the binary fluid velocity field undergoing spinodal decomposition, see Chapter 6.

Some of the analysis methods are also applied to the order parameter field of the binary fluid mixture, in Chapter 5, where presentation of the main work of this thesis is started.

Chapter 5

Spinodal decomposition: simulation results

5.1 Introduction

This chapter and the following two chapters report the results from the main investigation of this work, the late stage dynamics of the spinodal decomposition of a fifty-fifty binary mixture of simple fluids with the same density and viscosity, quenched far below their critical temperature. Using the lattice-Boltzmann simulation code described in Section 3.3, many runs were performed to cover the widest possible range of parameters. The order parameter data saved from these simulation runs were analysed to obtain the structure factor, and thence length scales characterising the domain size. The velocity field data were also saved and analysed to investigate the behaviour of the fluid during spinodal decomposition.

Results from the order parameter analysis are described in this chapter, while full analysis of the velocity field is presented in Chapter 6, including comparison with the single fluid turbulence system studied in Chapter 4. Of particular interest here is whether the binary fluid mixture shows signs of developing turbulence in the velocity field. Chapter 7 presents an analysis of the persistence behaviour of the spinodal system, and includes a brief comparison of the results from 2-D spinodal decomposition of fluids.

Using the AVS software visualisation package, the interface and velocity field data were imaged to illustrate the typical patterns of domain structure and fluid flow, see Appendix A.

The main aim of the work presented in this chapter is to compare the simulation results with theory, see Section 2.3. The main comparison is to see whether the growth rate of the fluid domains matches the theoretical prediction, after an initial diffusive period, of a linear regime where viscous hydrodynamics dominates, followed by a crossover to the slower growth rate of $t^{2/3}$ where inertial forces dominate the fluid dynamics. Note that there is no difference between the predictions of the simple scaling theory and those of the new theory presented in Section 2.4 for the domain growth rate. All the differences are in the behaviour of the velocity field, and will be explored in Chapter 6. The prediction by Grant and Elder (1999) of a further crossover to a scaling regime with exponent, $\alpha \leq 1/2$ will also be considered in the light of the simulation results. A summary of the main results in this chapter has been published in Kendon et al. (1999).

5.2 Run details

The simulations have been run using the LB code described in detail in Section 3.3. Tests on systems of lattice size 96^3 were run on the EPCC Hitachi parallel computer using 4 processors, while 128^3 and 256^3 sized runs were carried out on the EPCC Cray T3D parallel computer using 64 and 256 processors respectively. Typical runs took from six to twelve hours of clock time and used, in the 256^3 case, around 3000 processor hours of computer time. The runs on 96^3 and 128^3 lattices were used to test the parameters before committing to the large use of resources necessary for 256^3 runs.

The required input parameters to the simulation are:

- fluid density, ρ, set equal to unity for all runs;
- fluid viscosity, η, which also sets the time step of the simulation. Values for each of the 256^3 runs used for the main analysis are given in Table 5.1;
- mobility, M, which controls the rate of diffusion. Values are given in Table 5.1;

- the free energy parameters, A, B and κ, see Equation 3.28, which determine the interfacial tension, σ, the interface width, ξ, and the quench depth. For complete separation in the bulk phases the condition $-A = B$ was always chosen, along with $\sqrt{-\kappa/2A} = 0.57$ to determine the interface width. Values for A, B, κ and σ are given in Table 5.1;

- the number of time steps for which to run the simulation, usually around 10^4, and how often to record the order parameter and velocity fields, usually around every 300 time steps.

Also shown in Table 5.1 are the values of the scaling length, $L_0 = \eta^2/(\rho\sigma)$, and the scaling time, $T_0 = \eta^3/(\rho\sigma^2)$, see Section 5.3.3. The main difference between otherwise

Run	L_0	T_0	-A,B	κ	η	M	σ
Run028	36	935	0.083	0.053	1.41	0.1	0.055
Run022	5.95	71	0.0625	0.04	0.5	0.5	0.042
Run033	5.95	71	0.0625	0.04	0.5	0.2	0.042
Run029	0.952	4.54	0.0625	0.04	0.2	0.3	0.042
Run020	0.15	0.885	0.00625	0.004	0.025	4.0	0.0042
Run030	0.01	0.016	0.00625	0.004	0.0065	2.5	0.0042
Run019	0.00095	0.00064	0.00313	0.002	0.0014	8.0	0.0021
Run032	0.0003	0.00019	0.00125	0.0008	0.0005	10.0	0.00083

Table 5.1: *Parameters used in* 256^3 *lattice-Boltzmann runs.*

similar runs is usually in the mobility, M, which controls the diffusion rate; see Section 5.4.1 for discussion of the role played by diffusion.

Runs were started off in a completely mixed state with small random fluctuations, and generally continued until the domain size reached about one quarter of the system size, when finite size effects started to become apparent, see Section 5.4.

For each run, the order parameter, ϕ, (difference in density between the two fluids) and the fluid velocity vector at each lattice site were saved periodically for later analysis. The sampling frequency was limited by the available disk space. Typically, data was saved every 300 time steps over a run of 10^4 time steps, giving around 4Gb of data. For the 256^3 runs, this meant coarse-graining the data to 128^3 before saving it, even though

the simulation itself ran on the full 256^3 lattice. Results for all calculated quantities were compared between 256^3 and 128^3 runs with the same parameters, to identify any effects of coarse-graining. The 128^3 runs that correspond (matching L_0 and T_0 values) to the main 256^3 runs are shown in Table 5.2.

Run	L_0	T_0	-A,B	κ	η	M	σ
Run010	381	25656	0.125	0.08	5.71	0.5	0.084
Run026	36	935	0.083	0.053	1.41	0.25	0.055
Run027	36	935	0.083	0.053	1.41	0.1	0.055
Run014	5.95	71	0.0625	0.04	0.5	0.5	0.042
Run008	0.952	4.54	0.0625	0.04	0.2	0.5	0.042
Run018	0.15	0.885	0.00625	0.004	0.025	4.0	0.0042
Run015	0.00095	0.00064	0.00313	0.002	0.0014	8.0	0.0021
Run031	0.0003	0.00019	0.00125	0.0008	0.0005	10.0	0.00083

Table 5.2: *Parameters used in* 128^3 *lattice-Boltzmann runs.*

5.3 Order parameter analysis

The order parameter data saved from each run essentially provide an image of the state of the system at regular intervals. This can be processed using the AVS software visualisation package. (See Appendix A for examples of the interface from various stages of these runs.) The structure consists of two convoluted domains, one for each fluid, interlocking though a series of "necks" connecting larger rounded regions of fluid. The coarsening dynamics proceed through the necks thinning and breaking while the rounded domains grow larger through coalescence.

Each run begins with a diffusive period during which the completely mixed initial state separates into small domains of around twice the size of the interfacial width. Once the interfaces are sharp and well-defined the interfacial tension takes over as the dominant driving force in the separation, moving the fluid around hydrodynamically to allow the coarsening to proceed. It is this hydrodynamic regime that is of primary interest in this study, so it is important to discard data from early times where diffusion is still contributing significantly to the domain growth. Details of how the diffusive growth

was estimated are given in Section 5.4.1 and estimation of other sources of error and inaccuracy is made in Section 5.4.3.

In order to provide quantitative analysis of the dynamics of the phase separation, the order parameter data have been analysed numerically by the following procedure:

- Calculate the structure factor, $S(k)$ from the Fourier transform of the order parameter data.
- Obtain a length, $L(T)$ from the structure factor, corresponding to the domain size.
- Fit the domain size to a power law in time, $L(T) \sim (T - T_{\text{int}})^{\alpha}$.
- Use the characteristic length and time scales, L_0 and T_0, based on the viscosity and interfacial tension to scale the $L(T)$ data for each run so that all the results can be plotted on a single scaling plot.

This analysis has been applied to the data from each run in Tables 5.1, the details are described in Sections 5.3.1 and 5.3.2. At each step, checks have been made to determine how the data are affected by simulation errors and inaccuracies, and to match the results to any relevant theoretical predictions.

5.3.1 Structure factor scaling

The first step in the analysis of the order parameter data was calculation of the structure factor. The whole ϕ field saved from the simulation runs was processed through numerical Fourier transform routines, and from the resulting Fourier space field the structure factor was calculated,

$$S(k) = \frac{1}{n_k} \sum_{k-\frac{1}{2}<|\mathbf{k}|<k+\frac{1}{2}} \phi(\mathbf{k})\phi(-\mathbf{k}), \tag{5.1}$$

where $\phi(\mathbf{k})$ is the Fourier transform of the order parameter, n_k is the number of lattice sites in the shell of radius k and unit thickness in Fourier space, and $\mathbf{k}$ is the wave

vector in Fourier space, with $k = |\mathbf{k}|$. This is the standard definition of the structure factor used by experimentalists and theorists[1].

The scaling ansatz is that the domain shape is the same for any domain size. Therefore, $S(k)$ at different times, and for different simulation runs, should collapse onto a single plot when appropriately scaled,

$$\frac{S(k)}{[L(T)]^d} \quad \text{vs.} \quad kL(T), \qquad \text{where } d = 3 \text{ for 3-D,} \tag{5.2}$$

where $L(T)$ is the length used to characterise the size of the domains, obtained from the first moment of $S(k)$. Figure 5.1 shows plots of $S(k)$ scaled in this way for Run028 and Run032, in the linear and inertial regimes respectively (see Section 5.3.2 for discussion/identification of linear and inertial regimes).

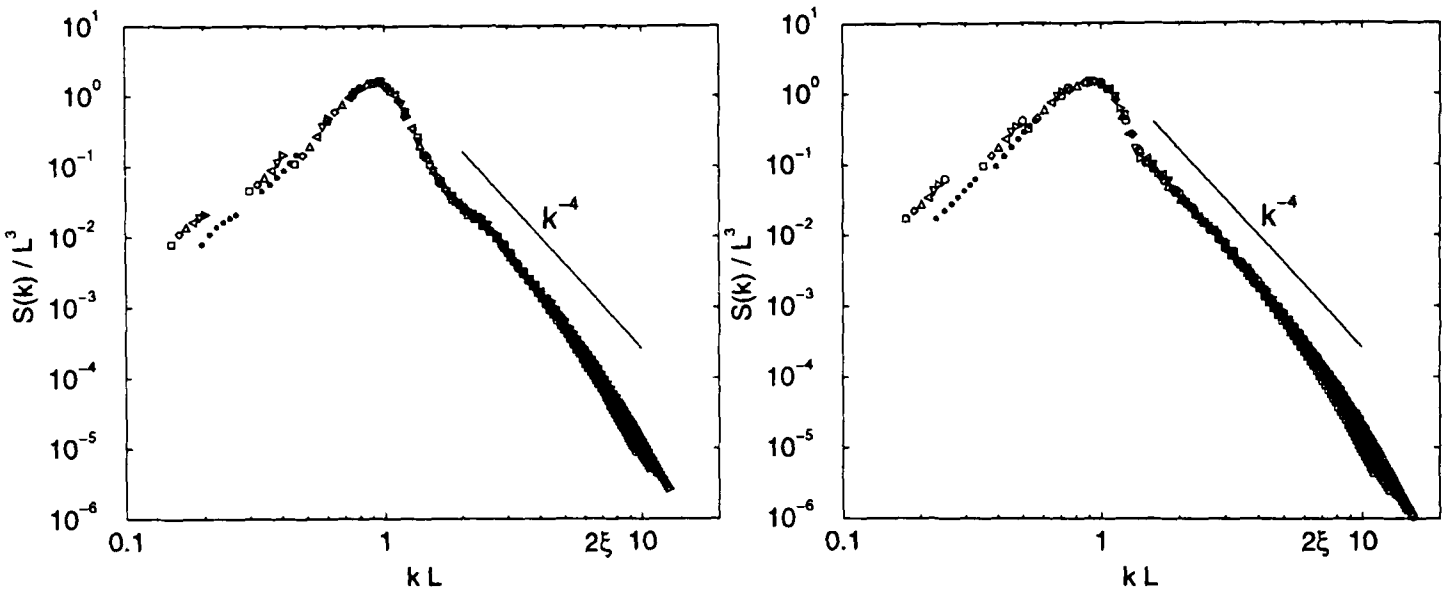

Figure 5.1: *Left: structure factor, $S(k)$, for Run028 (linear regime) for timesteps 14000 - 19000, $L(T) = 38 - 52$. Right: $S(k)$ for Run032 (inertial regime) for timesteps 11000 - 17000, $L(T) = 45 - 64$. Filled circles show the corrections for the average value of $|\mathbf{k}|$ for the first two shells from Table 4.2.*

Both these runs are on 256^3 lattices, and the order parameter data are therefore coarse-grained to 128^3 before the Fourier analysis is applied. In other words, all the information on length scales smaller than two lattice units has been lost. In Fourier space, information on length scales smaller than 2 lattice units is contained in the region

[1] A discussion of the approximations involved with using this method to calculate the structure factor can be found in Section 4.3, where a similar procedure is used to calculate the energy spectrum of a turbulence velocity field. The number of lattice points in each shell cancels out in the calculation of $S(k)$, so only the correction for the average value of $|\mathbf{k}|$ from Table 4.2 is required. This is shown as filled circles for the first two shells in the graphs in Figure 5.1.

with wavenumber $k > 256/4 = 64$. The coarse-graining process has therefore simply truncated the upper half of Fourier space. For the purpose of comparing the scaling collapse, only length scales larger than the interface width, $\xi \simeq 3$ lattice units, are relevant, so the coarse-graining makes no difference to these results. As a final check, the structure factor from the corresponding 128^3 runs was compared with the 256^3 data and found to be in good agreement.

The collapse of the structure factor data illustrated in Figure 5.1 is good for length scales larger than about twice the interface width (marked as 2ξ on the graphs) and there is a reasonable approximation of a k^{-4} Porod tail. The Porod tail should be found in the region $\xi \ll r \ll L(T)$, see Bray (1994), so between $\xi \simeq 3$ and $L_{\mathrm{max}} = 64$ there isn't much room to observe it unambiguously. The spread of $S(k)$ in the low kL region corresponds to the first couple of k-shells where the statistics are very poor, even with the correction applied for the average value of $|\mathbf{k}|$; they should not be considered reliable data compared to the higher wavenumber region. The collapse between different runs is also pretty good, but the shape is significantly different between the linear and inertial regimes, in particular, the shoulder round about where the Porod tail starts is lower in the linear regime than the inertial regime. This implies that the domains are a subtly different shape in real space, more evenly rounded in the linear regime perhaps since the peak is effectively a little sharper.

Studies of the scaling collapse of the structure factor may also be found in Jury (1999) whose results lie in between the linear and inertial regimes. The shape they produced for the structure factor is very similar to that found here, with the shoulder near the Porod tail fairly low, like the linear regime plotted above, Figure 5.1 (left). Appert et al. used a lattice gas simulation method, and also reported structure factor scaling resembling that found here.

There are various further predictions in Bray (1994) and Furukawa (1989), about the amplitude of $S(k)$ in the tail, etc., that could be tested if further work was done on this area, but given the limited range of relevant length scales, this has not been done in this study.

In summary, the main result from analysing the structure factor is that the basic scaling of the domains is good over the timescale of each simulation run, but that differences

are detectable between runs in different regimes of parameter space. This implies that analysis of further scaling quantities, such as the length scale of the domains considered in the next sections, may be expected to produce good results.

5.3.2 Length scale from the structure factor

In order to characterise the size of the domains in the system, a length scale, the first moment of the spherically averaged structure factor, $L(T)$, Equation (2.5), has been calculated,

$$L(T) = \sum_k S(k) / \sum_k kS(k). \tag{5.3}$$

No significant difference due to coarse-graining was observed for $L(T)$, as was expected, since the interesting range of $L(T)$ is much larger than the coarse-graining length scale of 2 lattice units, and, as was discussed in the previous section, the structure factor is unaffected above the coarse-graining length.

To determine the time dependence of $L(T)$, it was then fitted to (for each run separately),

$$L = v(T - T_{\text{int}})^{\alpha}, \tag{5.4}$$

where v, T_{int} and α are fitting parameters. Figure 5.2 illustrates how the fitting was done. The range of the data region used is defined by $L_{\text{min}} \leq L(T) \leq L_{\text{max}}$, where L_{min} is a lower limit determined from the residual diffusive growth (see Section 5.4.1), and L_{max} is equal to one quarter of the system size, determined from the domain size above which finite size effects became noticeable (see Section 5.4.2).

The built-in routines in the graph plotting program **xmgr** were used to do the fitting, and the fits always fell within the tolerance of 1% specified for the non-linear curve-fitting utility in **xmgr**. However, the actual uncertainty in determining the exponent, α, over a range of data covering less than a decade, is more like 10% for the first three runs in Table 5.1, and 5% for the rest. (See Section 5.4.3 for a detailed discussion of error estimation.)

Having determined the growth rate exponent, α, for each of the main 256^3 runs in Table 5.1, in principle, this determines whether each run lies in the linear, crossover

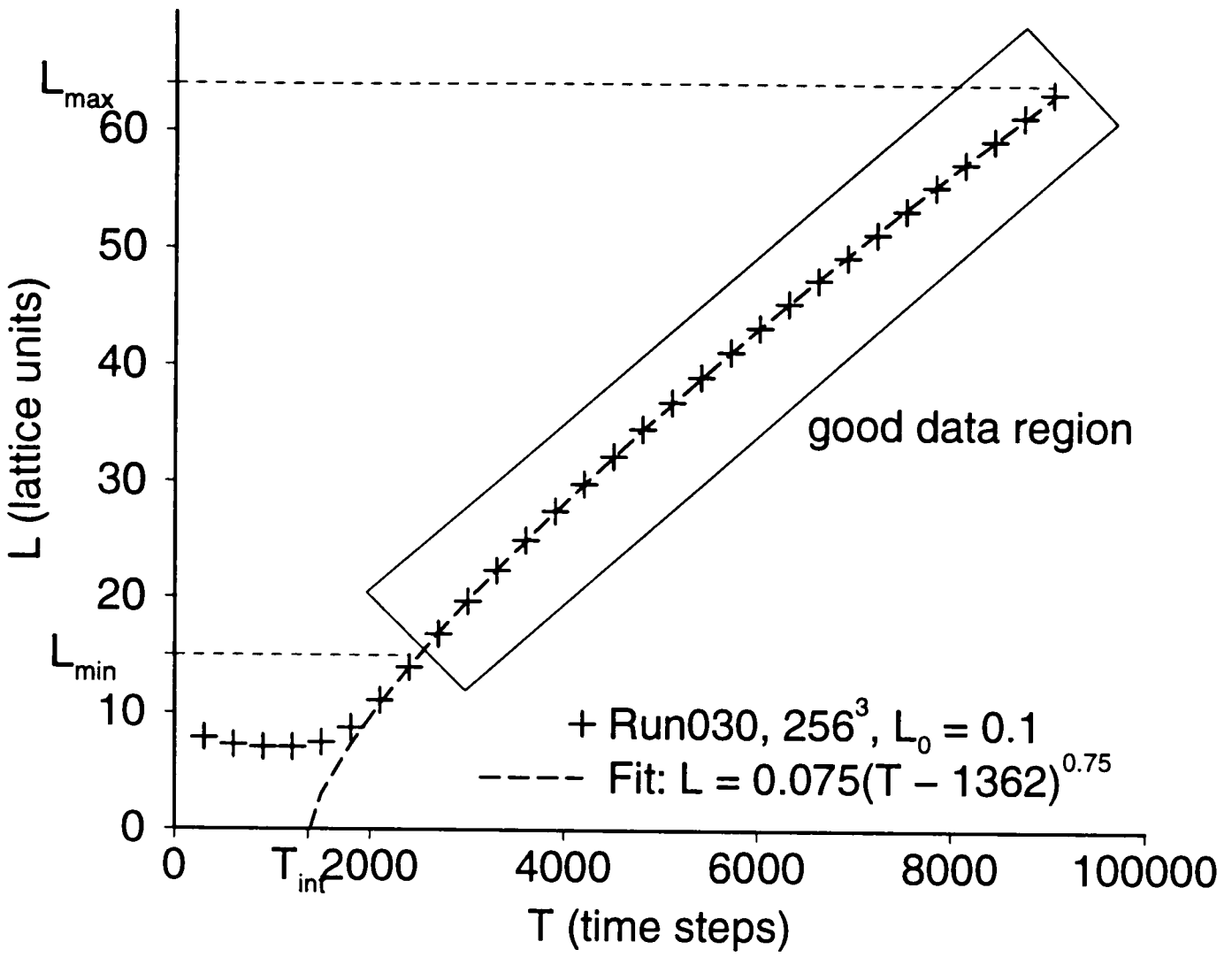

Figure 5.2: *L vs T graph (unscaled) for Run030, illustrating the fitting procedures.*

or inertial regions according to where α lies in the range $1.0 \lesssim \alpha \lesssim 2/3$. The runs do have a range of values of α from 1.0 (Run028, Run022 and Run033)[2] to 0.67 (Run019) and 0.69 (Run032), with intermediate exponents, 0.95 (Run029), 0.80 (Run020) and 0.75 (Run030). Thus, according to the fitted exponent, α, the simulation has covered the linear, crossover and inertial regions. The fitting graphs and full results are shown in Section 5.4.1, in Figures 5.4 – 5.5, where the full fitting analysis to determine the values of $L_{\min}$ is explained. The values of the fit parameters are given there in full in Table 5.3.

There are, however, (as will be shown later in discussion of other published work, Section 5.6), many reasons why the measured exponent might not accurately identify the true position of the run in the linear, crossover or inertial scaling regimes. The next section is the first of a number of extensions to the analysis designed to confirm that in the case of these LB simulations, the value of the exponent, α, does in fact accurately locate the runs in the correct scaling regime.

[2] Forced linear fits, see Section 5.4.3 for explanation of why these are the bests fits to this data.

5.3.3 Scaled lengths on final graph

In order to compare the results from all the runs together, and present them in a more visually informative way, this section shows how the data was scaled and plotted on a single log-log plot. This method for combining the data from different spinodal simulation runs follows Jury et al. (1999).

The only fit parameter needed for this scaling process is the intercept, T_{int}. Once T_{int} has been determined from the fitting procedure described in the previous section, $L(T)$ can be scaled using the characteristic length and time scales, L_0 and T_0 (see Section 2.3.2),

$$L = v(T - T_{\text{int}})^{\alpha} \quad \longrightarrow \quad \frac{L}{L_0} = \frac{v}{L_0/T_0^{\alpha}} \left(\frac{T - T_{\text{int}}}{T_0} \right)^{\alpha}, \tag{5.5}$$

i.e., L/L_0 plotted against $(T - T_{\text{int}})/T_0$ should give a straight line of slope α in a log-log plot. The scaled prefactor, $b(\alpha) = v/(L_0/T_0^{\alpha})$, is also now non-dimensional and should have the same value for all runs having the same value of the scaling exponent, α, so all the runs should line up with each other when plotted together. In terms of the non-dimensional length and time variables introduced in Section 2.3.2, $l = L/L_0$ and $t = (T - T_{\text{int}})/T_0$,

$$l = b(\alpha)t^{\alpha}. \tag{5.6}$$

In the linear regime where $t \ll t^*$, $b(1) \equiv b_1 =$ universal constant, and similarly $b(2/3) \equiv b_2 =$ universal constant in the inertial regime where $t \gg t^*$. The crossover time, t^*, is predicted to satisfy $1/b_1 < t^* < 1/b_2^{2/3}$ given that the crossover length is of the order of $l = 1$.

Figure 5.3 shows the data from all the runs in Table 5.1 scaled and plotted on a single graph. It can be seen that the individual runs do, as predicted, collapse onto a single scaling that is first linear, then crosses over to two thirds at large l, t. The positions of the runs on the graph are as predicted by the values of the scaling exponent, α, confirming that for the LB data in this work, the exponents determined from the fitting procedure do accurately reflect the scaling behaviour of the simulations. The breadth of the crossover region; $10^2 \lesssim t \lesssim 10^6$, justifies the use of a single exponent to fit each run in this regime, no single run is long enough to see a change in exponent from beginning to end beyond the estimated errors.

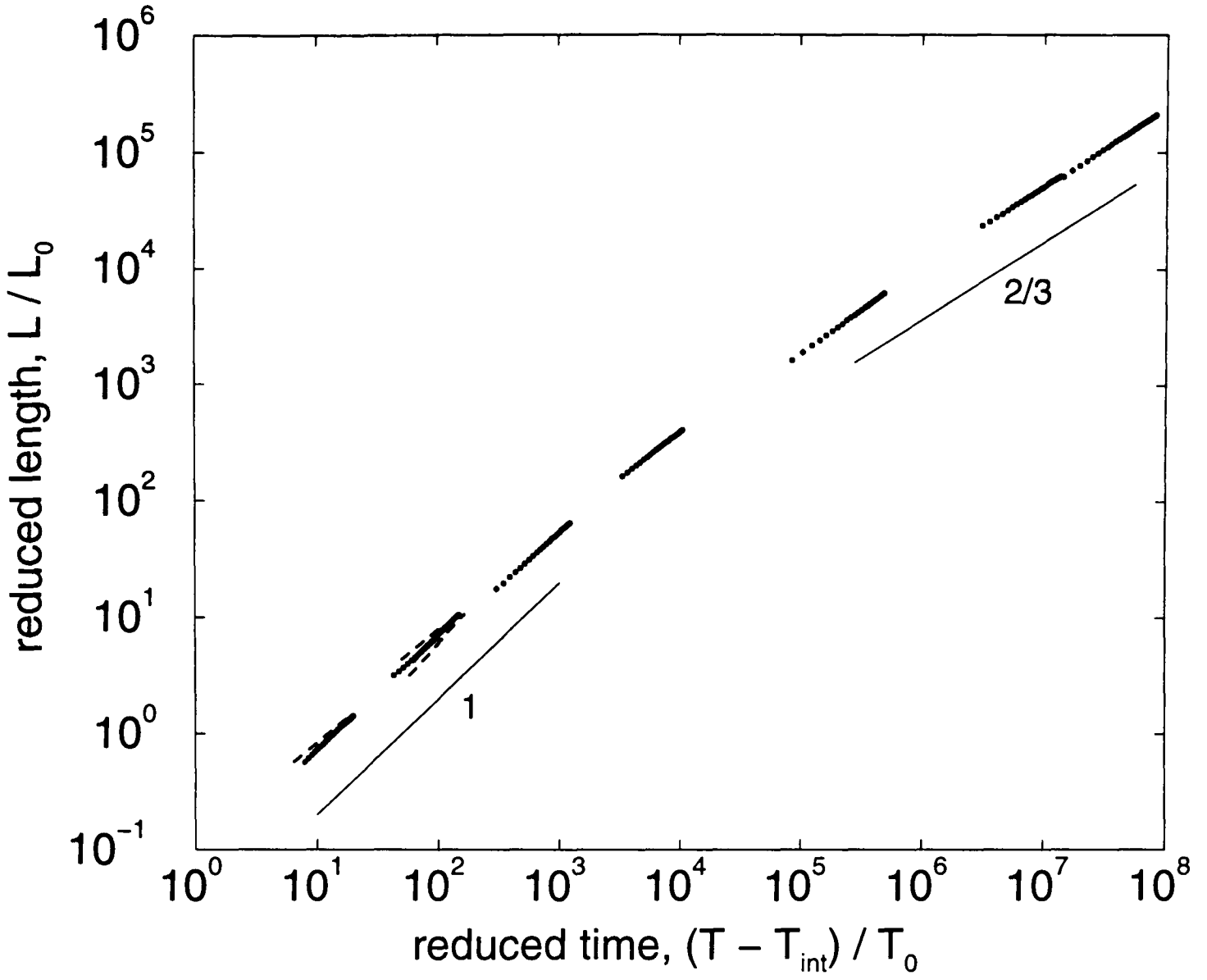

Figure 5.3: *Scaling plot in reduced variables (L/L_0, T/T_0) for 256^3 LB data. Dots (left to right) are the runs in Table 5.1 (top to bottom). Dashed lines show free exponent fits for the first three data sets in Table 5.1 for comparison with linear fits (dots).*

This is the main result of this section of work, agreement with the theory predicting exactly these exponents for the viscous (linear) and inertial regimes in 3-D. The runs in the inertial regime have exponents α determined from free exponent fits of 0.69 and 0.67, well within the estimated 10% error of the predicted value of 2/3. The runs in the linear regime have exponents, α, from free exponent fits (see Table 5.3), of 0.88, 0.86 and 1.16, slightly outside the estimated error, but the consistency of the values of the scaled prefactor from the linear fits, $b_1 \equiv v/(L_0/T_0) = 0.073, 0.072, 0.072 \pm 0.015$ confirm that the linear fits are the best fits. (See Section 5.6 for more discussion of the role of the prefactor in comparisons with other published work.)

In these results there is no hint that the exponent is reducing still further to $\alpha \leq 1/2$, as predicted by Grant and Elder (1999), although a further crossover beyond the range of these simulations cannot be ruled out. The predictions of Grant and Elder will

be discussed further in Section 6.3.4, once the velocity field has been analysed and Reynolds numbers calculated.

Note too, the huge range of length and time covered by the combination of eight simulation runs, five decades of length and seven decades of time. With present and forseeable computational resources, there is no way to obtain this result in a single run, it would require a lattice of size around a million cubed, run for around 10^{10} time steps.

This is the first time the inertial ($t^{2/3}$) regime has been clearly observed in 3-D simulation. See Section 5.6 for discussion of other published work. Before that, the next section fills in the details of the fitting procedure and error analysis, and in Section 5.5, the dynamics of the system are considered in more detail from the perspective of the relevant length scales.

5.4 Error analysis

Having achieved the main result that this study set out to obtain from these simulations, this section considers in detail the analysis carried out to determine the lower and upper limits to the $L(T)$ data that were used for the fitting procedure, the associated errors in determining the fit parameters, and the limitations of the simulation itself.

The lower limit on $L(T)$ data, L_{min}, is set by the residual diffusive growth in the simulation. This is calculated in Section 5.4.1. The upper limit, L_{max}, is set by finite size effects, which are discussed in Section 5.4.2. The errors associated with the fitting procedure on the usable data region, $L_{\mathsf{min}} \leq L(T) \leq L_{\mathsf{max}}$, are discussed in Section 5.4.3.

5.4.1 Residual diffusion

The simulation runs are started off in a completely mixed state, and the first stage of the evolution is entirely diffusive, until small, well-separated domains have formed with sharp interfaces. The interfaces then take over from diffusion in driving the separation process. Diffusive domain growth is relatively slow. Once the domains are formed, it

proceeds as $L \sim T^{1/3}$, see Section 2.2.3. Interface-driven hydrodynamic growth, where the interfaces rearrange themselves using bulk fluid flow, proceeds faster, as $L \sim T$ or $L \sim T^{2/3}$, so it soon dominates over the diffusive growth as the domains grow. Since this study is interested in the hydrodynamic growth rather than diffusive growth, it is important to limit the data used to the region where diffusive growth is negligibly small. The effect of a small amount of diffusive growth, $\sim T^{1/3}$, combined with hydrodynamic growth is to distort the shape of the $L(T)$ graph in the lower region such that the fitted exponent, α, will appear smaller than it really is for hydrodynamic growth alone. The fitting procedure is quite sensitive to small distortions in the $L(T)$ graph, so a tight constraint of 2% residual diffusion was set as the criterion for determining L_{min}.

To calculate this lower limit, L_{min}, the diffusive growth rate was estimated separately in a smaller simulation run in which the hydrodynamic growth was inhibited by turning the viscosity up to a very high value. A matching diffusion-only run was done for each main set of parameters in Table 5.1. These diffusion-only runs are shown in Figures 5.4 – 5.5, along with the $L(T)$ data from the corresponding main runs.

Given a diffusion-only run corresponding to a main run (same interfacial tension and mobility, viscosity $\rightarrow \infty$), the growth rates are calculated as follows. The fits, (see Section 5.3.2), provide numerical values for the parameters in $L = v(T - T_{\mathrm{int}})^{\alpha}$. The growth rate,

$$\dot{L} = v\alpha(T - T_{\mathrm{int}})^{\alpha-1} = \alpha L \left(\frac{v}{L}\right)^{1/\alpha}, \tag{5.7}$$

for the full runs can then be compared with the diffusion-only growth rate, obtained from Equation (5.7) by setting $\alpha = 1/3$,

$$\dot{L}_D = L/3 \left(\frac{v_D}{L}\right)^3, \tag{5.8}$$

for the corresponding diffusion-only run. From this, a lower bound, L_{min}, on the range of L used in the fitting procedure was calculated. For a 2% limit on diffusive growth, the requirement is that $\dot{L}_D \leq 0.02\dot{L}$. The values of L_{min} obtained this way are listed in Table 5.3. The diffusive contribution, $\dot{L}_D/\dot{L}$, falls off as L^{-2} to $L^{-1.5}$ so it reduces rapidly from the 2% upper limit as L increases above L_{min}.

Evaluating L_{min} and the fit parameters for each main run is an iterative process. $\dot{L}$ is first estimated by using a reasonable initial estimate, $L_{\mathrm{min}} = 15$. Then L_{min} is evaluated

		fits at 2% diffusion			*fit*	$L_{\min}$ *at diffusion*		*fit 1%*
Run	L_0	α	v	T_{int}	v_D	2%	1%	α
Run028	36	0.88	0.0096	1948	0.41	20.0	28.5	0.81
linear fit		1.0	0.00028	516				
Run022	5.9	0.86	0.023	304	0.64	26.0	38.0	0.88
linear fit		1.0	0.00605	-524				
Run033	5.9	1.16	0.0012	442	0.48	17.5	24.9	1.12
linear fit		1.0	0.0060	1445				
Run029	0.95	0.95	0.0175	1020	0.54	15.3	21.7	0.92
Run020	0.15	0.80	0.0418	603	0.60	23.4	34.9	0.80
Run030	0.01	0.75	0.0747	1362	0.51	14.8	22.4	0.76
Run019	0.00095	0.67	0.134	1008	0.60	21.5	33.8	0.66
Run032	0.0003	0.69	0.0833	1855	0.48	19.0	29.8	0.69

Table 5.3: *Fits and lower cut-off,* $L_{\min}$*, for* 256^3 *runs.*

using $\dot{L}$ and the value of L_D from the diffusion-only run. A new fit is done using the data defined by this new value of $L_{\min}$, and finally $\dot{L}$ and thence $L_{\min}$ are evaluated again to check that they didn't change significantly. In all cases the first evaluation of $L_{\min}$ was found to be accurate within 5%, so no further iterative cycles were required.

This whole procedure was repeated with a limit of 1% instead of 2% on the residual diffusion. The values of the fit exponent, α (last column in Table 5.3), did not change beyond the estimated errors so the limit of 2% diffusion was taken to provide sufficient accuracy for analysing the data.

Note that it is not possible just to turn the mobility parameter, M, down to very low values in order to eliminate residual diffusion; setting the rate of diffusion at the *appropriate* level is crucial to the success of the simulation. Too fast and diffusion will still contribute to domain growth at length scales well above the interface width, raising the value of $L_{\min}$ and reducing the size of the region that can be used as good data. Too slow and it takes too long for the interface to form in the initial stages, wasting computer resources. Additionally, the interface may not be able to break and rejoin fast enough to keep pace with the domain enlargement, since this reconnection process also depends on diffusion for its operation, see Section 5.5.1. Furthermore, if the interface is out of local equilibrium, it may not have the expected equilibrium value

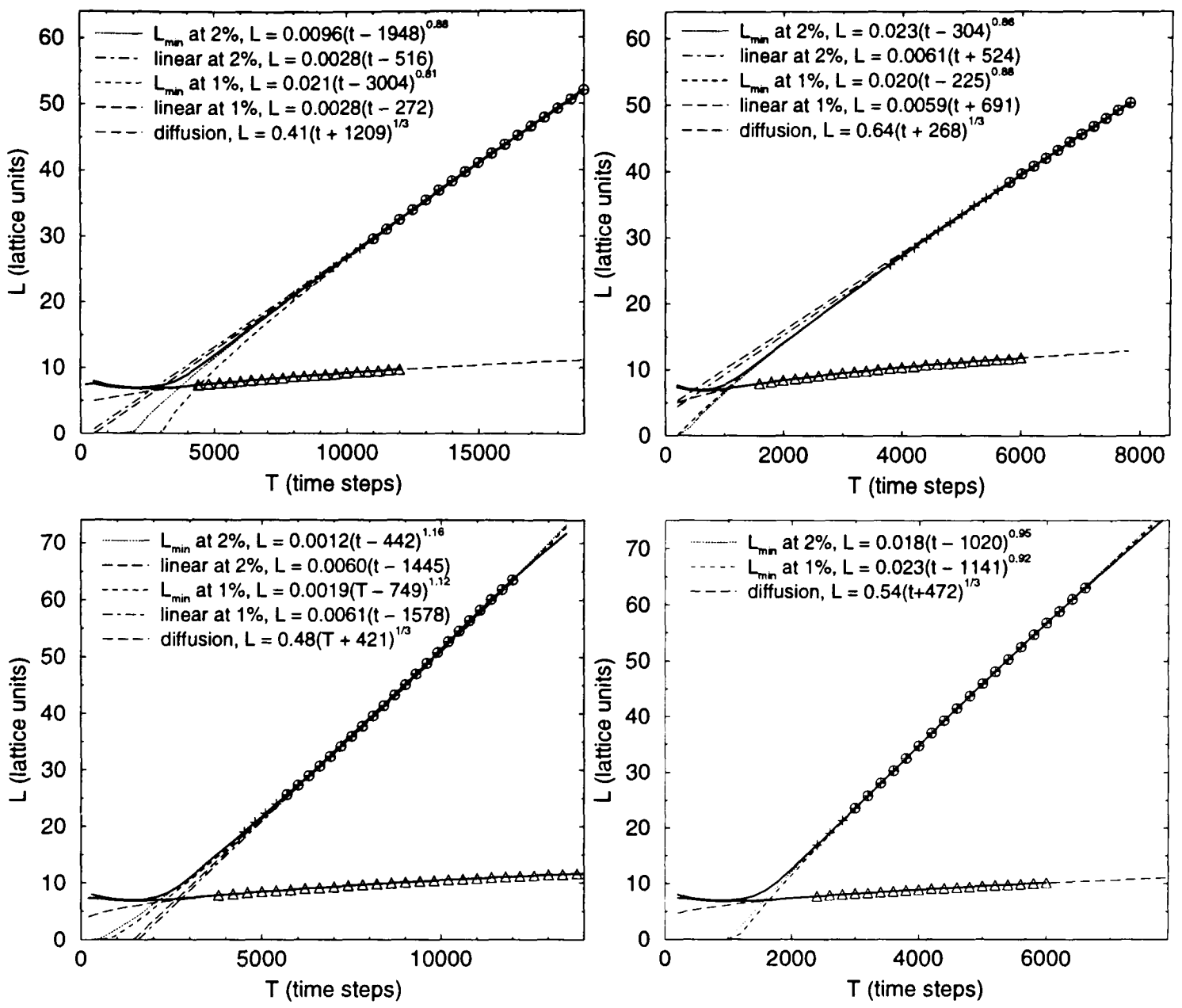

Figure 5.4: *Fitting $L(T)$ and $L_D(T)$. Upper left: Run028, $L_0 = 36$. Upper right: Run022, $L_0 = 5.9$. Lower left: Run033, $L_0 = 5.9$. Lower right: Run029, $L_0 = 0.95$. Solid lines indicate full set of recorded $L(T)$ data, + indicates data points used for fits with $L_{\min}$ set by 2% diffusion, ◯ indicates data points used for fits with $L_{\min}$ set by 1% diffusion, △ indicates data points used for fits to diffusion-only data. Table 5.3 summarises the main fit results.*

of interfacial tension, leading to anomalous dynamics. This problem is more acute for the low viscosity runs where hydrodynamic coarsening is fastest; larger mobilities are required for these.

5.4.2 Finite size effects

Having fixed the lower limit on the usable data by considering the effects of diffusion on the growth rate, the upper limit as the domain size becomes comparable to the system size must now be considered. For scaling growth to take place, each domain must be surrounded by domains of similar size and shape. When a domain's size reaches

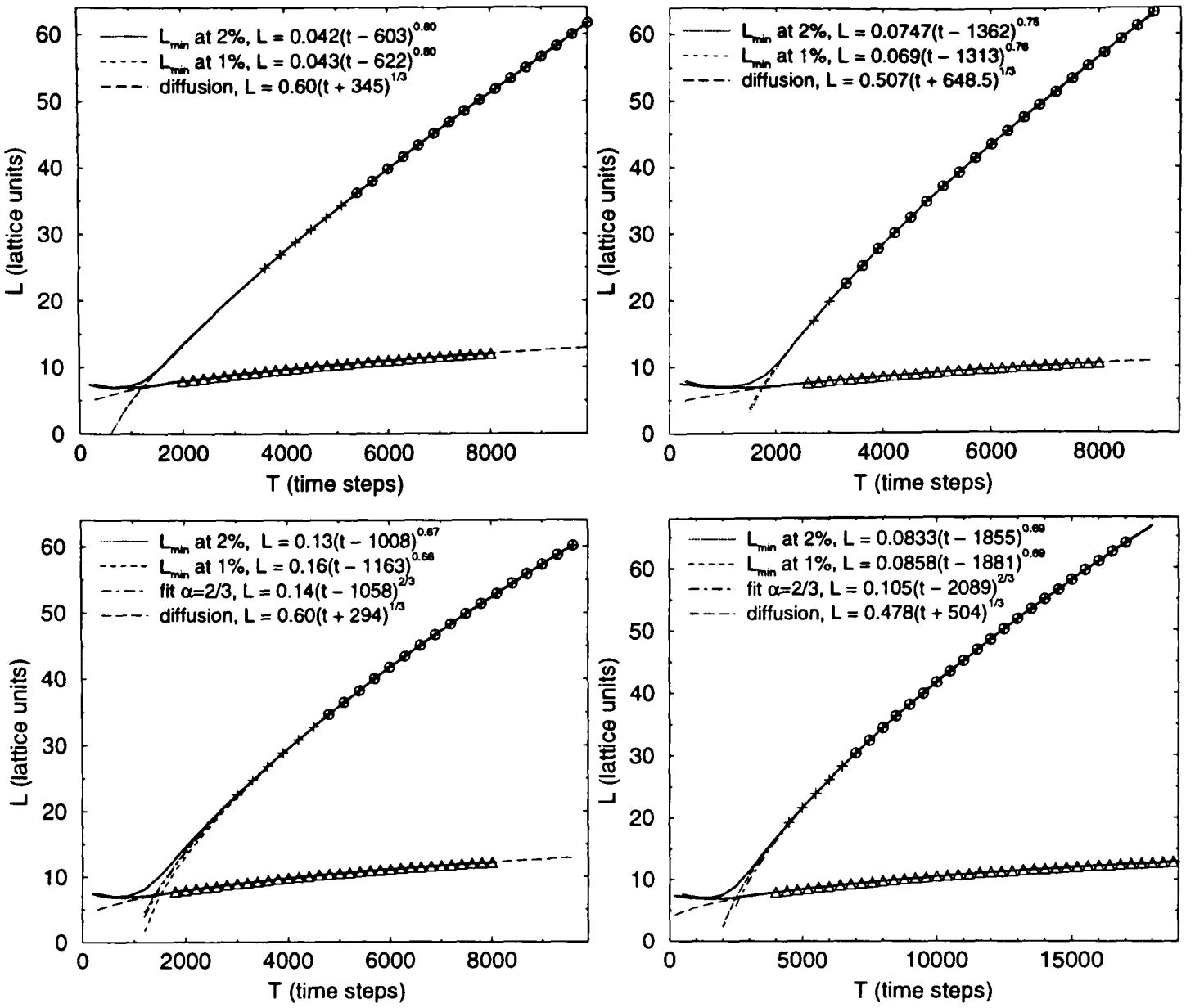

Figure 5.5: *Fitting $L(T)$ and $L_D(T)$. Upper left:Run020, $L_0 = 0.15$. Upper right: Run030, $L_0 = 0.01$. Lower left:Run019, $L_0 = 0.00095$. Lower right: Run032, $L_0 = 0.0003$. Solid lines indicate full set of recorded $L(T)$ data, + indicates data points used for fits with $L_{\min}$ set by 2% diffusion, ◯ indicates data points used for fits with $L_{\min}$ set by 1% diffusion, △ indicates data points used for fits to diffusion-only data. Table 5.3 summarises the main fit results.*

about one quarter of the system size, the domain structure is getting close to the point where the neighbouring domains on each side are actually the same domain, due to the periodic boundary conditions. This introduces extra constraints on the topology that can alter the growth rate.

In order to test for finite size effects more objectively, comparison was made between runs with the same parameters but different system size. Figure 5.6 shows comparison of $L(T)$ data between three pairs of runs from Tables 5.1 and 5.2. For the 128^3 system, the domain size reaches one quarter of the system size at $L(T) = 32$, and for the 256^3 systems, at $L(T) = 64$. The differences are small in the region $32 \lesssim L(T) \lesssim 64$, but

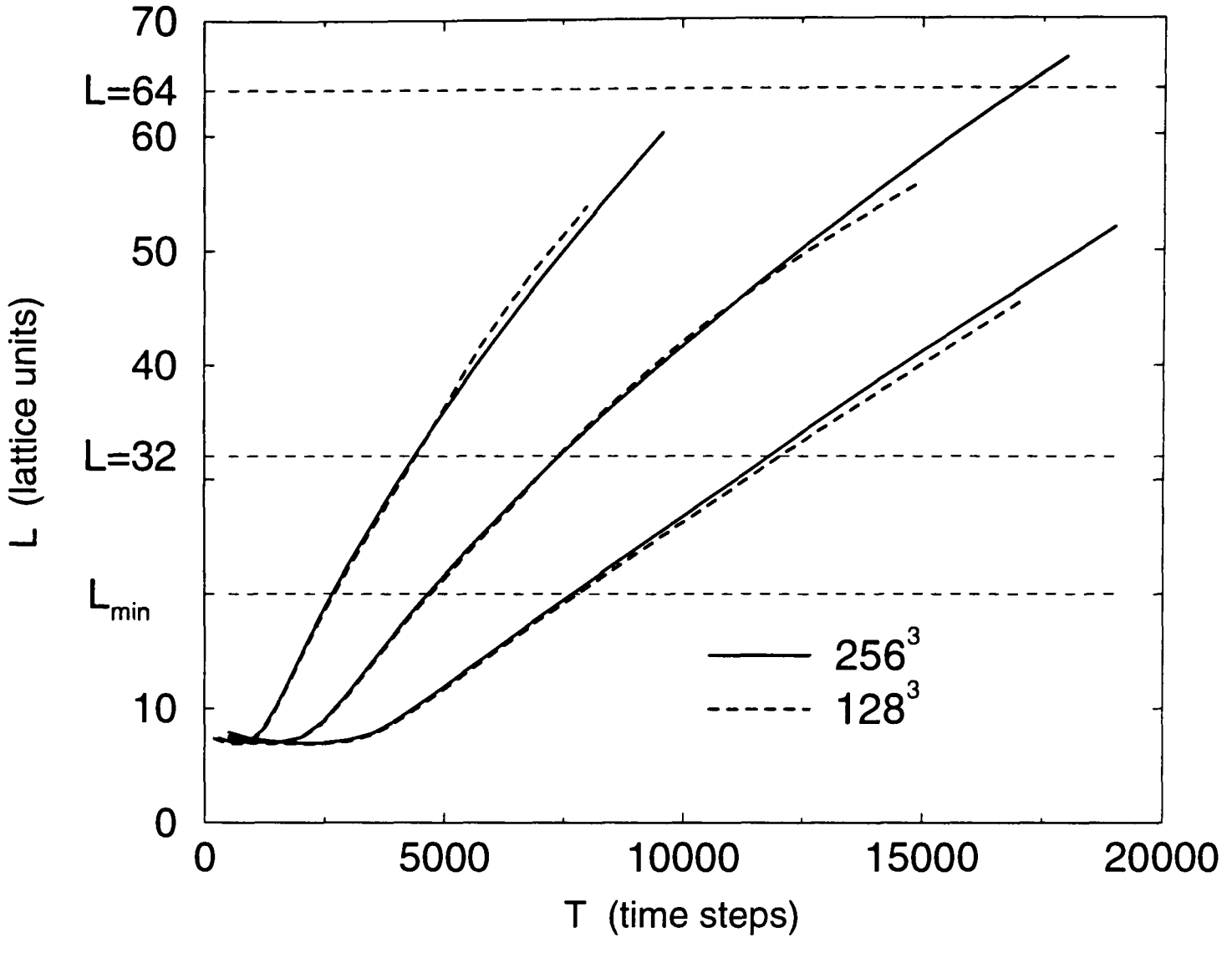

Figure 5.6: *Finite size effects in $L(T)$. Comparison between runs with the same parameters and system sizes of 256^3 and 128^3, (left to right) Run018 and Run020; Run031 and Run032; Run027 and Run028.*

unpredictable, and for the purposes of fitting a power law to the data, small statistical variations can make a relatively large difference to the fit obtained. To err on the side of caution, the upper cutoff, L_{max}, was therefore set to one quarter of the system size.

5.4.3 Fitting errors

From the results of the previous two sections, the range of usable $L(T)$ data has been determined to be around 5 lattice units for 96^3 runs, 12 lattice units for 128^3 runs and 40 lattice units for 256^3 runs. Clearly the range of usable data is much greater for the larger runs, and 96^3 runs were generally only used to test the parameters and their stability. Of greater importance to the fitting procedure is the relative change in $L(T)$ over the usable data, that is, the ratio of L_{max} to L_{min}, which is around 1.25 for 96^3 runs, 1.6 for 128^3 runs, and around 2.2 for 256^3 runs. It is difficult to get a reliable

estimate of the exponent in a free exponent fit of the type being applied to this data with less than about a factor of two between $L_{\mathbf{min}}$ and $L_{\mathbf{max}}$. Thus only the 256^3 data can provide reliable estimates of the growth exponent, α. Even these would not be reliable in isolation, but the combined data sets with the observed trend in α, as shown in Figure 5.3, appear convincing.

There are three separate parameters, v, T_{int} and α, determined from the free exponent fitting procedure, $L(T) = v(T - T_{\mathrm{int}})^{\alpha}$, described in the previous sections. The best fit values of these parameters are very dependent on each other; a small change in the value of α produces a large change in v, for example. The most straightforward way to get an estimate of the uncertainties from the fitting procedure is to hold α fixed at values close to the best fit value and see how a subsequent fit for the other two parameters changes them from the best fit values. Based on the results of such trial fits, the error estimation has been split into estimates for runs in the crossover and inertial regions, $\alpha < 0.85$, and estimates for runs in the linear region, $\alpha > 0.85$. Results of the trial fits are summarised in in Table 5.4.

Summarising from Table 5.4, the ranges of uncertainty in the values of the parameters

Runs with $\alpha < 0.85$ – crossover and inertial regions			
% change made in α	*produces change in v*	*produces % change in T_{int}*	
5%	1.4×	10%	(fit still looks OK)
10%	2×	20%	(fit visibly worse)
Runs with $\alpha > 0.85$ – linear region			
% change made in α	*produces change in v*	*produces % change in T_{int}*	
5%	1.6×	15%	
10%	2.5×	30%	
Linear fits on runs with $\alpha > 0.85$			
already have $\alpha = 1$	*% change made in v*	*produces change in T_{int}*	
	10%	2×	(fit visibly worse)

Table 5.4: *Error estimates from fitting α, v, and T_{int}.*

from the fitting procedure are therefore estimated to be,

- crossover and inertial region runs, ($\alpha < 0.85$):

  $\alpha \pm 5\%$ $\quad$ $v \pm 50\%$ $\quad$ $T_{\text{int}} \pm 10\%$

- linear region runs: $\alpha \pm 10\%$, but a linear fit is best fit taken overall, for which

  $v \pm 10\%$ $\quad$ T_{int} $+100\%$ -50% (factor of 2).

More has to be said about the runs in the linear region. Here, the claim is that the best fit is linear even when the free fit produces a value for the exponent, α, that deviates from linear by more than the estimated errors. The runs in the linear region have more fluctuations in the growth rate, i.e. the slope of $L(T)$ varies more, than the runs in the crossover and inertial regions. This is true of all the linear simulation runs carried out. Furthermore, the deviations are random; some push the fitted exponent higher than one, some lower, depending on where the fluctuations come in relation to the usable data region defined by L_{min} and L_{max}. The fact that the value obtained for α varies considerably when L_{min} is calculated from a 1% limit on diffusion instead of 2% adds support to this interpretation.

In the next chapter, when the fluid velocity field is analysed in detail, it will be seen that the length scale associated with the velocity (in the same way as $L(T)$ is obtained from the order parameter) becomes larger than the system size in the linear runs, see Section 6.2.2. The fluctuations can therefore be viewed as a finite size effect; the system is not large enough for them to be averaged out. One way round this is to do a number of runs with the same parameters but different random initial configurations and average the results. Unfortunately, the available computing resources did not permit this to be done for this study, but it should be noted in support of this interpretation that the free fit values of α for the three linear runs show deviations equally large either side of one, 0.88, 0.86, 1.16 respectively for the first three runs in Table 5.1. Additionally, the good agreement in the scaled values $b_1 = v/(L_0/T_0)$, of 0.073, 0.072 and 0.072 $\pm$0.015 further support the linear fits as the best. (The free fits give values of $b(\alpha) = vT_0^{\alpha}/L_0$ of 0.11, 0.15, 0.028 respectively.)

Next, other sources of uncertainty must be considered.

- Numerical errors from the simulation and analysis. The accuracy with which the simulation code solves the model equations is pretty good. Any errors are negligible compared to the uncertainty in the fitting process.

- The value of the interfacial tension, σ, obtained from the simulation parameters has an uncertainty of around 10%, see Section 3.6.3. There is an additional source of uncertainty in σ of around 5%, due to local equilibrium not always being maintained perfectly, see the end of Section 5.5.2. This makes a total uncertainty in the value of σ of around 12%. This affects the scaling length and time, L_0 and T_0, making their values uncertain by 12% for L_0, and 25% for T_0 (which depends on σ^2).

- The viscosity, η, is simply input to the simulation, and tests in sheared systems measure the input value of η to within a few percent. The density is also an input parameter, whose global average certainly doesn't vary (particle number is conserved), and local density values stay wthin a few percent of the global average. Errors from these two parameters are negligible compared to the errors from the interfacial tension and fitting procedure.

- Residual diffusion has been limited below 2% at the start of the usable data region by the choice of L_{min}. Since diffusive growth drops rapidly with increasing domain size, residual diffusive growth is far lower than 2% for most of the usable data region and is thus negligible in comparison with the other sources of error.

The simulation errors thus do not contribute any extra uncertainty to the value of the growth exponent, α. They do, however, contribute to the errors in the scaling plot, Figure 5.3, via the uncertainty in the values of L_0 and T_0, combined with the uncertainty in the value of T_{int}, the only fitting parameter used to produce the scaling plot. For the crossover and inertial region runs, the combined errors are about twice the width of the symbols used on Figure 5.3, while for the linear region, the larger errors in T_{int}, increase the horizontal error bars to about the same spread as the dashed lines showing the free exponent fits to Run033 and Run022. When v is scaled by L_0/T_0 to obtain b_1 for the linear runs, the combined error is $\pm$ 22%, or ± 0.015, as already quoted.

This completes the estimation of the numerical errors in the results presented in this chapter. The next section considers the role of the different length scales in the simulation and how they contribute to the accuracy and interpretation of the results.

5.5 Length scales

This section considers in more detail the length scales significant to the dynamics of the simulation, and the various different possible length measures for the domain size. As well as the macroscopic length scale defined by the domain size, and the overall system size, there is also a microscopic length scale of the order of the interface width. By restricting the usable data region to below one quarter of the system size it is expected that the system size is irrelevant to the dynamics. The fact that runs with different system size show good agreement supports this assertion (see Section 5.4.2). However, the microscopic length scale is the length scale over which diffusion is significant. The importance of this length scale to the system dynamics is discussed in Section 5.5.1.

Two other length scales are important to the fluid velocity; the Taylor microscale and the dissipation scale. These will be discussed in more detail in the next chapter. Both length scales are important for energy dissipation, in particular, the dissipation scale must be fully resolved on the lattice in order to ensure that dissipation is modeled correctly.

The main length scale of interest in this chapter is the domain size. So far, only one method of characterising the domain size has been considered; that derived from the first moment of the structure factor, $L(T)$. One important reason for considering alternatives to this length measure, is illustrated by the results of a similar study of 2-D symmetric spinodal decomposition by Wagner and Yeomans (1998). A simple scaling growth law was predicted for 2-D, see Bray (1994), with an exponent of $\alpha = 2/3$ in the viscous regime, as well as the inertial regime, but the simulation results of Wagner and Yeomans show that the growth doesn't really scale at all. The appearance of smaller droplets of the opposite phase trapped within the main percolating regions, and within those droplets yet smaller droplets, sets up a hierarchy of relevant length scales and slows the growth rate from the predicted $T^{2/3}$. The main tool used by Wagner and

Yeomans to analyse this behaviour was different length measures that were sensitive to different aspects of the coarsening process. (For a brief illustration of 2-D spinodal behaviour, see Section 7.5.)

Two other length measures are thus compared in Section 5.5.2. The most important lesson from this excercise in 3-D turns out not to be about different growth rates, but about the diffusion rate within the simulation. Finally, using a fourth, particularly simple length measure, the three main length measures are related to the physical pattern of the interface in Section 5.5.3.

5.5.1 Microscopic length scale

The smallest length scale that can be simulated on a discrete lattice is, of course, the lattice spacing. Even in a mesoscopic simulation method such as LB, in which there are no microscopic particles, and the simulation simply solves continuum model equations based on the model free energy, Equation (3.28), the small scale structures and processes on the scale of the lattice spacing are still important.

First, and most obvious, the interface width cannot be smaller than the lattice spacing. Actually, in this work, the main variation in $\nabla\phi$ extends over about 3 lattice spacings in order to model the varying concentration gradients over the interface at least to first order. The most basic problem with modelling a narrow interface on a Cartesian lattice is isotropy. This was discussed in Section 3.6.2, where it was shown that, while the interface doesn't behave in exactly the same way no matter where it is located and oriented with respect to the lattice, the differences are small.

There are, however, some further consequences of simulating a huge range of length scales with a simulation method in which the interface width, ξ, stays constant in *lattice* units, and thus varies dramatically when considered in scaled units, i.e. $\xi/L_0 \simeq 3/L_0$. Since $36 \geq L_0 \geq 0.0003$ over the simulation runs, the scaled interface width varies by a factor of 10^5. If the entire range of the scaled results on Figure 5.3 were being simulated in a single run, or measured experimentally on the same fluid mixture, the interface width would stay constant in *scaled* units.

Furthermore, consider the actual values of ξ/L_0. From 0.1 in the linear regime, it grows to 10^4 for the most inertial run. Real fluids have values of ξ/L_0 from around 0.05 (water) to 10^{-7} (glycerol); there are no real fluids with $\xi/L_0 \gg 1$. In the inertial regime where the simulation has $\xi/L_0 \gg 1$, the interface is "unnaturally thick": simulation runs that enter the inertial regime do so directly from their initial diffusive stage without an intervening viscous regime. However, this should not make any difference to the scaling results if the domain size scales onto a universal curve, as the LB results suggest (though the results of Jury et al. (1999) described in Section 5.6.4 call this into question).

The physical process associated with the smallest length scales, ξ, is diffusion. As has already been mentioned in Sections 5.3.3, and 5.4.1, setting the diffusion rate correctly is crucial to the success of the simulation. While diffusive growth needs to be suppressed over macroscopic length scales, it still plays an important role throughout the coarsening process. Whenever a fluid neck breaks, (an intrinsic part of the coarsening dynamics in which the topological connectivity of the interface is reduced), the neck first stretches becoming thinner and thinner until it has a radius only of the order of ξ. At this length scale, diffusion takes over to complete the process of breaking and reconnection as two parallel interfaces. A sequence of images showing a neck breaking can be found in Appendix A. Diffusion over the scale of ξ must take place rapidly in relation to the overall growth rate to ensure that the interface remains essentially in local equilibrium.

Diffusion clearly limits the accessible range of L/L_0 and T/T_0 at the lower end, where viscosity is so high that the timescales required to reach domain sizes where diffusion is negligible are beyond reasonable simulation resources. Less obviously, diffusion also limits the accessible range of L/L_0 and T/T_0 at the upper end, where, if L/L_0 and T/T_0 are too large (low viscosity, $\xi/L_0 \gg 1$); in order to achieve rapid topological reconnection of the "unnaturally thick" interfaces, the diffusion rate needs to be so high that it directly contributes to domain growth at macroscopic length scales.

5.5.2 Different structural length measures

The method used to calculate $L(T)$, Equation (2.5), the average domain size, is based on the structure factor for the order parameter, ϕ. This method was used because it is standard – enabling easy meaningful comparisons with other work, both simulational

and experimental – and because it turns out to be the most consistent and reliable method when compared with other possible choices.

Equivalent to the first moment of the structure factor, up to a numerical constant, is the alternative used by Laradji et al. (1996) and Appert et al. (1995), $L_C(T)$, the first minimum of the radial distribution function, $C(r)$. Since $C(r)$ is defined as the inverse Fourier transform of the structure factor, and since multiplication by ik in Fourier space is the equivalent of differentiation in real space, it is not difficult to see that these two length measures are essentially constructed from the same information about the domain size. Both Appert et al. (1995) and Jury et al. (1999) compared $L_C(T)$ with $L(T)$ and found them to be related by a constant scale factor, so $L_C(T)$ will not be considered further here.

In this section two further methods for characterising the typical length scale in the system will be compared with $L(T)$ and with each other. These comparisons also provide insight into some of the subtleties of the simulation and the dynamics of the system. A fourth, very simple length scale, the mean distance between interfaces, is considered separately in Section 5.5.3 in order to characterise what $L(T)$ actually corresponds to in real space.

The three length measures being compared here are:

- $L(T)$, the first moment of the circularly averaged structure factor, Equation (5.3), as used in the main analysis;
- $L_{\nabla\phi}$, a length based on the mean curvature, calculated from gradients in the order parameter field, Equation (3.35);
- L_ϕ, a length based on the volume of interface in the system, Equation (3.38).

Coarse-graining from 256^3 down to 128^3 data does not affect the values subsequently calculated for $L(T)$ but does have an effect on $L_{\nabla\phi}$ and L_ϕ. Therefore, data without coarse-graining from the 128^3 runs in Table 5.2 has been used for the comparisons.

Figure 5.7 (left) shows each length measure for Run026. There is good agreement between $L(T)$ and L_ϕ, while $L_{\nabla\phi}$ grows with the same exponent but slightly differ-

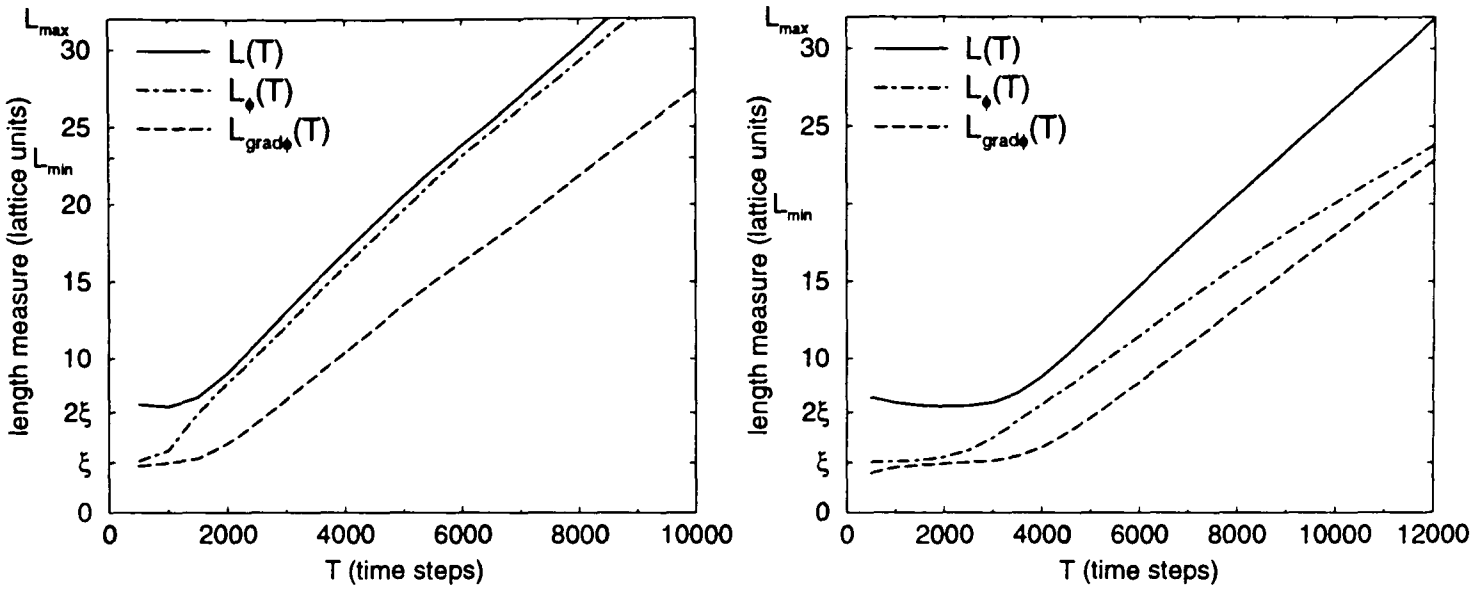

Figure 5.7: *Length measures. Left: Run026,* $L_0 = 36$, $M = 0.25$. *Right: Run027,* $L_0 = 36$, $M = 0.1$.

ent prefactor and intercept. So, unlike in 2-D (see Section 7.5), the three different length measures give basically the same answer as each other up to constant prefactors, confirming that the scaling growth law is a good approximation to the actual system dynamics in 3-D systems.

Now consider Figure 5.7 (right), the same length measures for Run027. The only difference between Run026 and Run027 is the mobility, i.e. the diffusion rate. For Run027, which has a lower mobility of $M = 0.1$ compared to $M = 0.25$ for Run026, the L_ϕ length measure grows more slowly than $L(T)$, with a growth exponent $\alpha' < 1$. Essentially, L_ϕ is a measure based on how much interface there is in the system. It assumes that the only departure from complete separation, $\phi = \pm 1$, is at the interfaces, and that the interfaces are properly in local equilibrium. The explanation for the lower values of L_ϕ compared to $L(T)$ is thus that the diffusion has been set slightly too low to keep the interface fully equilibriated.

It is therefore necessary to consider what errors this introduces into the main results from the 256^3 runs, some of which have low mobility values for which L_ϕ does not grow as fast as $L(T)$. If the interface is not properly equilibriated, the value of the interfacial tension will be less than the equilibrium value. The interfacial tension is used to calculate the values of L_0 and T_0 used to scale the results. It is difficult to estimate the effect on the interfacial tension directly, but first note that in the usable data region, between L_{min} and L_{max}, a difference of around 20% between $L(T)$ and L_ϕ corresponds to a difference of less than 2.5% in the value of ϕ_{rms}, because

of the reciprocal relationship between them. Studies in which the interfacial tension was measured (at equilibrium) for partially separated systems ($|\phi| < 1$) suggest that this means around a 5% error in interfacial tension. There is already a spread in the measured values of σ used to calculate L_0 of around 10% so it isn't as big an effect as the difference in length measures might suggest. This analysis does confirm that the simulation parameters have been pushed to their limits in all directions to achieve the results presented here.

5.5.3 Interpreting the length scales

The first moment of the structure factor, $L(T)$, certainly corresponds to the size of the domains in some consistent way, but, faced with a picture of the interlocking sponge structure of the domains, see Appendix A, it isn't clear what $L(T)$ actually corresponds to in real space. In order to find out, a simpler length measure is required that can be easily visualised and computed.

Consider the mean distance between interfaces, $L_{\mathbf{gap}}$, as the system is traversed in a straight line in any direction. This can be assessed roughly by eye looking at a cross-section of the system, and computed as a system average just by stepping along a lattice direction and noting how often an interface is crossed.

Using the order parameter data from a selection of runs in Table 5.1, each grid line in the x-direction was examined to find the distance between successive interfaces, and a system average computed to find $L_{\mathbf{gap}}$. Figure 5.8 shows $L_{\mathbf{gap}}$ for three runs compared to $L(T)$. It turns out that $L_{\mathbf{gap}} \simeq L(T)/1.27$ for all runs, independent of α, so clearly $L_{\mathbf{gap}}(T)$ is also a consistent length measure, since there is only a constant factor relating it to $L(T)$.

The first moment of the structure factor has thus been related to the morphology of the interface via another length measure, $L_{\mathbf{gap}}$, that has the virtue of being simple to estimate by eye from visualisations of the interface.

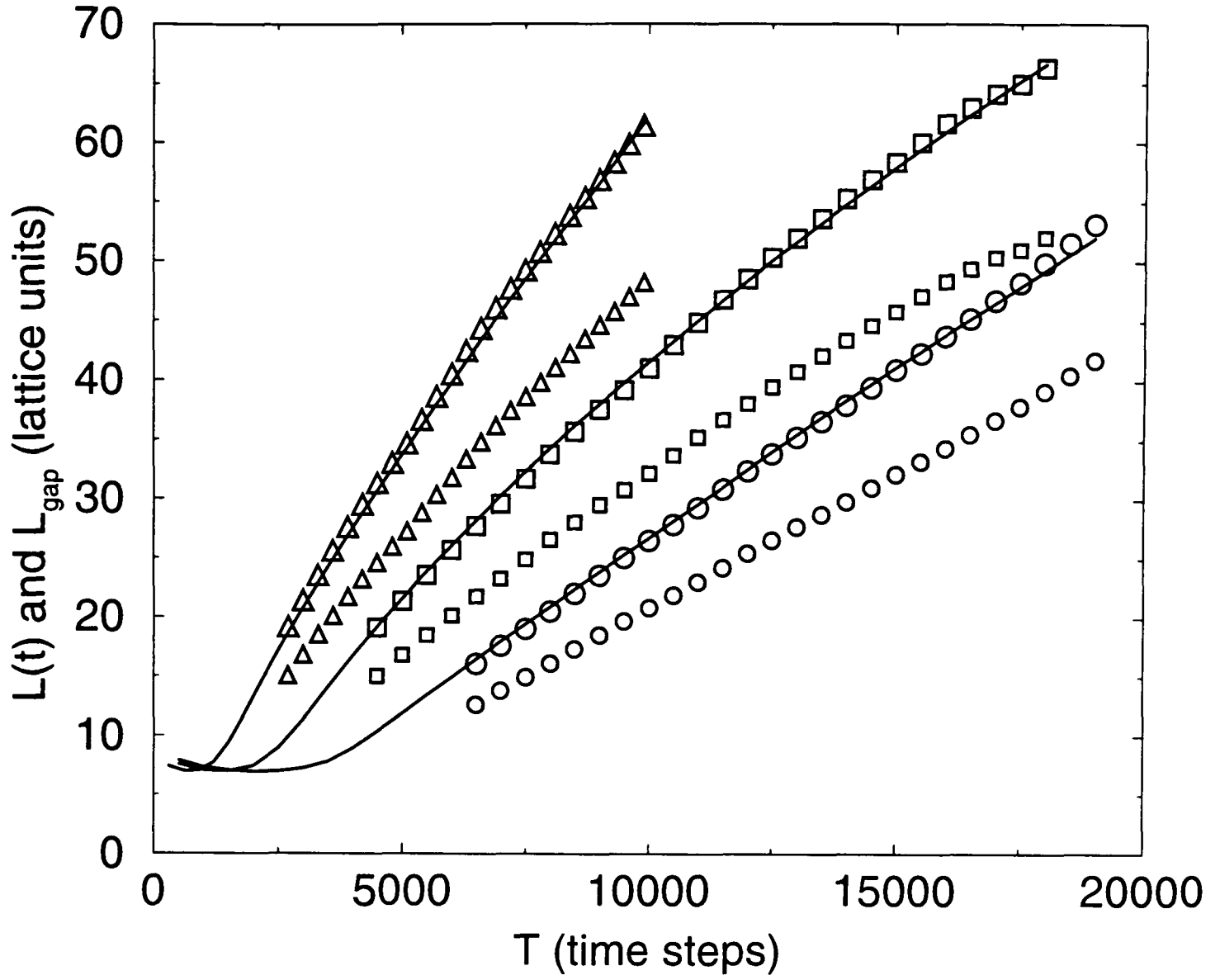

Figure 5.8: *Mean distance between interfaces evaluated along the x-direction of lattice (small symbols) and scaled by 1.27 (large symbols) to show it matches L(T) (lines). Run028 is circles, Run032 is squares and Run020 is triangles.*

5.6 Comparisons with other work

In order to compare these results with other published work, a similar scaling procedure must be applied to place the data onto the universal scaling plot in Figure 5.3. This is only possible if the work is reported in sufficient detail to enable values for L_0 and T_0 to be calculated. Recent 3-D work where comparison is possible includes that of Bastea and Lebowitz (1997), Laradji et al. (1996), Appert et al. (1995), and Jury et al. (1999). These four sets of results are shown along with the LB data in Figure 5.9. Simulations of 3-D spinodal decomposition with hydrodynamics for which quantitative comparisons were not possible include, Koga and Kawasaki (1991), Puri and Dünweg (1992), and Alexander et al. (1993), all of whom claimed to have simulated the linear regime; Shinozaki and Oono (1991), Ma et al. (1992), Lookman et al. (1996). The last

two claimed to have simulated the inertial regime but offered no evidence beyond their fitted exponent values for definitely having inertial rather than diffusive effects.

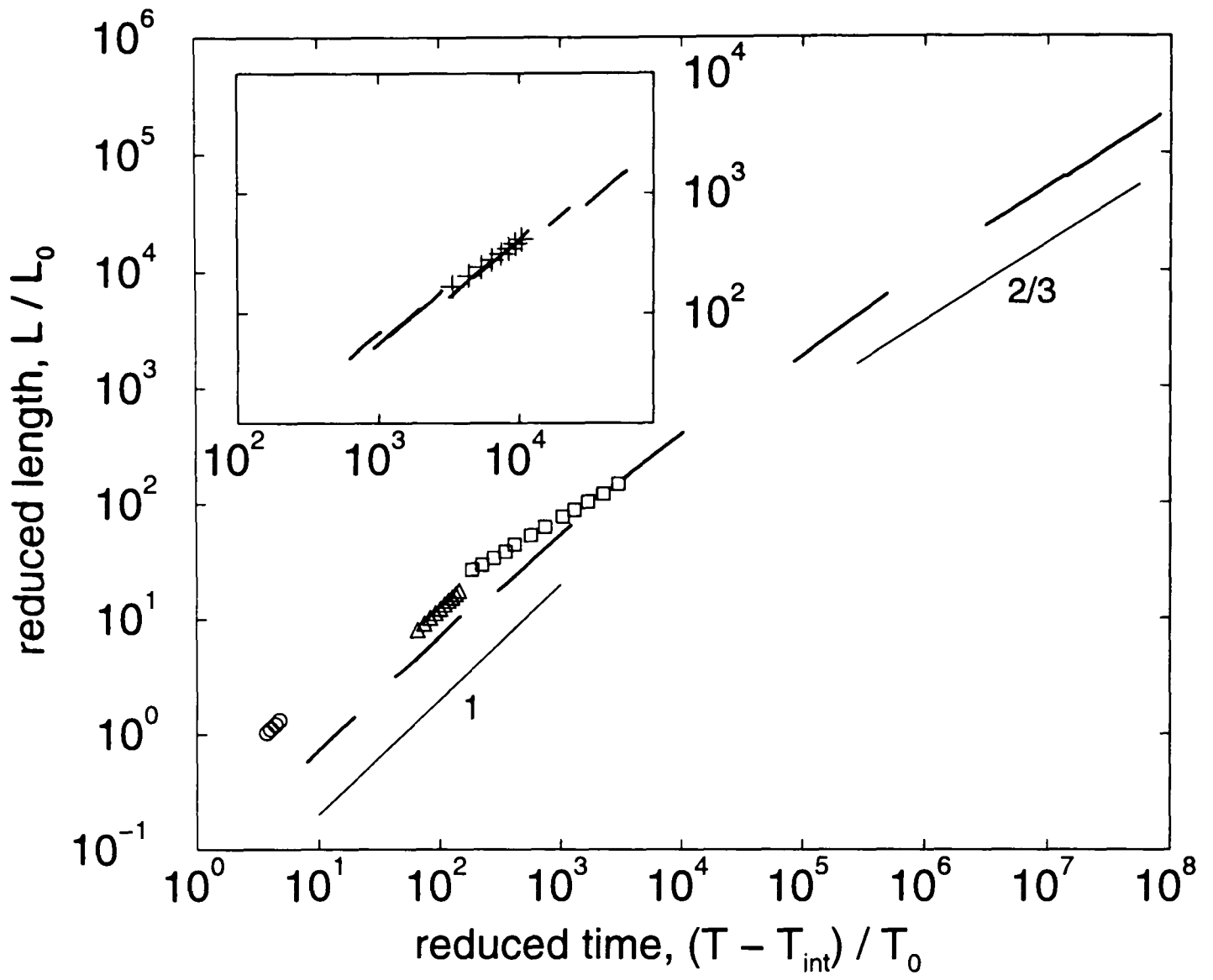

Figure 5.9: *Scaling plot in reduced variables (L/L_0, T/T_0) Bold lines (left to right) are LB 256^3 data from Table 5.1 (top to bottom). Also shown are results from other published work: squares Appert et al. (1995), triangles Laradji et al. (1996), circles Bastea and Lebowitz (1997), Inset: DPD data of Jury et al. (1999) (solid lines) with one LB data set ($L_0 = 0.15$, pluses) repeated for comparison.*

The four studies for which detailed numerical comparisons are possible will now be considered in turn.

5.6.1 Bastea and Lebowitz (1997)

Bastea and Lebowitz (1997) carried out a 3-D simulation containing about 1.4×10^6 particles whose motion was described mesoscopically by Boltzmann-Vlasov equations. They combined direct simulation Monte Carlo methods for the short range interaction with particle-in-cell methods for long range interactions. The fluid system is relatively

low-density; they describe it as a gas-gas phase separation. The necessary fitting and scaling for the results reported by Bastea and Lebowitz was done by Jury et al. (1999).

Bastea and Lebowitz calculated their length, $L_C(T)$, as the first zero of the spherically averaged pair correlation function, $C(r)$, see Section 5.5.2, which they obtained by applying an inverse Fourier transform to the structure function, $S(\mathrm{k}) = \phi(\mathrm{k})\phi(-\mathrm{k})$. Jury et al. converted this to $L(T)$ by using a constant scale factor deduced from a similar analysis on their own data. Bastea and Lebowitz present a set of curves for $L_C(T)$ fitted to $T^{1/3}$ in the lower region and a linear fit to the upper region, which, while it has clearly diverged from $T^{1/3}$, is by no means obviously straight. Their original graph is reproduced in Figure 5.10.

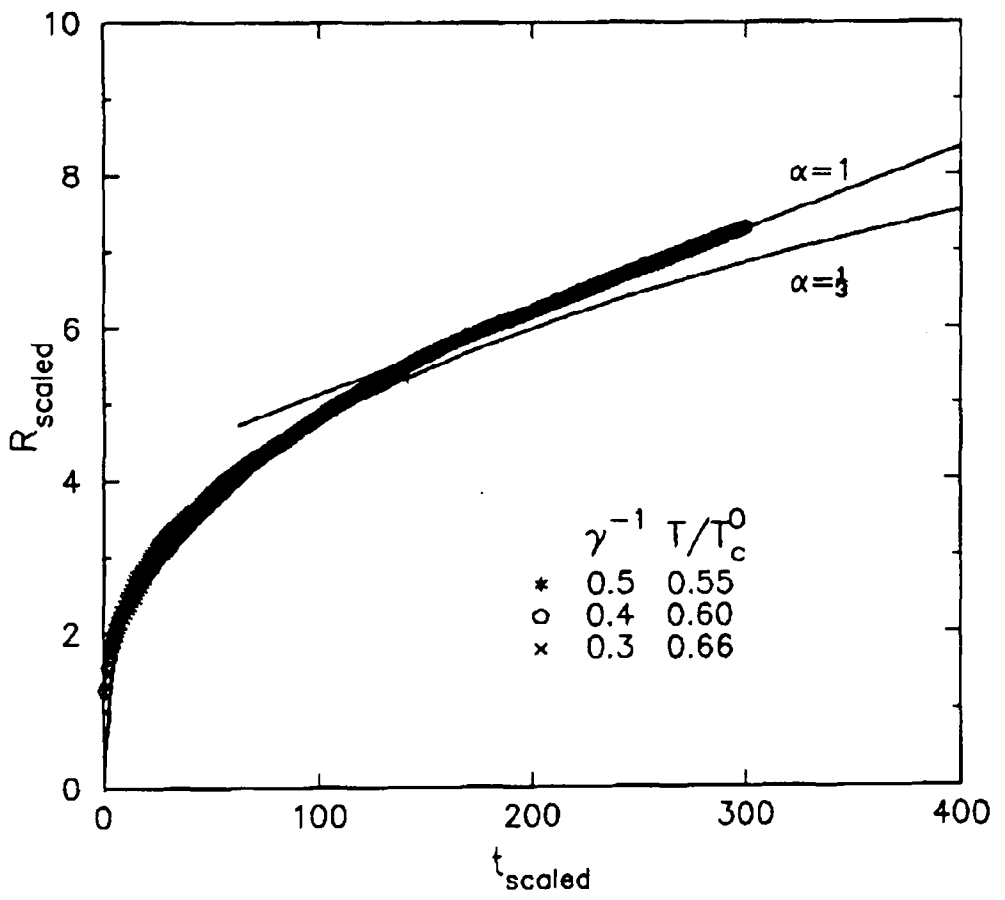

Figure 5.10: *Bastea and Lebowitz (1997) original results for $L_C(T)$ with fits. Scanned from their paper.*

On the universal scaling plot, Figure 5.9, the upper, supposedly linear region of the data from Bastea and Lebowitz is shown as circles. It lies in the lower left region of the graph, where the LB analysis finds linear behaviour, but well to the left of any of the LB results. The values of $L_0 = 58$ and $T_0 = 720$ worked out from their simulation parameters, combined with their measured L, T in simulation units in the range of $L \sim 10$ and $T \sim 250$, suggest that their data should, as observed, lie slightly further

into the linear region than the lowest LB run, Run028, which has $L_0 = 36$. The scaled value of the fit parameter, $b_1 = v/(L_0/T_0)$, from the refitting by Jury et al. is $b_1 = 0.3$. This compares with the considerably smaller values from the LB results of 0.073, 0.073, 0.072 $\pm$0.015, for the three LB runs in the linear region. The dynamical scaling hypothesis, as explained in Section 2.3.1, requires that the scaled value of the fit parameter, b_1, should be a universal constant in the linear regime.

In order to explain the discrepancy between the results of Bastea and Lebowitz and the LB results, first note that, as explained in Section 5.4.1, for the LB results special care was taken to ensure that the diffusive contribution to coarsening was small, by explicitly calculating it and only taking data where it was less than 2% of the total growth rate. Bastea and Lebowitz do not report the diffusion rate in their system in a form that can be used to apply the analysis of Section 5.4.1, but test LB runs have been done with high diffusion rates that produce LB data sets similar to those of Bastea and Lebowitz. Two such test runs, Run024 and Run010, are shown in Figure 5.11. On the left, Run024 is compared with Run028, one of the runs used in the final

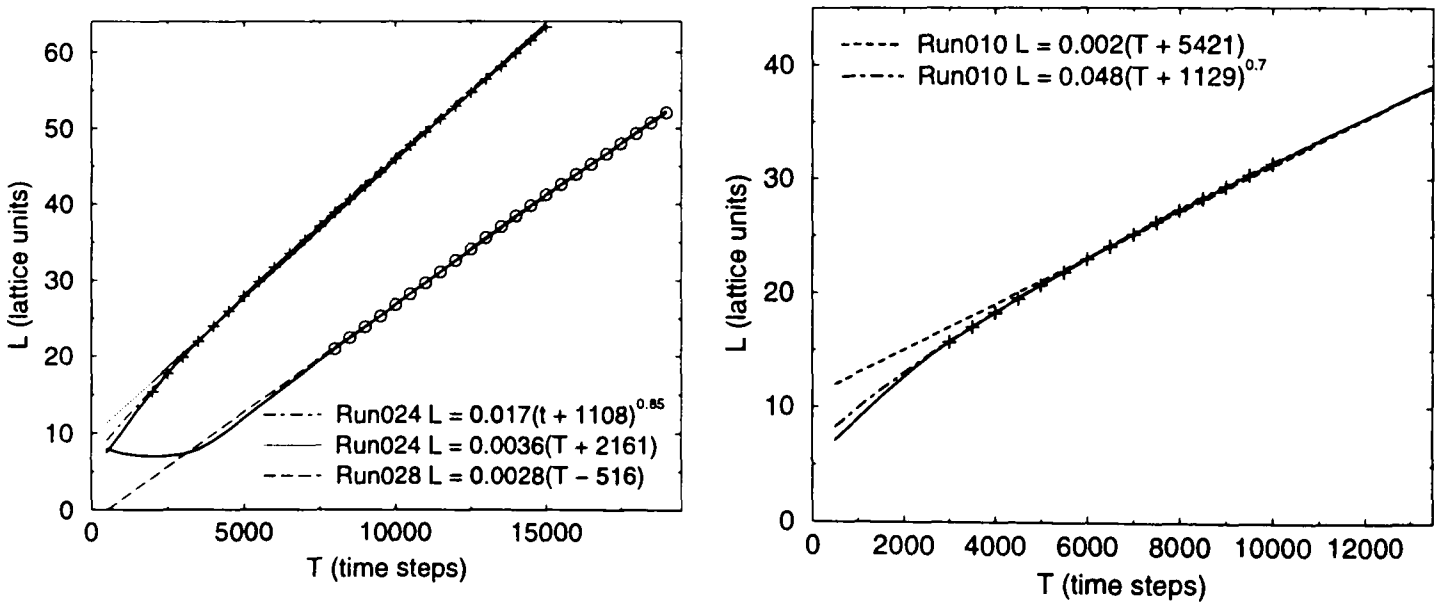

Figure 5.11: *Left:* 256^3, $L_0 = 36$, *Run024 with* $M = 0.8$ *compared with Run028* ($M = 0.1$). *Right: Run010,* 128^3, $L_0 = 381$, $M = 0.5$.

data analysis. Run024 has the same parameters as Run028 except for the mobility, which is eight times the mobility of Run028. Run024 fits a free exponent of $\alpha = 0.85$, which is similar to Run022 (also in the linear region). However, the lack of an initial flat diffusive region strongly suggests the diffusion is too strong for clear linear growth to be observed within the size of the simulation lattice. A linear fit to the upper part of the data produces a scaled value of $b_1 = 0.082$, compared with 0.073 for Run028.

On the right, Run010 has a value of $L_0 = 381$, larger than for any of the runs finally used, see Table 5.2. This should put it even further into the linear region than the rest of the runs. However, a fit with a free exponent produces $\alpha = 0.7$. A linear fit to the upper part of the data produces a value for the scaled fit parameter of $b_1 = 0.32$, i.e. about the same as the data from Bastea and Lebowitz. By comparison with these results from LB runs with high diffusion, it seems likely, therefore, that the data from Bastea and Lebowitz (1997) has strong residual diffusion, and the results they present are a mixture of linear and diffusive growth. Thus they have, as they claim, simulated the linear regime, but they have not been able to run a long enough or large enough simulation to produce linear growth clear of any diffusive contribution. Hence they obtain larger values of b_1.

5.6.2 Laradji, Toxvaerd, and Mouritsen (1996)

Laradji et al. (1996) used a large-scale molecular dynamics simulation of a Lennard-Jones model with 343000 particles. They describe their simulated system as a concentrated fluid, and avoided very deep quenches to stay out of the solid-gas coexistance regime. They calculated both the correlation function, $C(\mathbf{r})$ and the structure factor, $S(\mathbf{k})$, spherically averaged both and obtained lengths from both via the first zero, $L_C(T)$ and first moment, $L(T)$, respectively. Their comparison between their results for $L_C(T)$ and $L(T)$ confirms that the assumption of a simple constant scale between the two length measures made by Jury et al. to scale the data of Bastea and Lebowitz (1997) is reasonable.

The necessary fitting and scaling for the data of Laradji et al. was also done by Jury et al. (1999). The results are shown on Figure 5.9 as triangles lying, like those of Bastea and Lebowitz (1997), to the left of the LB data towards the lower left corner, again in the region found to be linear in the LB analysis, with $L_0 = 1.8$ and $T_0 = 1.64$[3] correctly indicating the expected position as below Run029 (which has $L_0 = 0.95$). Laradji et al. claimed their results confirmed the linear scaling, but they too have a rather different

[3] Since L_0 and T_0 are in simulation units, strictly speaking they can't be compared between different simulations. However, since most simulations tend to use values of L of the order of $10 < L < 100$ and values of T of between $10 < T < 10000$, in practice, comparing L_0 directly works rather well. All quantitative comparisons have, nonetheless, been done with properly non-dimensionalised scaled quantities.

value of the scaled fit parameter $b_1 = 0.13$. This is again larger than the values of b_1 found for the main LB data of 0.073, being instead in the range of the values found for the over-diffusive LB runs shown in Figure 5.11 of 0.082 and 0.32. It seems likely, therefore, that their results also include strong residual diffusion. The shape of their

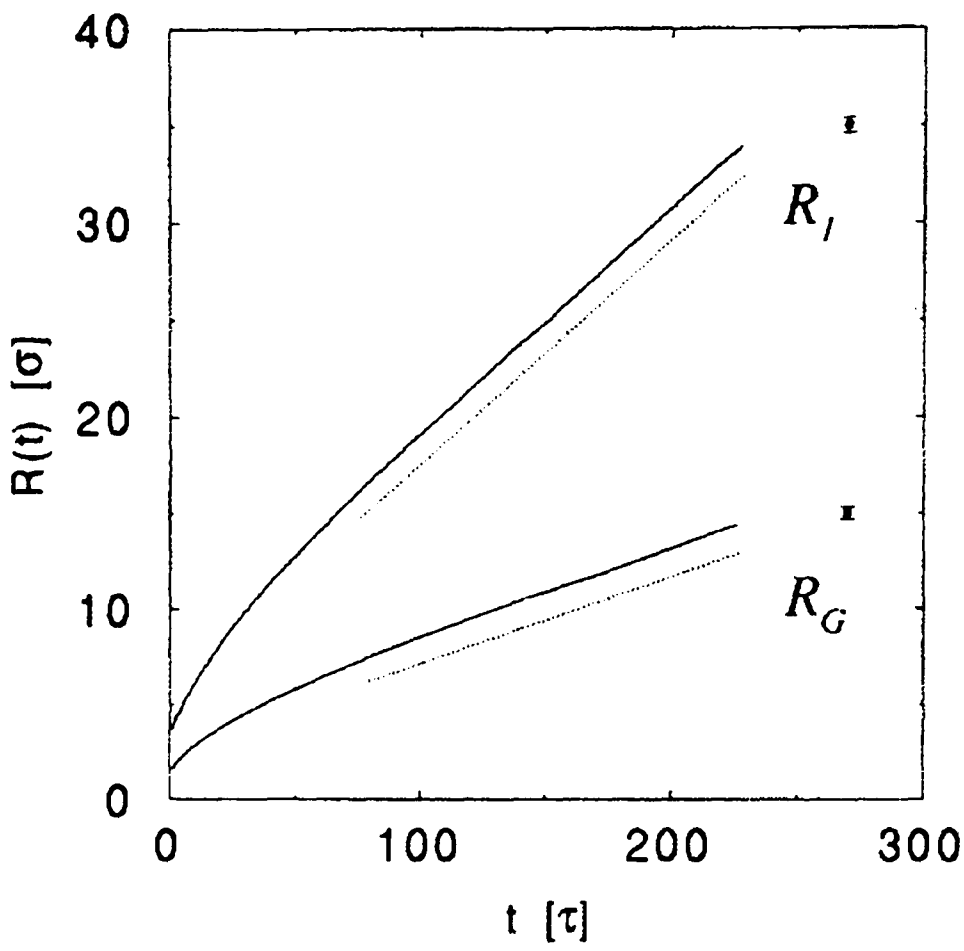

Figure 5.12: *Laradji et al. (1996) original results for $L_C(T)$ and $L(T)$, labeled R_g and R_l respectively. The two dots indicate typical size of error bars, and the two dotted lines are straight lines. Scanned from their paper.*

$L(T)$ and $L_C(T)$ curves, reproduced in Figure 5.12, matches that of Run024 in Figure 5.11 (left), i.e. there is no initial diffusive plateau before domain growth begins. In LB data this was always a sign that the run had too high a mobility and significant diffusive growth throughout.

5.6.3 Appert, Olson, Rothman, and Zaleski (1995)

Appert et al. (1995) used a 3-D lattice gas simulation to simulate spinodal decomposition. They use the first moment of the spherically averaged structure factor, $L(T)$, as their length measure for domain size. Their largest system size was 128^3 and they

also used 64^3 to test for finite size effects, which they observed for $L(T)$ greater than half the system size. This is in contrast to the LB data runs in which finite size effects were evident from one quarter of the system size, see Section 5.4. They claimed a fitted exponent of $\alpha \simeq 2/3$, which, if correct, would put their results in the inertial regime. The value of $L_0 = 0.33$ deduced from the values of density, viscosity and interfacial tension given in their paper suggests that their results should instead lie in the crossover region. Taking the section of data over which they claim to fit $T^{2/3}$, refitting it (giving an exponent, $\alpha = 0.62$), scaling it and plotting it on Figure 5.9 (squares), shows that it does indeed lie in the crossover region of the LB scaling plot, asymptoting to the LB data from above. This suggests that their fitted exponent is again too low because of diffusion.

There is no convenient way to compare values of the other fit parameters like v, because they are highly dependent on the value of the exponent, α. The shape of their $L(T)$ plot is, however, again lacking the initial diffusive plateau and so consistent with the diffusion being large enough to contribute significantly to the domain growth and thus pull the overall growth exponent to a lower value.

5.6.4 Jury, Bladon, Krishna, and Cates (1999)

Jury et al. (1999) carried out a series of simulations of a symmetric, binary fluid mixture using the DPD method. Their system contained 10^6 particles moving under the DPD algorithm, which combines soft interparticle repulsions with pairwise damping of interparticle velocities and pairwise random forces. They simulated a deep quench in a relatively dense system. As DPD only simulates liquids, no transitions to gas or solid phases are expected.

These authors found that each data set was well fitted by a linear scaling, $L = v(T - T_{\mathrm{int}})$, but with a systematic increase of $b_1 = v/(L_0/T_0)$ upon moving from upper right to lower left in the universal scaling plot, see Figure 5.9 (inset). These seven data sets have a range of L_0 values, $0.29 \leq L_0 \leq 0.013$, which places them all firmly in the crossover region found in the LB results, between Run029 ($L_0 = 0.95$) and Run030 ($L_0 = 0.01$).

Jury et al. suggested two alternative interpretations of the combination of their own data and that of Laradji et al. (1996) and Bastea and Lebowitz (1997), to explain the observed linear scaling within each run, but lack of consistency in the prefactor, b_1.

- A possible nonuniversality of the physics of topological reconnection of domains (fluid necks breaking) upsetting the scaling. Wagner and Yeomans (1998) report non-scaling behaviour for different topological reasons in their studies of spinodal decomposition in 2-D, (see also Section 7.5).

- All data sets being part of an extremely broad crossover region, $1 \lesssim T/T_0 \lesssim 10^4$ between the viscous and inertial regimes, corresponding to an effective power law $L \sim (T - T_{\text{int}})^{0.8}$. This explains the observed trend $b_1 \sim t^{-0.2}$, but doesn't explain the linear scaling within each run.

The LB results support the idea of a broad crossover region, but instead place it at $10^2 \lesssim T/T_0 \lesssim 10^6$. As discussed in the previous sections, a different explanation, based on excess diffusion, has been suggested for the discrepancies between LB and the data sets of Laradji et al. (1996), Bastea and Lebowitz (1997), and Appert et al. (1995). Unlike these, all the data sets of Jury et al. do lie very close to the LB results, see Figure 5.13. Since the DPD simulation method is very different from LB, being based on off-lattice molecular dynamics and with no assuptions about the form of the free energy, the correspondence with the position of the LB results lends support to the idea of a universal scaling, although the fact that each DPD run is best fit by a locally linear growth law is not consistent with this.

Apart from the overall problem of finding a consistent fit to data in the crossover region where the exponent is varying from run to run (at the time of fitting, Jury et al. did not know exactly which region their simulations were in), they could also have had problems due to finite size effects. To obtain enough data they included results for domain sizes up to half their system size, whereas LB data has been rejected for domain sizes larger than one quarter of the system size. As explained in Section 5.4.3, if the ratio of L_{max} to L_{min} is less than about two, there isn't enough variation over the range of usable data to determine a power law exponent with any degree of confidence. Jury et al. set L_{min} to around 10 in their simulation units, and with a system size of around 46 (the

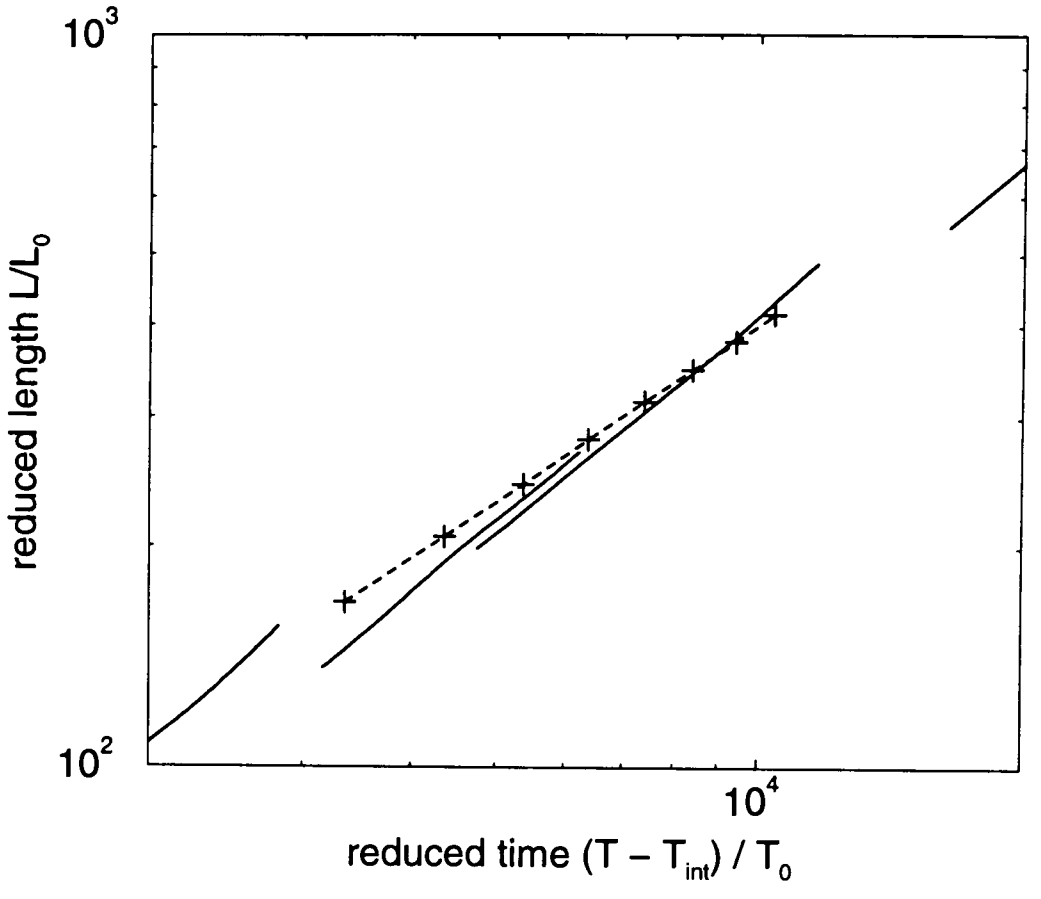

Figure 5.13: *Scaled data of DPD data from Jury et al. (1999), bold lines (left to right) with $L_0 = 0.29, 0.19, 0.13, 0.077$ (in DPD units). LB data (crosses) is Run020 (see Table 5.1) with $L_0 = 0.15$.*

range of the repulsive DPD interaction defines unity in their units), the minimum useful value of L_{max} is around 20, the value they used. In Section 5.4.2 it was shown that LB runs start to shown finite size effects when $L(T)$ exceeds one quarter of the system size. This does not prove that DPD simulations will definitely see the same limit. The same test (comparison of runs with different system size) was done by Appert et al. (1995) who found good agreement up to half the system size, but it is an important factor that cannot be ruled out without explicit checks. In fact, Jury et al. found considerable variation between different runs with the same parameters and different random initial conditions. Some of their data consists of averages of several runs. Given this intrinsic variability (itself a kind of finite size effect), tests with different system sizes might not have been very conclusive. However, the fact that finite size effects have not been systematically eliminated from the DPD data could explain the apparent success of the linear fits for DPD runs in the crossover region.

5.7 Conclusions

A thorough analysis of the order parameter data from the eight main 256^3 LB simulation runs of the spinodal decomposition of a symmetric binary fluid mixture has produced results in good agreement with theory. The structure factor shows a good scaling collapse over the region of the simulation runs from which data was used for the subsequent analysis of the domain size.

Using the first moment of the structure factor as the length measure characterising the domain size, all eight runs have been scaled onto a single plot covering five decades of non-dimensionalised length and seven decades of non-dimensionalised time. Within this plot, a linear scaling regime, $l = b_1 t$, with $b_1 \simeq 0.07$, proceeds into a broad crossover region from $10^2 \lesssim t \lesssim 10^6$, and finally to an inertial regime with $l = b_2 t^{2/3}$, with $b_2 \simeq 1$. The observed range of the crossover is, $10 \lesssim l \lesssim 10^4$, at larger l, than the simple dimensional analysis prediction of $l = L/L_0 \sim 1$, Equation (2.26). There is no sign of any further reduction in the growth exponent, but the predictions of Grant and Elder that the growth should finally slow to $t^{1/2}$ could still be valid further into the inertial regime than this study was able to reach. (This issue will be discussed further in the next chapter.)

Great care has been taken to eliminate any contribution from diffusive growth; along with the consistency between the fits to the two most inertial runs and the comparison with the runs in the crossover and linear regions, this provides strong evidence that the inertial regime has been clearly reached with these simulations. No other published work has achieved an unambiguous simulation of the inertial regime. Careful analysis of the work of Appert et al. (1995), for example, suggests that they in fact simulated the crossover region with significant residual diffusion distorting the observed growth exponent.

A careful evaluation of the uncertainties and errors involved in the simulation, analysis and fitting procedures has quantified the accuracy of the results to within sufficiently narrow bounds to be confident of the characterisation of the runs as being in the linear, crossover and inertial regions. The error analysis has also highlighted the importance of an informed choice of simulation parameters, particular with reference to the diffusion

level set by the mobility parameter. The diffusion must be low enough not to contribute to the domain growth in the hydrodynamic phase, while still being large enough to ensure the interface is maintained in local equilibrium when the necks between fluid domains break during coarsening.

The simulation method has been pushed to the limits in all directions within the available computing resources. The most linear runs are as far into the linear regime as can be achieved while still reaching a linear scaling regime with sufficiently reduced diffusion; the inertial regime runs have reached the point where further decrease in L_0 would require such high mobility to keep the interface in local equilibrium that the diffusive growth would compete with the hydrodynamics.

Areas where further analysis could be done include,

- more detailed comparison of the structure factor, $S(k)$, with the theoretical predictions of Bray (1994) and Furukawa (1989).
- calculation of a diffusion length to see how it compares with the interface width.
- analysis of the Euler number (number of "handles") of the interface as it coarsens to see if it reveals any topological differences in the domain structure in the linear and inertial regimes, see Jury (1999).

The analysis of the data from the main 256^3 LB simulations continues in the next two chapters. In particular, the next chapter includes further evidence, from the study of the velocity field, for having unambiguously simulated the inertial regime.

Chapter 6

Spinodal decomposition: velocity field

6.1 Introduction

The detailed study of spinodal decomposition in a binary fluid mixture using LB simulation methods that was started in the previous chapter, is continued here with presentation of the results obtained from analysing the velocity field. Visualisation of the velocity field has been done using the AVS package and examples are shown in Appendix A, where the flow patterns can be compared with the domain structure defined by the interface. The single fluid turbulence velocity field can also be compared with the spinodal results. There are no other reports of the statistical characteristics of the velocity field in a spinodal system with which these results can be compared; this is the first such detailed study.

In a similar manner to the order parameter analysis in the previous chapter, the velocity field was analysed statistically in both real and Fourier spaces. A wealth of information giving insight into the dynamics of the separation process was gained from comparisons with the order parameter results in Chapter 5 and with the single fluid turbulence results of Chapter 4. Velocity derivatives were calculated and analysed; in particular, the individual terms in the Navier-Stokes equation were computed and compared to show that the simulation really had reached the region where the inertial

terms play a full role in the dynamics. The time dependences of the NSE terms, the dissipation rate and the length scales, λ and λ_d, were investigated and compared with the theoretical predictions described in Chapter 2. Finally, a number of instances of non-scaling behaviour uncovered in the analysis of the velocity-related quantities have been drawn together and considered in more detail to elucidate their cause.

The many different features of the velocity field that have been investigated to build up a picture of how it behaves during the spinodal decomposition of a simple fluid mixture are grouped as follows:

- Quantities to be compared with results from the order parameter analysis:
  - Structure factor of the velocity field, $S_v(k)$, compared with the order parameter structure factor, $S(k)$.
  - Length scales, $L_v(T)$, from the velocity structure factor $S_v(k)$ compared with the domain size, $L(T)$, from the order parameter.
  - The rms fluid velocity compared to the interface velocity obtained by differentiating $L(T)$.
- Quantities to be compared with single fluid turbulence results:
  - Real space statistics of velocity components, including pdfs – single fluid turbulence has Gaussian statistics for the velocity components.
  - Velocity derivative statistics – the skewness of the longitudinal component tending to -0.5 would be a signature of turbulence.
  - Reynolds numbers based on various length scales.
  - The vorticity field, $\boldsymbol{\omega} = \nabla \wedge \mathbf{v}$.
- Quantities to be compared with theory:
  - The relative magnitudes of the terms in the NSE.
  - Structure factors of the terms in the NSE to show which length scales are important.
  - The growth rates of the terms in the Navier-Stokes equation.
  - The growth rate of the dissipation rate.

- The velocity derivative length scales – the Taylor microscale, $\lambda \sim L_{\nabla}$, and the dissipation scale, $\lambda_d \sim L_{\nabla^2}$.

These quantities are considered in detail in following sections. For details of the simulation runs under consideration, refer back to Section 5.2.

6.2 Comparison with order parameter results

The main quantity characterising the spinodal simulation is the length scale calculated in the previous chapter from the order parameter structure factor. This formed the basis for the main results, the time dependence for the domain size, $L(T)$. A measure of the speed with which the interface moves was also calculated in Section 5.4.1, in the guise of the growth rate, $\dot{L} = \mathrm{d}L(T)/\mathrm{d}T$. Corresponding quantities can be calculated from the velocity field and compared. The prediction for the velocity from both the simple and new scaling theories is that it should follow the interface, i.e. $\langle|\mathbf{v}|\rangle \simeq \dot{L}$.

The velocity field is analysed as a single, continuous field filling the whole simulation; there is no explicit information about the location of the interface. However, since the interface drives the fluid motion one might expect that length scales associated with the velocity will at least be related to the domain size in a simple way.

6.2.1 Structure factor from the velocity field

A velocity structure factor can be defined analagous to the structure factor for the order parameter, Equation (5.1),

$$S_v(k) = \frac{1}{n_k} \sum_{k-\frac{1}{2}<|\mathbf{k}|<k+\frac{1}{2}} \mathbf{v}(\mathbf{k}).\mathbf{v}(-\mathbf{k}). \tag{6.1}$$

The shape of the velocity structure factor has already been shown in Section 3.6.5, where the variation of the compressibility over the different length scales was investigated. Here $S_v(k)$ is compared with the order parameter structure factor, $S(k)$, studied in Section 5.3.1 where it was shown that $S(k)$ gave a good scaling collapse within and even between different runs. Figure 6.1 shows both the order parameter and velocity

structure factors for different runs, unscaled, but all for a domain size (measured by $L(T)$) of around 30 lattice units. As can be seen, the structure factors are very different

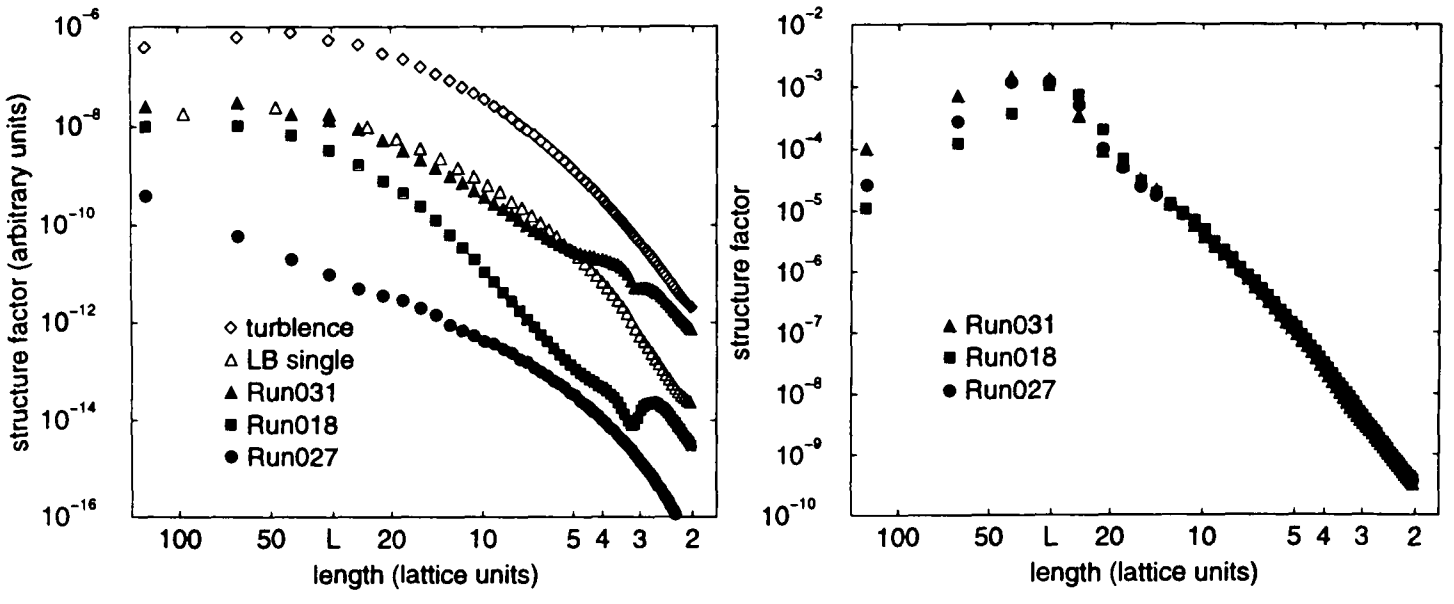

Figure 6.1: *Left: velocity structure factors for various runs in Table 5.2. Also shown: single fluid decaying turbulence simulation described in Chapter 4 (open diamonds), and an LB run which was converted to a single fluid part way through, see Section 6.3.3 (open triangles). Right: Order parameter structure factors for various runs in Table 5.2.*

shapes. While the order parameter structure factors show a fairly good scaling collapse (not as good as in Figure 5.1 because the domain size is not exactly equal for the timesteps chosen), the velocity structure factor changes shape from the linear to the inertial region, showing that the fluid flow patterns are changing significantly.

The order parameter structure factor shows no evidence of the interface width at the appropriate small scales, while the velocity structure factor shows a characteristic double peak around the scale of the interfacial width for runs where the inertial terms have become significant to the dynamics (crossover and inertial regions). The suggested reason for this (see Section 3.6.5), is capillary waves, although it is rather curious that they are not seen in the order parameter structure factor too.

One obvious reason why the velocity structure factors are not scaling even at larger length scales will be made clear in the next section, where it is shown that the dominant length scale in the velocity is not the same as the domain size. Thus the examples shown, for a domain size of 30 lattice units, would need different scaling for proper comparison.

6.2.2 Length scales from the velocity field

The velocity structure factor, $S_v(k)$, can be used to calculate a velocity length scale, $L_v(T)$, via the first moment in the same way as $L(T)$ is defined from the order parameter in Equation (5.3) (= Equation (2.5)),

$$L_v(T) = \sum_k S_v(k) / \sum_k k S_v(k). \tag{6.2}$$

The coarse-graining from 256^3 to 128^3, which, as discussed in Section 5.3.2, is equivalent to truncating the upper half of Fourier space, was found to make no more than 10% difference to the value of $L_v(T)$ except for the most viscous run, $L_0 = 36$, where the value of $L_v(T)$ is so large that finite size effects dominate the result. Data from 256^3 runs has therefore been used for these comparisons.

The same scaling procedure as was used to present $L(T)$ data on a single log-log graph (Figure 5.3) was applied to $L_v(T)$. The $T_{\rm int}$ values in Table 5.3 obtained from $L(T)$ were used, rather than fitting new ones, on the grounds that the diffusive time correction should have only one value for any given run[1]. The result is shown in Figure 6.2.

To a good approximation, the velocity length scale, $L_v(T)$, maintains $T^{2/3}$ growth through all the simulation runs. The deviations from $L_v(T) \sim T^{2/3}$ in the runs in the viscous region can be explained as finite size effects since here $L_v(T)$ is comparable with or larger than the system size. Over the crossover region, $L_v(T)$ converges on the domain size, $L(T)$, until they become equal within 10% in the inertial region. As noted in the previous section, the structure factor, $S_v(k)$ is a very different shape from the order parameter structure factor, so the convergence of the length scales does not mean the underlying structure of the velocity field is closely following the domains in the inertial region. In the viscous region, the observed scaling is not compatible with either the simple or the new scaling theory, both of which predict $L_v(T) \sim L(T)$ throughout.

The fact that the velocity length scales are of the order of the system size or larger in the viscous region is a type of finite size effect that probably helps to explain the

[1] There is the possibility that there is a "time delay" between the interface motion and the response in the bulk of the fluid. This would imply that larger, separately calculated values of $T_{\rm int}$ would be appropriate for the velocity analysis. Such a time delay would imply significant compressibility of the fluid, which is not seen except at small length scales, see Section 3.6.5. The shapes of the $L(T)$ and $L_v(T)$ time evolution also suggest that any such delay is small enough to be ignored.

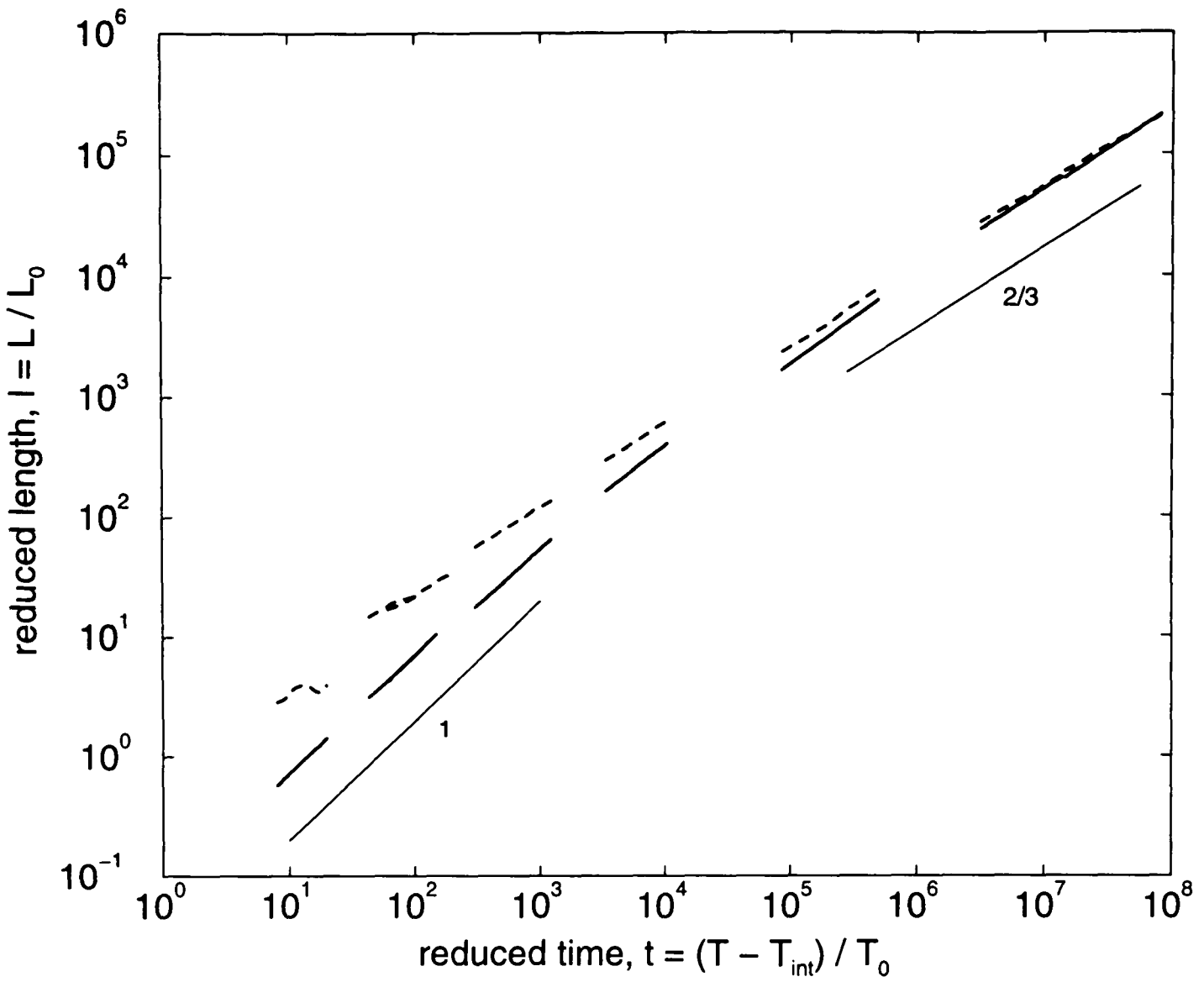

Figure 6.2: $L_v(T)$ *(dashed) compared with* $L(T)$ *(bold) for runs in Table 5.1.*

fluctuations[2] in these runs. Although the runs are following a linear growth law, if there are fluctuations of the order of (or larger than) the system size, they will not be averaged out over the size of the simulated system.

Unlike the order parameter, where a number of different length measures were available, there are no obvious alternative methods of obtaining a length scales associated with the velocity field that could help to interpret these results. One possibility is that the structure in the velocity field in the viscous "creeping flow" regime is dominated by fluctuations, and that these fluctuations scale differently from the rms value of the velocity itself.

[2]As described in Section 5.4.3, the $L(T)$ data for the runs in the viscous region show quite large fluctuations leading to free fit estimates of the growth exponent, α, that deviate either side of linear by more than the estimated errors.

6.2.3 Average velocities

Since the interface movement as the domains enlarge provides the force that drives the fluid motion, it is interesting to compare how the interface velocity relates to the fluid velocity. The simplest overall comparison can be done by taking the average fluid velocity, calculated as the rms-average over the whole system, and comparing this with the velocity obtained by differentiating $L(T)$ (see Section 5.4.1), which gives a measure of the interface velocity.

These two velocities have been calculated for all the runs in Table 5.1, and in order to facilitate comparison between different runs, the velocities have all been non-dimensionalized by scaling by L_0/T_0. The results are shown plotted against $t = (T - T_{\text{int}})/T_0$ in Figure 6.3.

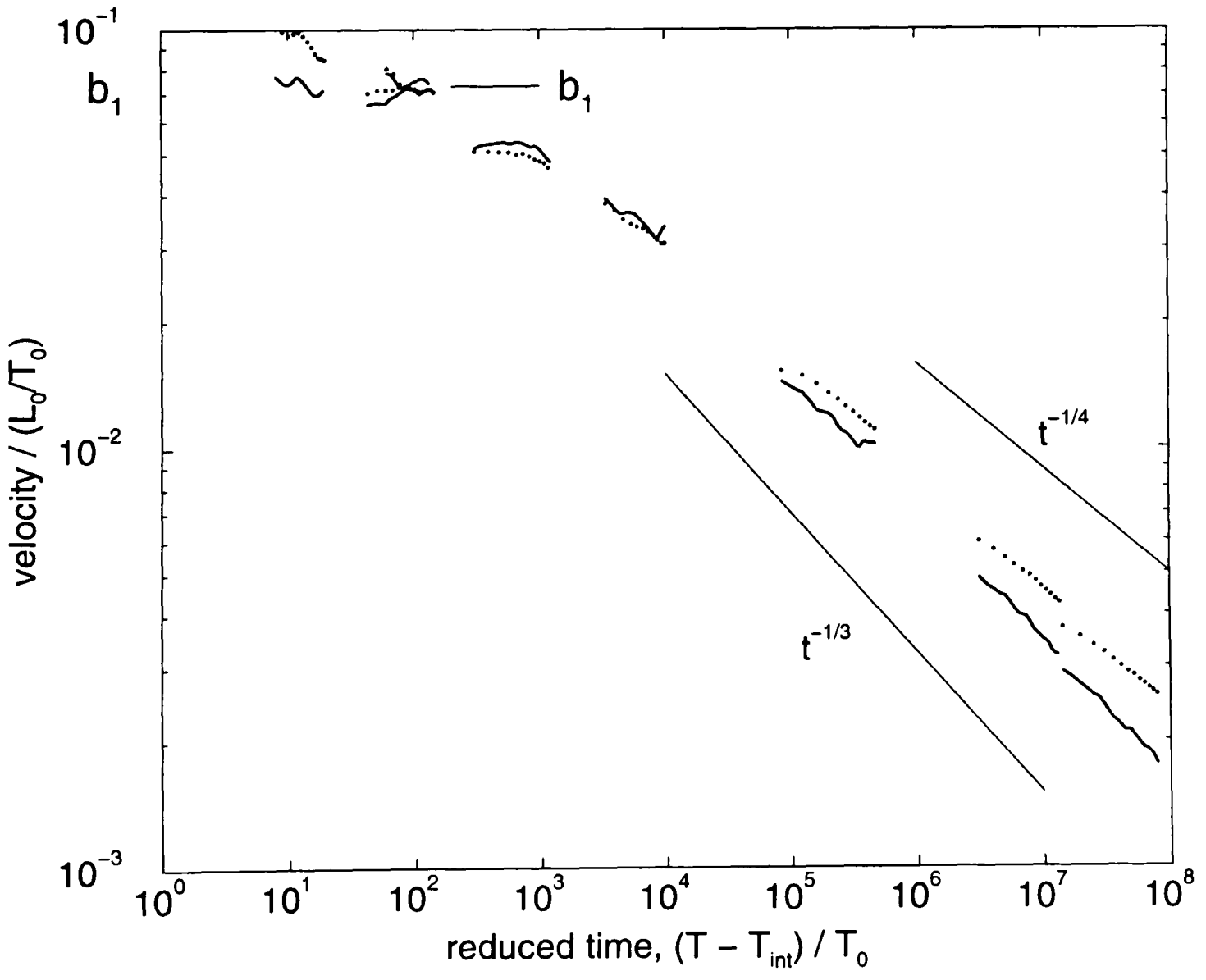

Figure 6.3: *For runs in Table 5.1, interface velocity, $\dot{L}(T)$ (bold) compared with the rms fluid velocity (dotted).*

The overall shape of this plot shows the interface velocity starting out roughly constant in the viscous region at the value of $b_1 = 0.073$, ($l = b_1 t$) and turning down through the crossover region towards $\dot{l} \sim t^{-1/3}$ in the inertial region, as predicted by scaling theory ($l \sim t^{2/3}$). The rms fluid velocity roughly matches the interface velocity in the early crossover region, but grows larger than the interface velocity in the inertial region, by about 40% at the end of Run032. The most inertial two runs (Run019 and Run032) have the rms velocity scaling approximately as $t^{-1/4}$ while the interface velocity, $\dot{l} \sim t^{-1/3}$. In the most viscous run, Run028, the rms velocity is also about 40% larger than the interface velocity. Both velocities are fluctuating quite far from the expected constant behaviour in the linear region, and the fluctuations are more or less in step.

Physically, the deviation between the rms fluid velocity and the interface velocity implies that energy is building up in the fluid motion to higher levels than predicted by either the simple scaling theory or the new scaling theory, both of which predict that the fluid velocity should follow the interface in all regimes. In the early crossover region, that prediction holds quite well. In the inertial region, a qualitative explanation for the excess velocity could be that the extra swirling motion within domains (turblence) increases v_{rms} above the interface velocity. However, it is also necessary to explain the discrepancy in the most linear run, Run028, where the fluid should be exactly following the interface and instead seems to be going on average 40% faster. This point will be returned to at the end of this chapter once all the various scalings and discrepancies in the velocity field have been described.

6.3 Comparison with single fluid turbulence

Single fluid turbulence was studied in Chapter 4 as a test case for the analysis methods, and to provide a reference for comparison with the velocity field in the two fluid system. Guided by the choices of key characteristics of fluid motion made by turbulence theorists, in this section the following four quantities will be be compared between single fluid decaying turbulence and the velocity field in the spinodal decomposition of symmetric, binary fluid mixtures: velocity statistics, velocity derivative statistics, Reynolds numbers, and the vorticity.

The presence of the interface between the two fluids provides both a characteristic length scale (the domain size) and a driving force not present in the single fluid system, and this can be expected to have a large effect on the statistics of the velocity field and quantities derived from it. Of particular interest is whether it is possible to detect signs of turbulence appearing in the spinodal system.

Note that because the turbulence simulation units are rather different from the LB units, it is really only straightforward to compare dimensionless or normalised quantities between the two simulations, and since the single fluid turbulence does not have an interface, the characteristic length and time scales, L_0 and T_0, are not available to facilitate comparisons.

6.3.1 Velocity statistics

When the pdf of the velocity components in a homogeneous isotropic turbulent fluid is examined, it is found to be very close to Gaussian, and uncorrelated both spatially and over time (apart from small scale and short time correlations). To find significant non-Gaussian behaviour over longer times and length scales, it is necessary to look at velocity increments and derivatives – where the correlations are found to take a universal form characteristic of all turbulence (see Section 2.5). Since the spinodal system has a typical length scale in it, the domain size $L(T)$, correlations can be expected at this macroscopic scale and hence the velocity components themselves should show non-Gaussian pdfs. The departure from Gaussian would be expected to show up in the fourth moment, the flatness, defined as $\langle v_\alpha^4 \rangle / \langle v_\alpha^2 \rangle^2 - 3$ (zero for a Gaussian distribution), since there is no preferred direction to cause skewness[3] ($\langle v_\alpha^3 \rangle / \langle v_\alpha^2 \rangle^{3/2}$).

Figure 6.4 (left) shows the flatness for runs in Table 5.2, divided between linear runs with $L_0 < 0.5$ and crossover/inertial region runs with $L_0 > 0.5$. It can be seen that the flatness is quite variable, but as a general trend it grows slightly with time through each run (larger domain size) and with decreasing L_0, i.e. more inertia. In all cases the flatness is larger than for single fluid turbulence, which is shown for comparison. The velocity pdfs show correspondingly wider tails and narrower peaks; an example

[3] The skewness was checked and found to be approximately zero as expected.

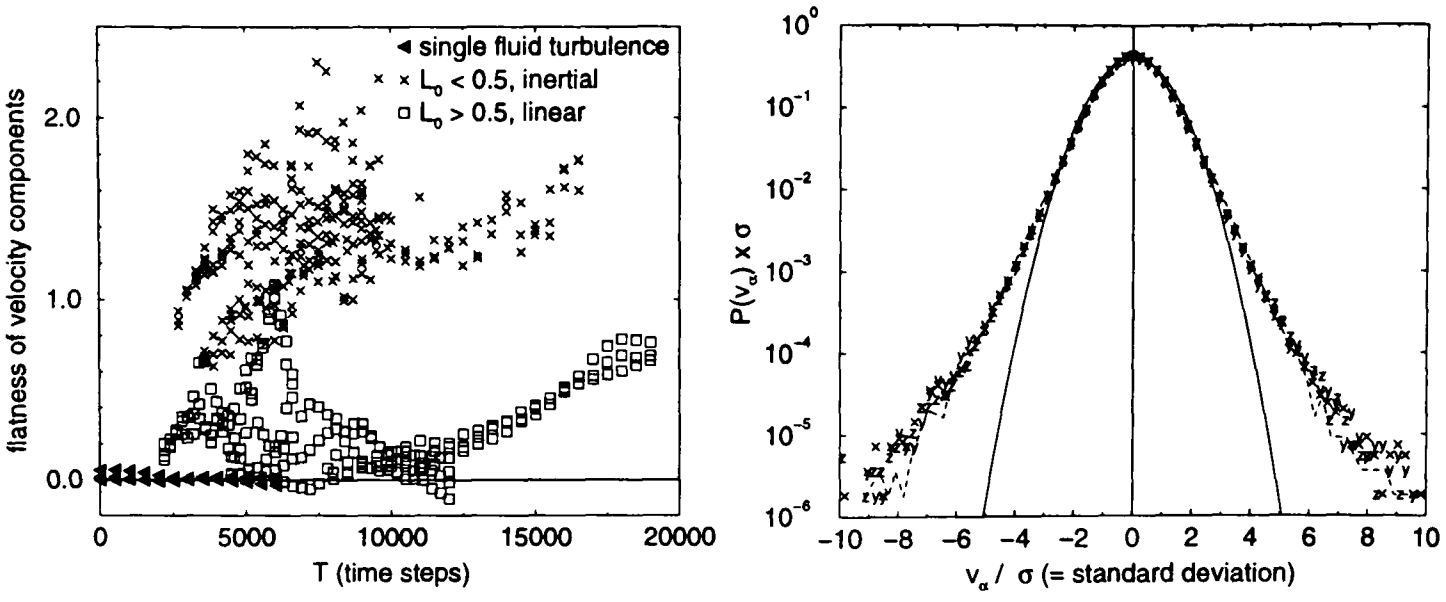

Figure 6.4: *Left: flatness of velocity components for runs in Table 5.1, runs with* $L_0 > 0.5$ *(crosses) and with* $L_0 < 0.5$ *(squares) with single fluid turbulence (filled triangles) shown for comparison. Right: pdfs of velocity components for Run032 at time step 12000, with Gaussian (solid) and transverse velocity derivative (dashed) shown for comparison.*

for Run032 is shown in Figure 6.4 (right). The shape is close to that found in the transverse velocity derivatives in the same system, (shown dashed for comparison).

As the expected, there is a basic difference in the statistics of the velocity components between single fluid turbulence and spinodal systems due to the presence of the interface providing extra correlations in the spinodal system. It is also significant to note that there is a statistical difference between the different spinodal simulation runs in the viscous and inertial regimes. In the inertial regime, the correlations induced in the velocity field by the interface appear to be larger (larger flatness, wider pdf tails), showing that the behaviour of the velocity is different in the viscous and inertial regimes.

6.3.2 Velocity derivative skewness

The statistics of the velocity derivatives provide some of the most important distinctive characteristics of fluid turbulence. Velocity derivatives come in two types, longitudinal, e.g., $\mathrm{d}v_x/\mathrm{d}x$, and transverse, e.g., $\mathrm{d}v_x/\mathrm{d}y$ or $\mathrm{d}v_x/\mathrm{d}z$. Fully-developed turbulence shows a key signature in the skewness of the longitudinal velocity derivatives distribution taking a value of -0.5. The transverse derivatives are symmetrical, but expected to have wider than Gaussian distributions, i.e. positive flatness.

Three selected velocity derivatives were calculated[4], $\mathrm{d}v_x/\mathrm{d}x$, $\mathrm{d}v_y/\mathrm{d}y$ (longitudinal) and $\mathrm{d}v_y/\mathrm{d}x$ (transverse), by multiplying the Fourier space velocity field components by the appropriate factor of ik_x or ik_y, and transforming back to real space. For derivative calculations, the small length scales are important, so coarse-grained data cannot be used. The analysis has therefore been done with the 128^3 data from the runs in Table 5.2.

Figure 6.5 (left) shows the skewness of two of the longitudinal velocity derivatives against time for the bottom three runs in Table 5.2 (i.e. most inertial). Also shown for comparison is the skewness from the decaying turbulence simulation described in Chapter 4. In the two most inertial LB simulation runs, the skewness of the longitudinal

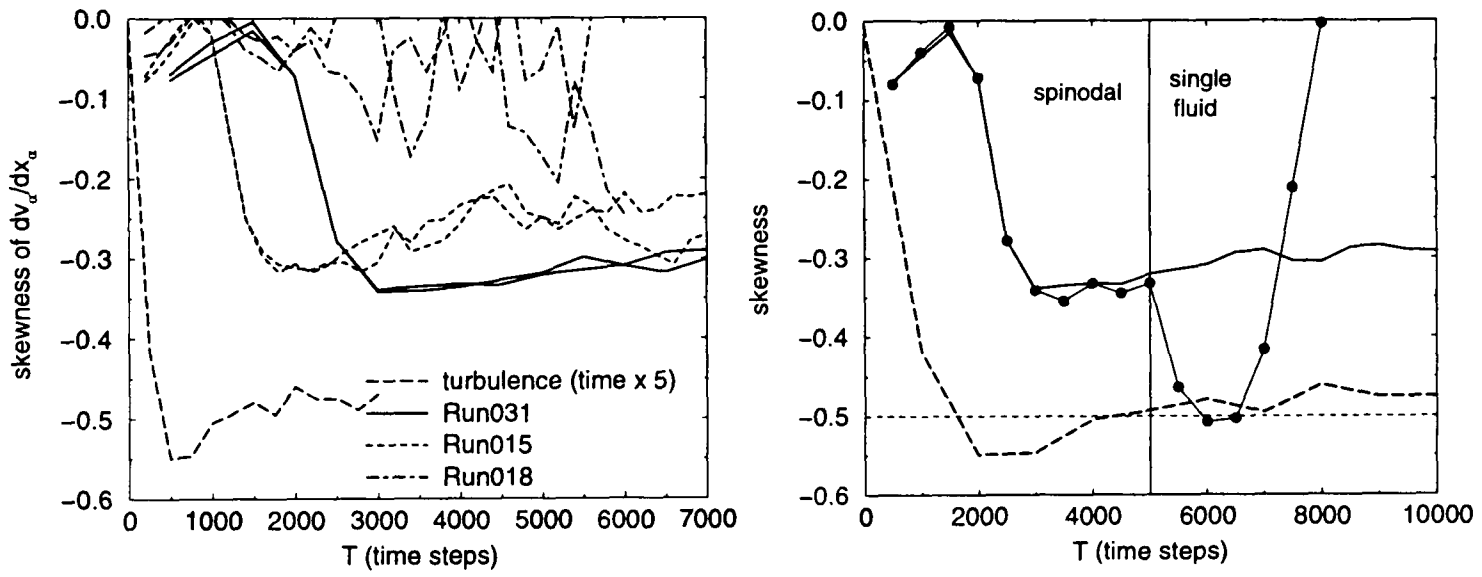

Figure 6.5: *Left: Skewness of the longitudinal velocity derivatives for Run031 (solid), Run015 (dashed), Run018 (dot dashed) and single fluid decaying turbulence (long dashed). Right: Skewness of a longitudinal velocity derivative for Run031 (solid), a* 96^3 *run with the same parameters in which the interface was removed at time step 5000 (filled circles), and single fluid turbulence (dashed). The time scale for the turbulence data has been multiplied by 5 (left) or 10 (right) to facilitate comparison with the LB data. (The time dependence is not of relevance here once the initial stages are passed in both simulation methods.)*

velocity derivative reaches around -0.35. A plausible interpretation of this result is that patches of turbulence are occuring, but not filling the whole system, so the patches have skewness -0.5, but the overall average is less. From visualisations (see Appendix A) the interface is clearly not disrupted by turbulent mixing, so it makes sense that there would be areas around the interface that are not turbulent which bring down the average over the whole system.

[4]limited to three by computer memory availability when running the analysis code. Since the system is isotropic, all other derivatives should be equivalent to one or other of these.

In order to test this idea further, a 96^3 run with the same parameters was done, and at timestep 5000 (when the domain size was about 21, i.e. into the usable data region) the interface was removed by setting the order parameter to 1 throughout the simulation, thus converting it to a single fluid with the same velocity field. This was then allowed to evolve, with the expectation that it would behave like single fluid decaying turbulence with a rather odd starting configuration. The skewness of a longitudinal velocity derivative for this run is shown in Figure 6.5 (right), with Run031 and the single fluid turbulence data repeated for comparison. Once the interface was removed, the 96^3 test system skewness quickly jumped to around -0.5 from -0.35, providing strong support for the "turbulent in patches" hypothesis; on removal of the interface, the turbulence rapidly infects the whole system[5].

6.3.3 Velocity derivative pdfs

The velocity derivative pdfs are expected to be non-Gaussian to match the observed skewness and flatness. Figure 6.6 (left) shows pdfs for Run031 for timestep 6000 when $L = 26$ lattice units. The longitudinal derivative is obviously skew, while the transverse derivative is symmetric. Both are clearly wider (larger flatness) than the Gaussian shown for comparison. The equivalent pdfs for single fluid turbulence (see Figure 4.5 (right)) show even larger flatness, and more pronounced skewness in the longitudinal derivative. Again, this can be explained if the spinodal simulation has patches around the interface that are not turbulent that bring down the averages (see previous section). Figure 6.6 (right) shows the equivalent pdfs for the 96^3 test after the interface was removed. The longitudinal pdf has shifted to the shape of the single fluid turbulence one, while the transverse pdf is not much changed, suggesting the memory of the interface may still persist in the fluid statistics after 1000 time steps. This is reasonable, since correlations on a scale of 21 lattice units will take at least a time of order $21/v_{rms} \simeq$ 8000 time steps to decay.

[5]The further evolution of the 96^3 test system once the interface was removed, was, however, not as expected. Despite the fact that no further energy is being input into the system, the removal of the interface rendered the dynamics unstable, and after a couple of thousand more time steps the skewness dropped to zero as the velocities became unfeasibly large. As a two-fluid system, it remains stable until much later times. The causes of this instability have not been investigated further, except to note that the velocity structure factor suggests that the instability arises first at the smallest length scales. The presence of the interface seems to act to stabilise the system; clearly it limits the turbulence to scales within the domain size, but this would suggest that the instability originates in the large length scales, in contrast to the evidence from the velocity structure factor.

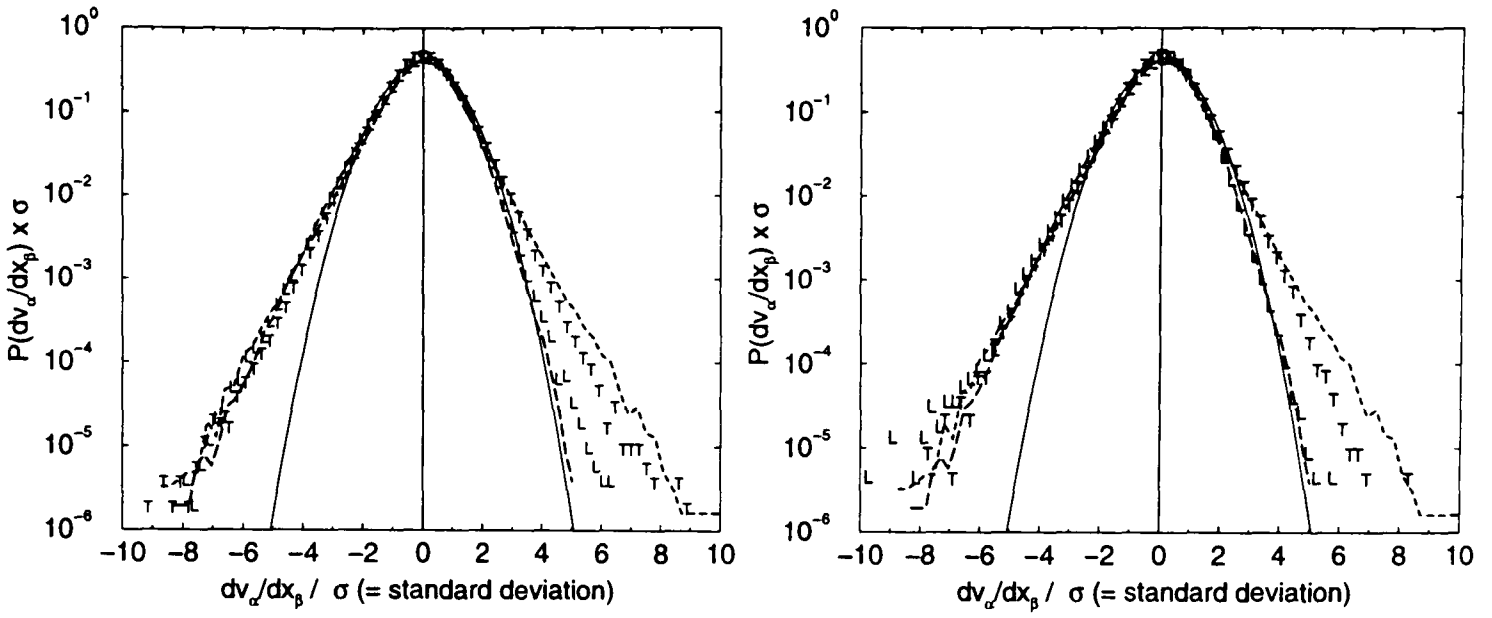

Figure 6.6: *Left: Pdf of longitudinal (L) and transverse (T) velocity derivatives for Run031, for timestep 6000 when $L = 26$ lattice units, with pdfs for single fluid turbulence shown short and long dashed, and Gaussian shown solid for comparison. Right: same pdfs at time step 6000 for a 96^3 run with the interface removed at time step 5000. The longitudinal pdf now matches the turbulence one, while the transverse pdf is unchanged.*

Turbulence theorists like to calculate ratios of higher moments to characterise these non-Gaussian pdfs (see Section 2.5). Given that this could only be meaningfully done on the fluid away from the interface, and that even if this separation were done, the statistics wouldn't be very good on the size of the remaining data set (see Section 4.4.2), there doesn't seem to be much chance of gaining useful insights from trying to do this on the spinodal velocity derivative data.

6.3.4 Reynolds numbers

Reynolds numbers, defined in Equation (2.32) as Re = (velocity $\times$ length)/(kinematic viscosity), are used to characterise the dynamics of fluid systems. In essense, they are either generalisations or estimates of the ratio, R_2, of the nonlinear term to the viscous term in the Navier-Stokes equation, Equation (2.31). Reynolds numbers depend on a sensible choice of characteristic length and velocity scales, if they are to have useful comparative meaning. In a single fluid with no boundaries, there are no immediately obvious length scales (apart from the system size itself), and turbulence theory constructs several length measures to characterise the fluid (see Section 2.5). These are, the integral scale, L_{int}, Equation (2.49), which is similar to the first moment of the

velocity structure factor, and the Taylor microscale, λ, Equation (2.52), which characterises the smaller length scales in which dissipation is taking place. The Kolmogorov microscale, λ_d, Equation (2.54), the smallest natural length scale in a turbulent fluid, marks the lower end of the dissipation length scales, and is not normally used to form a Reynolds number.

In both turbulence DNS and the LB spinodal systems, the same typical velocity can be used, $v_{rms} = (\langle v_x^2 \rangle + \langle v_y^2 \rangle + \langle v_z^2 \rangle)^{1/2}$. For the case of spinodal fluids, there is an obvious natural length scale in the size of the domains, $L(T)$. However, a Reynolds number, $\mathrm{Re}_L = \rho L(T) v_{rms}/\eta$, formed from this length, can only be used for comparisons with other similar systems; it should not be expected to compare meaningfully with Reynolds numbers in single fluid turbulence based on the integral scale or Taylor microscale[6]. In practice, most turbulence simulation studies use λ as the length to form a Reynolds number, Re_λ, since λ is generally the length that predicts the behaviour of the nonlinear term most accurately, because it is the length scale associated with the ∇ operator (see Section 2.5). Reynolds numbers for the decaying turbulence simulation studied in Chapter 4 can be seen in Figure 4.2. For the most inertial spinodal run, Run032, the integral and microscale Reynolds numbers are comparable with those for the turbulence simulation, adding weight to the evidence for partial turbulence being present in the spinodal case.

In the spinodal system, the velocity of the interface, $\dot{L}(T)$ can also be used as the typical velocity; this gives the conventional Reynolds number Re_ϕ already mentioned in Section 2.3.3, and used by Furukawa (1997) and Grant and Elder (1999). This Reynolds number, Re_ϕ, provides an alternative to the reduced length and time scales, $l = L/L_0$ and $t = (T - T_{\mathrm{int}})/T_0$, to characterise the range of the simulations, which extends over $0.1 \lesssim \mathrm{Re}_\phi \lesssim 350$. The crossover region occupies the range $1 \lesssim \mathrm{Re}_\phi \lesssim 100$.

The three main Reynolds numbers just discussed, Re_ϕ, Re_L and Re_λ, are shown on a scaled plot in Figure 6.7. Since λ is sensitive to small scales, data from 128^3 systems is used for Re_λ, the other two are shown for 256^3 data (it has been checked that this agrees well with 128^3 data). There is little difference between Re_ϕ and Re_L, the deviation that

[6] A forced turbulence DNS where the forcing is done (in Fourier space) at a single large length scale might perhaps be comparable if the forcing length was used to form the Reynolds number. Most turbulence DNS studies are, in fact, of forced simulations since higher Reynolds numbers can be achieved this way. However, the study in Chapter 4 was only of decaying turbulence DNS.

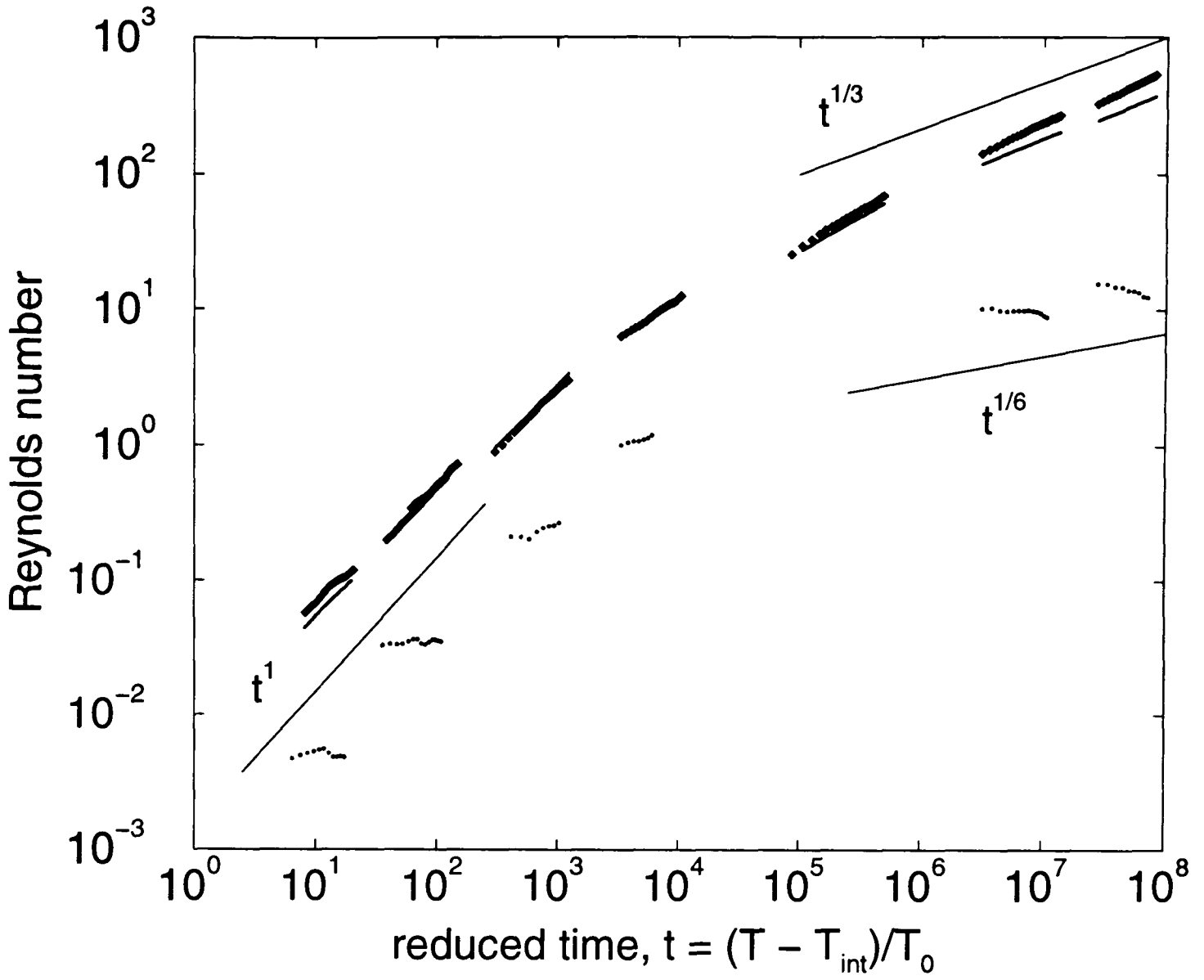

Figure 6.7: *For runs in Table 5.1, Re_ϕ, (bold line), and* Re_L *(diamonds) and for Runs in Table 5.2, Re_λ (dots).*

can be seen in the extreme viscous and extreme inertial runs is due to the difference between the interface velocity, $\dot{L}$, and rms fluid velocity (see Section 6.2.3). The final growth rate for Re_ϕ in the inertial region is approximately $\mathrm{Re}_\phi \sim t^{1/3}$ as predicted from dimensional analysis.

Both Re_ϕ and Re_L show reasonably good scaling behaviour, i.e., the individual runs line up close to a single universal curve, in agreement with the predictions of linear scaling of Re in the viscous region, and $t^{1/3}$ for the inertial region (see Table 2.1). In contrast, the data for Re_λ does not show good scaling behaviour. While the overall trend of linear scaling in the viscous region, and slower growth at around $t^{1/6}$ in the inertial region, is consistent with the new scaling theory (see Table 2.1), the individual runs do not line up onto a single curve. Instead they all have slower growth rates than the predictions. The non-scaling behaviour of Re_λ is entirely due to the non-scaling behaviour of λ itself, which is examined in more detail in Sections 6.4.4 and 6.5.3.

At this stage of the analysis it is clear that the prediction by Grant and Elder (1999) that the Reynolds number defined as Re_ϕ should saturate at some finite value (which they estimate to be in the range $10 \lesssim \mathrm{Re}_\phi \lesssim 100$), is not borne out by the results from these simulations, which have Re_ϕ continuing to grow as $t^{1/3}$ at $\mathrm{Re}_\phi \sim 350$. This is consistent with the analysis of the order parameter in the previous chapter where the growth rate of $L(T)$ was found to be $t^{2/3}$ up to the limit of the simulation runs, with no hint of a turn down towards $t^{1/2}$ as Grant and Elder suggest. A further transition to a region of slower domain growth beyond the range of these simulations cannot, of course, be ruled out, but if so, it must occur for Re_ϕ values significantly higher than those predicted by Grant and Elder.

6.3.5 Vorticity

Vorticity is another key quantity in turbulence; regions of high vorticity tend to form persistent structures such as thin tubes and flat sheets in fully developed turbulence. The vorticity is derived from the velocity field, $\boldsymbol{\omega} = \nabla \wedge \mathbf{v}$. One of the main motivations for considering the vorticity in turbulence theory is that it naturally appears in the analysis as a consequence of the nonlinear term in the NSE, $\mathbf{v}.\nabla\mathbf{v}$, which can also be written $-\mathbf{v} \wedge \boldsymbol{\omega}$. By considering the vorticity in the spinodal simulation, it may also be possible to gain insight into exactly where the nonlinear term in the NSE is most active in determining the dynamics in relation to the interfaces.

The vorticity was calculated from the velocity field via Fourier transforms for both the single fluid decaying turbulence and the spinodal fluid mixture, and the resulting field data viewed in AVS, see Appendix A. Basically, the pictures show lots of scattered patches of high vorticity in both single fluid turbulence and the most inertial spinodal simulations, beyond that nothing especially noteworthy. There is some suggestion of structures, but nothing very conclusive. The most likely explanation for this lack of obvious structure is that neither the single fluid decaying turbulence nor the spinodal simulations have high enough Reynolds numbers to really develop such features. Most published work discussing vortex tubes and sheets is based on forced turbulence simulations with $\mathrm{Re}_\lambda \gtrsim 80$, compared with $\mathrm{Re}_\lambda \lesssim 20$ for the simulations of this work. Furthermore, large-scale persistent structures like vortex tubes take some time after

the onset of turbulence to develop, longer than the time a decaying turbulence simulation is likely to maintain high enough Reynolds number. It seems likely, therefore, that the simulations under consideration here do not exhibit sufficiently fully-developed turbulence to contain complex structures such as vortex tubes.

Nonetheless, the vorticity still forms a useful quantity for comparison between the single fluid turbulence and the binary fluid spinodal systems. The same statistical analysis as was carried out on the velocity field was applied to the vorticity field, and the vorticity pdf was found to be even less Gaussian than the velocity and velocity derivative pdfs. The corresponding flatness is also larger, less variable and increasing steadily (linearly) with time. Figure 6.8 (left) shows the shape of the pdf compared with turbulence and Gaussian. As for the velocity and velocity derivative pdfs, the most likely explanation

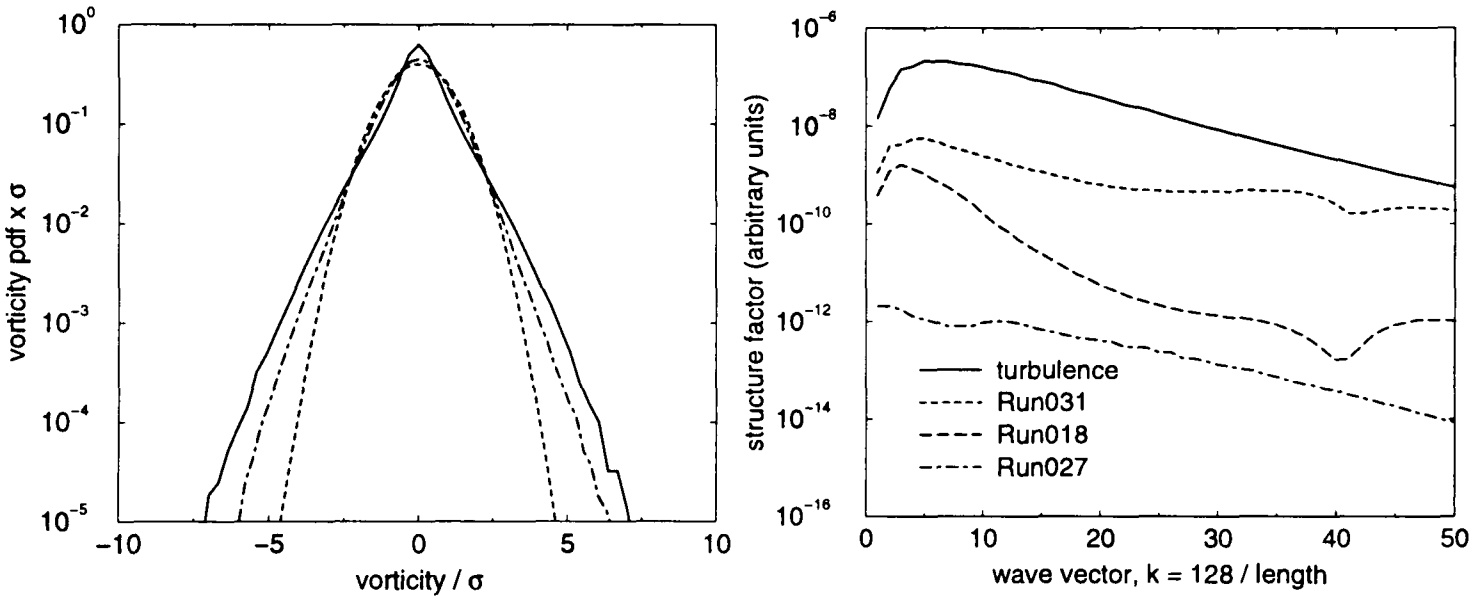

Figure 6.8: *Left: vorticity pdf for timestep 1200 for Run031 (solid) compared with vorticity pdf from single fluid turbulence (dot-dash) and Gaussian (dash). Right: structure factor for single fluid turbulence (solid), Run031 (dash), Run018 (long-dash) and Run027 (dot-dash); the structure factor axis is in arbitrary units, the data have been scaled so it doesn't overlap.*

for the difference is the presence of the interface and the extra correlations it induces.

Figure 6.8 (right) shows the structure factor for the vorticity for single fluid turbulence and spinodal systems of various L_0 from the linear, crossover and inertial regions. The same small-scale structures as are seen in the velocity structure factors, see Figure 6.1, are also seen the vorticity structure factors in the crossover and inertial region spinodal systems for wave vectors greater than about 30 (length scales smaller than around 4 lattice spacings). That apart, the inertial region structure factor looks quite like the

turbulent one for length scales larger than the interface, another good indication that the fluid behaviour is in part turbulent in the spinodal system.

6.4 Comparison with theory

A number of predictions were made in Section 2.4 that can now be compared with the observed results for the velocity field. These predictions, based on the new scaling theory, only differ from the simple scaling theory (Section 2.3.2) in the case of the velocity-related quantities. Even for these, in the viscous region the predictions of simple scaling theory are the same as the new theory, but in the inertial region, a number of quantities are predicted to scale differently, such as the nonlinear and viscous terms in the NSE, the dissipation rate, and the Taylor and Kolmogorov microscales. The new scaling predictions were summarised in Table 2.1.

The scaling behaviour of the average velocity, which is predicted to follow the interface in both simple and new scaling theories, has already been investigated in Section 6.2.3, where it was found to be larger than predicted in the extreme viscous and extreme inertial regions. In Section 6.3.4, Re_λ was found not scale: the overall magnitude between runs was in line with the new scaling theory while the behaviour within a single run showed a fall with time rather than slow growth. The observed departures from scaling will be summarised and discussed together in Section 6.5.

6.4.1 Ratios of terms in the NSE

In the previous chapter, analysis of the order parameter field from the simulation runs in Table 5.1 showed that the whole range of dynamical behaviour had been simulated, from linear domain growth through a broad crossover region to inertial behaviour. In Section 5.6 it was also shown that much of the previous published work in this area consisted of results contaminated by diffusive growth. In view of the importance of establishing without doubt that the LB simulations studied here are truly simulating the inertial region, in addition to the careful checks described in Chapter 5, it is important to

analyse the velocity field to see if its behaviour is consistent with the inertial regime having been achieved.

The most direct way to investigate this is to calculate the individual terms in the Navier-Stokes equation and compare their relative magnitudes. In the linear region the predictions are clearcut: the inertial terms in the NSE are expected to be negligibly small compared to the viscous term. In the inertial region, simple scaling theory predicts that the inertial terms will be larger than the viscous term. The new theory predicts that the asymptotic behaviour will have the nonlinear and viscous terms larger than the driving force and the acceleration term, with the deviation between their decays going slowly as $t^{-1/6}$, (the ratio between $t^{-7/6}$ and $t^{-4/3}$, see Table 2.1). However, at best these simulations have only just reached the inertial region, so it is unlikely that this final asymptotic behaviour will be observed. In the crossover region, since the two inertial terms are growing from small values relative to the driving force and dissipation, all terms are expected to be roughly the same order of magnitude. The overall sign of successfully simulating through the crossover region into the inertial region is therefore that the inertial terms rise in magnitude over the crossover region to be at least comparable with the viscous term, and then show signs of different scaling behaviour from the linear region.

In order to evaluate (rms-values of) the three relevant NSE terms, $\eta\nabla^2\mathbf{v}$, $\rho\partial\mathbf{v}/\partial T$ and $\rho(\mathbf{v}.\nabla)\mathbf{v}$, various first and second order derivatives must be estimated from the discrete, lattice-based velocity data. The accuracy of the calculations is thus sensitive to small scales, so coarse-grained data from 256^3 runs are not suitable and data from the main 128^3 runs in Table 5.2 were used. The Fourier transform method was used to evaluate the derivatives, see Section 3.4. The NSE terms are vector quantities defined for each point in the simulation lattice. An rms-average value for the magnitude of each term is calculated, $|Z|_{rms} = \sqrt{\langle Z_x^2\rangle + \langle Z_x^2\rangle + \langle Z_x^2\rangle}$, where Z_x, Z_y, and Z_z are the components of the vector $\mathbf{Z} = \eta\nabla^2\mathbf{v}$ (for example), and the average is taken over the whole system. A further complication is that to evaluate $\rho\partial\mathbf{v}/\partial T$, velocity data from consecutive time steps is required. Due to data storage space considerations, this was only collected for 96^3 systems. This is enough to compare values for a domain size just larger than $L_{\min}$ on a scaling plot, but not to determine the time dependence of this acceleration term

within a particular run[7].

An example of the raw data for each of the NSE terms from runs with the same parameters ($L_0 = 0.15$) but different system size is shown in Figure 6.9 (left). These

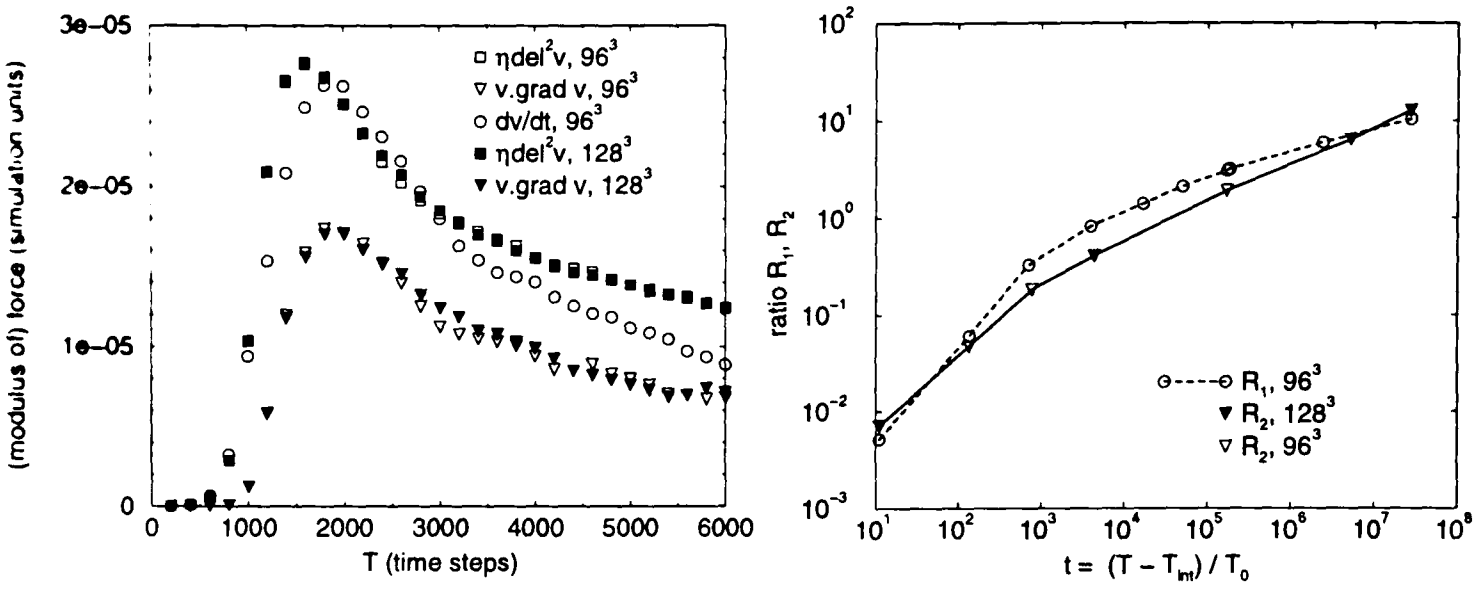

Figure 6.9: *Left: Time evolution of the terms in the NSE (rms) for runs with* $L_0 = 0.15$. *Right: comparison between inertial terms for runs with* $L_0 = 36$, 2.9, 0.59, 0.15, 0.054, 0.024, 0.01, 0.01 *(different parameters)*, 0.0016, 0.00095, 0.00039, 0.0003. *System sizes are* 96^3 *(open symbols) and* 128^3 *(filled symbols).*

data are in the middle of the crossover region so all terms are expected to be of the same order of magnitude, and there are no predictions for the scaling behaviour. Good agreement can be seen between the 128^3 and 96^3 systems for the viscous and nonlinear terms in the Navier-Stokes equation, and the acceleration term is of the same order of magnitude, suggesting that the 96^3 data for the acceleration term should be sufficiently reliable for basic comparisons to be made.

Comparisons involving different runs are more conveniently done using dimensionless quantities. Therefore, the two ratios defined in Equations (2.30) and (2.31) between the terms in the Navier-Stokes equation,

$$R_1 = \frac{|\rho \partial \mathbf{v}/\partial T|_{rms}}{|\eta \nabla^2 \mathbf{v}|_{rms}}, \tag{6.3}$$

and

$$R_2 = \frac{|\rho (\mathbf{v}.\nabla)\mathbf{v}|_{rms}}{|\eta \nabla^2 \mathbf{v}|_{rms}}, \tag{6.4}$$

[7]Simulation accuracy and stability require that the time step be small enough that the difference between consecutive time steps should give a good approximation to $\rho \partial \mathbf{v}/\partial T$, although there is no easy way to estimate the likely errors.

have been evaluated. These ratios, R_1 and R_2, are expected to be $\ll 1$ in the viscous region where the viscous term dominates. In the inertial region, predictions differ between the simple scaling theory ($R_1 \simeq R_2 \sim t^{1/3} \gg 1$) and the new theory, which says that R_2 should reach some asymptotic value large enough for a significant turbulent energy cascade to have developed, but not grow indefinitely. For R_1, the new theory predicts that the final behaviour will be falling as $t^{-1/6}$, but since it must first rise from zero over the crossover region, there will be a maximum at some point in the early inertial regime.

In Figure 6.9 (right), the ratios R_1 and R_2 are shown for 96^3 and 128^3 systems with a range of L_0 values spanning all seven decades of reduced time, $t = (T - T_{\text{int}})/T_0$, of the combined simulation results. The values of R_1 and R_2 are not precisely equal, but do remain the same order of magnitude throughout, while varying over three orders of magnitude, from $R_2 \sim 10^{-2}$, indicating the viscous term is dominant by two orders of magnitude, to $R_2 \sim 10^1$, indicating that the inertial terms are dominant by one order of magnitude. This provides clear confirmation of the claims made in Chapter 5 that the simulation has reached a region where the inertial terms are dominant in the dynamics.

The ratio R_2 has also been calculated for the single fluid decaying turbulence simulation studied in Chapter 4, and found to be approximately 10, i.e. comparable with the most inertial of the LB binary fluid runs. This confirms that the turbulence simulation data should provide a good comparison with the LB data since the relative importance of the NSE terms is similar. Also, since the turbulence simulation is an example of a system with $R_2 \sim 10$ showing fully developed turbulence, it makes it very plausible that the LB spinodal system should also show signs of being turbulent, as were found in Section 6.3.2.

Looking more closely now at the behaviour of R_1 relative to R_2, there is a significant difference in the crossover region, by around a factor of two ($R_1 > R_2$). Then, in the inertial region, upper right of Figure 6.9 (right), R_1 becomes less than R_2 by about 50% and appears to be heading for a lower growth rate. This deviation between R_1 and R_2, suggests that the asymptotic behaviour of these two ratios is perhaps going to be different. This is consistent with the new theoretical predictions for the asymptotic behaviour in the inertial region, that $R_1 \sim t^{-1/6}$ while $R_2 \rightarrow$ constant, but clearly

neither term is as yet anywhere near to its final asymptote if the theory is correct.

That the simulation is still far from the final asymptotic behaviour in the inertial region is supported by turbulence theory. The regime of Reynolds numbers, $\mathrm{Re}_\lambda \sim 20$, in which both the single fluid turbulence study of Chapter 4 and the spinodal decomposition simulations in the inertial region are located is, by turbulence standards, a "low" Reynolds number region. Turbulence doesn't exhibit truly Reynolds number independent scaling behaviour until the Reynolds numbers are very large, large enough for an appreciable "inertial range" to form between the large scales where the energy driving the turbulence is input, and the small scales where energy dissipation is taking place. Thus the asymptotic behaviour of the spinodal system should not be reached until the dissipation scales have been decoupled from the driving scales by a significant "inertial range". As noted in Chapter 4, such a regime is barely attainable for single fluid turbulence DNS with today's computational resources, so for the spinodal problem it will not be easy to test this using simulation methods in the near future[8].

6.4.2 Structure factors of the NSE terms

Further information on the behaviour of the NSE terms can be obtained by calculating the structure factor for each term. This will provide information on the dominant length scales associated with them, showing whether each term is most active at a narrowly defined single length scale or over a broad range. For example, intuitively one might expect that the viscous term would be associated with small length scales since dissipation usually takes place through small scale fluid motion, while the nonlinear term would be associated with intermediate length scales between the domain size and the dissipation scales since this term is associated with energy transport from large to small scales (in turbulence theory, the "energy cascade").

Figure 6.10 shows structure factors for the NSE terms for two runs, Run027 from the viscous region and Run031 from the inertial region. Looking first at Figure 6.10 (left), the run in the viscous region (where the viscous term can be seen to be dominant over the inertial terms as expected), the structure factor of the viscous term takes the

[8] Unless, perhaps, some form of large eddy simulation (LES) method can be combined with a two-fluid model.

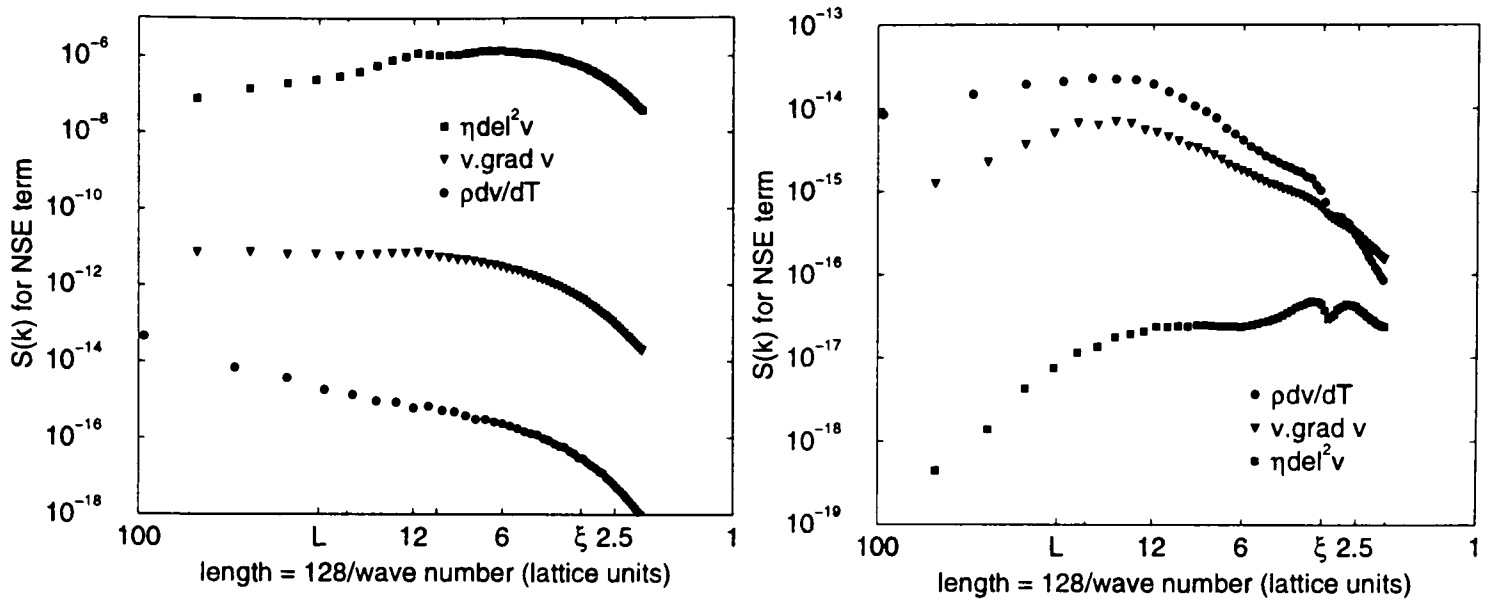

Figure 6.10: *Structure factor of the viscous (squares) and nonlinear (triangles) terms in the NSE. Left: Run027 is in the linear region with* $L_0 = 36$. *Right: Run031 is in the inertial region with* $L_0 = 0.0003$. *Both are shown on a log-log plot for the timestep at which* $L \simeq 25$ *lattice units.* $L = 25$ *is marked on the x-axis along with the interface width,* $\xi \simeq 3$. *(The* $\rho\partial \mathbf{v}/\partial T$ *data is from the corresponding* 96^3 *runs.)*

form of a broad peak stretching from a small secondary peak at around 12 lattice units (which is around half the domain size, $L(T) = 25$), down to the interface width, $\xi \simeq 3$. As anticipated, then, the dissipation is taking place over the smaller length scales in the system. The small peak at around 12 lattice units is a manifestation of the domain size in the dynamics, it is present at around $L(T)/2$ throughout the run.

In Figure 6.10 (right), the run in the inertial region, the viscous term is, as expected, smaller than the inertial terms, but dissipation is always relevant in fluids, even at very high Reynolds numbers, because there must always be a way to dissipate energy in the system. At length scales of around 6 lattice units, the structure factor of the viscous term is within a factor of 80 of the inertial terms, which means the terms themselves are within a factor of 9 of each other. At the length scale of the domain size, around 25 lattice units, this increases so the terms are around a factor of 25 apart. The shapes of the structure factors show peaks at different lengthscales. The viscous term is similar in shape to that in the viscous region (Figure 6.10 (left)), with the addition of two large peaks around the size of the interface width. In Section 3.6.5 such peaks (in the velocity structure factor) were shown to arise from the interface. This implies that the largest dissipative forces, and therefore most dissipation, are happening close to the interface.

The acceleration term has a broad peak in the structure factor around the size of the interface at 25 lattice units, and tails off quite sharply below 10 lattice units. The nonlinear term has a structure factor with a broad peak centred around 15 lattice units, intermediate between the length scale of the interface, $L(T) = 25$, and the dissipation length scales. which are concentrated at less than 12 lattice units. This corresponds to what would be expected from turbulence theory (see Section 2.5) where the nonlinear term is the mechanism by which energy is transported from large to small scales without much dissipation of energy taking place in the intermediate length scales. But there is still considerable overlap between the length scales for each term, which is also what would be expected for relatively "low Reynolds number" turbulence.

Analysis of the structure factor for the viscous and nonlinear terms of the NSE in the viscous and inertial regions has thus confirmed the expected length scales pertaining to these terms. Strong differences beteween the viscous and inertial regions are observed in the structure factors, and the basic features of the smaller scale structure of the fluid have been highlighted, showing that energy is transferred from the scale of the domain size down to smaller scales where dissipation takes place.

6.4.3 Dissipation rate

The dissipation rate is crucial to the energy balance in the simulation. Energy is being transferred from the interface to the fluid motion at roughly the expected rate since the domain growth rate implies the corresponding shrinkage rate for the interfacial area (see Section 2.3.1), and the domain growth, $L(T)$ is observed to follow the scaling predictions (see Section 5.3.3). To complete the energy balance, energy must also be removed from the simulation at the correct rate through dissipation. This is dependent on the small length scales being modeled correctly in the fluid, since dissipation takes place through small scale fluid motion – velocity gradients in the model equations. The dissipation rate can be calculated directly from the velocity field,

$$\varepsilon = \eta \sum_{lattice} k^2 S_v(\mathbf{k}) = \eta \langle (\nabla \mathbf{v})^2 \rangle_{lattice}. \tag{6.5}$$

Simple scaling theory predicts that the dissipation rate will always scale as t^{-2}. The new scaling analysis of Section 2.4 predicts the scaling to be $\varepsilon \sim t^{-2}$ in the viscous

region, (unchanged), and $\varepsilon \sim t^{-5/3}$ in the inertial region, see Table 2.1. A scaling plot of the dissipation rate can be seen in Figure 6.11. The dissipation rate for each run has

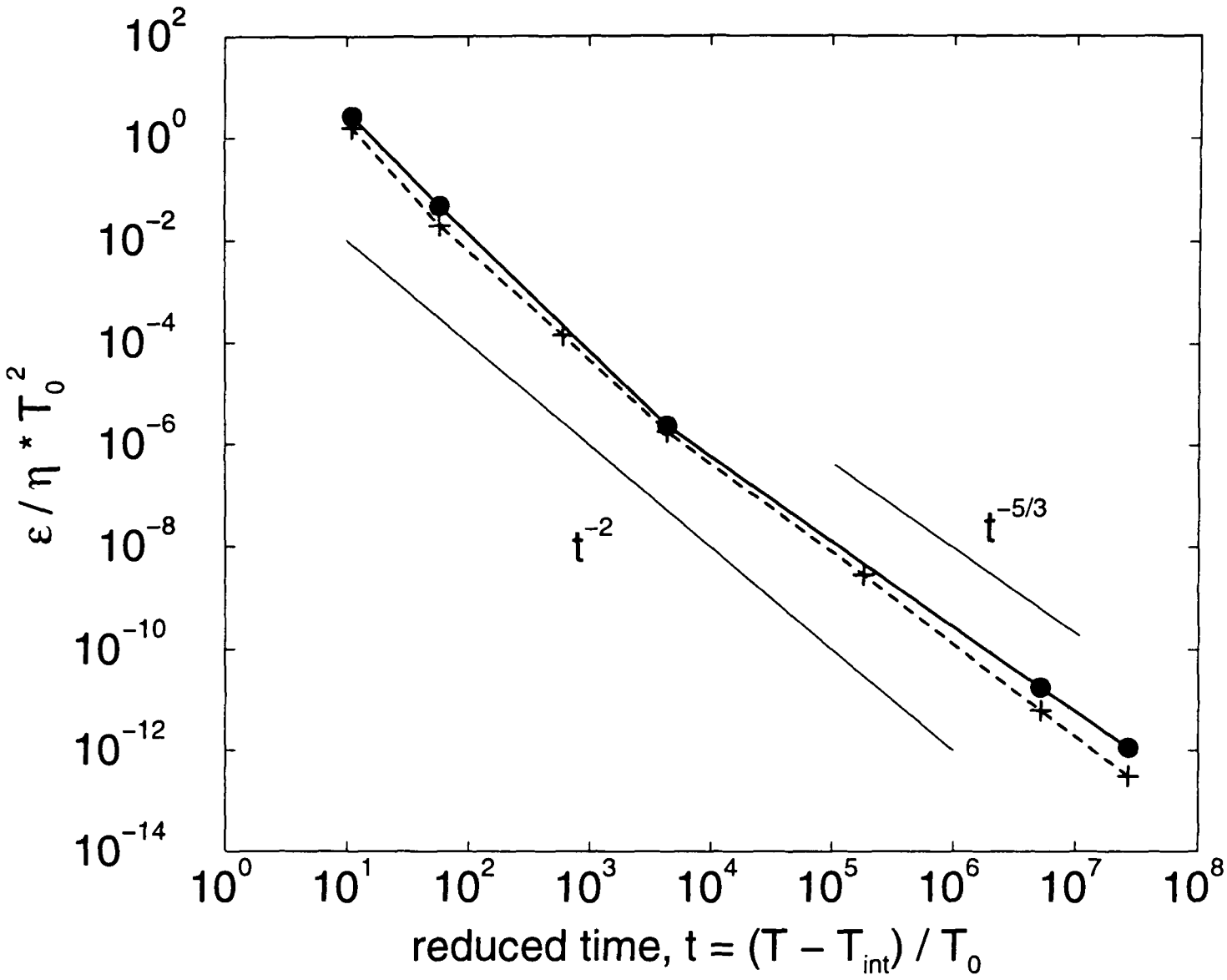

Figure 6.11: *Dissipation rate at time step when domain size is 30 simulation units for Runs in Table 5.2 (circles, solid line) and Runs in Table 5.2 (plus, dotted).*

been scaled by T_0^2/η to non-dimensionalise it, while the time has as usual been scaled as $(T - T_{\text{int}})/T_0$ using the intercept obtained from the $L(T)$ scaling, see Section 5.3.2. Individual points for domain size $L(T) = 30$ are shown, both 256^3 coarse-grained data and 128^3 data are plotted.

In the inertial region, the agreement with the prediction of the new scaling theory of $t^{-5/3}$ is reasonable. However, in the viscous region, the results deviate somewhat from the prediction (by both simple and new scaling theory) of t^{-2}. The observed dissipation rate is higher than predicted by scaling theory. Anomalies have already been noted in the viscous region in Sections 6.2.2 and 6.2.3, where the velocity itself and associated length scale, $L_v(T)$ were analysed. These will be returned to in Section 6.5.

6.4.4 Taylor and Kolmogorov microscales

The predictions of the new scaling theory presented in Section 2.4 included two new length scales associated with the fluid velocity. These were identified with the well-known length scales from turbulence theory, the Taylor microscale, $\lambda = \sqrt{5\eta\langle v^2\rangle/\varepsilon}$, Equation (2.52), associated with first derivatives of the velocity, and the Kolmogorov microscale, $\lambda_d = 2\pi(\eta^3/\rho^3\varepsilon)^{1/4}$, Equation (2.54), associated with second derivatives of the velocity (in the inertial region). The new scaling theory predicts that λ and λ_d should both scale differently from $L(T)$ in the inertial region; $\lambda \sim t^{1/2}$, and $\lambda_d \sim t^{5/12}$. (In simple scaling theory, λ is predicted to scale the same way as $L(T)$, while λ_d, being a microscopic length scale (associated with the dissipation), is predicted to scale differently, as $t^{1/2}$ throughout.)

To compare λ and λ_d with $L(T)$, Figure 6.12 shows both in simulation units for each run in Table 5.1 and Table 5.2, evaluated at the timestep for which the domain size is 30 lattice spacings. This is equivalent to plotting $\lambda/L(T)$ and $\lambda_d/L(T)$, since $L(T)$ is held constant in simulation units, but also allows the values to be compared with the size of the lattice spacing and the system size. Since small length scales are involved, coarse-grained data is likely to introduce significant errors[9]. Data from 128^3 systems has therefore been used for the remainder of the calculations in this section.

As can be seen in Figure 6.12, $\lambda/L(T)$ is to a first approximation constant over all the runs (which would indicate $\lambda \sim L(T)$), although it is roughly a factor of two larger in the crossover region compared to the viscous and inertial regions. The new scaling theory predicts that $\lambda/L(T) \sim t^{-1/6}$ in the inertial region, and the 128^3 data isn't far off this. In contrast to this, $\lambda_d/L(T)$ clearly does not scale as $t^{-1/2}$ in the viscous region, as predicted by both scaling theories. In the inertial region, though, $\lambda_d/L(T)$ is not far from the prediction of the new scaling theory of $t^{-1/4}$ (simple scaling predicts $t^{-1/6}$). In summary, then, in the inertial region both λ and λ_d are approaching the predictions of the new scaling theory, while in the viscous region, both show substantial deviations from the common predictions of new and simple scaling theory.

[9]The values from the coarse-grained 256^3 data in Figure 6.12 don't look very different from the 128^3 data on a log-log plot but the differences are in fact of the order of 35%.

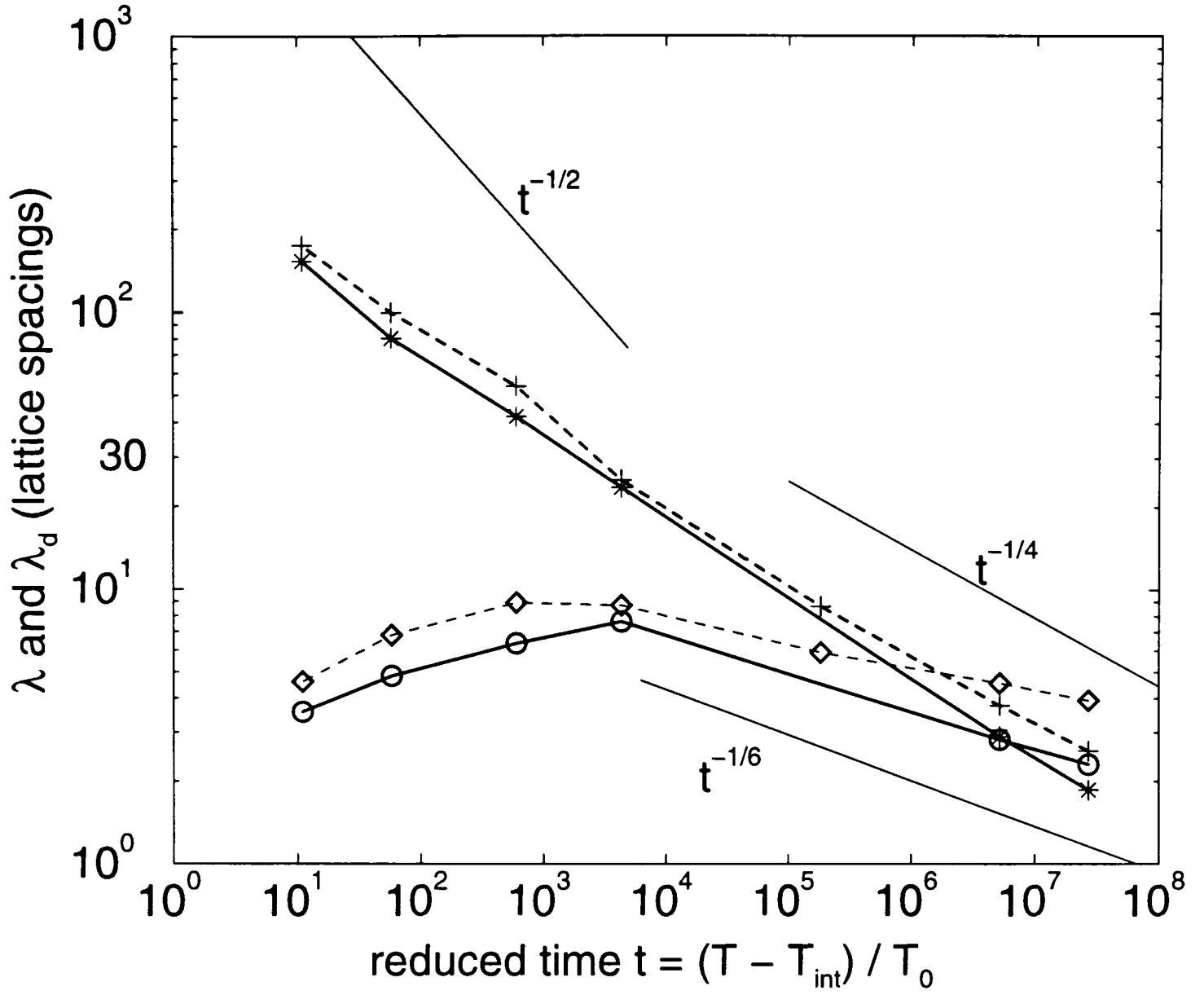

Figure 6.12: *Dissipation scale, λ_d, for runs in Table 5.1 (plus, dashed), and runs in Table 5.2 (stars, solid); Taylor microscale, λ for same runs (diamond, dashed; circles, solid respectively). All in lattice units for domain size of 30 lattice units.*

6.4.5 Resolution of the energy cascade

The Kolmogorov microscale has a further significance that is especially important for numerical simulation. In a turbulent fluid, λ_d is expected to be smaller than λ, and to mark the smallest length scale that is important in the system for dissipation. Clearly, for the dissipation to be correctly modeled in simulations, it is important that smallest relevant length scale is fully resolved on the lattice. There is some dispute over exactly how small λ_d can be in relation to the lattice spacing for the dissipation to remain correctly modeled, a factor of 1.0 to 1.6 has been put forward, see for example, Eswaran and Pope (1988), Yeung and Brasseur (1991).

It can be seen from Figure 6.12 that λ_d is only smaller than λ for the most inertial 128^3 run, where (for $L(T) = 30$) $\lambda_d = 1.8$ and $\lambda = 2.3$ (lattice units). Elsewhere, the

smallest length scale in the velocity field is λ, and in the most linear run, $\lambda = 3.5$, having dropped from a peak at 7.5 in the crossover region. All of these values for the length scales are larger than the lattice spacing. Since they characterise the lengths over which the velocity gradients are evaluated, this should indicate that the velocity is being modeled correctly at small scales, although the value of $\lambda_d = 1.8$ is quite close to the limit in the most inertial run. However, no estimate of errors has yet been made for the evaluation of the derivatives used to estimate λ_d. The method used to calculate the derivatives (Fourier space) has been compared with a real space finite difference method in Section 3.6.4, where significant differences were found beteween the methods, especially at small scales. An error of the order of a factor of two might therefore not be unreasonable for the uncertainty in the value of the derivative, leading to errors in λ of 100% and λ_d of 40% (due to the fractional powers of ε in the expressions for λ and λ_d).

A further factor that could produce a misleading estimate of these two lengths is that much of the dissipation occurs in the boundary layer near the interface where the velocities are largest. Therefore, calculations that average over the whole system (as have been used here), while fine for single fluid, isotropic, homogeneous turbulence, may not accurately predict the smallest relevant length scale in the two-fluid spinodal system.

On balance, it appears that the energy cascade is fully resolved in most of the simulations, but the most inertial runs may be marginal in this respect. In common with several other aspects of the simulations (such as the diffusion, see Section 5.4.1), these runs define the boundary of what is possible using this simulation method with current computational resources.

6.5 Apparent scaling violations in velocity statistics

In the previous sections, overall it has been found that, comparing *between different* runs, the various velocity-related quantities scale in reasonably good agreement with the new scaling theory in the inertial regime. In comparison, the simple scaling theory does not do so well for the inertial region. In contrast to this in the viscous region, where

both simple and new scaling theories predict the same scaling, significant deviations from the predictions are found.

So far, only the overall scaling between different runs has been considered in detail. It has already been seen in Figure 6.7 for the Reynolds number based on the Taylor microscale, Re_λ, that significant differences in the scaling *within a single run* and between different runs also exist in some cases. This section will look more systematically at the quantities showing this type of non-scaling behaviour, attempt to draw out some patterns, and make suggestions for the possible causes.

6.5.1 Scaling behaviour of the NSE terms

Data from various 96^3 (for the acceleration term) and 128^3 runs has been scaled and plotted on a single scaling plot, see Figure 6.13. Each data set shows the time evolution

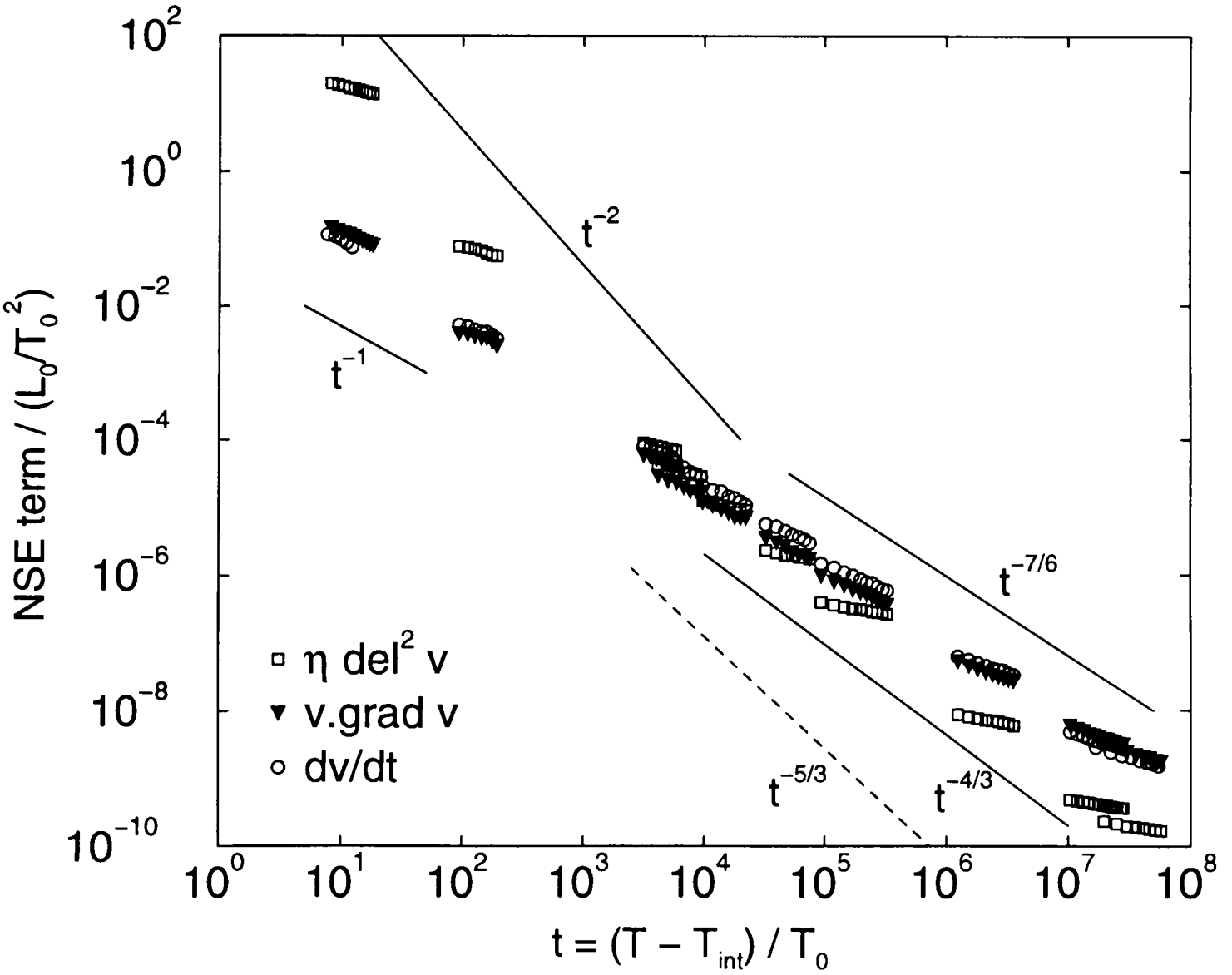

Figure 6.13: *NSE terms for all runs scaled. Most of this data is for* 96^3 *systems, with* 128^3 *data where available.*

of one of the NSE terms from a single run, nondimensionalised by dividing by L_0/T_0^2, and with the time scaled according to $t = (T - T_{\text{int}})/T_0$ (see Section 5.3.3).

Clearly none of the terms are showing good scaling behaviour since none of the sets of lines join up into a single curve. But overall, the relative positions of the lines are following the predicted scaling behaviour of t^{-2} in the linear region for the viscous term, and $t^{-4/3}$ or $t^{-7/6}$ in the inertial region[10], see Table 2.1. Even the scaling of t^{-1} for the nonlinear term in the viscous region is as predicted by the new scaling theory, see Appendix B, Equation (B.6). However, within each run the quantities are falling more slowly than the predictions.

There are two computational factors that could be contributing to this non-scaling behaviour:

- The data has been scaled using the same intercept, T_{int} as was determined from the fitting procedure for $L(T)$. If there is a time delay between the impulse from the interface and the response in the NSE term, a different time intercept would be appropriate. However, this would only be expected to affect the nonlinear and viscous terms in the inertial region, since the acceleration term, $\rho\partial\mathbf{v}/\partial T$, is expected to follow the interface. Furthermore, a larger value of T_{int} would affect the scaling by making the slope of the lines even shallower. Therefore, although the value of T_{int} might certainly be contributing to the inaccuracy, it cannot explain the observed non-scaling.

- The use of 96^3 data for obtaining $\rho\partial\mathbf{v}/\partial T$ may be subject to finite size effects that mask the true scaling. There is only a range of about 5 lattice spacings over which data from 96^3 systems is within the usable data constraints set in Section 5.4.3 for the order parameter data. More than this has been plotted in Figure 6.13 for the sake of clarity, but there does not seem to be any trend whereby data for early times has better scaling.

Thus, while both of the above factors may be relevant to the accuracy of the results, neither can explain why all three terms from the NSE fail to scale in both the viscous and inertial regions.

[10] With no claim to distinguish between $t^{-4/3}$ and $t^{-7/6}$ at this accuracy, though the $t^{-5/3}$ predicted by the simple theory for the viscous term in the inertial region does look too fast.

6.5.2 Non-scaling in the dissipation rate

A scaling plot of the dissipation rate can be seen in Figure 6.14. Like the NSE terms, it

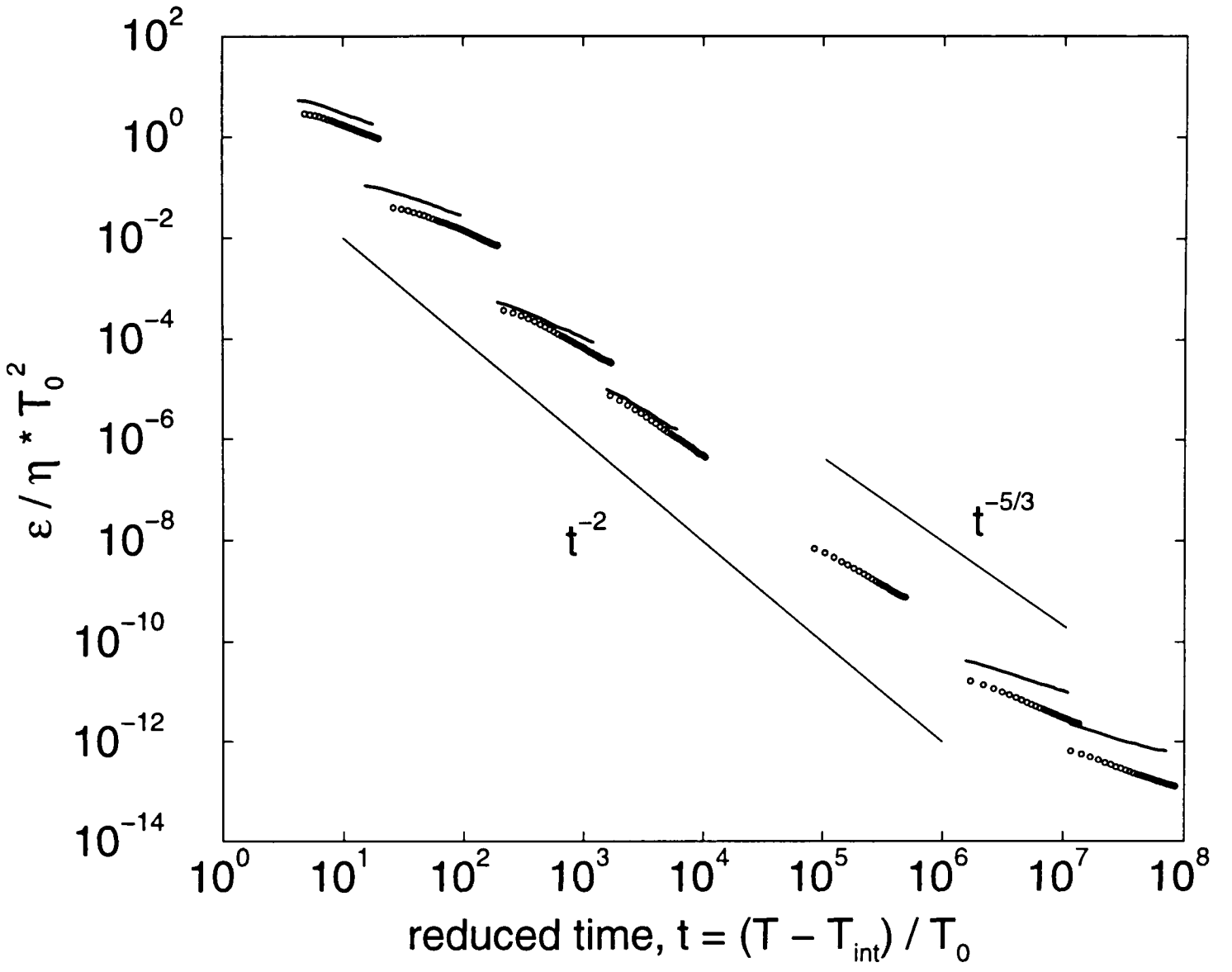

Figure 6.14: *Dissipation rate for Runs in Table 5.2 (solid line) and Runs in Table 5.2 (open circles).*

is immediately obvious that the dissipation rate is not showing good scaling behaviour. The deviations from the predicted scaling behaviour are most pronounced in the viscous region (top left of Figure 6.11), where the prediction is t^{-2}, while the observed scaling within runs is closer to t^{-1}. In the crossover region, the scaling within each run is fairly close to the overall scaling between runs. (There is no prediction for what scaling should be seen in the crossover region, but what is observed is around $t^{-5/3}$, the prediction from the new scaling theory for the inertial region.) In the inertial region, the scaling within runs is slower than the predicted $t^{-5/3}$. Both are considerably slower than the simple scaling prediction of t^{-2} throughout both the viscous and inertial regions.

The most viscous and most inertial runs also show the largest deviations between the

results from the 128^3 systems and the coarse-grained results from the 256^3 systems. The observed deviation is in the magnitude of the dissipation only, rather than the time dependence, suggesting that the coarse-graining alone is enough to account for this, and there is no dependence on the system size contributing to the non-scaling behaviour. This was confirmed by coarse-graining the 128^3 data, whereupon it agreed with the coarse-grained 256^3 data. This suggests that it is effects at the microscopic length scales that are the source of the non-scaling behaviour.

6.5.3 Non-scaling in the Taylor and Kolmogorov microscales

To see how λ and λ_d scale within runs, scaling plots have been done of both lengths, i.e. λ/L_0 and λ_d/L_0 against t. This is shown in Figure 6.15. Clearly λ and λ_d don't scale

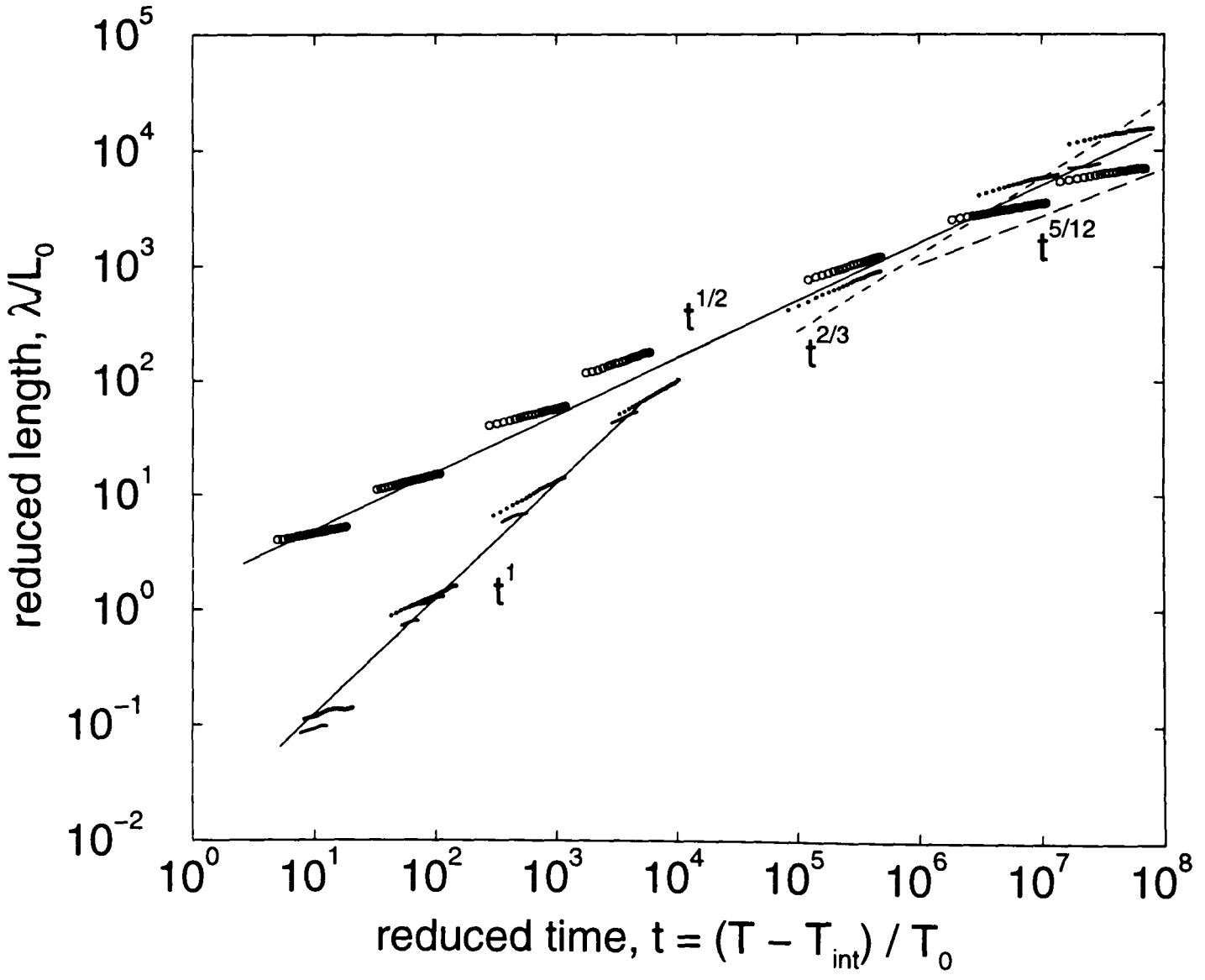

Figure 6.15: *Dissipation scale, λ_d, for runs in Table 5.2 (open circles), Taylor microscale, λ for same runs (shorter solid lines) and runs in Table 5.1 (filled circles). All in reduced units.*

within single runs in the same way as they scale between runs except in the middle of the crossover region. This is the same pattern as has already been seen for the NSE terms and the dissipation rate[11].

6.5.4 Summary of the non-scaling observations

Sections 6.5.1 – 6.5.3 have described in detail how for the NSE terms, the dissipation rate, and the Taylor and Kolmogorov microscales, the time dependence observed within runs is not the same as the time dependence between different runs on the appropriate scaling plot. It has also been noted that between runs, the new scaling predictions are followed fairly well in the inertial region, while in the viscous region, where all the scaling predictions are the same, there are significant deviations. In addition, it was shown in Section 6.2.3 (Figure 6.3), that the rms velocity does not scale as expected.

In order to try to build up a coherent picture of what is happening in the simulation, consider the energy flow through the system. The energy input from the interface to the fluid motion must be following the predicted scaling. This follows since the interfacial energy is proportional to the interfacial area, A_ξ, and $A_\xi \sim 1/L(T)$; with $L(T)$ observed to be scaling as predicted. As noted in Section 6.2.3, however, the total kinetic energy, although it is more or less as predicted in the crossover region, in the viscous region is larger than predicted by about 40%, and in the inertial region it is falling only as $\mathbf{v} \sim t^{-1/4}$ rather than the predicted $\mathbf{v} \sim t^{-1/3}$. In other words, there is excess energy building up in the velocity field at the extreme ends of the simulation range. Since energy is going *into* the fluid motion at the predicted rate, this implies that it is being removed by dissipation *slower* than the predicted rate. In other words, the dissipation rate must be smaller than expected. However, when the dissipation rate is calculated, it is observed to be decreasing more slowly with time than predicted, which implies that at later times it must become *larger* than predicted, not smaller. This strongly suggests that, somewhere along the line, there is a discrepancy in the evaluation of the dissipation rate. This could be due to limitations in the simulation code itself, **Ludwig**, or in the analysis code, or both.

[11] Indeed, the Kolmogorov microscale is directly calculated from the dissipation rate, so must show corresponding behaviour.

Consider first the suggestion that the analysis code is incorrectly calculating the dissipation rate and related quantities. It is true that large errors, of the order of 100%, have been suggested as realistic for derivative related quantities, but these would simply alter the magnitude of the results, not the time dependence. To produce a different time dependence from the analysis code, a systematic error that increases or decreases with successive velocity data files in the time series is required. There is certainly no error of a simple programming type, since consistent results are obtained whatever order the data files are processed in. Furthermore, it cannot be due to the method used to evaluate the derivatives, since checks have been done using finite difference gradients that produce the same results for the time dependence.

If, instead, the problem is in the simulation code, **Ludwig**, then the implication is that the smallest length scales (on which the dissipation depends) are not, after all, being adequately modeled. In Section 6.4.5, where this issue was discussed in relation to the size of the Taylor and Kolmogorov microscales, it was noted that though all the calculated values were larger than the lattice spacing, the uncertainties in the calculations pushed these values rather close to the limit. The smallest values of λ and λ_d were found in the most inertial and most viscous runs, consistent with the observations of the greatest departure from the predicted scaling in these regions. In both the linear and inertial regions, it seems plausible that the discrepancies arise when the velocity gradients become too steep for the lattice to fully resolve them, leading to underestimates[12]. In the viscous region this would be because the high viscosity damps the fluid motion over a short distance, while in the inertial region the turbulent flow introduces small scale eddies that approach the size of the lattice spacing. This suggests that a limitation has been reached in the simulation method in relation to modeling the dissipation both in the linear and inertial regions. It is interesting that both dissipation and diffusion (see Section 5.4.1) seem to set similar limits on the range of parameters available to the simulation.

The consequences for the veracity of the model are less clear, since excellent results

[12] Compare Section 3.6.3 and 3.6.4, where modification of the interfacial tension due to the discrete numerical approximation of the order parameter gradients across the interface is discussed. As in the case of the interfacial tension (where everything was self-consistent provided the value of the interfacial tension used in subsequent analysis was adjusted to compensate), the underestimation of the dissipation rate in the LB simulation may also be "internally self-consistent", although a simple compensatory adjustment such as altering the effective value of the viscosity, is not possible.

were obtained from the order parameter despite the discrepancies in the velocity data. One possibility is that there simply hasn't been time since the start of each simulation run for the discrepancies to build up far enough for the effects to show at all levels. The buildup of excess energy in the velocity field could lead to instabilities that cause the simulation to fail, and the simulation runs do, indeed, sometimes fail before reaching domain sizes beyond one quarter of the system size.

Another possibility is that the discrepancies in the dissipation rate *are* affecting the viscous runs, pushing them off linear scaling as observed, while in the inertial region the energy cascade is starting to decouple the length scales sufficiently to contain the discrepancies, resulting in good $l \sim t^{2/3}$ scaling. The discrepancy in $\rho\partial\mathbf{v}/\partial T$ is then due to an excess of small scale motion, with the large scales following the interface. It has not been possible, in the scope of this work, to distinguish between these possibilities.

6.6 Conclusions

Analysis of the individual terms in the Navier-Stokes equation has confirmed the result from the previous chapter that the simulation runs with a domain size growing as $t^{2/3}$ are truly simulating the inertial region. The magnitude of the inertial terms in the NSE compared to the viscous term shows the inertial terms dominating by an order of magnitude. In contrast, the simulation runs in the linear region have the viscous term dominating over the inertial terms by two orders of magnitude.

There are strong indications that the fluid behaviour in the inertial region of the separation process is at least partially turbulent. The skewness of longitudinal velocity derivatives is found to be -0.35 (cf -0.5 in turbulence), and the inertial scale and microscale Reynolds numbers correspond to those in the single fluid turbulence simulation, implying that the fluid is under conditions where turbulence can be expected. The pdfs are dominated by the correlations induced by the interface, so cannot be interpreted in themselves as unambiguously indicating the presence of turbulence, but the similarity of the structure factor of the vorticity with the corresponding single fluid turbulence structure factor also supports the presence of turbulence in the most inertial spinodal simulation run.

The length scale obtained from the velocity structure factor, $L_v(T)$, shows an interesting departure from the domain size, $L(T)$, measured from the order parameter. It appears that $L_v(T)$ follows a $t^{2/3}$ growth law not just in the inertial region, but throughout the range of t studied. This does not correspond to any of the predictions of the scaling theory presented in Chapter 2, but may be related to the finite size effects seen in the Taylor microscale affecting the velocity derivatives in the viscous region.

The smallest length scales associated with the velocity, the Taylor and Kolmogorov microscales, have been calculated and shown to be larger than the lattice spacing for all simulation runs. This should mean that the dissipation is being adequately modeled throughout the simulations. However, evidence from the non-scaling behaviour of the dissipation rate itself in the extreme viscous and inertial runs suggests otherwise, and it seems more likely that another limit has been reached in relation to the capabilities of the simulation. Many other quantities related to the velocity also do not scale as predicted within individual runs, and some also fail to do so between runs. All the non-scaling results are consistent with the dissipation rate being too low in both the viscous and inertial regions, leading to excess energy building up in the fluid motion.

Much of this analysis finally ran into limitations of resolution, accuracy and simulation parameters. Undoubtedly the most interesting further work would require an increase in computing power and possibly also extensions of the simulation method to reach further into the inertial region. Further work that could be done with the existing velocity field data to clarify and extend the work presented here could include:

- Further investigation into the dynamics on the scale of the interface to elucidate what is happening at the dissipation scales.
- Compare the results of a system with no inertial terms at all, with a viscous run (full NSE), to see if the observed velocity length scale, $L_v(T)$, differs. This would test the idea that the inertial terms are having a perturbative effect on the velocity field that is producing the observed difference between the order parameter and velocity length scales.
- Look at the energy balance and transport through different modes in the system to see how long it takes for energy input from the interface to finally dissipate, and what it does along the way.

- Investigate the dynamics in the crossover region in more detail to elucidate exactly how the inertial terms build up their contribution to the fluid dynamics, with a view to developing a quantitative theory of crossover region dynamics. The simulation seems to work best in this region of parameter space, allowing more precise tests to be done.

- Further investigation of single fluid turbulence using lattice-Boltzmann methods and comparison with the two-fluid spinodal system, to understand why the presense of the interface seems to have a stabilising effect on the system.

These suggestions are left for future work.

Chapter 7

Spinodal decomposition: persistence behaviour

7.1 Introduction

The final piece of analysis that has been carried out on the data from the LB simulations of spinodal decomposition of a binary fluid mixture, is a study of the persistence behaviour of the order parameter field. Persistence exponents were first investigated by Bray et al. (1994) and Derrida et al. (1994) in the context of one dimensional diffusive systems. Persistence exponents can be defined for systems where there is an order parameter whose time evolution can be followed at each point. It is most easily understood for an order parameter that takes just two equilibrium values (spin up/down), but the concept is easily generalised (e.g. red/blue fluid for binary fluid mixtures). The density of points that never see a change in order parameter from the initial value as the system coarsens, the "no-flip fraction", N_F, will, for a conserved order parameter, or a quench to zero temperature, typically decay as a power law, $T^{-\theta}$, where θ is the persistence exponent. For example, for the q-state Potts model in one dimension, Derrida et al. (1994) found from simulations, and later proved analytically (Derrida et al., 1995), that $\theta \simeq 0.37$ for $q = 2$, $\theta \simeq 0.53$ for $q = 3$ and $\theta \to 1$ as $q \to \infty$. It is also possible to define persistence exponents for systems with non-conserved order parameters at finite temperature by coarse-graining, see Cueille and Sire (1999). (In

general, N_F defined for a single site in a system with non-conserved order parameter will decay exponentially at finite temperature due to thermal noise.)

Derrida et al. (1996) and Majumdar et al. (1996) claim that the persistence exponent, θ, is a further independent exponent in addition to the two independent static, and two dynamic exponents already known. As with most other critical systems, analytical calculations are difficult; a few exact results exist, see Bray et al. (1994) and Derrida et al. (1995). Some mean field calculations have been done by Majumdar et al. (1996), however, mean field approximations also predict that θ is not independent of the other critical exponents. This rests on the assumption that the order parameter dynamics is a Markov process, and Derrida et al. (1996), Majumdar et al. (1996) argue that in general this is not the case, and thus θ is, in fact, independent of the other critical exponents.

In this Chapter, the order parameter data from the spinodal decomposition of the 3-D binary fluid system discussed in the Chapter 5 has been used to investigate the behaviour of the persistence exponent in a system dominated by hydrodynamics rather than diffusion. First, some simple theory is outlined for the persistence exponents in the hydrodynamic spinodal binary fluid system. Next, the simulation results are presented, and finally the case of a two-dimensional binary fluid mixture is briefly considered.

7.2 Theory

For the 3-D binary fluid system it is unrealistic to expect to derive anything but the simplest approximate results using a theoretical approach. However, this will serve to illuminate the persistence-related quantities under discussion in this chapter, and show how they behave in the symmetric binary fluid mixture undergoing spinodal decomposition that has already been well-studied in the previous chapters. The simple results to be derived in this section will then be of assistance in the numerical analysis that follows.

Consider the time evolution of the value of the order parameter at a single point as the system phase separates and coarsens from the initially completely mixed state.

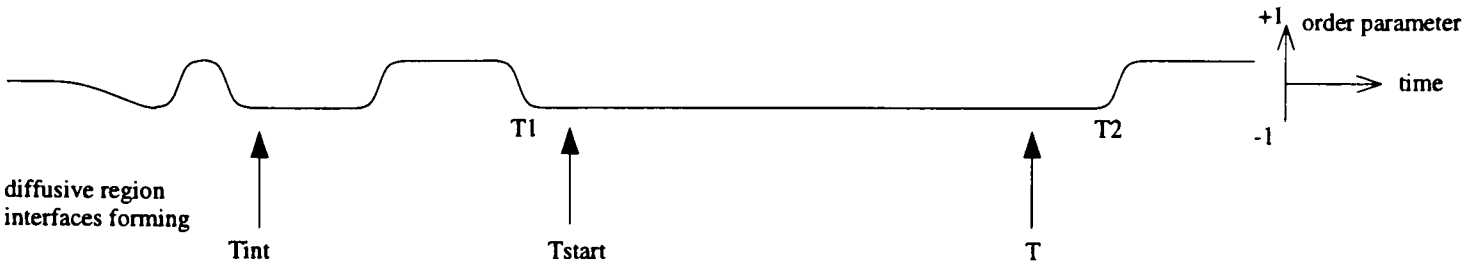

Figure 7.1: *Persistence timeline.*

This is represented as a graph in Figure 7.1. In order to focus on the behaviour in the hydrodynamic region, an initial state is chosen at a reference point, $T_{\mathbf{start}}$, a time corresponding to a domain size around $L_{\mathbf{min}}$, at which diffusive growth has fallen below 2% (see Chapter 5.2). The "no-flip fraction", $N_F(T/T_{\mathbf{start}})$ is then defined[1] as the density of sites that have not changed colour since $T_{\mathbf{start}}$.

In order to derive an approximate functional form for $N_F(T/T_{\mathbf{start}})$, it is useful to define two further quantities,

- the flip rate, $P_F(T)$ is simply the proportion of sites that changed colour between time step $T-1$ to T, and,

- the flip probability, $P(T, T_1)$, is the probability that a site changes colour at time T, *given that it last changed colour at time* T_1.

These two quantities are related as follows:

$$P_F(T) = \int_{T_{\mathbf{int}}}^{T} \mathrm{d}T_1 \, P_F(T_1) \, P(T, T_1), \tag{7.1}$$

where $T_{\mathbf{int}}$ is the zero point on the time scale, the time at which, (ignoring the finite width of the interfaces), the domain size is zero so that, in effect, every site flipped at $T = T_{\mathbf{int}}$. This equation says that the flip rate at time T is given by all the points that last flipped at time T_1 and are due to flip again at time T, i.e. $P(T, T_1)$, integrated over all possible prior flip times, $T_{\mathbf{int}} < T_1 < T$, and weighted by the number of sites with prior flip time T_1, i.e. $P_F(T_1)$.

[1] Scaling by $T_{\mathbf{start}}$ is equivalent to setting $T_{\mathbf{start}} = 1$, which is in any case the value of the initial reference time used in other studies.

7.2.1 Flip-rate model

Equation 7.1 is an integral equation in two unknown functions, $P(T, T_1)$ and $P_F(T)$. A solution for $P(T, T_1)$ can be obtained by making some assumptions about the asymptotic form of the simpler quantity, $P_F(T)$, for the 3-D hydrodynamic system. It has already been predicted from theory, and confirmed in Chapter 5, that the dynamics are determined by the basic scaling growth law, Equation (5.4), $L(T) = v(T - T_{\rm int})^{\alpha}$, where $L(T)$ is the characteristic domain size obtained as the first moment of the structure factor. This also identifies the zero point on the time scale with the intercept found from fitting the order parameter data in Section 5.3.2; henceforth $T_{\rm int}$ will be usually be set to zero, to simplify the algebra. Once the initial diffusive period is over, and the domains of red and blue fluid are separated by well-formed interfaces, lattice site changes colour from red to blue when an interface moves across them as the domains grow in size. The flip rate, $P_F(T)$, is thus given by the rate at which the interface moves through the system sweeping out a volume of points that change colour. So, an estimate of the area of the interface, and its average speed, will yield an estimate for $P_F(T)$.

The area of the interface is given approximately by $A_\xi(T) = V/L_{|\phi|}$ where V is the system volume and $L_{|\phi|}$ is a length measure described in Section 3.5, Equation (3.37). In that section it was shown from the data that, provided the diffusion isn't too low, $L(T) \simeq c_L L_\phi$, thus identifying the interfacial area per unit volume with c_L/L, where c_L is a prefactor close to two. As the system coarsens, the interfaces must move to accommodate the enlargement of the domains. It has already been shown in Section 6.2.3 that the average fluid velocity is comparable in magnitude with $\mathrm{d}L/\mathrm{d}T$, so it is reasonable to estimate the speed of the interface as $c_v\,\mathrm{d}L/\mathrm{d}T$, where c_v is a prefactor of order unity. In general, c_v depends on the geometry of the domains in relation to their size, $L(T)$. The domain geometry is very similar (though not identical, see Section 5.3.1) for all systems, whatever the value of the growth exponent, α, in part because of the topological constraints imposed by minimising the surface area in a symmetric fluid mixture, i.e. the interface has to be the same average "shape" under interchange of the red and blue fluids. The prefactor, c_v, can, therefore, like c_L, be expected to a first approximation to have the same value for all runs and all times large enough for the initial configuration to be forgotten.

The volume swept out per unit time will be $A_\xi(T)\, c_v\, \mathrm{d}L/\mathrm{d}T$, combining both c_L and c_v into a single prefactor, c, the flip rate per unit volume will be approximately,

$$P_F(T) = c\frac{1}{L}\frac{\mathrm{d}L}{\mathrm{d}T} = \frac{c\alpha}{T}. \tag{7.2}$$

As already mentioned, this approximation for $P_F(T)$ only applies once diffusive growth has ceased to be relevant to the domain growth, so the condition, $T \gg 0$ should be applied.

Substituting $P_F(T) = c\alpha/T$ into Equation 7.1 gives,

$$\int_0^T \mathrm{d}T_1\, \frac{T}{T_1} P(T, T_1) = 1, \tag{7.3}$$

where have set $T_{\mathrm{int}} = 0$.[2] This has solutions of the form,

$$P(T, T_1) = (\beta - 1) T_1^{\beta-1} T^{-\beta}, \qquad \beta \neq 1, \tag{7.4}$$

where β is an arbitrary exponent, as can readily be verified by substitution. The condition,

$$\int_{T_1}^{\infty} \mathrm{d}T\, P(T, T_1) = 1, \tag{7.5}$$

(i.e. all sites do, eventually, flip) is also satisfied, so $P(T, T_1)$ is a properly normalised probability.

7.2.2 "No-flip fraction", N_F

An expression can now be written down for the "no flip fraction", $N_F(T/T_{\mathrm{start}})$, the fraction of sites that have not changed "colour" since T_{start},

$$N_F = \int_0^{T_{\mathrm{start}}} \mathrm{d}T_1 \int_T^{\infty} \mathrm{d}T_2\, P(T_2, T_1) P_F(T_1), \tag{7.6}$$

i.e. count every point whose last flip was before T_{start} and whose next flip is after time T. Substituting for P_F and $P(T_2, T_1)$ gives,

$$\begin{aligned} N_F &= c\alpha \int_{T_{\mathrm{int}}}^{T_{\mathrm{start}}} \mathrm{d}T_1\, (\beta - 1) T_1^{\beta-2} \int_T^{\infty} \mathrm{d}T_2\, T_2^{-\beta}, \\ &= \frac{c\alpha}{\theta}\left(\frac{T_{\mathrm{start}}}{T}\right)^{\theta}, \qquad \theta > 0, \end{aligned} \tag{7.7}$$

[2] and where the condition $T_1 \gg 0$ has been ignored for the moment at the lower limit of the integral. This can be justified later by requiring any solution for, $P(T, T_1)$, to be small for $T_1 \gtrsim 0$ so that the contribution from this region of the integral is negligible. The proposed form of the solution, Equation (7.4) satisfies this condition.

setting $\theta = (\beta - 1)$ as the critical exponent.

Notice that the flip-rate model has provided an expression for N_F that has the exponent, θ, in the prefactor as well as being the asymptotic power of the decay. This puts helpful constraints on the data analysis, although for it to be really useful, the prefactor, c, has to be pinned down as precisely as possible. In a log-log plot,

$$\log N_F = \log(c\alpha/\theta) - \theta \log(T/T_{\text{start}}). \tag{7.8}$$

so plotting N_f against T/T_{start} should give a straightish line when viewed log-log, with slope $-\theta$ for $T \gg T_{\text{start}}$. The initial data near $T \gtrsim T_{\text{start}}$ will depart from this asymptotic behaviour and tend to $N_F = 1$ because by definition nothing flipped yet for $T = T_{\text{start}}$. The fit to the asymptotic slope should, however, have an intercept at $c\alpha/\theta$ for $T = T_{\text{start}}$.

7.2.3 "One-flip fraction", O_F

It is possible to go on to define a hierarchy of persistence quantities, of which N_F is the first. The "one flip fraction", O_F is the density of points that have changed colour exactly once since time T_{start}. Within the flip-rate model, an expression for O_F for this system can be derived in the same way as for N_F. The "one flip" occurs at time T_f with $T_{\text{start}} < T_f < T_2$. The probability of an initial flip before T_{start} at T_1 with $0 < T_1 < T_{\text{start}}$, then flipping at time T_f is $P(T_f, T_1)$. The probability of flipping again at time T_2 is then $P(T_2, T_f)P(T_f, T_1)$, provided the two flip events are independent of each other (so the probabilities can be multiplied). In other words, this model assumes that the flip probability, $P(T_2, T_f)$ is only dependent on the last time the site flipped, it has no memory of earlier flips. This requires a Markov process for the coarsening dynamics, which Derrida et al. (1996), Majumdar et al. (1996) claim is not generally the case for the non-hydrodynamic systems they have considered. This therefore constitutes another untested assumption in the flip-rate model under consideration.

To get the expression for O_F, integrate out T_1 and T_f, and integrate T_2 from $T \to \infty$. There will be a factor of $P_F(T_1)$ for the fraction of states that flip at time T_1,

$$O_F(T/T_{\text{start}}) = \int_T^\infty \mathrm{d}T_2 \int_{T_{\text{start}}}^{T_2} \mathrm{d}T_f \int_0^{T_{\text{start}}} \mathrm{d}T_1 \, P(T_2, T_f)P(T_f, T_1)P_F(T_1). \tag{7.9}$$

Substituting for P_F and $P(T_2, T_1)$ as before gives,

$$\begin{aligned} O_F &= \int_T^\infty \mathrm{d}T_2 \int_{T_{\mathrm{start}}}^{T_2} \mathrm{d}T_f \int_0^{T_{\mathrm{start}}} \mathrm{d}T_1 \, \frac{c\alpha}{T_1} \, \theta \frac{T_f^\theta}{T_2^{\theta+1}} \, \theta \frac{T_1^\theta}{T_f^{\theta+1}} \\ &= \frac{c\alpha}{\theta} \left(\frac{T_{\mathrm{start}}}{T} \right)^\theta \left[1 - \ln \left(\frac{T_{\mathrm{start}}}{T} \right)^\theta \right], \end{aligned} \tag{7.10}$$

after integrating by parts. This has a dominant logarithmic term so doesn't have an asymptotic power law decay, unlike the 1-D Ising model, in which O_F appears to have the same asymptotic behaviour as N_F, see Derrida et al. (1994, 1995). Again, this expression is only valid for $T \gg T_{\mathrm{start}}$ since $O_F \to 0$ for $T \to T_{\mathrm{start}}$. As with N_F, the (same) critical exponent θ appears both as an exponent and as a prefactor so providing an extra constraint on any fits to simulation data.

7.2.4 Other dimensions

Nothing in the theory so far is specific to three space dimensions, so there is the possibility that it may apply to two dimensional systems as well. The most likely flaw is that the approximation $P_F = c\alpha/T$ may not work since the interface doesn't completely interconnect in 2-D symmetric binary spinodal decomposition, see Wagner and Yeomans (1998). This will be investigated in more detail in Section 7.5.

7.3 Analysis method

Now that the basic theory has been described, providing some useful predictions on the form expected for the results, analysis of the data from the spinodal decomposition simulations will be considered. The data available for analysis from the largest spinodal decomposition runs, see Table 5.1, is typically saved every 200 to 500 time steps, $\Delta T_{\mathrm{stride}}$. It is also coarse-grained from a 256^3 lattice down to 128^3 by averaging over groups of eight neighbouring lattice points. This data can be used to calculate the four key quantities discussed in the previous section, P_F, $P(T_1, T_2)$, N_F and O_F, provided the spatial and temporal coarse-graining makes no significant difference to the results.

To investigate the effect of coarse-graining, a special run on a 96^3 grid was done with the key quantities calculated every time step. This extra computation significantly slows

down the computer run time so it isn't practical to perform larger simulations with single-step calculations. The results from a single-step calculation were then compared with the same run analysed over a stride of 100 time steps. The result of this comparison is shown in Figure 7.2 (left), with excellent agreement between the single-step and strided estimates of $P_F(T)$. The errors introduced by analysing only every ΔT_{stride}

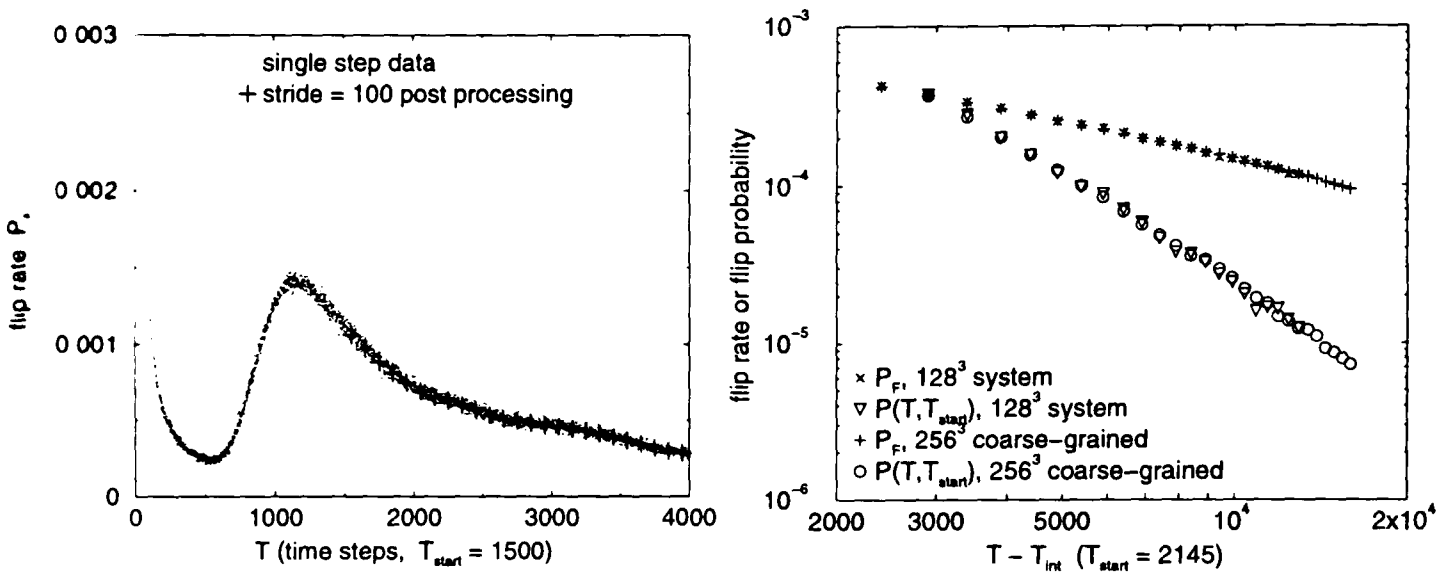

Figure 7.2: *Left: flip rate, P_F, for 96^3 system single step (dots) and stride=100 (crosses). Right: flip rate, P_F, and flip probability, $P(T, T_1)$, for 128^3 and 256^3 systems with otherwise identical parameters.*

steps rather than every single step centre on miss-counting sites that flip more than once in that period. If the flip rate, $P_F(T)$, is small then the number of multiple flips will be much smaller still so the errors will negligible. In all runs analysed, P_F, was found to be small even over the largest ΔT_{stride} used[3].

The shape of $P_F(T)$ in Figure 7.2 (left) for times $T < T_{\text{start}}$ clearly shows a transition from diffusive to hydrodynamic behaviour in the initial fall (diffusion), rise (interfaces start to move) and fall again (hydrodynamic). Thus $P_F(T)$ is a sensitive indicator of the system dynamics, and the choice of $T_{\text{start}} = 1500$ in this system is confirmed to be located, as desired, near the beginning of the hydrodynamic region but not too close to the transition from diffusive behaviour.

In order to analyse the order parameter data saved from previous simulation runs, code was written to read in successive order parameter files, use the specified start time as the reference configuration, and compare subsequent order parameter files to see how many sites have flipped in the intervening time interval, ΔT_{stride}, of 200 to 500 time

[3] In other words, $P_F \times \Delta T_{\text{stride}} \ll 1$ (a flip rate of one would mean every site flipped).

steps. From this, good statistics for P_F, N_F and O_F can be obtained as every point can be assessed according to if/when it next flips after T_{start}. The statistics are not so good for estimating $P(T, T_{\mathrm{start}})$, because the reference base is reduced to only those sites that flip between T_{start} and $\Delta T_{\mathrm{stride}}$ rather than the whole system; recall that $P(T, T_{\mathrm{start}})$ refers to the first flip happening exactly at T_{start}.

The effect of spatial coarse-graining was then checked by comparing the results of analysing strided data from 128^3 and 256^3 runs (with identical parameters apart from system size). The results of this comparison are shown in Figure 7.2 (right) for Run031 (128^3) and Run032 (256^3) for both $P_F(T)$ and $P(T, T_{\mathrm{start}})$. The only discrepancies are in the lower region of $P(T, T_{\mathrm{start}})$, and can be explained by poor statistics in this region.

The same comparisons were also done for the other two key quantities, N_F and O_F, with good agreement in all cases. The conclusion, therefore, is that spatial and temporal coarse-graining on the scale used in this analysis does not introduce significant errors into the results, and analysis of the largest data sets from the 256^3 runs can can be carried out in anticipation of reasonably accurate results.

7.4 Results

Analysis of the main data sets from Table 5.1 provides a range of results over the linear, crossover and inertial regions. The actual process of fitting the data, is, however, somewhat complicated, because of the limited range of data available for determining exponents. The procedures described here are as follows:

- First, the flip rate, P_F, is considered in detail to see what value is observed for the prefactor, c, and to see what variation there is between the behaviour in the linear and inertial regions.

- Next, the "no-flip fraction", N_F, is considered. Since it is necessary to continue to allow for variation in the prefactor, c, a family of fits to the tail of N_F is constructed, and the predictions for the value of the persistence exponent, θ, considered as a function of the prefactor, c.

- Results from N_F alone are not sufficient to produce good predictions on the value of θ, so the results from the "one-flip fraction", O_F, are considered in combination with the results already obtained for N_F. This provides further constraints on the possible values for θ.

- Finally, the results for the flip probability, $P(T, T_{\text{start}})$, are checked for consistency with the estimates for θ. Since the expression derived for the flip probability doesn't depend on the prefactor, c, or the growth exponent, α, this is a useful check, however, since the statistics are not so good for $P(T, T_{\text{start}})$, in practice this does not pin down the value of θ to much further precision.

- The overall results for the value of θ in the linear and inertial regions are then summarised.

The steps outlined above are now elaborated in the following five sections.

7.4.1 Flip rate, P_F

The main question to be investigated by analysing the flip rate is whether it really follows the approximate theoretical expression, $P_F = c\alpha/T$, Equation (7.3), derived in Section 7.2.1, and whether the prefactor, c, can be evaluated or constrained sufficiently to allow a strongly constrained fit to be done for θ in the analysis of N_F and O_F. Values for the growth rate exponent, α, and the zero time offset, T_{int}, are available for all the 256^3-sized runs, see Table 5.3. Fitting P_F as obtained from the simulation data with $c\alpha/T$ using the previously determined values of α and T_{int} for each run produces values for the prefactor, c, that vary with α, see Figure 7.3. In addition, the measured flip rates are somewhat variable when compared to $1/T$ (the straight line in Figure 7.3), although this can partly be explained since early times can be expected to differ from asymptotic behaviour. In order to determine the values and variation in c more accurately, a linear plot of the flip rate, P_F, scaled by $(T - T_{\text{int}})/\alpha$ was done, Figure 7.3 (right). It can be seen that the results roughly split into two groups corresponding to the runs found to be in the viscous and lower crossover regions of spinodal decomposition scaling, with prefactors around $c \simeq 1.25$, and runs in the inertial region with $c \simeq 2.2$.

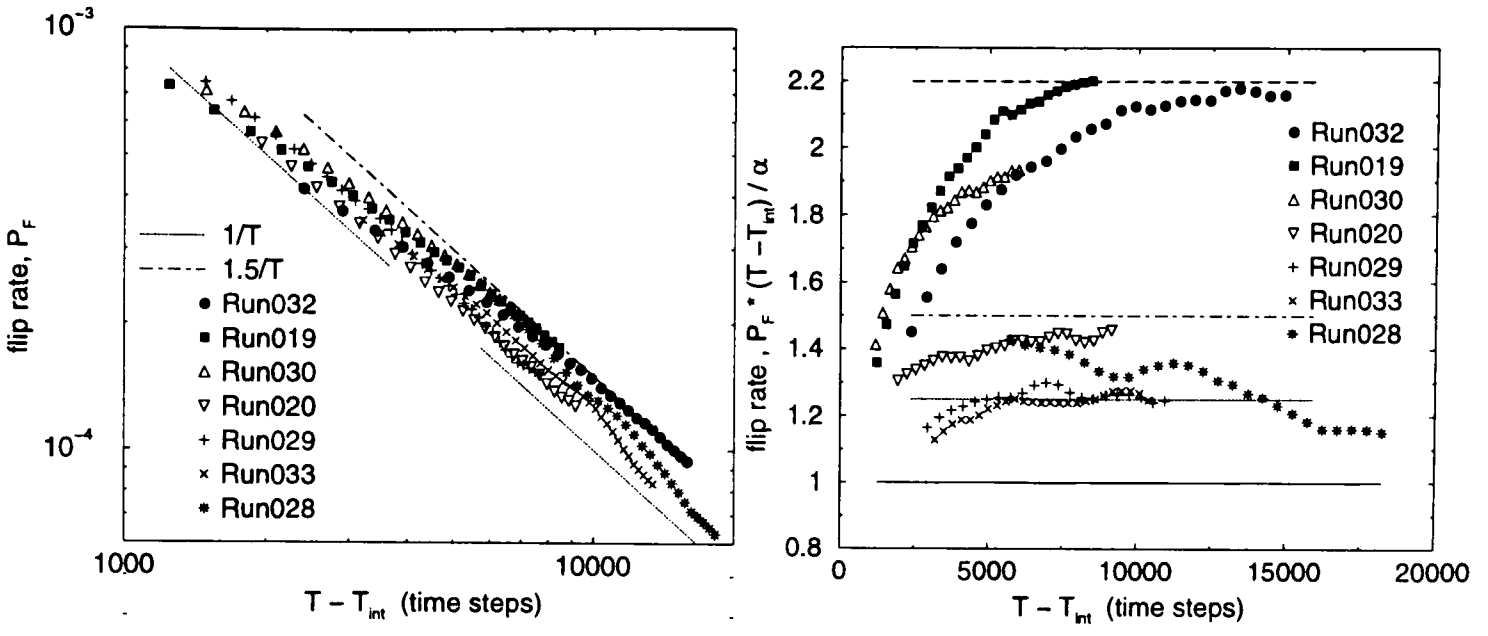

Figure 7.3: *Left: flip rate, P_F, for runs in Table 5.1, log-log plot. Right: flip rate, P_F, rescaled by $(T - T_{\text{int}})/\alpha$ on a linear plot so values of the prefactor, c, can be read off the ordinate axis.*

If this difference in the value of c is real, it implies that the geometry of the separating domains really is different between the linear and inertial regions. Any such difference is not apparent to the eye in visualisations of the interface, see Appendix A, but could be quite subtle and more linked to the dynamics (which have not been visualised in animation). There is some evidence from the structure factor analysis, Section 5.3.1, that there is a topological difference in the domain structure, but it is unclear whether this is enough to account for the observed difference in the value of c.

However, there is another possible reason why the measured flip rate may be higher than $c\alpha/T$ for the inertial region runs. Once the viscosity is low enough for inertial effects to become significant, the interface may exhibit capillary waves (see Section 3.6.5). This oscillation of the interface could increase the measured flip rate as sites near the interface repeatedly flip back and forth, but without contributing to the sweeping that removes sites from the "no flip" category. This motion isn't included in the $\mathrm{d}L/\mathrm{d}T$ assumption used to derive the expression for the overall flip rate. If this is a significant factor, the correct value of c to use in the subsequent fitting should be lower than the measured value for runs in the inertial region.

A variable prefactor, c, has therefore been carried through the fitting process so a better assessment can be made of whether the observed values of c in the flip rate analysis apply to the behaviour of the "no-flip" and "one-flip" fractions.

7.4.2 "No-flip fraction", N_F

The "no flip fraction", N_F, is the primary quantity of interest in this chapter, and the quantity from which the persistence exponent θ, is defined, $N_F \sim T^{-\theta}$. N_F has been calculated for the runs in Table 5.1[4]. The results, with the time step scaled as $(T - T_{\text{int}})/T_{\text{start}}$ and points for times at which $L(T) > L_{\text{max}}$ removed, are plotted in Figure 7.4 (left). In the data available ($\sim 20 \leq L \leq 64$) there is barely one decade

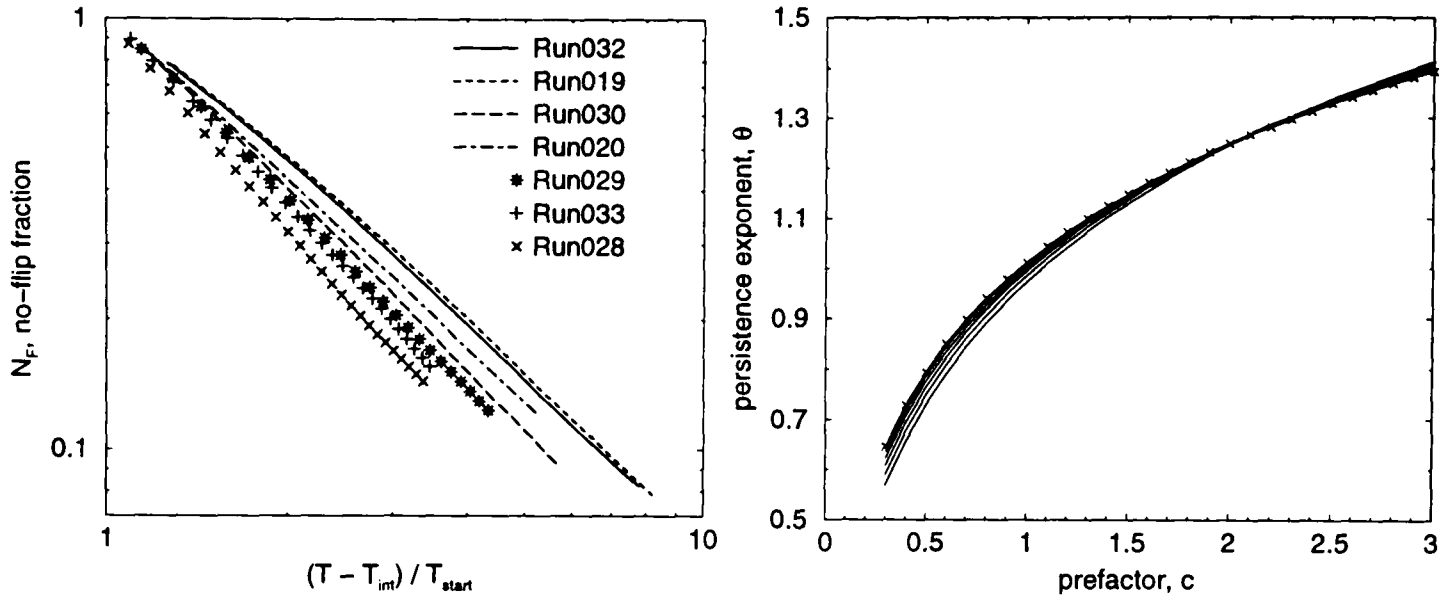

Figure 7.4: *Left: no-flip fraction, N_F, for runs in Table 5.1. Right: fitting N_F for Run032, θ against c curves.*

over which to estimate the slope of the tail, so a simple linear fit cannot produce a very accurate result, but superficial inspection suggests that θ is slightly greater than unity. The runs in the inertial region have tails that dip to around $N_F = 0.08$, while the linear runs stop (reach domain size $L = 64$) at around $N_F = 0.15$. The fitting procedure used is therefore somewhat complicated, in order to allow the effect of various values of the prefactor, c, to be assessed.

For each data point (N_F, T) in the tail region of a particular run, Equation (7.8),

$$N_F = \frac{c\alpha}{\theta}\left(\frac{T_{\text{start}}}{T}\right)^{\theta}, \qquad \theta > 0, \tag{7.11}$$

has been treated as an equation for θ as a function of c. After numerical solution for θ over a range $0.3 < c < 3.0$, this produces a family of curves, one per data point, shown in Figure 7.4 (right) for Run032 (for which the growth exponent, $\alpha = 2/3$). The crosses mark the line for the last data point. The curves can be seen to fan out in time step

[4]except Run022, which is rather a short run so wouldn't add much to the analysis.

order at each end, and a pivot region is apparent at around $c = 2$, where the curves cross. Closer examination of the data shows that the local pivot, i.e. the point at which neighbouring curves cross, is moving to the left with increasing time.

The local pivot point indicates the values of (c, θ) for which N_F as calculated from Equation (7.8) most closely matches the slope of the measured value of N_F at that point. However, since Equation (7.8) is an asymptotic form for N_F, this isn't necessarily the best estimate for θ; with the tail this short θ might still be expected to be some way from its large T asymptote. Nonetheless, the direction in which the pivot is moving should indicate which side the asymptotic values of (c, θ) lie, provided N_F is not oscillating around the asymptote.

For Run032, at the end of the tail of N_F, the pivot point is between $1.4 \leq c \leq 1.9$, corresponding to $1.13 \leq \theta \leq 1.23$. In contrast, for the value of $c = 2.2$ found from the flip rate in Section 7.4.1, $\theta = 1.28$ and is in the region of Figure 7.4 (right) to the right of the pivot where it is approaching the asymptote from above, which is inconsistent with the direction in which the local pivot is moving[5]. Thus, it seems that the best estimate of the value of the exponent, θ, as obtained from N_F, is inconsistent with the value of the prefactor, c, determined from P_F in the previous section. This is not necessarily a problem, as there are reasons why the measured value of c may be too high, but the limited data available for N_F precludes sufficient precision in the analysis to be confident on this point. In order to make further progress based on the available data, the fits for O_F and $P(T, T_{\text{start}})$ have to be considered alongside the fits for N_F.

7.4.3 "One-flip fraction", O_F

The "one-flip fraction", O_F, that measures how many lattice sites see exactly one change of fluid "colour", can be calculated from the order parameter data in the same way as N_F. The expression derived for O_F in Section 7.2.3, Equation (7.9), also contains both the prefactor, c, and the persistence exponent, θ, although it is not a simple power law like the expression for N_F. The data for O_F is shown in Figure 7.5 (left). It is

[5] These results must also be qualified by noting that there is further uncertaintly due to the errors in determining α (see Section 5.4), in calculating N_F, and in the fitting procedure.

difficult to assess whether it is approaching asymptotic behaviour in the tails since the theoretical approximation is not a simple power law, but contains a logarithmic term.

The same complicated fitting procedure as was used for N_F in the previous section (using c as a parameter for θ in Equation 7.10 for each data point in the tail) can also be applied to O_F. Figure 7.5 (right) shows the results for Run032 plotted along with the (c, θ) curves for N_F from Figure 7.4 (right). The curves for O_F show the same basic

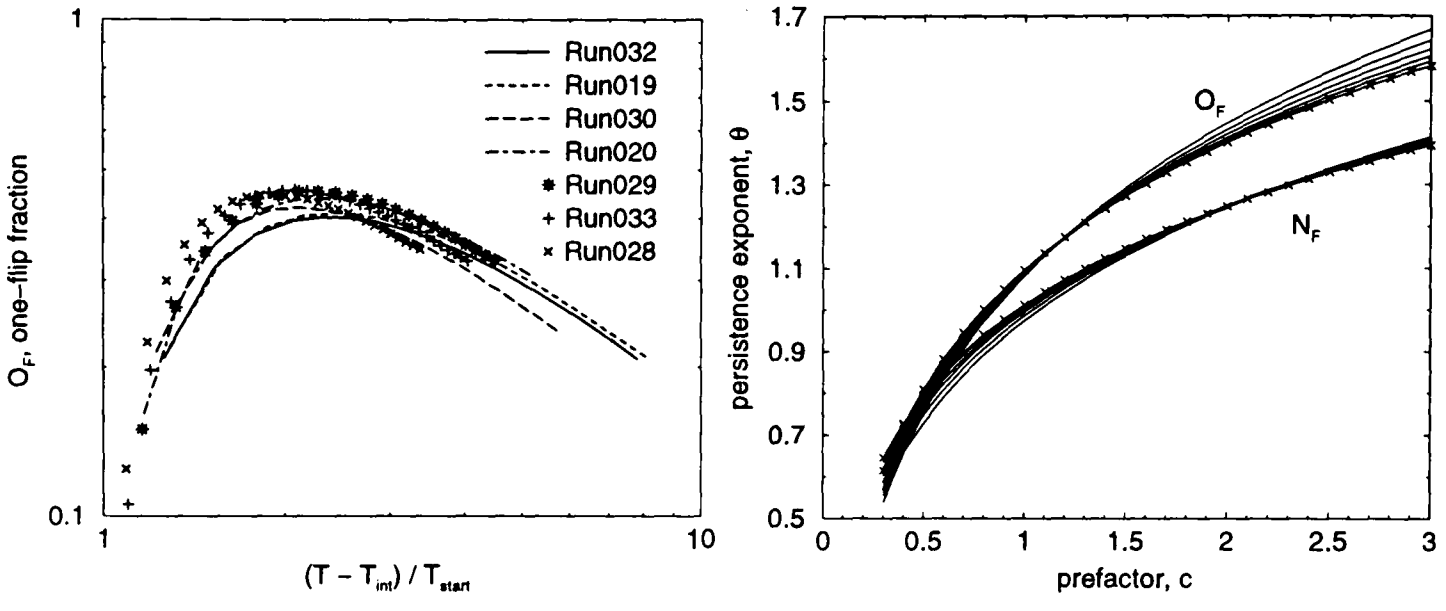

Figure 7.5: *Left: one-flip fraction, O_F, for runs in Table 5.1. Left: N_F and O_F fitting curves for θ against c for Run032.*

structure, fanned out at the ends in time step order, and with a pivot region at around $c = 1.1$, a much lower value than for N_F, which was at around $c = 2$. Investigation of the direction in which the local pivot point is moving in the O_F curves finds that it is moving to the right, towards the N_F pivot.

In the limit of O_F and N_F approaching their asymptotes, both local pivot points must coincide at the asymptotic values of θ and c. Thus the correct values of θ and c should lie between the pivots. The separation between neighbouring curves (corresponding to successive time steps) gives an indication of the rate of approach to the asymptote. It can be seen that, in the region between the pivots, the curves are closer in the N_F family than the O_F family, implying that N_F is closer to its asymptote than O_F, which seems reasonable given the relative size of the tail region in the data.

For Run032, at the end of the tail of O_F, the pivot point is between $1.3 \leq c \leq 1.4$, corresponding to $1.21 \leq \theta \leq 1.24$. In contrast, for the value of $c = 2.2$ found from the

flip rate in Section 7.4.1, $\theta = 1.44$, and though the pivot is moving towards this point, it is still a long way off at the end of the available data. The range of values of c and θ found from the fitting procedure applied to the N_F and O_F data are just beginning to overlap, but given the other sources of uncertainty there isn't enough information to gauge their likely final values more accurately than the range given in the previous section for N_F, i.e., $1.4 \leq c \leq 1.9$ and $1.13 \leq \theta \leq 1.23$. The results from analysing O_F have thus added weight to the consistency of the results from N_F.

7.4.4 Flip probability, $P(T, T_{\text{start}})$

There is one final quantity calculated from the order parameter data that can be used to assist in the process of estimating the persistence exponent, θ. Since the expression for its asymptotic form of, Equation (7.4),

$$P(T, T_1) = \theta T_1^{\theta} T^{-(\theta+1)}, \qquad \theta \neq 0, \tag{7.12}$$

is independent of α and c, it provides an important check on the fits obtained from N_F and O_F, even though the statistics are not so good for $P(T, T_{\text{start}})$. Note that $P(T, T_{\text{start}})$ cannot be scaled by T_{start}, so displaying all the runs on a single graph isn't useful. Instead, the data for Run032 has been plotted in Figure 7.6 (left), along with Equation (7.4) using various values of θ determined by the range of values of c suggested from the fits to the P_F, N_F and O_F data. The values of θ shown are, $\theta = 1.28$ (corresponding to $c = 2.2$), $\theta = 1.23$ (corresponding to $c = 1.9$), $\theta = 1.13$ (corresponding to $c = 1.4$), and $\theta = 1.0$ (corresponding to $c = 1.0$). The consistency of the lines corresponding to Equation (7.4) with the simulation data is encouraging given the limited quality of the data and the approximate nature of Equation (7.4). Since $P(T, T_{\text{start}})$ is concave downwards, it can be expected to approach its asymptote from above. Therefore, values of θ less than about 1.2 are inconsistent with the $P(T, T_{\text{start}})$ data since they lie slightly above the lower data points. Combining this with the results for N_F and O_F, the most likely value of θ for Run032 has thus been constrained to $1.20 \leq \theta \leq 1.23$ corresponding to a range of values of the prefactor of $1.5 \leq c \leq 1.9$.

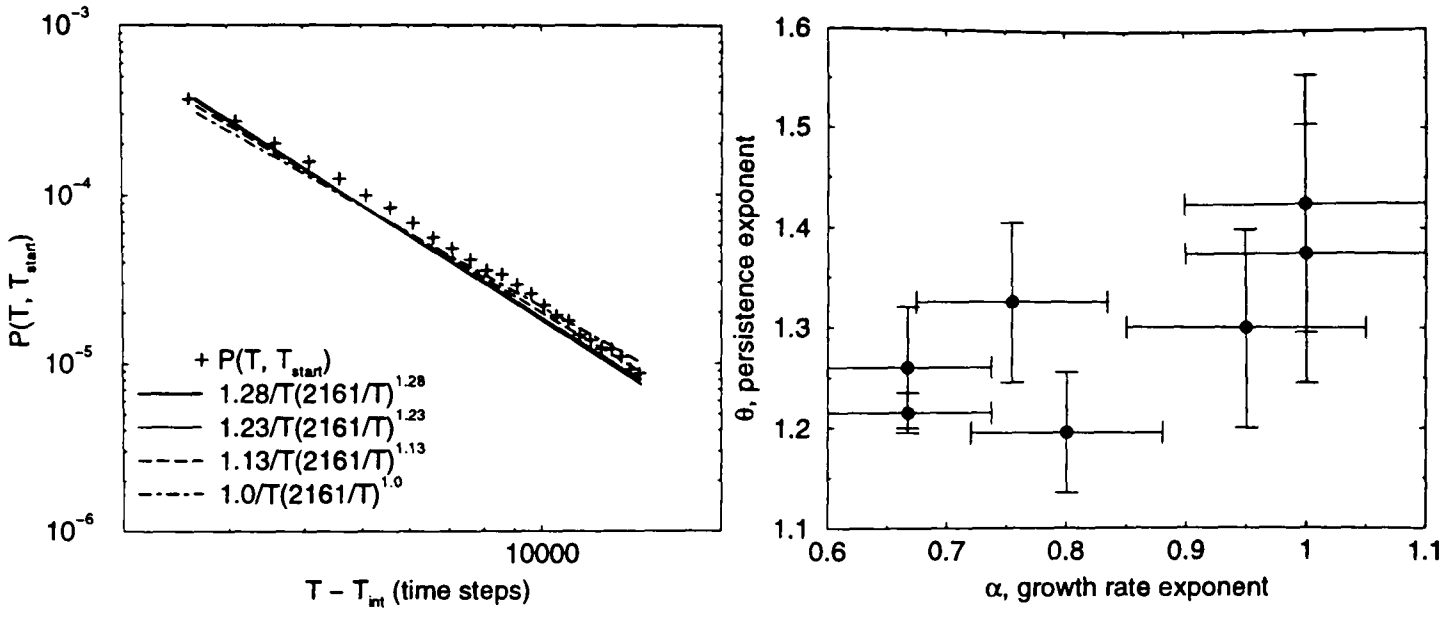

Figure 7.6: *Left: flip probability, $P(T, T_{\text{start}})$, for Run032, (crosses) with fits for θ = 1.28, 1.23, 1.13, 1.0. Right: persistence exponent, θ, against spinodal growth rate exponent, α, for runs in Table 5.1. The error bars are the range of θ from Table 7.1, and the error estimates for α from Section 5.4.3 of 10% (linear region) and 5% (crossover and inertial region).*

7.4.5 Best estimate of exponent, θ.

In the previous three sections only one run was examined, to illustrate the careful fitting procedure necessary to extract the range of values of the persistence exponent, θ, consistent with the data. The same procedure has been applied to all the runs in Table 5.1 (except Run022) and the results for the best estimate of the range of θ and c are shown in Table 7.1. The complete set of estimates for θ from Table 7.1 is shown

Run	α	*prefactor, c*	*exponent, θ*
Run028	1.0	0.85 - 1.3	1.30 - 1.55
Run033	1.0	0.85 - 1.4	1.25 - 1.50
Run029	0.95	0.85 - 1.4	1.20 - 1.40
Run020	0.80	1.0 - 1.5	1.15 - 1.24
Run030	0.75	1.3 - 1.9	1.25 - 1.40
Run019	0.67	1.5 - 2.2	1.20 - 1.32
Run032	0.67	1.5 - 1.9	1.20 - 1.23

Table 7.1: *Results from combined fits for persistence exponent, θ, for all runs in Table 5.1 (except Run022).*

against the growth exponent, α with error bars in Figure 7.6 (right). The results are consistent with the prefactor, c being as low as 1.0 for linear runs and rising to nearer

2.0 for inertial region, while the persistence exponent, θ, lies somewhere around 1.37 for the linear region and 1.23 for the inertial region. A single value of $\theta = 1.333$ is also just about consistent with the data, although some variation with α seems more likely. However, a value of $c = 2.2$ as implied by the measured flip rate for the inertial region appears to be inconsistent with the persistence data for N_F, O_F, and $P(T, T_{\text{start}})$. The flip rate is thus sufficiently sensitive to distinguish between viscous and inertial region dynamics, and suggests the presence of some mechanism such as capillary waves in the inertial region that raises the measured flip rate above that predicted by the growth of the domains.

This study has not, therefore, been able to provide a very accurate determination of the persistence exponent, θ, in a 3-D hydrodynamic system, but it has been possible to place limits on the likely value, and to show that the possibility of some variation with the growth exponent, α, must be allowed for in any future studies. The best estimate of θ for the linear region ($\alpha = 1$), is $\theta = 1.37 \pm 0.2$. (These error limits do not allow for systematic errors arising from the use of the flip rate model itself.) From the point of view of fundamental critical exponents, the value of θ in the inertial region is perhaps more significant, since this is (at least on current evidence) the asymptotic behaviour for spinodal decomposition, and here the best estimate is $\theta = 1.23 \pm 0.1$. These represent the first estimate of θ in a system dominated by hydrodynamics rather than diffusion.

7.5 Spinodal decomposition in 2-D

Since the precision of the results for the persistence exponent, θ, from the 256^3 3-D systems is limited by the system size and thus by the available computing power, and since the simple theory used to analyse the persistence behaviour in hydrodynamic systems is not necessarily specific to 3-D, a large 2-D system (512^2) was simulated and analysed to see if it could provide better results. The simulation was run using the same code as for 3-D simulations with one lattice dimension set equal to unity, and the same analysis code was used to process the resulting order parameter data. Pictures of the interface from 2-D spinodal decomposition are shown in Figure 7.7 for a 512^2 system.

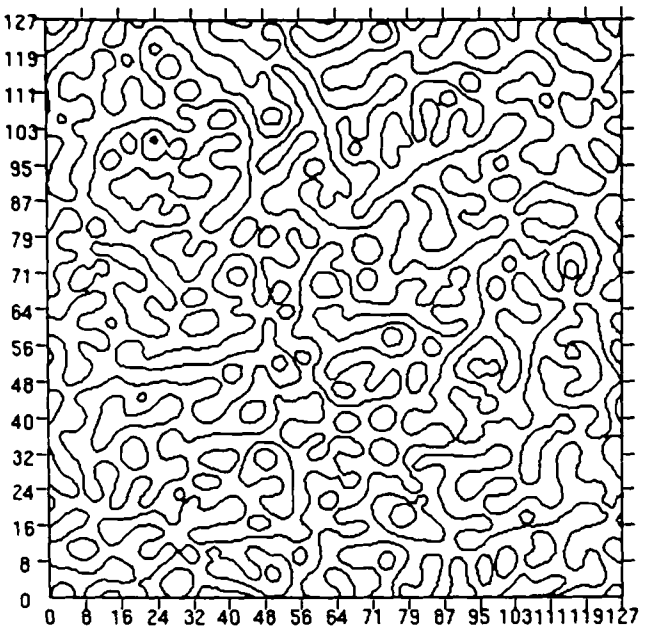

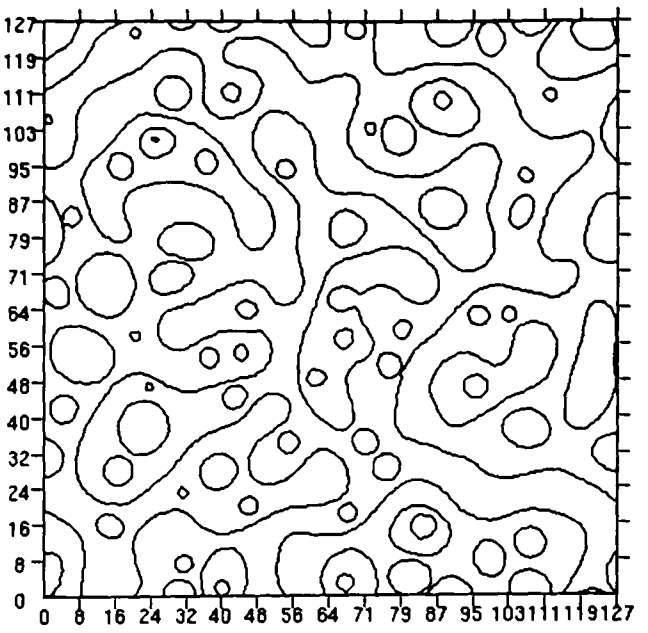

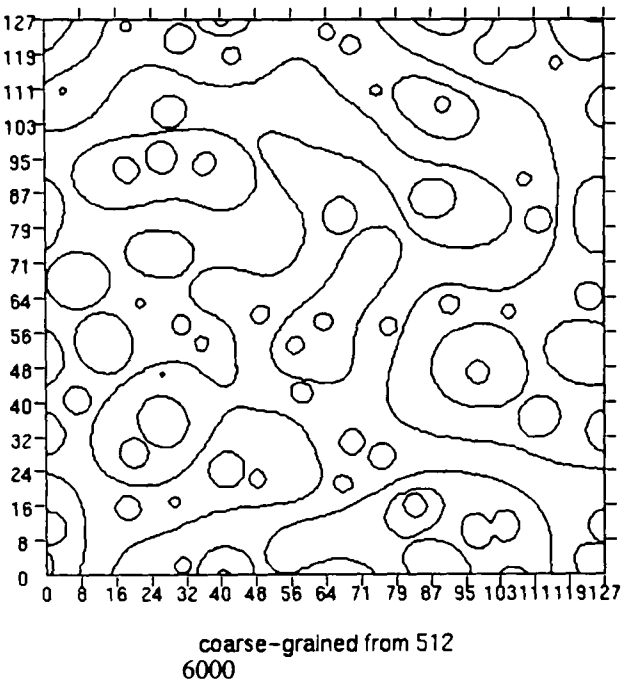

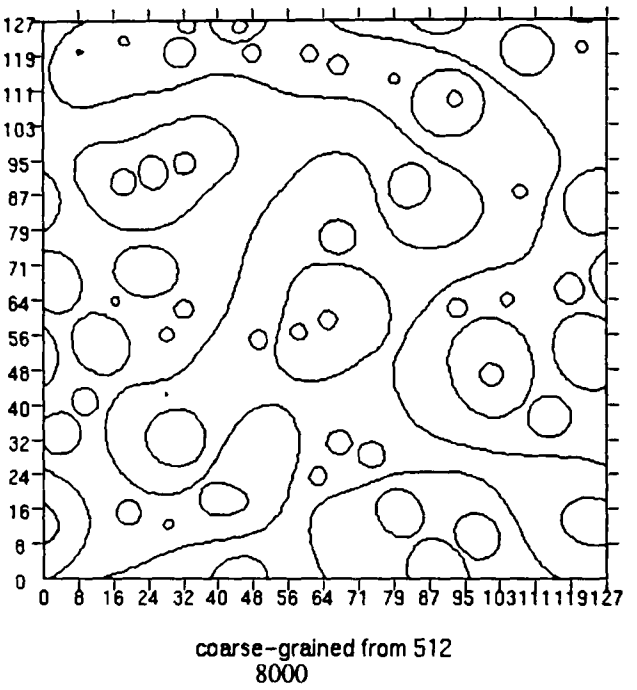

Figure 7.7: *2-D system: interface at successive time intervals of 2000 time steps.*

The first thing to note about 2-D systems is that the domain structure doesn't scale smoothly as it does in 3-D; see Wagner and Yeomans (1998). Simple scaling arguments like those used in Sections 2.3.1 and 2.4 to obtain the scaling predictions for 3-D systems can also be applied to 2-D systems, producing a prediction of $t^{2/3}$ for both the viscous hydrodynamic and inertial regions. Figure 7.8 (left) shows $L(T)$ and $L_{\nabla\phi}(T)$, see Section 5.5.2. In 3-D these length measures are not equal, but do grow with the same exponent over the whole late-stage coarsening process. In 2-D there is a clear divergence between the two length measures starting at 3500 time steps. This strange behaviour is due to the development of "bubbles within bubbles" within the larger irregular regions

of each fluid. This is an effect specific to 2-D due to the topological restriction on the possible connectivity. Bubbles that are already circular cannot evolve further without bumping into other bubbles or interfaces, so slowing the coarsening rate from the simple prediction of $t^{2/3}$. A free exponent fit to $L(T)$ gives $L = v(T - 1133)^{0.59}$, however, the 2-D system clearly isn't "scaling" in the sense of being self-similar (in time) in the same way as the 3-D system, so any such fits cannot be taken too seriously.

The fact that the interface is not a continuous structure in 2-D suggests that the approximation used to get a simple expression for the flip rate, P_F by considering the whole interface to be "sweeping" over the set of points that flip, see Section 7.2.1, is unlikely to be valid in 2-D. To investigate this, values for N_F, O_F, P_F and $P(T, T_{\text{start}})$ were recorded every time step, and the results compared with analysis done over a stride of $\Delta T_{\text{stride}} = 100$ time steps. The flip rate, P_F, is shown in Figure 7.8 (right)

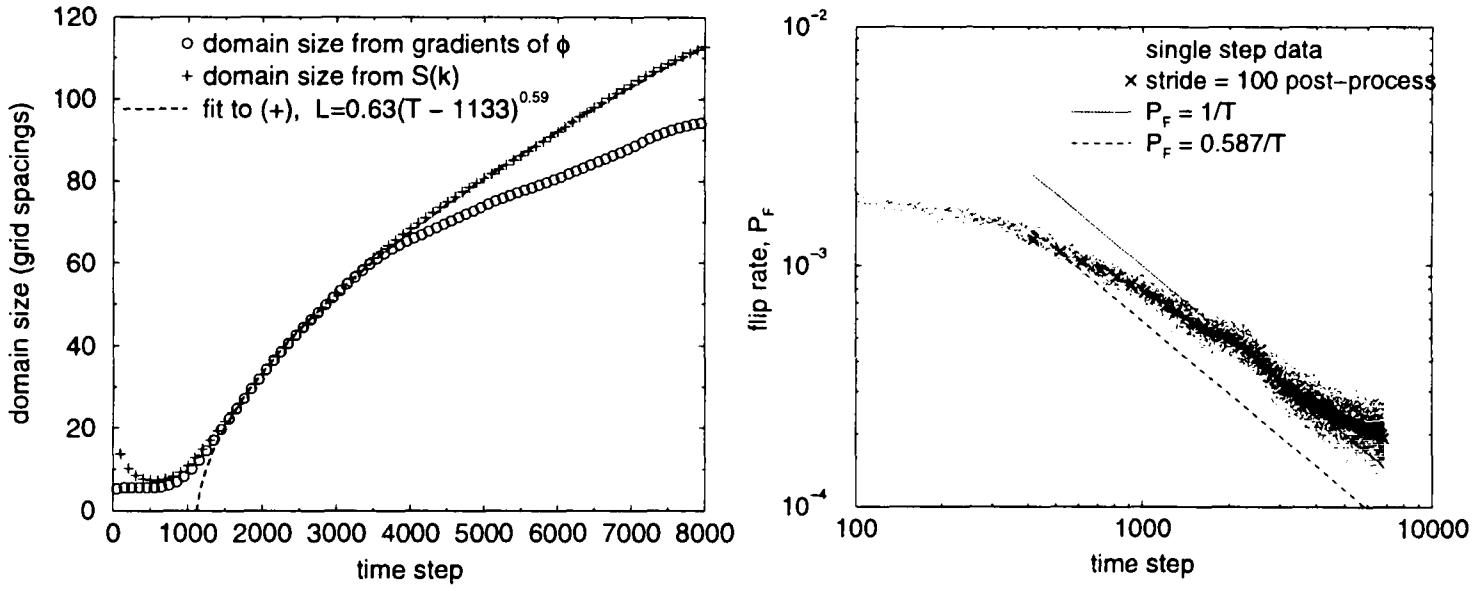

Figure 7.8: *Left: length measures $L(T)$ and $L_{\nabla\phi}(T)$ for 512^2 2-D system. Right: flip rate, P_F, for 512^2 2-D system.*

from which it is clear that the flip rate is quite variable over the evolution of the run. In order to see whether the asymptotic form fits $P_F = c\alpha/T$, Figure 7.9 (left) shows P_F scaled by $(T - T_{\text{int}})$. Clearly the fit isn't good, and for the tail of the distribution the flip rate has become almost constant, as can be seen in the linear plot of P_F with no scaling in Figure 7.9 (right).

Obviously there is little point in going on to consider N_F, O_F and $P(T, T_{\text{start}})$ within the same framework as the 3-D analysis as they are not going to provide information on the 3-D scaling exponent, θ. Given that the growth behaviour in 2-D is itself not

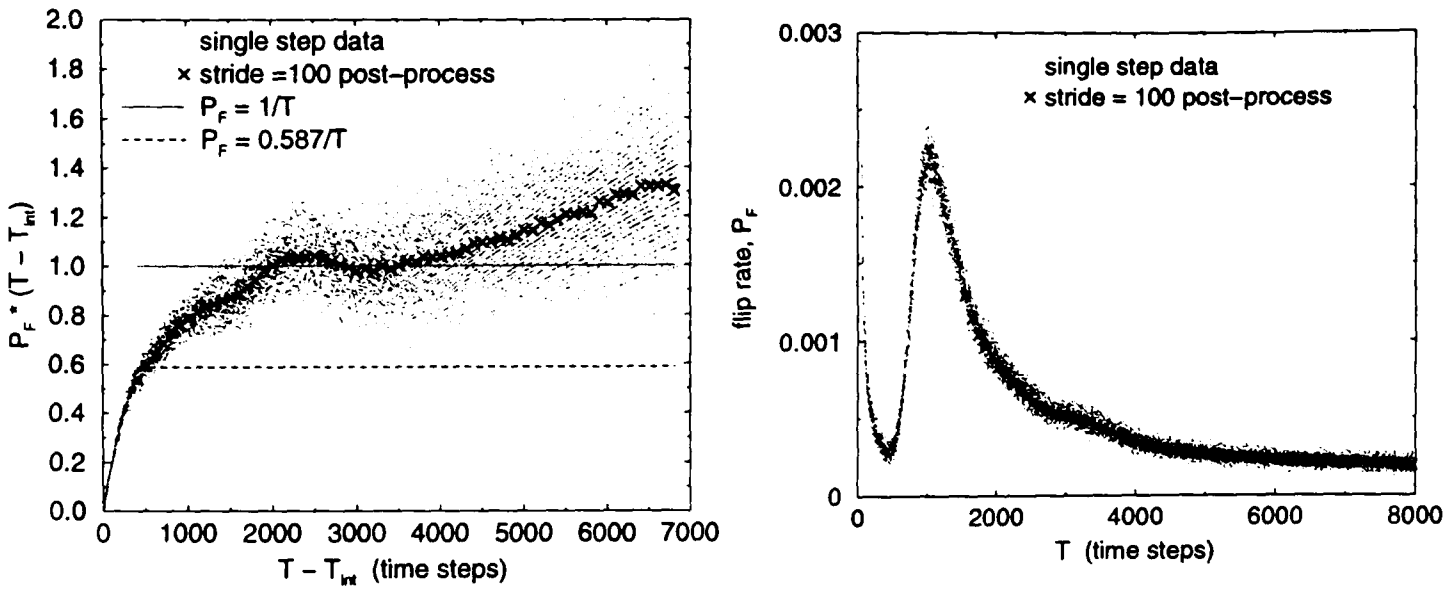

Figure 7.9: *Left: flip rate, P_F, scaled by $(T - T_{\rm int})$ for 512^2 2-D system. Right: P_F, on a linear plot with no scaling.*

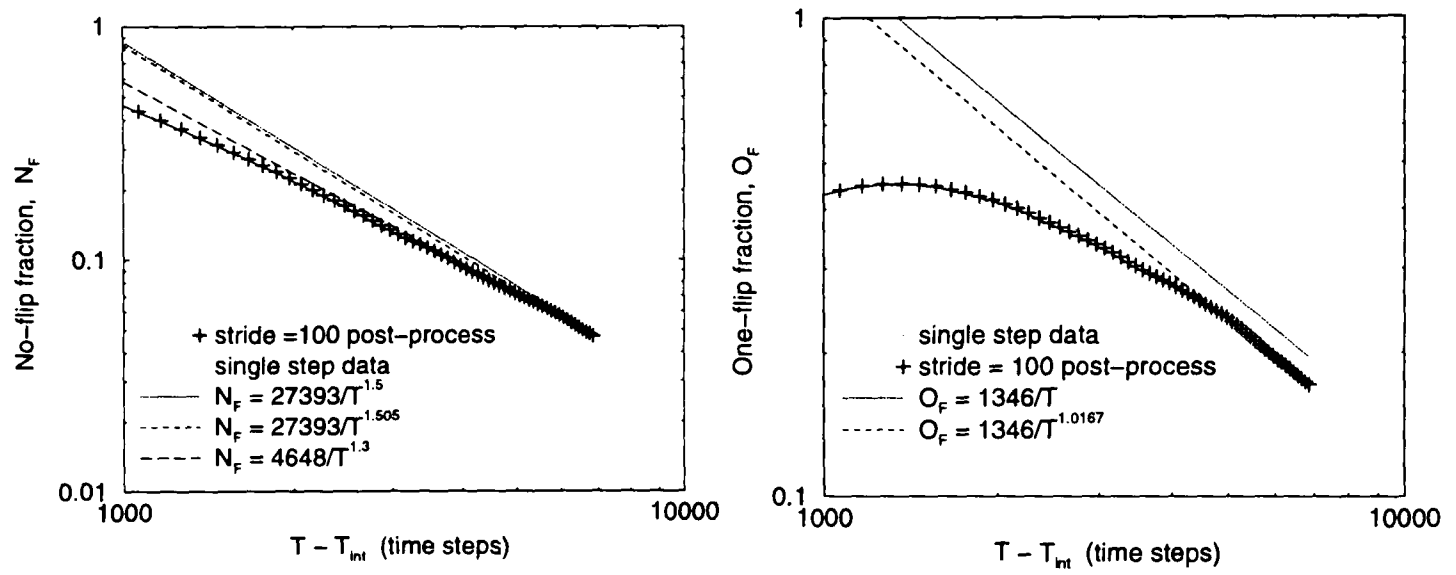

Figure 7.10: *Left: no-flip fraction, N_F, for 512^2 system. Right: one-flip fraction, O_F, for 512^2 system.*

scaling, it isn't clear that a sensible persistence exponent can be expected for such a system at all. The "no flip fraction", N_F, and the "one-flip fraction", O_F, are both shown in Figure 7.10 (left and right) together with a couple of possible fits, to show that it is at least possible to fit the tail of both to power laws, $\theta_{NF}^{(2D)} \simeq 1.5$, and $\theta_{OF}^{(2D)} \simeq 1.0$[6]. The statistics for the flip probability, $P(T, T_{\rm start})$, are very poor for the 2-D system and without a theory for the asymptotic form, no attempt has been made to fit the data.

In conclusion, the asymptotic form of the flip rate, P_F, does not follow the same form as in 3-D, so the theory developed in Section 7.2.1 does not apply.

[6]Note that the uncertainty in the value that should be taken for $T_{\rm int}$ due to the lack of a good power law fit to the $L(T)$ data contributes to the errors in determining these exponents to an extent that is difficult to estimate, but which reduces at late times, $T \gg T_{\rm int}$.

7.6 Conclusions

The persistence exponents for a 3-D hydrodynamic spinodal system have been investigated. It has been determined that the decay of the "no-flip fraction", N_F, is a power law (as opposed to exponential).

With the help of a simple theory for the approximate asymptotic forms of N_F, O_F, P_F and $P(T, T_{\text{start}})$, upper and lower estimates have been determined for the persistence exponent, θ, defined by $N_F \sim (T_{\text{start}}/T)^{\theta}$, for a range of values of the spinodal growth exponent, α from linear to the inertial ($\alpha = 2/3$) region, see Table 7.1. In the linear region, $\theta = 1.37 \pm 0.2$, and in the inertial region, $\theta = 1.23 \pm 0.1$.

This is the first attempt to determine these exponents for a hydrodynamic system, all measurements and theory so far have pertained to solids undergoing diffusive dynamics, such as spin systems. More accurate determination from simulations would likely require significantly larger system sizes, which is difficult to envisage at present computing power.

The persistence quantities were also found to be sensitive to the differences in the dynamics in the linear and inertial regions of spinodal decomposition. The flip rate, $P_F = c\alpha/T$ was found to have a different value of the prefactor, c in the linear and inertial regions. The flip rate measured at early times also clearly showed the transition from diffusive to hydrodynamic behaviour.

Although the theory in Section 7.2 is not specific to three dimensions, the assumption of a simple sweeping interface used in the theory is not applicable to 2-D. This is because 2-D spinodal fluid systems do not show scaling growth in the same way as 3-D systems, see Wagner and Yeomans (1998), It is, however, possible to determine reasonably accurate values for persistence exponents directly from the tails of the 2-D data, and furthermore, larger 2-D systems could easily be run (say 4096^2) to provide better values than have been measured here. However, since the spinodal growth itself doesn't follow good scaling behaviour in 2-D, it is not clear that any such exponents have fundamental significance.

Chapter 8

Conclusions

8.1 Summary of results

The lengthy and detailed investigation into the kinetics of the phase separation of a binary mixture of simple fluids undergoing spinodal decomposition described in the previous chapters, has produced a number of substantial new results. Simple scaling theory has been extended in the inertial region, and simulation data analysed to provide results from both the order parameter and velocity fields.

First, and most important, the combined data sets from the main simulation runs collectively cover the full range of parameters from the viscous region (linear domain growth) through a broad crossover into the inertial region, where domain growth scaling as $t^{2/3}$ has been unambiguously observed in 3-D simulation for the first time. Taken together, the data sets span five decades of reduced length and eight of reduced time (Figure 5.3), exceeding all previous results combined.

Many careful checks have been done to confirm that the results truly represent hydrodynamic growth. In particular, the importance of controlling the diffusion rate was highlighted as the source of problems in several other studies of spinodal decomposition. Diffusion is also crucial to maintaing the interface in local equilibrium, so it is not possible just to reduce the diffusion to very low levels. The spread of simulation runs used for the final analysis was determined by the diffusion rates that could be used,

both at the viscous end and the inertial end of the range.

Extensions were made to the scaling theory used to predict the growth rate of the domain size by considering the energy balance equation as well as the Navier-Stokes equation for the fluid dynamics. To obtain consistency between both equations, it was necessary to introduce two new length scales associated with the velocity derivatives in the inertial region, one for the first derivative ($\nabla \mathbf{v}$), and one for the second ($\nabla^2 \mathbf{v}$). These lengths were identified with long-established length scales from turbulence theory, the Taylor and Kolmogorov microscales, providing strong support for the new scaling theory.

The new scaling theory predicts the same growth rate for the domain size as the simple theory; the differences lie in the behaviour of the individual terms in the Navier-Stokes equation and related quantities derived from the velocity, and then only in the inertial region. In particular, the ratio of the nonlinear term to the viscous term in the Navier-Stokes equation (R_2, Equation (2.31)) is predicted to approach a constant asymptote, in contrast to the simple scaling theory in which R_2 is predicted to increase forever with time.

Reynolds numbers (Re $\equiv$ length$\times$velocity/kinematic viscosity) are based on the ratio R_2, although the choice of length and velocity measures may not always provide an accurate estimate of R_2. Grant and Elder (1999) suggested that the prediction from the simple scaling theory that the Reynolds number increases without bound was unphysical, but, because they were using a Reynolds number defined from the domain size, $\mathrm{Re}_\phi \equiv \rho L \dot{L}/\eta$, they concluded that the domain growth rate had to reduce to $t^{1/2}$ or below in order to keep the Reynolds number finite. The new scaling theory answers this by pointing out that the relevant Reynolds number is actually R_2, which (in the new theory) remains finite while the domain growth still proceeds as $t^{2/3}$.

The simulation results are consistent with the new theory in this respect, the growth rate in the most inertial run is firmly at $t^{2/3}$ for values of $\mathrm{Re}_\phi \simeq 350$, while Grant and Elder predicted a crossover to $t^{1/2}$ in the range $10 \lesssim \mathrm{Re}_\phi \lesssim 100$. Of course, further crossovers as higher Reynolds numbers beyond the reach of the simulations are always possible, but if the new scaling theory is correct, then none are expected.

Having obtained reliable results from the order parameter analysis, the velocity field of the spinodal fluid mixture was considered next. There are no existing studies of such a velocity field, so all these results are new. The velocity field was analysed as a single fluid, although since the interface provides the driving force in the system, the fluid flow should reflect the presence of the interface. Thus, an analysis of the velocity structure factor would be expected to yield a similar length scale to $L(T)$, the domain size obtained from the order parameter structure factor. Calculation of $L_v(T)$ turned up a surprise: it appears to vary as $t^{2/3}$ throughout all the simulations, whereas $L(T)$ scales as $t^{2/3}$ only in the inertial region. While $L_v(T) \simeq L(T)$ in the inertial region, in the viscous region, $L_v(T)$ becomes much larger, and in the simulation systems, it becomes comparable or larger than the system size itself. The reasons for this seem likely to be related to the importance of fluctuations in the viscous region dynamics, but further tests would be required to confirm this.

The velocity field data from the simulations was also used to calculate the terms in the Navier-Stokes equation. Comparison of the relative magnitudes of these terms demonstrated that in the viscous runs, the viscous term was larger than the inertial terms by two orders of magnitude, clearly dominating the dynamics. In contrast, in the inertial runs, the inertial terms are larger than the viscous term by one order of magnitude, providing additional confirmation that the simulation has reached the region where the inertial terms dominate the dynamics.

The skewness of the longitudinal velocity derivatives was calculated for the spinodal velocity field, and found to reach -0.35 in the most inertial run. This compares with -0.5 for fully developed turbulence, strongly suggesting that the spinodal system is partially turbulent – in the bulk fluid away from the interfaces. Reynolds numbers are also comparable in magnitude between the most inertial spinodal run and the turbulence simulation described in Chapter 4, supporting the idea that the spinodal system has developed turbulence, and filling out a consistent picture of inertial region dynamics in hydrodynamic spinodal decomposition.

The new scaling theory differs from the simple theory only in the inertial region for velocity-related quantities. By comparing the scaling behaviour between different simulation runs for the terms in the Navier-Stokes equation, the dissipation rate and the

Taylor and Komogorov microscales, it was found that they tend to scale in line with the new theory where differences between new and old exist. Given that the inertial runs are only just inside the inertial region, so the asymptotic behaviour has not yet been reached, these results are suggestive rather than conclusive support for the new scaling theory. Additionally, in the viscous region, where there is no difference in the theoretical predictions, significant departures from scaling were also observed. These are likely to be caused by the fluctuations in the viscous region dynamics being on larger scales than the system size so they don't average out over a single run. However, the additional runs required to further investigate this were not possible with the resources available to this project.

On examining the scaling within each simulation run, as well as between different runs, for the various velocity-related quantities, more obvious non-scaling behaviour was found. This was most pronounced in the dissipation rate, where, for the most viscous and most inertial runs, the dissipation rate is falling more slowly with time within each run than between runs (see Figure 6.14). The non-scaling behaviour can be explained if what is happening is that the dissipation is taking place more slowly than expected in the simulation due to inaccurate evaluation of velocity gradients on the discrete lattice when the gradients are too steep, but further tests would be required to confirm this. Another limit to the simulation method thus seems to have been identified, based on the resolution required for the velocity gradients at small scales to ensure that the dissipation is modeled properly.

Finally, the persistence behaviour has been investigated for the first time in a hydrodynamic system and approximate values for the exponent obtained in both the viscous and inertial regimes. Although accuracy of the results was limited by the system size, significantly larger systems are not feasible with current computational capabilities, so these results represent a useful first step in widening the study of persistence exponents to hydrodynamic systems.

Overall, this study has considerably expanded the existing knowledge of both the theoretical and computational details of the kinetics of hydrodynamic spinodal decomposition in 3-D. The new results in the inertial region will also hopefully inspire experimental work in this direction, having revealed that this is an interesting area in which

experiment may prove more able than numerical simulation or theory in the near future.

8.2 Suggestions for future work

While this work has provided much new information about hydrodynamic spinodal decomposition, certainly there are also still many open questions. Further work that would help to find answers could include the following:

- A study of capillary waves and small scale dynamics of the fluid is clearly of interest, since many of the unresolved questions in the present study revolve around behaviour on the dissipation length scales.

- It may be fruitful to attempt to divide the system into a boundary layer region near the interface, and the bulk fluid away from the interface. These two regions could then be analysed separately to see how they differ statistically, and to see what determines the thickness of the boundary layer. Both dissipation and diffusion may be relevant here.

- Further analysis of the viscous region to investigate the observed fluctuations and finite size effects, starting with simple repeat runs with different random initial conditions to confirm that the fluctuations are just that, and not systematic in some way. Comparison with a simulation done with purely viscous fluid dynamics (no inertial terms at all) would be interesting, to see if the inertial terms, though small, are still perturbing the system enough to be the source of the fluctuations.

- The new scaling theory makes predictions about the flow of energy through the system that could be investigated in more detail. In the inertial region this corresponds to mapping out the "energy cascade" from large through to small length scales. This could also help to understand exactly what is going on when the dissipation seems to be happening too slowly and excess energy builds up in the velocity field.

Generalisations and extensions to this basic system also readily suggest themselves as avenues for future investigations. A few of the more obvious include:

- Consider the implications of the new theory for two dimensions. This requires a knowledge of turbulence in 2-D, which has rather different phenomenology than the 3-D turbulence described in this work.

- More complex fluids, where the fluid properties may influence the dynamics such as polymers. Computationally this would require suitable methods and models; but experimental investigations could also be very fruitful.

- Adding an applied shear immediately adds a further set of length and time scales to the problem. The thorough understanding of the unsheared system obtained here will be an aid to future studies of sheared spinodal systems.

- Sheared systems are already possible with moving boundaries in the **Ludwig** simulation code. Adding Lees-Edwards boundary conditions for shear would provide an important comparison, since boundaries introduce extra toplogical constraints that affect the coarsening process. Shear also induces significant velocity gradients, making the development of more isotropic gradient evaluation methods a high priority.

- Although Jury et al. (1999) found that DPD did not produce clear results for the spinodal growth exponent, it seems likely that, through comparison with the LB system, new DPD simulations could be done with more confidence. There are two important advantages of DPD over LB for for extending the work to sheared systems. Firstly, higher shear rates are possible in large system sizes because the DPD method does not use a lattice, and secondly, simple surfactants are easily added to DPD systems by linking two DPD particles of opposite colour together into a dimer.

Many more complex systems than a simple binary fluid mixture, such as those suggested above, have great relevance to industrial products and processes, as well as being of theoretical interest in their own right. It is to be hoped that the work accomplished in this study will provide useful information and motivation for much further study of these and other areas.

Appendix A

Visualisation of the simulations

A.1 Single fluid turbulence

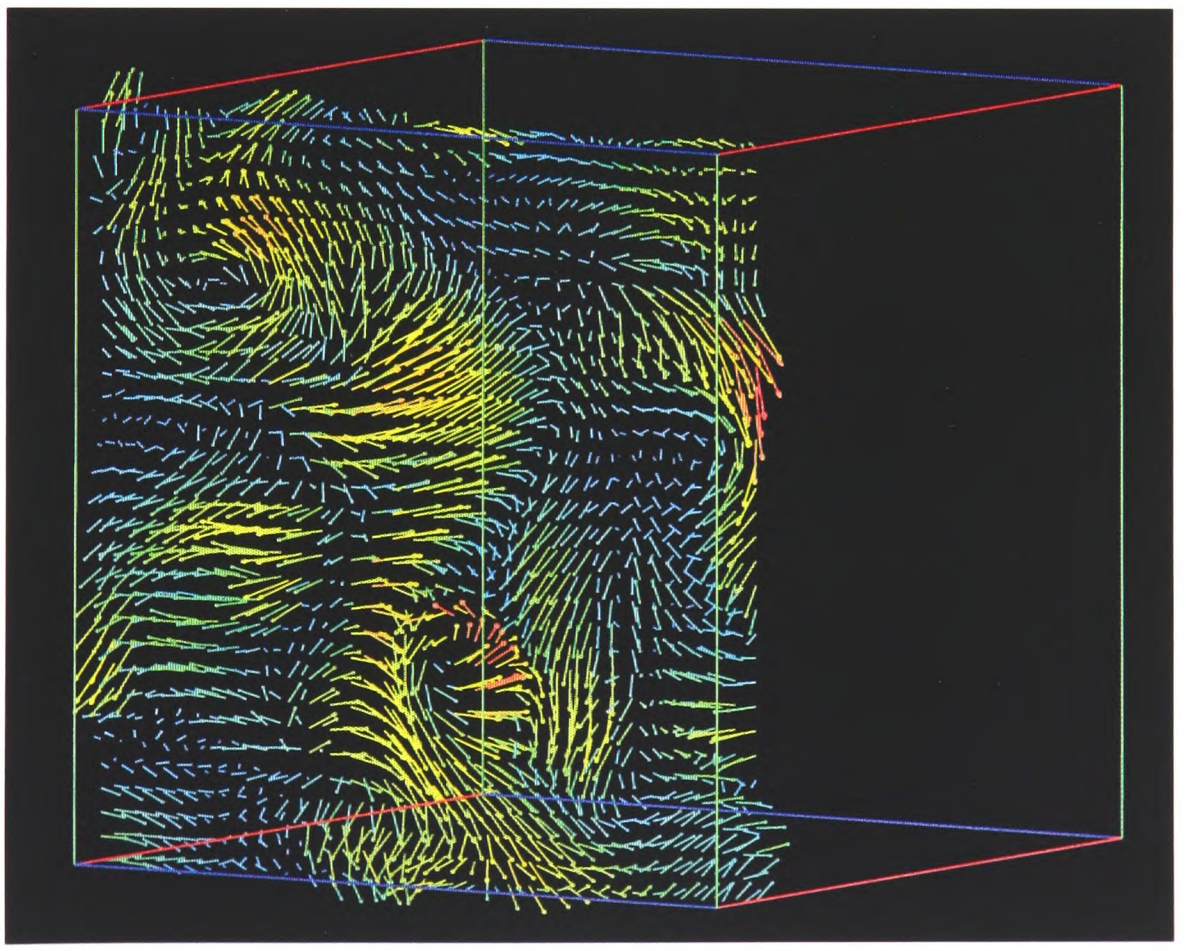

Figure A.1: *The velocity field from the single fluid decaying turbulence simulation described in Chapter 4, at time step 500. For clarity, the velocity field is shown for only two lattice layers in a* 32^3 *section from the* 128^3 *system. The velocity at each lattice point is represented by an arrow in the direction of the velocity. The colour and the length of the arrows both indicate the magnitude of the velocity.*

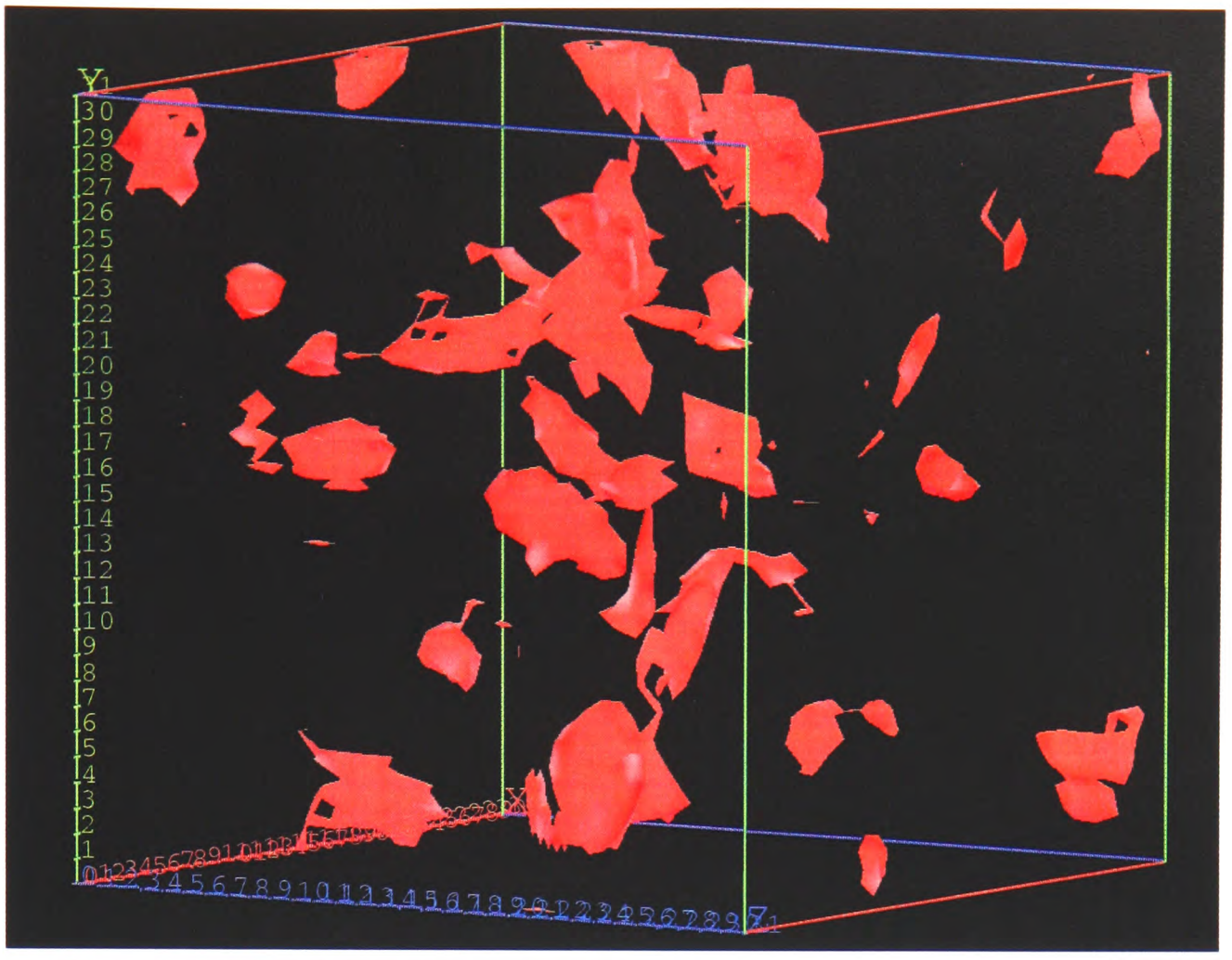

Figure A.2: *The vorticity field from the single fluid decaying turbulence simulation described in Figure A.1. The red interface is set to show a contour at 50% of the maximum vorticity, and thus encloses regions of high vorticity.*

A.2 Spinodal

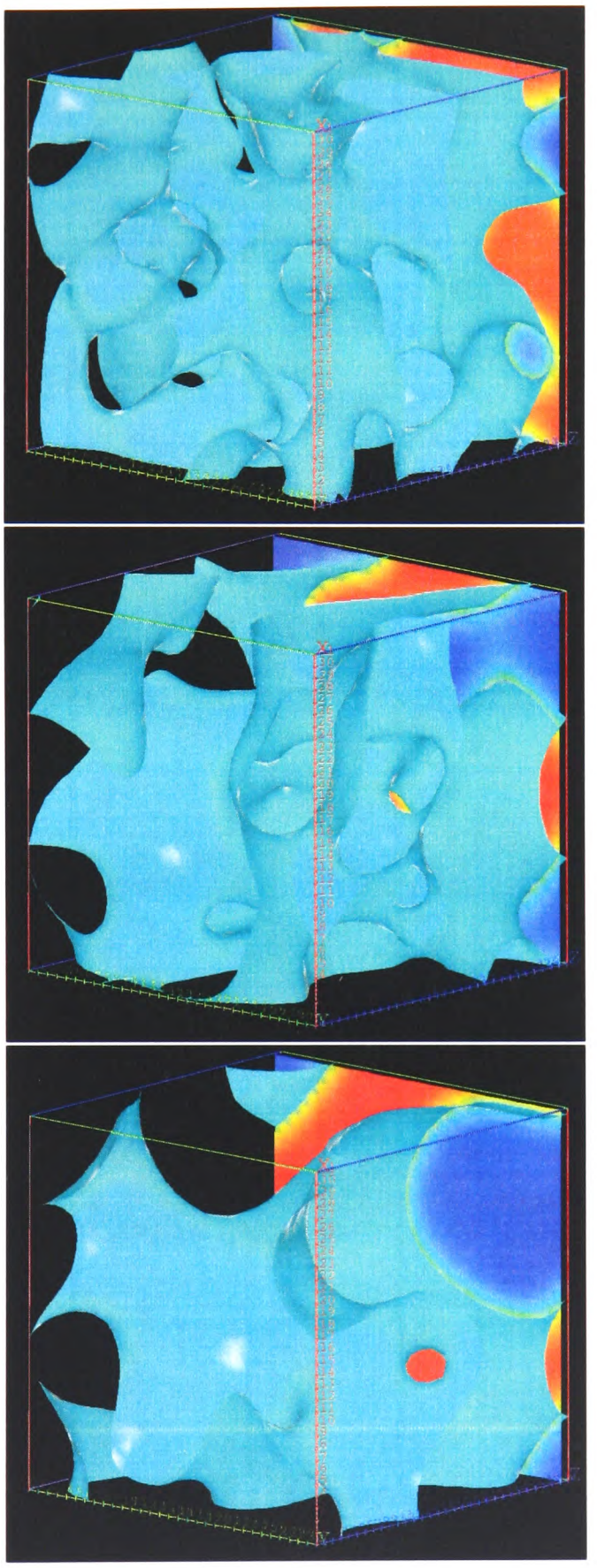

Figure A.3: *Interface for Run018 (crossover region) for time steps 2000 (top), 2600 (middle), and 3400 (bottom), corresponding to domain size ($L(T)$) of 13, 18, and 28 lattice units respectively. The system size is 128^3, only a 32^3 section is shown. The light blue surface represents the locations in the simulation where the order parameter is zero. The coloured plane (right back) shows the value of the order parameter on the plane with red $= -1$ and blue $= +1$.*

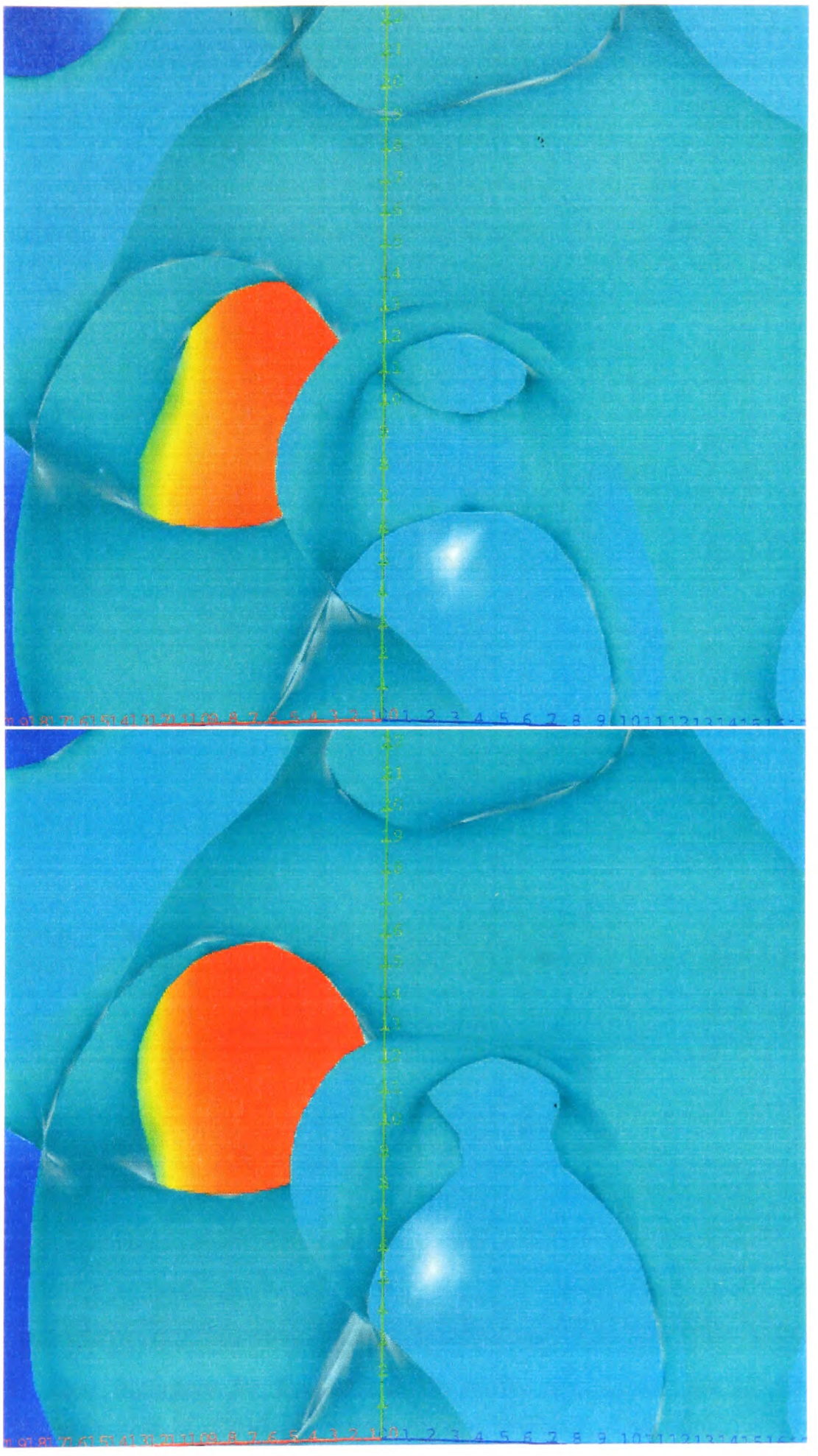

Figure A.4: *Interface for Run014 for time steps 2800 (top) and 3000 (bottom) showing pinch-off of a narrow neck between larger domains. A small section of the* 128^3 *system is shown, the axes are marked in lattice units, and part of the coloured plane showing the value of the order parameter as described in Figure A.3 is visible on the left.*

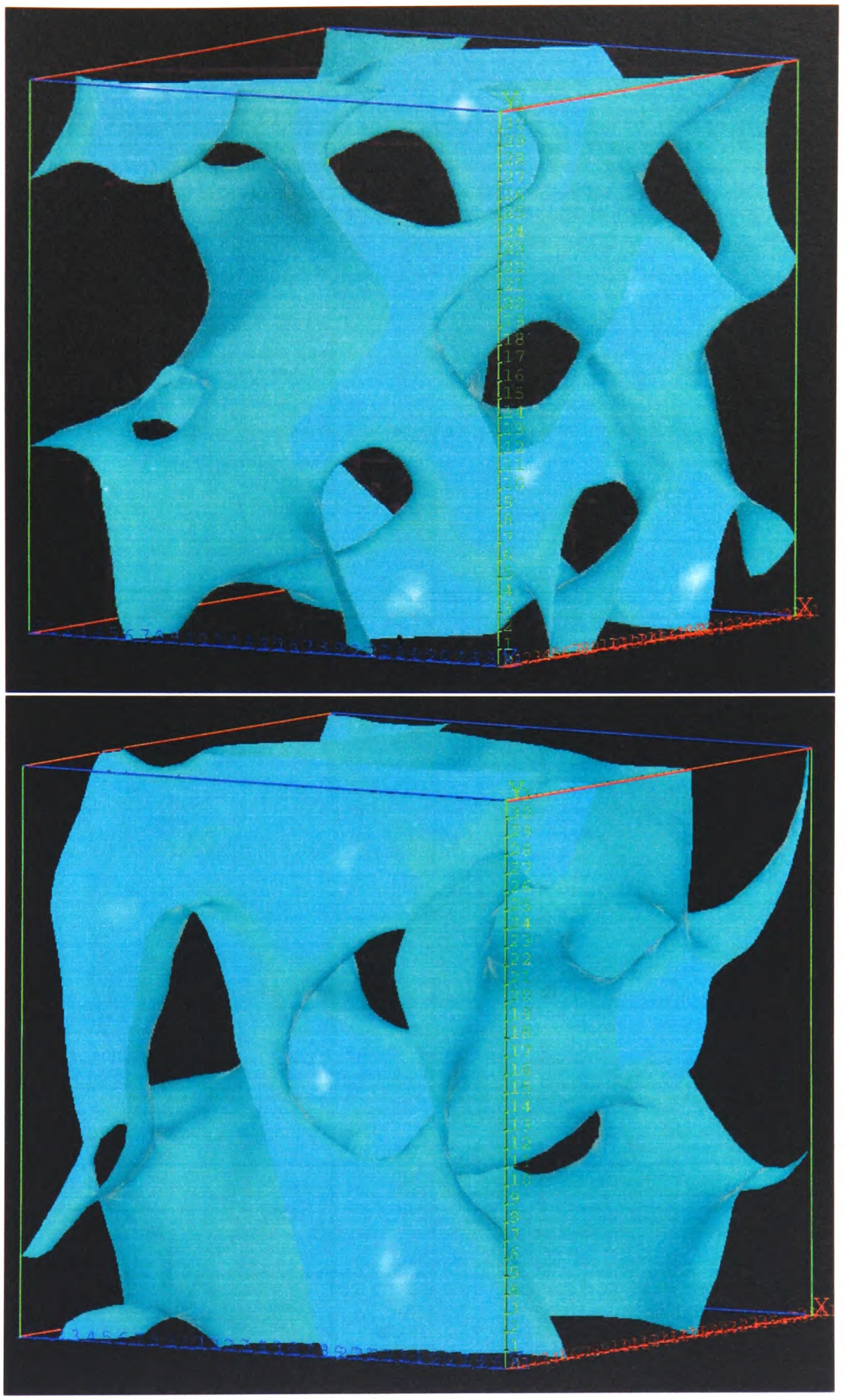

Figure A.5: *Top: Interface for Run027, a run in the viscous regime, for time step 8500, when the domain size is about 21 lattice units. Bottom: Interface for Run031, a run in the inertial regime, at time step 5000 when the domain size is about 22 lattice units. Both images are* 32^3 *sections of* 128^3 *systems, the axes are labeled in lattice units.*

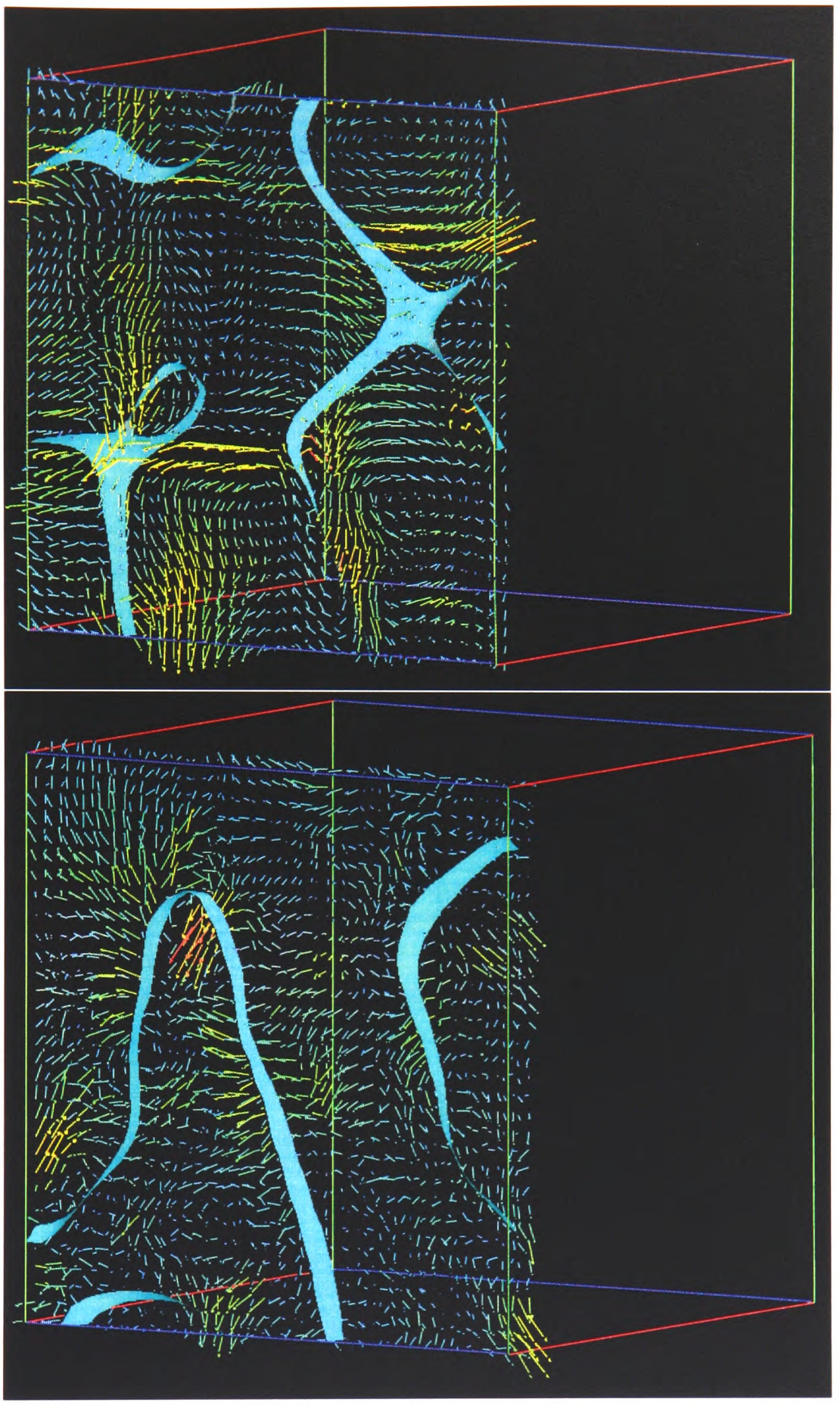

Figure A.6: *Top: velocity for Run027 at time step 8500. Bottom: velocity for Run031 at time step 5000. (Same runs as in Figure A.5.) As in the turbulence velocity field shown in Figure A.1, the velocity is only shown for 2 lattice layers for clarity. The arrows represent the direction of the velocity at the lattice site at their base, while their length and colour both represent the magnitude of the velocity. The interface is also shown light blue, it appears wider where it passes through the two layers at an oblique angle.*

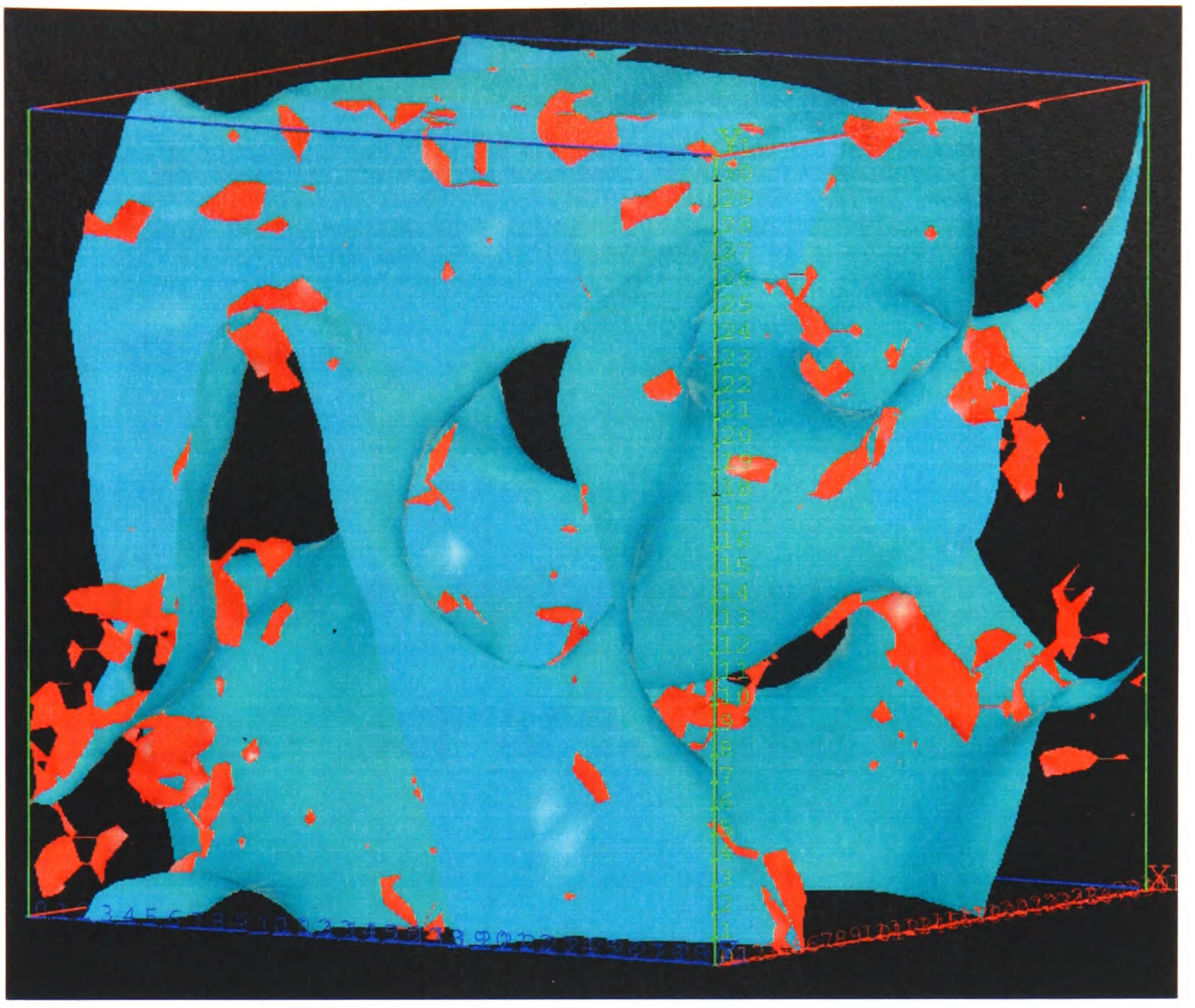

Figure A.7: *Vorticity for Run031 at time step 5000, a run in the inertial region. The vorticity is shown as a red contour at 50% of the maximum vorticity. The interface between the two fluids is also shown for comparison with the location of regions of high vorticity. For comparison with the vorticity in single fluid turbulence, see Figure A.2.*

Appendix B

NSE and energy balance: complete set of scaling cases

In Section 2.4, the extra scaling exponents needed to balance all the terms in the global energy balance equation, as well as the Navier-Stokes equation, were introduced one at a time as each attempt without them failed. In this Appendix, the full set of exponents will be considered systematically in both the NSE and energy balance equation, to check all possible solutions and show that the results quoted in Section 2.4 are the only physically sensible ones.

The starting equations are the Navier-Stokes equation, Equation (2.18),

$$\rho\left[\frac{\partial \mathbf{v}}{\partial T} + (\mathbf{v}.\nabla)\mathbf{v}\right] = \eta\nabla^2\mathbf{v} - \nabla.\underline{\underline{\mathcal{P}}},$$

where the pressure tensor contains a term to allow for the force from the interface, $-\phi\nabla\mu$, and the global energy balance equation for the kinetic energy of the fluid, Equation (2.35),

$$\frac{\mathrm{d}}{\mathrm{d}T}\left(\rho\langle\mathbf{v}^2/2\rangle\right) = \varepsilon_{\mathrm{in}} - \eta\langle(\nabla\mathbf{v})^2\rangle,$$

where $\varepsilon_{\mathrm{in}}$ is the energy transfered to the fluid from the interface. Note that a choice has been made here to work with the global energy balance equation rather than the local energy equation that more naturally forms a set with the NSE,

$$\frac{\partial}{\partial T}(\rho v^2/2) + \mathbf{v}.\nabla(\rho v^2/2) = \mathbf{v}.\nabla.\underline{\underline{\mathcal{P}}} - \eta(\nabla\mathbf{v})^2 + (\eta/\rho)\nabla^2(\rho v^2/2), \qquad \text{(B.1)}$$

where $\mathbf{v}.\nabla.\underline{\underline{\mathcal{P}}} = \varepsilon_{\text{in}}$. The two extra terms, the convective part of the derivative on the l.h.s, and the diffusive term on the r.h.s., represent flows of energy in or out of the local region under consideration. Globally, such flows must average to zero. The physical motivation for this choice is that momentum is conserved, so globally the average is zero and the useful information is to be found in the local force balance represented by the NSE. On the other hand, there is both a "source" and a "sink" for the kinetic energy, so the global average contains the important information. While the local fluctuations in kinetic energy density may be of interest when looking in detail at the dynamics, they are not necessary for determining the overall scaling. At the end of each subsection, the solutions found using the global energy balance equation will be checked in the local energy equation as a final test of consistency.

The NSE and global energy balance equations are turned into scaling equations by using the following scaling quantities and associated exponents:

- domain size, $L(T) \sim T^{\alpha}$
- order parameter first derivative, $\nabla \sim 1/L(T) \sim T^{-\alpha}$
- fluid velocity, $\mathbf{v} \sim T^{\beta}$
- fluid velocity first derivatives, $\nabla \sim 1/L_{\nabla} \sim T^{-\alpha'}$
- fluid velocity second derivative, $\nabla^2 \sim 1/L^2_{\nabla^2} \sim T^{-2\alpha''}$
- energy input from the interface to the fluid motion, $\varepsilon_{\text{in}} \sim \sigma \dot{L}/L^2$ (see page 25).

Using these, and writing the equations as powers of T, gives for the Navier-Stokes equation and the energy balance equation,

$$\text{NSE:} \qquad \rho\beta T^{\beta-1} + \rho T^{2\beta-\alpha'} \sim \eta T^{\beta-2\alpha''} + \sigma T^{-2\alpha} \tag{B.2}$$

$$\text{energy:} \qquad \rho\beta T^{2\beta-1} \sim -\eta T^{2\beta-2\alpha'} + \sigma T^{-\alpha-1}, \tag{B.3}$$

where the prefactors have been left in to facilitate identification of the terms. The local energy equation, Equation (B.1), becomes,

$$\rho\beta T^{2\beta-1} + \rho T^{3\beta-\alpha'} \sim -\eta T^{2\beta-2\alpha'} + \sigma T^{-\alpha-1} + (\eta/\rho) T^{2\beta-2\alpha''}, \tag{B.4}$$

Case of $\beta = 0$

The first case to consider is the simplest one, $\beta = 0$. The scaling equations, Equations (B.2) and (B.3), then become,

$$\begin{aligned} \rho T^{-\alpha'} &\sim \eta T^{-2\alpha''} + \sigma T^{-2\alpha} \\ \eta T^{-2\alpha'} &\sim \sigma T^{-\alpha-1} \end{aligned} \tag{B.5}$$

Physically, this case corresponds to no net change in the fluid velocity, ($\mathbf{v} \sim T^{\beta=0}$), so the energy input to the fluid from the interface must go straight out again as dissipation. In the energy balance equation, this corresponds quite straightforwardly to the exponents in the two remaining terms being equal, giving, $\alpha = 2\alpha' - 1$. Since the domain size (energy input) is thus coupled to the energy dissipation, the simple scaling solution with $\alpha = \alpha' = 1$ is the one that makes sense.

Considering the NSE next, and eliminating α', gives,

$$\rho T^{-(\alpha+1)/2} \sim \eta T^{-2\alpha''} + \sigma T^{-2\alpha} \tag{B.6}$$

On the r.h.s., if the force from the interface is balanced against the force from dissipation, then $\alpha'' = \alpha$ and there is just the one length scale in the system, that of the domain size, $L(T)$. However, the l.h.s., which was assumed to be negligible in the original simple scaling argument, appears to be decaying more slowly (T^{-1}) than the r.h.s. terms (T^{-2}). Recalling that the viscous regime is not an asymptotic regime, and is therefore only expected to hold for times earlier than some crossover time T^*, before which the nonlinear term will be smaller than the other two terms, this apparent difficulty is eliminated. This leaves the familiar viscous region solution of a single length scale growing as $L(T) \sim T$. Checking this solution in the local energy equation, Equation (B.4),

$$\rho T^{-1} \sim -\eta T^{-2} + \sigma T^{-2} + (\eta/\rho) T^{-2}, \tag{B.7}$$

it can be seen that, again, this is consistent once the convective term on the l.h.s. is disregarded.

However, there is another solution for $\beta = 0$, that can be obtained by simply solving Equations (B.5) for the remaining exponents, α, α', and α'', without regard for the

physical interpretation, giving,

$$\alpha = 1/3 \quad \alpha' = 2/3 \quad \alpha'' = 1/3. \tag{B.8}$$

The NSE then scales like,

$$\rho T^{-2/3} \sim \eta T^{-2/3} + \sigma T^{-2/3}, \tag{B.9}$$

so the ratio R_2, between the nonlinear and viscous term is constant. Physically, this looks like it would correspond to turbulent remixing (if it is possible to get there). The length scale for velocity gradients is related to the domain size by $L_\nabla \sim L^2(T)$, suggesting that the nonlinear term is mixing on scales larger than the domain size. In the local energy equation, Equation (B.4), this solution looks like,

$$\rho T^{-2/3} \sim -\eta T^{-4/3} + \sigma T^{-4/3} + (\eta/\rho) T^{-2/3}. \tag{B.10}$$

The extra local terms are both scaling as $T^{-2/3}$, and thus balance each other, while the energy input balances (as it must) with the dissipation, both decaying faster at $T^{-4/3}$. This is thus consistent with the suggested interpretation; in turbulent remixing there would be a lot of energy moving around in the turbulent fluid flow compared with the energy input and dissipation. However, since breaking up the interface is liable to invalidate the assumptions made in deriving the scaling approximation for the interfacial force, although this appears to be a consistent solution to the NSE and energy balance equations, it seems unlikely that the system could, in fact, ever reach such a scaling regime[1].

Case of $\beta \neq 0$

With $\beta \neq 0$, the energy in the fluid velocity is changing over time, and there must, therefore, be a three-way balance between the terms in the energy balance equation, Equation (B.3), giving for the exponents,

$$2\beta - 1 = 2\beta - 2\alpha' = -\alpha - 1. \tag{B.11}$$

[1] Another possibility (that has not been investigated further here) is that this solution represents the asymptotic behaviour in 2-D. The turbulent energy cascade moves energy from small to large scales in 2-D, so $L_\nabla > L$ does not necessarily imply turbulent remixing as it would seem to in 3-D.

This gives $\alpha' = 1/2$, and $\beta = -\alpha/2$. Substituting these back into the NSE gives,

$$\rho T^{-\alpha/2-1} + \rho T^{-\alpha-1/2} \sim \eta T^{-\alpha/2-2\alpha''} + \sigma T^{-2\alpha}. \tag{B.12}$$

There is no solution to this with all four terms in balance with the same exponent; solutions can instead be found by considering the terms balanced off in pairs. Numbering the terms 1–4 from left to right, the pairing that gives the inertial region scaling is term 1 with term 4, and term 2 with term 3, giving $\alpha = 2/3$, and $\alpha'' = 5/12$, with $\beta = -\alpha/2 = -1/3$. The terms in the NSE thus have the following scaling,

$$\rho T^{-4/3} + \rho T^{-7/6} \sim \eta T^{-7/6} + \sigma T^{-4/3}. \tag{B.13}$$

The physical interpretation of this (as given in Section 2.4), is that energy from the interface goes first into large scale velocity motion via $\rho \partial \mathbf{v}/\partial T$. The nonlinear term, $\mathbf{v}.\nabla\mathbf{v}$, then transfers the energy from large length scales to small length scales where it is finally removed by dissipation, $\eta\nabla^2\mathbf{v}$. This is the turbulence "energy cascade". The Reynolds number, the ratio of the nonlinear to viscous terms, remains finite (satisfying the physical demand of Grant and Elder (1999)), while the domain size grows as $T^{2/3}$ (contrary to their own deduction that $\alpha \leq \frac{1}{2}$). The length scales associated with ∇ and ∇^2 both grow more slowly than $L(T)$, with $L_\nabla \sim T^{1/2}$, and $L_{\nabla^2} \sim T^{5/12}$, so there is a growing separation of length scales within the system. The dissipation is thus decoupled from the energy input from the interface, and no longer affects the domain growth rate. With this scaling, the local energy equation, Equation (B.4), looks like,

$$-\frac{\rho}{3}T^{-5/3} + \rho T^{-3/2} \sim -\eta T^{-5/3} + \sigma T^{-5/3} + \frac{\eta}{\rho}T^{-3/2}. \tag{B.14}$$

As with the case of turbulent remixing, the convective and diffusive terms balance each other, and are dominant, representing the energy moved around by the turbulent fluid flow.

The other possible pairings of terms must now be considered, to see if they produce any further viable solutions. First of all, it is not possible to balance term 1 with term 2, because the nonlinear term is a force perpendicular to $\mathbf{v}$ (this is obvious when it is written in the alternative form, $-\mathbf{v} \wedge \nabla \wedge \mathbf{v}$) and therefore it cannot change the magnitude of $\mathbf{v}$, impying $\beta = 0$, contrary to the original assumption.

The final possible pairing, term 1 with term 3, and term 2 with term 4, gives a solution

for the exponents of,

$$\alpha = 1/2 \quad \alpha' = 1/2 \quad \alpha'' = 1/2 \quad \beta = -1/4, \tag{B.15}$$

with the NSE terms looking like,

$$\rho T^{-5/4} + \rho T^{-1} \sim \eta T^{-5/4} + \sigma T^{-1}. \tag{B.16}$$

This solution has just one length scale in the system, as in the viscous region, but the velocity is decoupled from the interface, with $\mathbf{v} \sim T^{-1/4}$, while $\dot{L}(T) \sim T^{-1/2}$. This solution corresponds to the suggestion by Grant and Elder (1999) that the growth should slow to $L(T) \sim T^{1/2}$, so that the Reynolds number formed from $L\dot{L}$ would stay finite. However, the ratio of the non-linear to the viscous terms, R_2, actually grows with time, $R_2 \sim T^{1/4}$, corresponding to $\rho L\mathbf{v}/\eta$. So, quite apart from being physically rather strange to have only one length scale in the system but the velocity not following the interface, rather ironically, this solution, which corresponds to the concluded scaling of Grant and Elder, fails to satisfy their own criterion of producing a finite Reynolds number in the long time limit. In the local energy equation, Equation (B.4), this solution looks like,

$$-\frac{\rho}{4}T^{-3/2} + \rho T^{-5/4} \sim -\eta T^{-3/2} + \sigma T^{-3/2} + \frac{\eta}{\rho}T^{-3/2}, \tag{B.17}$$

so it also fails to balance energy locally, with the convective term dominating over all the other terms, thus it cannot represent an asymptotic solution.

Appendix C

Lattice symmetry

The aim of lattice-based models of fluids is to model the macroscopic equations that are isotropic while the underlying lattice is highly anisotropic – like a crystal. It was already known that a triangular lattice produces macroscopic isotropy (up to second rank tensors), from the study of the elastic moduli of hexagonal crystals, e.g. noted by Landau and Lifshitz (1959). Once the hexagonal lattice was shown to work in two dimensions, other lattices with the same property were quickly identified, for example, the 4-D face-centred hypercubic lattice. By projecting out the fourth dimension, 3-D simulations can be performed with this lattice. However, it is almost impossible to visualise or draw this 4-D lattice, and it is possible to get the same effect by instead considering more than one link between each site, so this is the scheme more generally used in practice.

The general condition for a lattice to be isotropic is as follows. In the LGA and LB models, each lattice direction has a velocity, $\mathbf{c}_i$ associated with it. The speed, $c_i = |\mathbf{c}_i|$, is chosen such that the propagation step moves all particles (n_i in LGA models) or distributions functions (f_i in LB models) to the next lattice site in exactly one time step. This means that the speed is some constant times the length of the link (e.g. 1 for a lattice direction, $\sqrt{2}$ or $\sqrt{3}$ for diagonals). There is also a set of weights, ω_i, that are chosen to make the lattice properties sufficiently isotropic. That is, the lattice velocities and weights must satisfy the following conditions,

$$\sum_i c_{i\alpha}\omega_i = 0, \tag{C.1}$$

where $c_{i\alpha}$ is the cartesian component in direction α of the lattice velocity $\mathbf{c}_i$.

$$\sum_i c_{i\alpha} c_{i\beta} \omega_i = 3c^2 \delta_{\alpha\beta}, \tag{C.2}$$

$$\sum_i c_{i\alpha} c_{i\beta} c_{i\gamma} \omega_i = 0, \tag{C.3}$$

$$\sum_i c_{i\alpha} c_{i\beta} c_{i\gamma} c_{i\epsilon} \omega_i = c^4 \{\delta_{\alpha\beta}\delta_{\gamma\epsilon} + \delta_{\alpha\gamma}\delta_{\beta\epsilon} + \delta_{\alpha\epsilon}\delta_{\beta\gamma}\}, \tag{C.4}$$

In other words, the fourth moment of the velocities must be equal to a sum of products of second moments (Wolfram, 1986). This last equation determines the weights, ω_i, for any given set of velocities, $\mathbf{c}_i$ (which define the lattice). In general, there will also be terms in the expansion of the fourth moment of the velocity vectors involving $\delta_{\alpha\beta\gamma\epsilon}$ (which is equal to 1 only if $\alpha = \beta = \gamma = \epsilon$), and the weights must be chosen so that these other terms cancel.

Appendix D

The BGK approximation

In this appendix, a brief description of the BGK approximation, (Bhatnagar, Gross, and Krook, 1954), is provided. The Boltzmann equation (real statistical mechanics, not numerical simulation) can be written,

$$\frac{\partial f(\mathbf{r},\mathbf{v},t)}{\partial t} + \mathbf{v}.\nabla f(\mathbf{r},\mathbf{v},t) = \mathcal{C}[f(\mathbf{r},\mathbf{v},t)] \tag{D.1}$$

where $f(\mathbf{r},\mathbf{v},t)$ is the one particle distribution function for a particle at position $\mathbf{r}$ with velocity $\mathbf{v}$. The collision operator $\mathcal{C}[f]$ can be written,

$$\mathcal{C}[f] = \int \mathrm{d}\mathbf{v}_1 \int \mathrm{d}\mathbf{\Omega}\, \sigma(\chi;g) g [f' f_1' - f f_1] \tag{D.2}$$

where $g = |\mathbf{v} - \mathbf{v}_1|$ and $\sigma(\chi;g)$ is the scattering cross-section, with f_1 denoting the particle being collided with (integrated over all velocities $\mathbf{v}_1$) and primes denoting the corresponding post-collision distribution functions.

This is far more detail than is manageable when the aim is a macroscopic statistical description of the system. Using dimensional analysis, the Boltzmann equation can be simplified as follows. The total scattering cross-section, $\int \mathrm{d}\mathbf{\Omega}\, \sigma(\chi;g)$, can be approximated by r_0^2, the range of the interparticle forces. The factor $g \sim \langle \mathbf{v} \rangle$, the average velocity. Thus the integral over $\mathbf{v}_1$ becomes, $\int \mathrm{d}\mathbf{v}_1\, g\, f_1 \sim n\langle \mathbf{v} \rangle$, taking one factor of f out of the brackets, where n is the number density of particles. This produces,

$$\mathcal{C}[f] \approx n\langle \mathbf{v} \rangle r_0^2 (f^{eq} - f), \tag{D.3}$$

where the choice of f factors in the brackets ensures that $C[f]$ vanishes at equilibrium. The numerical prefactors can be combined to give $nr_0^2\langle \mathbf{v} \rangle \sim 1/\tau_r$, an empirical factor of the order of the collision frequency. Thus Equation (D.1) becomes,

$$\frac{\partial f}{\partial t} + \mathbf{v}.\nabla f = -\frac{1}{\tau_r}\{f - f^{eq}\}, \tag{D.4}$$

the BGK approximation, first derived (more rigorously than this presentation) by Bhatnagar, Gross, and Krook in 1954. The BGK approximation works pretty well, it gives the Navier-Stokes equation, but doesn't get the transport coefficients quite right.

Appendix E

Moments of the χ and χ^2 distributions

In Chapter 4, reference is made to the moments of χ and χ^2 distributions. These are given here for $n = 1$ to 6.

n	mean	variance	skewness	flatness
1	0.7979	0.3634	0.9953	0.8692
2	1.2533	0.4292	0.6311	0.2451
3	1.5958	0.4535	0.4857	0.1082
4	1.8800	0.4657	0.4057	0.0593
5	2.1277	0.4729	0.3542	0.0370
6	2.3500	0.4777	0.3179	0.0251

n	mean	variance	skewness	flatness
1	1.	2.	2.8284	12.
2	2.	4.	2.	6.
3	3.	6.	1.6330	4.
4	4.	8.	1.4142	3.
5	5.	10.	1.2649	2.4
6	6.	12.	1.1547	2.

Table E.1: *Moments of χ_n (left) and χ^2_n (right) distributions.*

The χ distribution of the standardised variable x with unit variance is given by,

$$\frac{2^{-n/2+1}}{\Gamma(n/2)} x^{n-2} \exp(-\frac{x^2}{2}), \tag{E.1}$$

where $\Gamma(n/2)$ is the gamma-function. The χ^2 distribution of x is given by,

$$\frac{2^{-n/2+1}}{\Gamma(n/2)} x^{n/2-1} \exp(-\frac{x}{2}). \tag{E.2}$$

Appendix F

Correlation measures

In Chapter 4, the question of whether two quantities are statistically independent was considered. This appendix provides further discussion of the various ways to characterise correlations and dependencies in data analysis of continuous variables.

Correlation functions alone are not a sufficient test of whether two variables are independent of each other. Like pdfs, where it is necessary to know all the moments to decide whether or not they are the same, one would have to check correlation functions to all orders. A sufficient condition (definition) for quantities A and B to be independent is

$$prob(A, B) = prob(A)prob(B) \quad \forall \quad A, B.$$

Attempting to evaluate this directly for numerical data involves discretisation errors from the need to evaluate pdfs by binning the data into bins of finite width. Furthermore, there are no easy standardised quantitative measures that would characterise how badly the test failed or succeeded.

Cramér (1946) gives a test for discrete variables,

$$\varphi^2 = \sum_{i,k} \frac{(p_{i,k} - p_i p_k)^2}{p_i p_k} = \sum_{i,k} \frac{p_{i,k}^2}{p_i p_k} \; - \; 1, \tag{F.1}$$

where the mean square contingency, φ^2, is zero for independent variables and $\varphi^2 \leq m-1$ where m is the smallest dimension of the matrix formed by the probabilities $p_{i,k}$. As it

stands, this test does not generalise to continuous variables, but replacing $p_{i,k}/(p_i p_k)$ by $\log(p_{i,k}/(p_i p_k))$ produces,

$$\begin{aligned} \varphi_K &= \int \mathrm{d}x\,\mathrm{d}y\, P_{x,y} \log(P_{x,y}) - \int \mathrm{d}x\,\mathrm{d}y\, P_{x,y} \log(P_x) - \int \mathrm{d}x\,\mathrm{d}y\, P_{x,y} \log(P_y) \\ &= K(P_x) + K(P_y) - K(P_{x,y}) \geq 0, \end{aligned} \tag{F.2}$$

where $K(P_x)$ is a measure chosen to resemble informational entropy measures, and to make the continuous version of Equation (F.1) finite. For independent variables x and y, $\varphi_K = 0$. For completely dependent variables, $K(P_x) = K(P_y) = K(P_{x,y})$ so the maximum value of φ_K is just $K(P_x)$. In other words, if $K(P_x)$, etc., can be determined accurately, φ_K should be a good test of the dependence of variables.

The problem with evaluating $K(P_x)$, is that again, it requires evaluation of pdfs, and is therefore subject to the related binning errors. To calculate $K(P_x)$ for numerical data,

$$K(P(u)) = -\sum P(u)\Delta \log\{P(u)\Delta\}, \tag{F.3}$$

where Δ is the bin size used to form the distribution, $P(u)$. The formula for adjusting for different bin sizes and variances, is,

$$K(P(\sigma x, \sigma^2), \Delta) = K(P(x,1), \Delta/\sigma^2) = K(P(x,1),1) - \log(\Delta/\sigma^2), \tag{F.4}$$

where x is the normalised variable (in units of the standard deviation, σ), and $K(P(x,1),1)$ is the value of the entropy measure obtained by integrating the distribution,

$$K(P(x,1),1) = -\int P(x) \log(P(x))\,\mathrm{d}x,$$

(equivalent to summing over unit bins with no finite bin size errors).

Cramér gives one other test of dependence that involves the difference between linear regression and the actual value observed, that also captures any dependence to all orders of moments. This test also involves binning the data, so doesn't seem to have any obvious advantage over φ_K.

In this work, the probability distributions have been calculated by binning the data into 64 bins across a range of 16 standard deviations (σ), following the scheme of Briscolini and Santangelo (1994). Each bin was thus of width $\sigma/4$, which is quite a significant coarse-graining. Errors due to finite bin width can be quite large and

unpredictable, depending on where the bin falls in relation to the shape of the pdf, especially in regions where the shape is changing fast. A number of different theoretical and numerical methods were used to estimate the errors due to finite size bins in the pdfs and related quantities calculated in this study. The overall conclusion is that it is better to use moments and correlation functions rather than pdfs for quantitative comparisons wherever possible, especially where the data set is small so accuracy is limited. In practice, considering higher order correlations can put sufficient limits on dependence for most practical purposes, especially in this case where the errors in the measurement of higher moments are large. Therefore, $\langle A^2B^2 \rangle$ has been considered as well as $\langle AB \rangle$ to investigate correlations in the work presented this thesis. Ultimately, there is no way round the fact that if the data set is too small, it does not contain enough information to determine the higher moments or correlations of the distribution it is drawn from.

Bibliography

F J Alexander, S Chen, and D W Grunau. Hydrodynamic spinodal decomposition: growth kinetics and scaling functions. *Phys. Rev. B Rapid Comm.*, 48(1):634–637, 1993.

C Appert, J F Olson, D H Rothman, and S Zaleski. Phase separation in a three-dimensional, two-phase, hydrodynamic lattice gas. *J. Stat. Phys.*, 81(1/2):181–197, 1995.

S Bastea and J L Lebowitz. Spinodal decomposition in binary gases. *Phys. Rev. Lett.*, 78(18):3499–3502, 1997.

P Bhatnagar, E P Gross, and M K Krook. *Phys. Rev.*, 94:511, 1954.

P Bladon and J-C Desplat. **Ludwig** – a general purpose Lattice-Boltzmann code. *in preparation*, 1999.

A J Bray. Theory of phase-ordering kinetics. *Adv. Phys.*, 43:357–459, 1994.

A J Bray, B Derrida, and C Godrèche. Non-trivial algebraic decay in a soluble model of coarsening. *Europhys. Lett.*, 27:175, 1994.

M Briscolini and P Santangelo. The non-Gaussian statistics of the velocity field in low-resolution large-eddy simulations of homogeneous turbulence. *J. Fluid Mech.*, 270:199–217, 1994.

J Buckles, R Hazlett, S Chen, K G Eggert, D W Grunau, and W E Soll. Flow through porous media using lattice Boltzmann method. *Los Alamos Sci.*, 22:112–121, 1994.

M E Cates, V M Kendon, P Bladon, and J-C Desplat. Inertia, demixing and fluid flow in binary mixtures. *Faraday. Disc. Roy. Chem. Soc.*, 1999. To appear.

J R Chasnov. Simulation of the Kolmogorov inertial subrange using an improved subgrid model. *Phys. Fluids A*, 3(1):188–200, 1991.

S Chen, G Doolen, J R Herring, R Kraichnan, S A Orszag, and Z-S She. Far-dissipation range of turbulence. *Phys. Rev. Lett.*, 70(20):3051–3054, 1993a.

S Chen, G Doolen, R Kraichnan, and Z-S She. On statistical correlations between velocity increments and locally averaged dissipation in homogeneous turbulence. *Phys. Fluids A*, 5(2):458–463, 1993b.

S Chen and G D Doolen. Lattice Boltzmann method for fluid flow. *Annu. Rev. Fluid Mech.*, 30:329–364, 1998.

S Chen and T Lookman. Growth kinetics in multicomponent fluids. *J. Stat. Phys.*, 81 (1/2):223–235, 1995.

S H Chen, D Lombardo, F Mallamace, N Micali, S Trusso, and C Vasi. *Prog. Coll. Polymer Sci.*, 93:331, 1993c.

H Cramér. *Mathematical methods of statistics.* Princeton University Press, 1946.

S Cueille and C Sire. Block persistence. *Euro. Phys. J B*, 7(1):111–127, 1999.

B Derrida, A J Bray, and C Godrèche. Non-trivial exponents in the zero temperature dynamics of the 1d ising and potts models. *J. Phys. A*, 27:L357–L361, 1994.

B Derrida, V Hakim, and V Pasquier. Exact first-passage exponents of 1d domain growth: Relation to a reaction-diffusion model. *Phys. Rev. Lett.*, 75(4):751–754, 1995.

B Derrida, V Hakim, and R Zeitak. Persistent spins in the linear diffusion approximation of phase ordering and zeros of stationary gaussian processes. *Phys. Rev. Lett.*, 77(14):2871–2874, 1996.

B Efron. *The Jackknife, the Bootstrap and Other Resampling Plans.* Society for Industrial and Applied Mathematics, 1982.

J Eggers. Theory of drop formation. *Phys. Fluids.*, 7(5):941–953, 1995.

A N Emerton, P V Coveney, and B M Boghosian. Lattice-gas simulations of domain growth, saturation, and self- assembly in immiscible fluids and microemulsions. *Phys. Rev. E*, 55(1B):708–720, 1997.

V Eswaran and S B Pope. An examination of forcing in direct numerical simulations of turbulence. *Comp. and Fluids*, 16(3):257–278, 1988.

D Forster, D R Nelson, and M J Stephen. Large-distance and long-time properties of a randomly stirred fluid. *Phys. Rev. A*, 16(2):732–749, 1977.

M Frigo and S G Johnson. FFTW: An adaptive software architecture for the FFT. *ICASSP conference proceedings*, 3:1381, 1999.

U Frisch. *Turbulence: The Legacy of A N Kolmogorov.* CUP, 1995.

U Frisch, D d'Humières, B Hasslacher, P Lallemand, Y Pomeau, and J-P Rivet. Lattice gas hydrodynamics in two and three dimensions. *Complex Systems*, 1:649–707, 1987.

H Furukawa. Effect of inertia on droplet growth in a fluid. *Phys. Rev. A*, 31(2): 1103–1108, 1985.

H Furukawa. Multi-time scaling for phase separation. *J. Phys. Soc. Japan*, 58:216, 1989.

H Furukawa. Fluid n-vector model and its hydrodynamic ordering processes. *Phys. Rev. E*, 56(2):1437–1444, 1997.

M Grant and K R Elder. Spinodal decomposition in fluids. *Phys. Rev. Lett.*, 81(1): 14–16, 1999.

D Grunau, S Chen, and K Eggert. A lattice Boltzmann model for multiphase flows. *Phys. Fluids A*, 5:2557–2562, 1993.

A K Gunstensen, D H Rothman, S Zaleski, and G Zanetti. Lattice Boltzmann model of immiscible fluids. *Phys. Rev. A*, 43:4320–4327, 1991.

J Hardy, O de Pazzis, and Y Pomeau. Molecular dynamics of a classical lattice gas: Transport properties and time correlation functions. *Phys. Rev. A*, 13(5):1949–1961, 1976.

J Hardy, Y Pomeau, and O de Pazzis. Time evolution of a two-dimensional model system. I. Invariant states and time correlation functions. *J. Math. Phys.*, 14(12): 1746–1759, 1973.

T Hashimoto, H Jinnai, H Hasegawa, and C C Han. Late-stage spinodal decomposition in binary critical fluids – scaling function obtained over a wide q-space of 4 orders of magnitude. *Physica A*, 204(1-4):261–276, 1994.

F J Higuera, S Succi, and R Benzi. Lattice gas-dynamics with enhanced collisions. *Europhys. Lett.*, 9(4):345–349, 1989.

I Hosokawa and K Yamamoto. Intermittency of dissipation in a directly simulated fully-developed turbulence. *J. Physical Society of Japan*, 59(2):401–404, 1990.

S I Jury. Computer simulation of complex fluids using dissipative particle dynamics. *PhD Thesis, Edinburgh University*, 1999.

S I Jury, P Bladon, S Krishna, and M E Cates. Tests of dynamical scaling in 3-D spinodal decomposition. *Phys. Rev. E Rap. Comm.*, 59(3 PtA):R2535–2538, 1999.

V M Kendon, J-C Desplat, P Bladon, and M E Cates. 3-d spinodal decomposition in the inertial regime. *Phys. Rev. Lett.*, 1999. Accepted. *Electronic archive cond-mat/9902346.*

R M Kerr. Higher-order derivative correlations and the alignment of small -scale structures in isotropic numerical turbulence. *J. Fluid Mech.*, 153:31–58, 1985.

R M Kerr. Velocity, scalar and transfer spectra in numerical turbulence. *J. Fluid Mech.*, 211:309–332, 1990.

S Kida and Y Murakami. Statistics of velocity gradients in turbulence at moderate Reynolds numbers. *Fluid Dyn. Res.*, 4:347–370, 1989.

T Koga and K Kawasaki. Spinodal decomposition in binary fluids – effects of hydrodynamic interactions. *Phys. Rev. A*, 44(2):R817–R820, 1991.

A N Kolmogorov. Local structure of turbulence in an incompressible fluid at very high Reynolds numbers. *Dokl. Akad. Nauk. SSSR*, 30:299, 1941.

A N Kolmogorov. A refinement of previous hypotheses concerning the local structure of turbulence in a viscous incompressible fluid at high Reynolds number. *J. Fluid Mech.*, 13:82, 1962.

R K Kraichnan. The structure of isotropic turbulence at very high Reynolds numbers. *J. Fluid Mech.*, 5:497, 1959.

K Kubota, N Kuwahara, H Eda, and M Sakazume. Spinodal decomposition in a critical isobutyric acid and water mixture. *Phys. Rev. A*, 45(6):R3377–R3379, 1992.

A J Ladd. Numerical simulations of particulate suspensions via a discretized Boltzmann equation. Part 1. Theorectical foundation. *J. Fluid Mech.*, 271:285–309, 1994a.

A J Ladd. Numerical simulations of particulate suspensions via a discretized Boltzmann equation. Part 2. Numerical results. *J. Fluid Mech.*, 271:311–339, 1994b.

L D Landau and E M Lifshitz. *Theory of elasticity.* Pergamon, New York, 1959.

M Laradji, S Toxvaerd, and O G Mouritsen. Molecular dynamics simulations of spinodal decomposition in three-dimensional binary fluids. *Phys. Rev. Lett.*, 77(11):2253–2256, 1996.

I M Lifshitz and V V Slyozov. *J. Chem. Solids*, 19:35, 1961.

T Lookman, Y Wu, F J Alexander, and S Chen. Spinodal decomposition in fluids: diffusive, viscous and inertial regimes. *Phys. Rev. E*, 53(5):5513–5516, 1996.

V S L'vov and I Procaccia. Turbulence: a universal problem. *Physics World*, 8:35–40, 1996.

W Ma, A Maritan, J R Banavar, and J Koplik. Dynamics of phase-separation of binary fluids. *Phys. Rev. A*, 45(8):R5347–R5350, 1992.

L Machiels. Predictability of small-scale motion in isotropic fluid turbulence. *Phys. Rev. Lett.*, 79(18):3411–3414, 1997.

S N Majumdar, A J Bray, S J Cornell, and C Sire. Global persistence exponent for nonequilibirum critical dynamics. *Phys. Rev. Lett.*, 77(18):3704–3707, 1996.

N N Mansour and A A Wray. Decay of isotropic turbulence and low Reynolds number. *Phys. Fluids*, 6(2):808–814, 1994.

D O Martinez, S Chen, G D Doolen, R H Kraichnan, L-P Wang, and Y Zhou. Energy spectrum in the dissipation range of fluid turbulence. *J. Plasma Phys.*, 57(1):195–201, 1997.

D O Martínez, WH Matthaeus, S Chen, and D C Montgomery. Comparison of spectral method and lattice Boltzmann simulations of two-dimensional hydrodynamics. *Phys Fluids*, 6:1285–1298, 1994.

O Métais and M Lesieur. Spectral large-eddy simulation of isotropic and stably stratified turbulence. *J. Fluid Mech.*, 239:157–194, 1992.

A S Monin and A M Yaglom. *Statistical Fluid Mechanics vol 2.* MIT, 1975.

S A Orszag. Numerical methods for the simulation of turbulence. *Phys. Fluids Suppl. II*, pages 250–257, 1969.

S A Orszag. Numerical simulation of incompressible flows within simple boundaries. 1. Galerkin (spectral) representations. *Studies in Applied Maths.*, L(4):293–327, 1971.

S A Orszag and G S Patterson. Numerical simulation of three-dimensional homogeneous isotropic turbulence. *Phys. Rev. Lett.*, 28(2):76–79, 1972.

W R Osborn, E Orlandini, M R Swift, J M Yeomans, and J R Banavar. Lattice-Boltzmann study of hydrodynamic spinodal decomposition. *Phys. Rev. Lett.*, 75(22): 4031–4034, 1995.

S Puri and B Dünweg. Temporally linear domain growth in the segregation of binary fluids. *Phys. Rev. A*, 45(10):R6977–R6980, 1992.

Y H Qian, D d'Humières, and P Lallemand. Lattice BGK models for Navier-Stokes equation. *Europhys. Lett.*, 17(6):479–484, 1992.

Y H Qian and S A Orszag. Scalings in diffusion-driven reation A + B → C: Numerical simulations by lattice BGK models. *J. Stat. Phys.*, 81(1/2):237–253, 1995.

D H Rothman and J M Keller. Immiscible cellular-automaton fluids. *J. Stat. Phys.*, 52(3/4):1119–1127, 1988.

D H Rothman and S Zaleski. Lattice-gas models of phase separation: interfaces, phase transitions and multiphase flow. *Rev. Modern Phys.*, 66(4):1417–1479, 1994.

T Sanada. Cluster statistics of homogeneous fluid turbulence. *Phys. Rev. A*, 44(10): 6480–6489, 1991.

U Schumann and G S Patterson. Numerical study of pressure and velocity fluctuations in nearly isotropic turbulence. *J. Fluid Mech.*, 88(4):685–709, 1978.

Z-S She, E Jackson, and S A Orszag. Structure and dynamics of homogeneous turbulence: models and simulations. *Proc. Royal Soc. Lond. A*, 434:101–124, 1991.

Z-S She and S A Orszag. Physical model of intermittency in turbulence: inertial-range non-Gaussian statistics. *Phys. Rev. Lett.*, 66(13):1701–1704, 1991.

A Shinozaki and Y Oono. Asymptotic form-factor for spinodal decomposition in 3-space. *Phys. Rev. Lett.*, 66(2):173–176, 1991.

E D Siggia. Late stages of spinodal decomposition in binary mixtures. *Phys. Rev. A*, 20(2):595–605, 1979.

E D Siggia. Numerical study of small-scale intermittency in three-dimensional turbulence. *J. Fluid Mech.*, 107:375–406, 1981.

E D Siggia and G S Patterson. Intermittency effects in a numerical simulation of stationary three-dimensional turbulence. *J. Fluid Mech.*, 86(3):567–592, 1978.

G Stolovitzky, K R Sreenivasan, and A Juneja. Scaling functions and scaling exponents in turbulence. *Phys. Rev. E*, 48(5):R3217–R3220, 1993.

S Succi, R Benzi, and F J Higuera. The lattice-Boltzmann equation – a new tool for computational fluid dynamics. *Physica D*, 47:219–230, 1991.

M R Swift, E Orlandini, W R Osborn, and J Yeomans. Lattice Boltzmann simulations of liquid-gas and binary fluid systems. *Phys. Rev. E*, 54:5041–5052, 1996.

H Tanaka. Double-phase separation in a confined, symmetrical binary mixture – interface quench effect unique to bicontinuous phase-separation. *Phys. Rev. Lett.*, 72(23): 3690–3693, 1994.

O Theissen, G Gompper, and D M Kroll. Lattice-Boltzmann model of amphiphilic systems. *Europhys. Lett.*, 42(4):419–424, 1998.

A Vincent and M Meneguzzi. The spatial structure and statistical properties of homogeneous turbulence. *J. Fluid Mech.*, 225:1–20, 1991.

J von Neumann. *Theory of self-reproducing automata.* edited and completed by A Burks; University of Illinois, Urbana/Chicago, 1966.

A J Wagner and J M Yeomans. Breakdown of scale invariance in the coarsening of phase-separating binary fluids. *Phys. Rev. Lett.*, 80(7):1429–1432, 1998.

C Wagner. *Z. Elektrochem.*, 65:581, 1961.

S Wolfram. Cellular automaton fluids .1. Basic theory. *J. Stat. Phys.*, 45(3-4):471–526, 1986.

V Yakhot and S A Orszag. Renormalization Group analysis of turbulence. I. Basic theory. *J. Sci. Comp.*, 1(1):3–51, 1986.

K Yamamoto and I Hosokawa. A decaying isotropic turbulence pursued by the spectral method. *J. Physical Society of Japan*, 57(5):1532–1535, 1988.

J M Yeomans. *Statistical Mechanics of Phase Transitions.* Oxford Scientific, 1992.

Yeung and Brasseur. The response of isotropic turbulence to isotropic and anisotropic forcing at the large scales. *Phys. Fluids. A*, 3(5 pt1):884–897, 1991.

P K Yeung and Y Zhou. Universality of the Kolmogorov constant in numerical simulation of turbulence. *Phys. Rev. E*, 56(2):1746–1752, 1997.

A J Young. Investigation of renormalization group methods for the numerical simulation of isotropic turbulence. *PhD Thesis, Edinburgh University*, 1999.